②

EVALUATION OF CORROSION PROTECTION METHODS FOR ALUMINUM METAL MATRIX COMPOSITES

by

Harold J. Greene

DTIC
ELECTE
AUG 2 0 1992
S A D

A Dissertation Presented to the
FACULTY OF THE GRADUATE SCHOOL
UNIVERSITY OF SOUTHERN CALIFORNIA
In partial Fulfillment of the
Requirements for the Degree
DOCTOR OF PHILOSOPHY
(Materials Science)
August 1992

This document has been approved for public release and sale; its distribution is unlimited.

Harold J. Greene

401815

289 pg

REPORT DOCUMENTATION PAGE

Form Approved
OMB No. 0704-0188

1. AGENCY USE ONLY *(Leave blank)*

2. REPORT DATE 9 July 1992

3. REPORT TYPE AND DATES COVERED Final

4. TITLE AND SUBTITLE
Evaluation of Corrosion Protection Methods for
Aluminum Metal Matrix Composites

5. FUNDING NUMBERS NA

6. AUTHOR(S)
Harold J Greene, Major, US Army

7. PERFORMING ORGANIZATION NAME(S) AND ADDRESS(ES)
Corrosion and Environmental Effects Laboratory
Department of Materials Science, University of
Southern California
Los Angeles, CA 90089-0241

8. PERFORMING ORGANIZATION REPORT NUMBER NA

9. SPONSORING/MONITORING AGENCY NAME(S) AND ADDRESS(ES)
NA

10. SPONSORING/MONITORING AGENCY REPORT NUMBER NA

11. SUPPLEMENTARY NOTES
Ph.D dissertation completed by US Army Officer studying under the Army fully funded graduate schooling program.

12a. DISTRIBUTION/AVAILABILITY STATEMENT

This document has been approved for public release and sale; its distribution is unlimited.

12b. DISTRIBUTION CODE

13. ABSTRACT *(Maximum 200 words)*

See Attached

14. SUBJECT TERMS
Aluminum Metal Matrix Composites; Electrochemical
Impedance Spectroscopy; Anodizing; Chromate Conversion
Coating; Polymer coatings; SEM/

15. NUMBER OF PAGES 288

16. PRICE CODE

17. SECURITY CLASSIFICATION OF REPORT Unclassified

18. SECURITY CLASSIFICATION OF THIS PAGE Unclassified

19. SECURITY CLASSIFICATION OF ABSTRACT Unclassified

20. LIMITATION OF ABSTRACT Unlimited

NSN 7540-01-280-5500

Standard Form 298 (Rev. 2-89)
Prescribed by ANSI Std. Z39-18

ACKNOWLEDGMENTS

I owe many people thanks for their support and encouragement. My wife, Susan Myers, and my son Matthew, were always there to support me when I lost my bearings and became too consumed in my studies. My extended family, particularly my mother, father, mother-in-law and father-in-law, was always available when the task seemed too large or complex.

I am grateful to my advisor, Professor Florian Mansfeld. He took me on as a student without a research contract to support my work. He constantly challenged and encouraged me. I also appreciate the efforts of Professors Goo, Sadhal, Gershenzon, Langhon and Salovey who served on my Guidance and Dissertation Committees. The US Army paid my tuition, fees and salary for the past four years without which I never could have pursued a Ph.D. I was also assisted in this work by Dr. Bill Harringan of DWA Composites, Mr. Steve Holcombe of Duralcan USA, Mr. Andy Greer of ACMC and Mr. Russell Colon of Colonial Coatings who graciously supplied materials used in this research. Mr. Jack Worrall of the Center for Electron Microscopy and Microanalysis at USC assisted me in the SEM/EDS work and was a tremendous source of ideas. Mr. Subodh Ghonge printed the SEM micrographs. I owe a debt of gratitude to the

staff of the Science and Engineering Library at USC, particularly Dr. Bruce Bennion and Ms. Najwa Hanel. Bruce and Najwa went beyond the call of duty to locate obscure references and perform literature searches. I would like to express my thanks to my peers in the Corrosion Lab. I particularly thank Dr. C.H. (Raymond) Tsai for lending me his laser printer at a critical point in the preparation of this manuscript. Finally, I would like to acknowledge Dr. Hong Shih, Mr. Wang You and Mr. Hong Xiao for their insight and stimulating discussions.

Evaluation of Corrosion Protection Methods for Aluminum Metal Matrix Composites

Page

LIST OF TABLES

LIST OF FIGURES

Figure Page

Figure Page

ABSTRACT

Corrosion protection of Aluminum Metal Matrix Composites (MMC) using anodizing, chromate conversion coating and polymer coatings was investigated. Electrochemical Impedance Spectroscopy, DC polarization measurements, and Scanning Electron Microscopy (SEM) with Energy Dispersive X-ray Spectroscopy (EDS) were used. The materials studied included 6061/SiC, A356/SiC, 2009/SiC, 2014/Al_2O_3 and 6061/Al_2O_3 in various reinforcement concentrations. The electrochemical behavior of the MMCs without protection was also investigated.

MMCs were found to have similar corrosion and pitting potentials as the matrix alloy. The cathodic current density were found to be higher for MMCs with the current density increasing with reinforcement concentration. The increased current density is attributed to the interface between the matrix and the reinforcement particles which increases the corrosion rate.

Anodizing was performed on both Al alloys and MMCs. A new model is proposed for Al alloys. Anodizing and hot water sealing on MMCs was less effective than on Al. Improved results were noted for dichromate sealing.

SEM/EDS showed that the oxide was of the appropriate thickness, but that reinforcement particles had breached the barrier layer and were also integrated into the porous layer. The decreased effectiveness with the MMCs is believed to be due to a more porous oxide structure due to the reinforcement particles. The anodizing voltages on MMCs were found to be higher than on Al alloys.

Chromate conversion coating was also found to be less effective on MMCs than on Al alloys. SEM/EDS showed that the oxides formed were of similar thickness on both Al and Al MMCs. The decreased effectiveness was attributed to the reinforcement particles breaching the oxide and providing an improved cathode site. Polymer coatings on MMCs showed evidence of degradation with the degree of degradation increasing with reinforcement concentration.

Standard corrosion protection methods such as anodizing, chromate conversion coating and polymer coating are less effective on MMCs than on aluminum alloys. The effectiveness of corrosion protection methods decreased with increasing reinforcement concentration for all of the methods investigated. The effectiveness of the corrosion protection methods was also a function of the matrix alloy, but not a function of the reinforcement material. The reduction in effectiveness is believed to be due to the interface between the particles and the matrix.

1. INTRODUCTION

Aluminum alloys are used extensively in many applications, particularly within the aerospace industry. The demand for improved mechanical performance and weight savings in many applications has focused interest on Metal Matrix Composites (MMC). These materials are formed by the addition of a second phase, generally a ceramic material, to a metal matrix. The advantage of these materials is that improved mechanical performance can be combined with a decrease in weight. For instance, a 50 % modulus increase with a 10 % reduction in weight compared to the unreinforced matrix has been reported for Al/SiC MMCs (1).

Harrigan (2) has provided a history of the development MMCs. In general, research and development has focused on the use of light metals such as aluminum, magnesium, titanium, copper and nickel for matrix materials. The reinforcements have taken the form of continuous fibers or discontinuous fibers, whiskers or particles. These materials are fabricated by powder metallurgy methods, infiltration of liquid metal into preforms of the reinforcement, casting or spray deposition (3). The type of reinforcement impacts on the available fabrication method. Continuous fibers are used to make the strongest composites.

Continuous fibers can not be worked into final shape using standard metal working techniques due to the brittle nature of the fibers. Metal working also disturbs the distribution of the reinforcement which greatly affects the mechanical properties. Continuous fiber composites are also the most expensive to produce (3). For commercial applications, interest has focused on the use of discontinuous reinforcement. These materials are not as strong as continuous fiber composites, but they are less expensive and capable of being worked from billets into final shape. The most common reinforcement used is SiC particles (1). Aluminum MMCs produced with SiC particles are being used in the aerospace and automotive industry. The MMCs used in this study are commercially available were provided by manufacturers actively producing materials for applications.

The corrosion resistance of aluminum and aluminum alloys has been extensively studied. Aluminum alloys form a protective oxide film when exposed to air (4). Aluminum is an extremely reactive metal, but the oxide film causes aluminum to have good corrosion resistance in neutral solutions, where the oxide is stable. Aluminum is subject to general corrosion in alkaline or acidic solutions, where the oxide is soluble (5). In neutral solutions containing specific aggressive cations, including the halides, aluminum is susceptible to localized corrosion such as pitting and crevice corrosion. In view of this, many corrosion studies on aluminum are conducted in solutions containing chlorides.

Their are numerous accepted methods for protecting aluminum and aluminum alloys from corrosion. Three widely used methods are anodizing, chromate conversion coatings, and polymer coatings (6). These methods have been widely discussed in the literature and are commonly used alone or in combination in industrial practice.

In contrast to aluminum alloys, relatively little has been written in the literature about corrosion and protection of MMCs. Traszkoma (7) recently published a review of the available literature. A number of authors have reported that aluminum MMCs pit in chloride containing solutions, similar to aluminum alloys (8-16). Far fewer papers (8,17-19) address the application of standard aluminum protection schemes to aluminum MMCs.

The intent of this research was to evaluate the effectiveness of standard protection methods for Al alloys when applied to Al-based MMCs. Anodizing, conversion coating, and polymer coatings were chosen as the methods due to their frequent use in commercial applications. The materials used were discontinuously reinforced composites with various reinforcement types and volume fractions and different matrix alloys. All samples were tested in a solution containing chloride in which the samples without protection are known to be susceptible to localized corrosion. The intent of the research was to determine the effectiveness of standard protection methods for Al alloys on Al-based MMCs. In addition, the effect of reinforcement type, volume fraction and matrix alloy on the effectiveness of corrosion protection methods was investigated.

2. LITERATURE REVIEW

As background for the remainder of this dissertation, a review of aluminum corrosion, methods of corrosion protection of aluminum alloys and Al-based MMCs and corrosion studies of MMCs is provided in this chapter.

2.1 Corrosion and Protection Methods for Aluminum Alloys

Aluminum alloys have commercial applications in many industries. As a result, there is a wealth of information on corrosion and corrosion protection of Al alloys. The most relevant results are presented.

2.1.1 Corrosion of Aluminum and Aluminum Alloys

Aluminum in aerated solutions forms a natural protective oxide about 5 nm thick (5,20,21). As a result, Al alloys show good corrosion resistance in aerated solutions of pH 4 to 9. At high and low pH values, the oxide is soluble and uniform corrosion of aluminum occurs. The naturally formed oxide is an insulator. This suppresses the oxidation-reduction reactions necessary for corrosion to occur due to the high resistance to transfer of electrons across the film (5). The rate of uniform corrosion is higher on aluminum alloys with higher copper contents or intermetallic precipitates. The increase in corrosion rate has been attributed to the lower resistivity of the oxide film caused by the incorporation of copper or lower resistivity precipitates in the oxide (5) and to galvanic coupling between copper and aluminum (22).

The major corrosion problem with aluminum alloys is the localized breakdown of the passive film in the presence of an aggressive ion. Halide ions, including the Cl^- ion, are known to cause pitting on aluminum. In addition, the metal must be polarized above a critical potential known as the pitting potential. For aluminum in neutral, aerated solutions, the pitting potential is near the open circuit potential of the metal (23).

Preferred sites for pit initiation are flaws in the passive film. Electron microscopy studies suggest that surface films contain enough flaws to provide sites for pitting to initiate. Flaw density increases with increasing alloy content, particularly for copper, so that aluminum alloys containing significant copper levels are more susceptible to pitting (22,23).

2.1.2 Anodizing

Aluminum tends to form an oxide film when oxygen is available. Aluminum oxide is an insulator. In anodizing, the aluminum alloy is anodically polarized by the application of a constant voltage or a constant current in a suitable electrolyte. The applied polarization produces an electric field sufficient to move ions through the oxide and grow a thicker oxide (5,24). In addition, aluminum oxide is hard producing a more abrasive resistant surface (24).

Anodized aluminum may be produced in solutions in which the oxide is not soluble such as borate or tartrate solutions. Films formed in this way are thin, non-porous and insulating. The film growth will be limited by the applied potential. It is more common practice to anodize in solutions where the oxide is soluble such as phosphoric acid, chromic acid and sulphuric acid (25). Sulphuric acid is the most common electrolyte in industrial practice (24) and was used in this investigation. In solutions where the oxide is soluble, a duplex film is formed. The inner layer is commonly referred to as the barrier layer. It is thin, dense and highly resistive. The barrier layer thickness depends on the applied voltage, with the thickness being approximately 10 to 14 Å/V (6,21,24). The outer layer is commonly referred to as the porous layer and is thicker and porous

(6). The porous layer has been observed to have columns of hexagonal,close packed cells with a central pore in each cell (6). The pore structure has been observed with Transmission Electron Microscopy (TEM) to be uniformly distributed across the surface with the pores running perpendicular to the metal surface (6,21). The cell diameter and pore diameter are proportional to the formation voltage (6).

The principal reactions occurring in sulphuric acid anodizing have been summarized by Tajima (24):

$$Al ----> Al^{3+} + 3e^{-} \qquad (2.1)$$

$$2Al^{3+} + 3H_2O ----> Al_2O_3 + 6H^{+} \qquad (2.2)$$

$$SO_4^{2-} ----> SO_3 + O^{2-} \qquad (2.3)$$

$$2Al^{3+} + 3O^{2-} -----> Al_2O_3 \qquad (2.4)$$

The growth of the oxide layer in sulphuric acid involves the simultaneous formation of a new barrier layer as pores are being formed in the previous barrier layer (24). A barrier layer will form in approximately 25 seconds. After the initial formation of the barrier layer, a balance occurs between the barrier layer formation and its dissolution at the base of the pore. Growth takes place at both the metal/oxide interface and the oxide/electrolyte interface. At the metal/oxide interface, growth occurs by migration of the oxygen ion through the oxide under the influence of the applied electric field. At the oxide/electrolyte interface, the growth occurs due to the migration of the Al^{3+} cations through the oxide (6,21). A volume increase of about 50% occurs due to the formation of Al_2O_3 from Al. The film will penetrate the base metal for approximately 2/3 of the thickness and grow out from the original metal interface about 1/3 of the oxide thickness.

The corrosion resistance provided by the oxide film can be improved by sealing the porous outer layer. This can be done by placing the anodized piece in a steam environment or by boiling in solutions of distilled water, nickel acetate, or dichromate (25). In sealing, the oxide film is hydrated according to the reaction (24):

$$Al_2O_3 + nH_2O \text{----}> Al_2O_3 \cdot nH_2O \quad (2.5).$$

Values of n have been reported to be 1,2 or 3 (22,24,26). Hydration of the porous layer is acompanied by a volume increase. Hoar and Wood proposed that sealing occurred by an inward movement of the pore walls and a plugging of the pore ends (26). Evidence of the closing of the pore mouth has been provided by impedance studies, electron microscopy studies, and the inability to dye the oxide after sealing (6,22,26). The porous layer is easily dyed prior to sealing. After sealing, dying of an anodized piece is not possible due to the plugging of the pores (22). The reaction is not complete throughout the porous layer however.

Diffraction and TEM studies indicate that the unsealed oxide layer is amorphous. As sealing continues, crystalline hydrated oxide is seen originating at the surface. The crystalline structure does not extend through the porous layer. This is believed to be due to the plug which forms at the mouth of the pore and impedes the circulation of water into the porous layer to complete the sealing throughout the layer (6).

Dichromate sealing is used as an alternative to hot water sealing. In dichromate sealing, a boiling, aqueous solution of $Na_2Cr_2O_7$ or $K_2Cr_2O_7$ is used as the sealing bath. Dichromate sealing is a combination of sealing by hydration and the insertion of a reservoir of passivating agent in the form of hexavalent chromium (6,27).

Chromate ions chemisorb on the pore walls (19,21,22). In solutions of pH 2-6, chromium will be present in solution as $[HCrO_4]^-$ and $[Cr_2O_7]^{2-}$ (28). Hexavalent chromium is an extremely strong oxidizing agent as shown by the following reactions and standard potentials, E_o (27,29):

$$[HCrO_4]^{2-} + 7H^+ + 3e^- \text{---->} Cr^{3+} + 4\,H_2O;\ E_o = -1.35\text{ V} \quad (2.6)$$

$$[Cr_2O_7]^{2-} + 14H^+ + 6e^- \text{---->} 2Cr^{3+} + 7\,H_2O;\ E_o = -1.232\text{ V} \quad (2.7).$$

For chromium to be reduced from the 6+ to the 3+ valence state, a source of electrons is required. For barrier layers of anodized aluminum without flaws, the high resistivity of the layer to ion and electron flow will screen the metal from the strong oxidizing potential of hexavalent chromium. If defects form in the film, the hexavalent chromium will be reduced at the defect to form a protective chromium oxide and the exposed aluminum will be oxidized. The chromium oxide will repair the flaw in the protective film. This has process has been verified by X-ray Photoelectron Spectroscopy (XPS) studies. Chromium was found in the 6+ valence in the outer layers of aluminum oxide and in the 3+ valence at defect sites in the barrier layer (27). Sealing with dichromate solutions involves a compromise between hydration and sealing of the pores, which occurs best at neutral pH values, and incorporation of hexavalent chromium, which is most effective at low pH values (6,20,22,30). For aluminum alloys, a neutral solution is recommended to achieve a high degree of sealing, while still incorporating some of the hexavalent chromium.

2.1.3 Chromate Conversion Coating

Chromate conversion coatings are surface layers of low solubility, hydrated chromium oxide (6). The chromate conversion process is widely used as a surface pretreatment for aluminum alloys in the aerospace industries. A major reason for the widespread use of chromate conversion coatings is the self-healing nature of the coatings. The presence of hexavalent Cr is believed to provide a passivating agent in the coating to repair defects (6). Conversion coatings are formed by reaction of the chromate solution with the aluminum surface. A standard solution used in industrial practice contains chromic and hydrofluoric acids with potassium ferricyanide added as an accelerator. Typical films are from 10 nm to a few μm thick. Conversion coatings are formed by an oxidation-reduction reaction without an applied potential as opposed to the formation of anodized films under an applied potential (28,31).

There is much discussion in the literature about the formation mechanism for chromate conversion coatings. However, there is general agreement that the formation mechanism involves the reduction of hexavalent chromium to trivalent chromium. As mentioned in the discussion of dichromate sealing, hexavalent chromium is a strong oxidizing agent. The only substance available to be oxidized is the aluminum metal. The two primary reactions in the formation of conversion coatings are then (31):

$$Cr^{6+} + 3e^- \longrightarrow Cr^{3+} \quad (2.8)$$

$$Al \longrightarrow Al^{3+} + 3e^-. \quad (2.9)$$

Fluoride is found at the metal/film interface. The hydrofluoric acid is believed to remove the existing aluminum oxide to allow passage of the reacting species to the bare metal (31,33). The reactions that are believed to form the film are (6,31,33,34):

$$Al_2O_3 + 6HF \longrightarrow 2AlF_3 + 3H_2O \quad (2.10)$$

$$8H^+ + 2HCrO_4^- + 2Al \longrightarrow 2Al^{3+} + Cr_2O_3 \cdot nH_2O + (5-n)H_2O, \ n=1,2, \text{or } 3 \quad (2.11).$$

In the first reaction, the existing aluminum oxide is broken down, exposing the bare metal, which then is oxidized with the formation of a protective chromium oxide layer.

Surface studies of conversion coated aluminum show two distinct regions in the coating (31-32,35-36). The inner region has a thin layer of Al_2O_3 with evidence of some fluoride. The outer surface layer is composed primarily of hydrated Cr_2O_3.

There are conflicting results concerning the valence of chromium in the outer layers, however all studies agree that the chromium in the inner layer is in the trivalent state. Some studies report finding no hexavalent chromium in the outer layer (31-32,35-36). There is evidence that this result may be an artifact caused by ion milling and the use of high vacuum in XPS (34). Other studies have found that there is hexavalent chromium present in the outer layers, but that it is reduced during the surface analysis. In those cases where hexavalent chromium has been found, it has been at a low concentration, no more than 10 atomic percent, and it has been concentrated in the outer layers of the film (33-34,37-38). Even this low concentration is believed to explain the ability of conversion coatings to repair the passive layer after minor scratches or defects are introduced.

Chromate conversion coatings do not provide the same degree of corrosion protection as anodizing, but they are a substantial improvement over the as-received surfaces. Testing of conversion coated panels has revealed that the alloy composition and heat treatment are important in determining the effectiveness of conversion coatings. Heat treatment of AA 7075 to the T73 temper causes precipitation of copper precipitates which serve as pit initiation sites (39-41). These precipitates improve the mechanical properties of the alloy, but are detrimental to the corrosion resistance of the conversion coated Al.

2.1.4 Polymer Coatings

Polymer coatings are extensively used to protect aluminum surfaces. They are frequently used in conjunction with conversion coating or anodizing. Organic coatings protect metals by lowering the permeability to corrosive agents (42). In early studies of polymer coating protection, it was assumed that the coating acted as an impermeable membrane. However, permeability studies of water and oxygen through polymer coatings have shown that sufficient water and oxygen are available for the corrosion reaction to occur (43). It is now believed that diffusion of ions through the coating may be the rate controlling step (43). In the case of aluminum, the natural surface oxide is known to provide good corrosion protection in the absence of aggressive ions such as Cl^-. Therefore, the diffusion of Cl^- to the aluminum oxide-polymer coating interface is believed to be the rate controlling step for the corrosion reaction (44). Organic coatings can absorb up to a few percent by weight of water. Uniformly distributed water is not a problem, since it is only when the water begins to aggregate at the interface between the metal oxide and the coating that it will serve as an electrolyte for the corrosion reaction (44-45).

Kendig and Mansfeld (46) did an extensive study of the factors determining the effectiveness of organic coatings. They concluded that the initiation and propagation of corrosion are related to coating defects and loss of adhesion. The corrosion of polymer coated metals was found to involve the processes of defect formation, penetration of corrodents, and loss of adhesion leading to significant corrosion and failure of the part. Initially, the coating represents a barrier to transport of corrodents. Some transport of corrodents is to be expected for all coatings, but defect formation greatly increases the speed of the penetration (44). Defect formation also provides initiation sites for the corrosion reaction. After initiation of the corrosion reaction, the mechanical strength and adhesion properties of the coating become critical. Corrosion under the coating produces corrosion products which are less dense than the base metal. The volume expansion accompanying corrosion produces mechanical stresses on the coating causing loss of adhesion and cracking (46). In addition, the cathodic reaction under the coating produces a high pH (44):

$$1/2\ O_2 + H_2O + 2e^- \longrightarrow 2OH^- \quad (2.12).$$

Alkaline solutions are believed to have an adverse effect on adhesion of the coating to the metal. The loss of adhesion allows the transport of the corrodents parallel to the interface and leads to further corrosion of the metal. In addition, the protective oxide on Al is soluble at high pH values (5) leading to attack of the Al. In designing polymer coatings for protection of metals, the mechanical strength and adhesion of the coating to the surface as well as the permeability to water, oxygen and aggressive ions must be considered (46). Organic coatings can provide effective corrosion protection, but they can not be expected to completely isolate the metal from the environment.

2.2 Metal Matrix Composites

Metal Matrix Composites (MMCs) are of interest for their combination of higher strength, higher modulus and lower weight compared to their base alloys. They are formed by the addition of a second phase material to reinforce the metal matrix. The second phase materials used in this work were all ceramics. The reinforcing phase can be in the form of continuous fibers, whiskers or particulates. The best mechanical properties are provided by continuous fibers. However, these materials have the disadvantage of being the most expensive to produce. In addition, they have to be fabricated in their final shape. If these materials are mechanically worked to form them, the fiber distribution will be disturbed and the brittle fibers are likely to break causing a significant degradation in mechanical properties (2,3). For this reason, discontinuously reinforced composites are preferable. Discontinuous reinforcement provides slightly worse mechanical properties, but is significantly cheaper to produce and can be worked into the final shape. Most current applications of MMCs use discontinuous reinforcement. The most common reinforcement is SiC particles. The majority of the materials used in this study contain SiC reinforcement. All of the materials used were discontinuously reinforced composites provided by companies actively producing MMCs for commercial applications.

The methods used for fabrication of composites include powder metallurgy, liquid metal infilitration into forms(squeeze casting), standard casting of molten metal, and spray deposition of the matrix on the reinforcement. The most common methods of production for discontinuous composites are powder metallurgy and casting. These two methods were used to produce all of the materials for this study.

To produce composites using powder metallurgy, metal particles are mixed with reinforcement particles. SiC particles are commercially available in sizes from 0.5 microns to 100 microns. The volume fraction of the reinforcement phase ranges up to 40% in commercially available materials. The particles are then vacuum hot pressed to form a billet. The billet is then hot worked to a usable shape. The metal and oxide particles used to manufacture the composite will have an oxide skin on them. Working is critical for powder metallurgy composites to break down the oxide skins and promote bonding between the metal matrix and the reinforcement (2).

Cast composites are produced by mixing reinforcement particles with liquid aluminum. The composite can then be cast to a near final shape. Cast composites have a limit of about 20 volume percent reinforcement caused by viscosity limitations. In addition, casting introduces difficulties in maintaining uniformity of the reinforcement distribution due to the differences in density between the aluminum and the reinforcing phase. Cast composites will have the dendritic microstructure typical of casting.

A significant issue for both powder metallurgy produced composites and cast composites is the interface between the matrix and the reinforcement. Interface effects in composites have been extensively studied for their effect on the mechanical properties of MMCs. Interfaces in MMCs often include second phase particles, precipitate free zones, and solute enrichment or depletion. These can be caused by interfacial reactions, heterogeneous nucleation, interfacial diffusion, or a combination of these (47). These inhomogeneities can be expected to have significant effects on the corrosion behavior of the composite.

In cast composites, the reinforcement distribution may not be uniform as a result of settling due to the density difference between the matrix metal and the reinforcement. In addition, during the solidification of cast composites, the reinforcement phase tends to segregate between the dendrites of the cast microstructure (2). Aluminum carbide has been reported in Al MMCs with SiC reinforcement, particularly in MMCs produced by casting. During production of cast composites, liquid aluminum is in contact with SiC. Pure SiC is thermodynamically unstable in molten aluminum and aluminum carbide, Al_4C_3, may form (48):

$$4Al + 3SiC \text{ -------}> Al_4C_3 + 3Si \quad (2.13).$$

Aluminum carbide is soluble in water (49). The presence of a soluble phase in the oxide may be a source of defects in the oxide formed on the Al MMCs. In cast composites, a high Si content is usually added to improve the viscosity and also cause the formation reaction for Al_4C_3 to be favored in the opposite direction. Friend et al. (50) showed that in a cast AA6061/alumina composite, the interface was enriched in magnesium compared to the matrix.

There have been many studies of the interface structure and the homogeneity of composites produced by powder metallurgy. Lee et al. (51) studied the interface between aluminum and SiC using Transmission Electron Microscopy (TEM) with Energy Dispersive X-ray Spectroscopy (EDS) and found Al, Al_4C_3, SiC and Si at the interface. Strangwood et al. (52) found that the ceramic reinforcements caused major changes in the aging behavior of MMCs. In AA2000 and 7000 series based MMCs, they found segregation of Mg, Zn, and Cu to the interfaces. Nutt and Carpenter (47) studied the interface of AA2124 with SiC_w reinforcement and found MgO crystals. They also noted oxide particles on the reinforcement, which were attributed to oxide present on the particles prior to formation. In a 6061/SiC MMC, Nutt and co-workers using TEM found a 2 to 3 nm wide polycrystalline layer at the particle-matrix interface which contained Al, Mg, Si and oxygen. They concluded that it was Mg_2Si and non-crystalline Al_2O_3. Matrix compositions have also been seen to vary due to interface effects. In a AA2124/SiC composite, enrichment of Mg was seen in an area about 50 nm wide at the Al-SiC interface with a corresponding depletion of Mg in the matrix. $CuMgAl_2$ precipitates were also noted at the interface. SiC particle reinforcements tend to end up at grain boundaries. Grain boundary precipitation is commonly seen in Al alloys (47). In a study of AA2014/SiC_p (53), $CuAl_2$, $(Mn,Fe)_3SiAl_{12}$, $Cu_2Mg_8Si_6Al_5$ and Al_4C_3 were found at the matrix-reinforcement interface. The boundaries of the interface region contained MgO precipitates with traces of copper. In addition, zones free of $CuAl_2$ were found around the SiC particles with precipitation on the Al-SiC interface.

2.3 Corrosion of Aluminum Metal Matrix Composites (MMCs)

In contrast to the vast library of knowledge on corrosion of aluminum, there is relatively little in the literature about corrosion of Metal Matrix Composites

(MMCs). Trzaskoma recently published a review of the available literature (7).

Similar to aluminum alloys, the predominant mode of corrosion for Al MMCs is not general corrosion, but localized corrosion (7-15,54). The density of pits on a MMC has been reported to be greater than on the matrix alloy for the same immersion conditions. Pits on the MMCs are reported to be more uniform, shallow and widespread (7-8,11-14). A number of different theories have been proposed for the increased number of pits on the MMC. Aylor and Moran (8) attribute the increased number of pits to crevices formed at each matrix-reinforcement interface. Hihara and Latanision (9) believe that the corrosion on the MMC is greater due to coupling between the reinforcement acting as a cathode site and the aluminum matrix. Anodic and cathodic polarization curves were measured for the matrix and a cathodic polarization curve was measured for SiC. Using mixed potential theory, the corrosion current density was estimated for the matrix coupled to an equal area of SiC and was found to be 2.5 times larger than the matrix alone.

Measurements of the pitting potential for MMCs by Trzaskoma and co-workers (7,11-14), Shimzu et al (15) and by Sun et al.(10) indicate that the open circuit potential and the pitting potential in neutral, aerated solutions are in general the same for the MMC and the matrix.

It has been proposed that pits initiate at the interface between the matrix and the reinforcement. However, studies by a number of authors indicate that the interface is not a preferential site for pit nucleation (7,11-15,54). McCafferty et al. (11) constructed a model pit to verify that pits are not initiated at the interfaces. A surface was prepared with an exposed SiC particle on a polished aluminum matrix. The sample was polarized above the pitting potential and pits were allowed to develop. Pits developed away from the SiC/Al interface, but not at the interface. It was concluded that the interface was not a preferential site for pit initiation.

As in aluminum alloys, it has also been suggested that pits initiate at flaws in the oxide film formed on the aluminum matrix of the composite. Trzaskoma and co-workers (14) found that pits initiate at second phase precipitates in the matrix. These second phase precipitates were smaller and greater in number on the MMC than on the unreinforced matrix. The greater number of second phase precipitates provide more nucleation sites for pits on the MMC. Similar results were reported by Reynolds et al. (7). Paciej and Agarwala (54) found very different corrosion behavior between the exterior and interior of a AA7091/SiC$_w$ MMC. The matrix was not homogeneous and the surface was much more porous than the interior. Corrosion resistance of the surface was greatly improved by modifying the tempering procedure to homogenize the matrix. Paciej and Agarwala suggested that pitting sites result from elemental segregation and precipitation of impurities during forming.

There are a few evaluations of corrosion protection measures on MMCs in the literature. Trzaskoma and McCafferty (11,13) studied anodized composites and found that fewer pits formed on the anodized composites than on the as-received samples. The pitting potential shifted to more anodic values after anodizing. They concluded that this shift was due to the formation of a continuous barrier layer as on aluminum alloys. This conclusion is inconsistent with later results (12), where they measured the impedance of the anodized MMCs. The measured impedances were orders of magnitude below those expected for a continuous barrier layer of aluminum oxide. Mansfeld and co-workers (17,19) measured the impedance of Al/SiC MMCs and concluded that the oxide layers formed on the MMCs were different from those on Al alloys. Anodizing was found to be less effective on MMCs than on aluminum alloys, but provided an improvement over the as-received MMC. Aylor and Moran (8) reported the results for Al/SiC

MMCs exposed in a marine environment and concluded that the most effective protection was provided by polymer coatings or thermal sprayed aluminum and alumina. Mansfeld and co-workers (16,55-56) demonstrated that the corrosion resistance of AA6061/SiC was less than that of the AA6061 alloy. Impedance measurements on samples protected by anodizing, a chromate conversion coating, passivation in $CeCl_3$ solutions and by polymer coatings indicated much better corrosion resistance compared to that of the unprotected MMC. However, the protection methods were not as effective as on the matrix alloy.

3. ELECTROCHEMICAL TECHNIQUES

Potentiodynamic Polarization Measurements and Electrochemical Impedance Spectroscopy were used to characterize the corrosion behavior of the MMCs. The background of these techniques is presented here.

3.1 Potentiodynamic Polarization Curves

Polarization measurements are a common technique in electrochemistry and corrosion science. A corrosion reaction consists of two half cell reactions. The anodic reaction is an oxidation reaction and the cathodic reaction is a reduction reaction. The cathodic reaction in a neutral aqueous solution is the reduction of oxygen. The cathodic and anodic reactions for Al in a neutral, aqueous solution are (57):

$$Al \text{ -------> } Al^{3+} + 3e^{-} \quad E^{\circ}=-1.66\ V \quad (3.1)$$

$$0_2 + 2H_2O + 4e^{-} \text{ --------> } 4OH^{-} \quad E^{\circ}=0.401\ V \quad (3.2).$$

Both the anodic and cathodic reactions have a reversible potential, E°, at which the rate of the forward reaction is equal to the back reaction for that half cell reaction. When aluminum is exposed to a solution with O_2, the anode will be polarized toward the cathode and the cathode will be polarized toward the anode.

The corrosion potential, E_{corr}, will be at the intersection of the anodic polarization curve with the cathodic polarization curve. At the corrosion potential, the current from the anodic reaction will exactly equal the current from the cathodic reaction (57). To polarize the cell away from E_{corr}, an external current (or potential) source must be inserted. The excess current (or voltage) supplied is recorded. By polarizing to a more positive potential (anodically) from E_{corr}, the anodic reaction will dominate and the current supplied will be the anodic current at the given potential. Similarly, polarizing to a more negative potential (cathodically) allows the study of the cathodic reaction. For potentiodynamic polarization curves, the potential is varied at a given rate and the current supplied by the potentiostat is recorded. Typical anodic and cathodic polarization curves are shown in Figure 3.1. The potential is commonly plotted versus the logarithm of the current density, i. The intersection of the anodic and cathodic polarization curves will be at E_{corr}. The cathodic polarization curve will typically show a limiting current where the current density will be independent of potential. This limiting current is due to mass transport limitations (57). The anodic polarization curve for Al typically shows a region where the current density is nearly independent of the potential. This is the passive region and is due to the passive oxide film on Al (5). The breakdown of the oxide and the initiation of pitting will take place at a characteristic potential referred to as the Pitting Potential, E_{pit}. At E_{pit}, the current density will show a great increase (5). For Al alloys in aerated solutions, E_{pit} is near E_{corr} (23). In order to study the anodic polarization curve and accurately determine E_{pit}, the oxygen concentration of the solution is frequently lowered, or deaerated, by passing N_2 through the solution. Lowering the oxygen concentration shifts the oxygen polarization curve and lowers the limiting current density as shown in Figure 3.1. The resulting E_{corr} ($E_{corr,d}$ in Figure 3.1) is in the passive region of the anodic polarization curve. This allows the pitting potential and passive current densities to be determined. In this work, potentiodynamic polarization was done anodically in deaerated 0.5 N NaCl to determine the pitting potentials and the passive current densities for the MMCs. Cathodic polarization was performed in aerated 0.5 N NaCl.

3.2 Electrochemical Impedance Spectroscopy (EIS)

Electrochemical Impedance Spectroscopy has rapidly developed into an important technique for corrosion science and technology. EIS was used extensively in this work for in-situ monitoring. The background and application of EIS will be discussed as preparation for the discussion which follows.

3.2.1 Background

The increasing use of EIS in corrosion science and electrochemistry has led to the publication of a number of excellent reviews of the methods and techniques for measuring and analyzing EIS data. Recent reviews by Mansfeld and Lorenz (58), Gabrielli (59), Macdonald (60-61) and the book by MacDonald (62) are recommended. EIS is a non-destructive technique which is suitable for in-situ monitoring of many corrosion processes. EIS uses a small amplitude signal applied to an electrochemical cell to measure the impedance over a wide frequency range. A typical frequency range used might be from 65 kHz to the mHz region. It allows the study of many high impedance systems which were inaccessible with traditional DC electrochemical techniques. In addition, DC techniques use polarizations large enough to change the properties of the system under study. EIS uses a small amplitude signal, typically 10 mV or less, so that damage is minimal. A small amplitude signal is also necessary to insure that the system response is linear.

The impedance is measured around a fixed potential. To minimize the damage to the electrode, this potential is commonly the corrosion potential. The impedance of a system is measured by applying a small amplitude perturbation to the system and measuring the response. Commonly, an applied sinusoidal voltage signal is applied and the output is a current. The impedance may then be calculated as the input voltage divided by the output current remembering that both the input and output are vectors with a magnitude and phase. The frequency is varied during the measurement and the impedance is recorded as a function of frequency. With modern Frequency Response Analyzers (FRA) such as the Schlumberger model 1250 used in this study, the data is converted to the frequency domain via a Laplace Transform. The FRA calculates the impedance and records the impedance as a function of frequency. The impedance is a complex quantity with both a modulus and phase angle in the complex plane. Alternately, the impedance can be represented as a real and imaginary impedance component.

Impedance data may be displayed in a number of different forms. The two most common forms are the Bode plot and the Nyquist plot. In the Bode representation, the phase angle and the logarithm of the impedance modulus, Z, are plotted versus the logarithm of the frequency. In this representation, the frequency dependence of the impedance is shown directly. In this dissertation, the phase angle in the Bode representation is shown as a positive value for a capacitance. In the Nyquist format, Z", the imaginary component of the impedance, is plotted versus Z', the real component of the impedance. In this method, the frequency dependence is not shown explicitly. In addition, the axes are a linear scale causing the plot to be dominated by the higher impedances commonly seen at lower frequencies. Mansfeld (63) has argued that the standard plot for impedance should be a Bode plot. In this work, all data will be presented in the Bode format, however the Nyquist plot will be used to supplement the Bode plots when appropriate.

3.2.2 Equivalent Circuit Models (ECM)

The analysis of impedance data requires appropriate models based on the physical and chemical properties of the system under study. Modeling of the system with equivalent circuits allows the data to be numerically analyzed. In equivalent circuit modeling, the system is modeled by a network of resistors, capacitors and inductors which are correlated to the physical and electrochemical properties of the system. The impedance of common circuit elements is shown in Table 3.1.

A simple example of an ECM is the model for a charge transfer controlled reaction (figure 3.2) (58). R_s accounts for the ohmic resistances in the system. C_{dl} and R_p model the electrochemical interface. C_{dl} represents the double layer

Table 3.1 Impedance of common circuit elements

Element	Impedance
R	R
C	1/jωC
L	jωL

w=angular velocity=2πf; j=(-1)$^{0.5}$

capacitance at the metal-electrolyte interface. The double layer is an array of dipoles and charged particles at the corroding interface. The collection of oppositely charged particles at the interface is equivalent to a capacitance (64). R_p is referred to as the polarization resistance. The corrosion rate is inversely proportional to the polarization resistance (58). The impedance of this simple ECM is given as:

$$Z = R_s + \frac{R_p}{1+j\omega C_{dl} R_p} \quad (3.3).$$

Insertion of Z' and Z" in place of Z and rearrangement leads to:

$$(Z' - R_s - R_p/2)^2 + (Z")^2 = (R_p/2)^2 \quad (3.4).$$

This is the equation for a circle in the Z"-Z' plane (Nyquist format) with R_p as the diameter. Alternately, the impedance may be plotted in the Bode format. In the Bode format, the capacitor will act as a short circuit at high frequencies and R_s will be seen. At intermediate frequencies, the impedance is dominated by C_{dl} and the impedance will vary as the inverse of the frequency. At low frequencies, the capacitor will act as an open circuit and the impedance will be the sum of R_s and R_p (58).

Frequently, the impedance in regions where a capacitance is dominating the impedance will show non-ideal behavior. The impedance of an ideal capacitor would vary as the inverse of the frequency. In the Bode format, an ideal capacitor would have a slope of -1 in the modulus plot and a phase angle of 90°. The capacitance may be expressed as:

$$C=\varepsilon\varepsilon_o A/d \quad (3.5)$$

where ε is the dielectric constant of the material, ε_o is the permittivity of free space, A is the area normal to current flow and d is the thickness of the dielectric material. In the most general case, solid state physicists consider ε to be function of frequency and a complex number with both real and imaginary components (65). Therefore, a real capacitor may not exhibit a constant capacitance over a wide frequency band. This has been noted in many corrosion studies. Frequently, the Nyquist plot will show a depressed semi-circle and the Bode plot will show a phase angle less than 90° with the absolute value of the slope in the modulus plot less than 1. Many reasons have been proposed for this behavior including surface roughness, frequency dispersion of time constants due to local inhomogeneities in the dielectric material, porosity, mass transport effects and relaxation effects (62,66-70). In order to account for these effects,, non-ideal capacitors have been modeled according to the theory proposed by Jonscher (71) as:

$$Z_C=(jwC)^{\alpha} \quad (3.6).$$

The value of α for an ideal capacitor is -1. This model was only used for absolute values of α greater than 0.85.

ECMs have been developed for a number of frequently studied systems. These ECMs have been utilized by numerous authors. Mansfeld et al. (72) have given a review of the most common ECMs. The ECMs used in this study are presented in the following sections.

3.2.2.1 Corroding Aluminum Alloys

Aluminum alloys form a thin oxide layer when exposed to air. When these alloys are exposed to electrolytes containing Cl^- or other aggressive ions, the oxide layer is locally attacked resulting in the formation of pits. Mansfeld et al. (73-75) noted a characteristic impedance spectrum for pitting aluminum. The ECM is shown in Figure 3.3. The terms are defined in Table 3.2. Frers et al. (76) studied Al alloys in 0.5 N NaCl after polishing and deoxiding to remove the oxide layer.

Table 3.2 Description of Circuit Elements in the Pitting Model (73-75)

Element	Physical Significance
R_s	Ohmic resistances in the cell
R_p	Resistance of passive oxide layer
C_p	Capacitance of passive oxide layer
C_{pit}	Capacitance in pit
R_{pit}	Resistance in the pit
W	Transmission line term to describe the low frequency impedance
F	Area fraction of the surface which is pitted

They found that the impedance fit the ECM shown in Figure 3.4. They attributed C* to a thin oxide film in series with the double layer capacitance. L was believed to be due to a relaxation effect in the oxide and C was believed to be due to the formation of a soluble chloride salt.

3.2.2.2 Anodized Aluminum

The model for anodized aluminum in the recent literature (19,66,77-80) is shown in Figure 3.5. The model reflects the two-layer structure of anodized aluminum with a parallel RC combination for the porous layer, R_{po} and C_{po}, and a similar RC combination for the barrier layer, R_b and C_b. This model provides a good fit to the impedance spectra in the regions dominated by C_{po} and C_b, but shows significant deviations in the intermediate frequency range which is dominated by R_{po}. This is seen clearly in Figure 3.6, where experimental data for anodized aluminum (curve 1) are shown versus the fitted result using this model (curve 3). There are significant deviations in the range from 100 mHz to 1 kHz. In this range, the impedance has a slight frequency dependence which is likely due to the nature of the pores. The pores are modeled as a simple resistor. It is known from extensive TEM studies (6) that sealing does not completely fill the pores, but that a plug forms at the outer end of the pore. In the pore, there is incomplete sealing. A schematic of the electrical network for this case is proposed in Figure 3.7. The resistance of a pore is replaced by a plug resistance at the end of the pore in series with a pore solution resistance and a capacitance due to sealing products in the pore. The anodized surface has a regular pattern of these pores in parallel. To improve the model, R_{po} was replaced with Z_{po} as shown in Figure 3.8. Z_{po} is a frequency dependent impedance empirically expressed as:

$$Z_{po}=K(jw)^{-n} \quad (3.6).$$

K has the units of ohms or ohm-cm^2 when normalizing for the area. The term in parentheses is assumed to be dimensionless due to the addition of a constant equal to 1 sec/rad. This type of impedance relation is typical for porous electrodes with distributed resistances and capacitances in a network (60-62,81). The improvement in the fit is apparent in Figure 3.6, where the fit using the new model (curve 2) is essentially indistinguishable from the experimental data (curve 1).

3.2.2.3 Conversion Coated Aluminum

Mansfeld (39-40) proposed the use of the ECM in figure 3.9 for chromate conversion coated Al. The coating is characterized by a coating capacitance, C_c, in parallel with a coating resistance, R_c.

3.2.2.4 Polymer Coated Metals

The coating model in Figure 3.10 was proposed by Mansfeld and Kendig (46) for polymer coated metals. The terms are defined in Table 3.3. For very resistive, adhesive coatings without defects, the pore resistance will be very high. In those cases where there are no effective pores, R_{po} is essentially the coating resistance. The impedance at low frequencies will be the sum of R_s, R_{po} and R_p and the impedance spectrum will resemble the one-time-constant-model shown in Figure 3.9.

Table 3.3 Description of Circuit Elements in the Coating Model (46)

Element	Physical Significance
R_s	Ohmic resistance in the system
C_c	Capacitance of the polymer coating
R_{po}	Resistance of conductive paths through the polymer
C_{dl}	Double layer capacitance at corrosion sites on the metal substrate
R_p	Polarization resistance at corrosion sites

3.2.3 Fitting of Experimental Data to ECMs

ECMs allow the system to be characterized in terms of circuit elements with a physical significance. With the use of appropriate software, numerical fits of the ECMs to the experimental data may be performed. A number of different programs are available. The analyses presented here were done on an IBM compatible personal computer using software developed by Boukamp (82). This software uses a non-linear least squares fit methodology to vary the fit parameters to minimize the error between the fitted result and the experimental data. The details of non-linear least squares fitting can be found in the work of Macdonald (62).

4. EXPERIMENTAL APPROACH

This chapter will describe the materials used in this work, the details of sample preparation, the parameters used in the electrochemical testing and the electron microscopy experimental arrangement.

4.1 Materials

The MMCs used in this study (Table 4.1) were supplied by three manufacturers. The A356 samples were cast composites, while the remaining

Table 4.1-Materials List

Matrix Alloy	Reinforcement	Volume Percent Reinforcement	Manufacturer
6061	SiC particles	0,15,20,25,40	DWA
6061	Al_2O_3 particles	0,10,20	Duralcan
2009	SiC particles	20	ACMC
2009	SiC whiskers	15	ACMC
A356	SiC particles	0,10,20	Duralcan
2014	Al_2O_3 particles	0, 10	Duralcan

Manufacturers:

DWA Composites, Chatsworth, CA

Duralcan USA, San Diego, CA

Advanced Composite Materials Corporation (ACMC), Greer, SC

MMCs were produced by powder metallurgy. The alloying elements in the matrix alloys are shown in Table 4.2 (49,83).

Table 4.2-Matrix Composition (wt %)

Alloy	Cu	Mg	Fe	Si	Mn	Cr
A356	<0.2	0.35	<0.2	7		
2009	4.0-4.1	1.2-1.3	0.05			
2014	4.4	0.5		0.8	0.8	
6061		1		0.6	0.28	0.2

The high silicon content in A356 is necessary for fluidity in casting (49) and is used in composites to suppress the formation of Al_4C_3 (48). The high copper content in the 2009 and 2014 alloys is significant since studies of Al-4% Cu alloys have shown an increased tendency to pit. This has been attributed to an increased conductivity of the barrier oxide layer due to the presence of copper (5). The 2009 alloy from ACMC is a modified 2000 series (Al-Cu-Mg) alloy with a lower Mg concentration to minimize undesirable second phase precipitates (83). Even the relatively minor alloying elements shown for the 2009, 2014 and 6061 alloys are significant. The 2000 series (Al-Cu-Mg alloys) and the 6000 series alloys (Al-Mg-Si) are heat treatable alloys. Heat treatment and aging are performed to form intermetallic precipitates to improve the mechanical properties of the alloys (49). These precipitates have been found to preferentially segregate to the matrix-reinforcement interface in composites (47,51-52).

4.2 Sample Preparation

Samples for corrosion testing were prepared from sheets of the aluminum alloys and MMCs. Square samples approximately 8.3 cm (3.25 inches) on a side were cut. The sample size was chosen to allow immersion testing of circular areas of 20 cm^2 without approaching the edges. Prior to application of a protective coating, it is standard industrial and scientific practice to prepare the surface to provide a uniform and chemically active surface (25,84). Accordingly, the samples were degreased, cleaned and deoxidized prior to treatment with the appropriate protection method.

4.2.1 Sulphuric Acid Anodizing

The sample surfaces were degreased, cleaned and deoxidized prior to anodizing using the following procedure:

1) AA6061/SiC_p MMCs received from DWA had a surface smut as a result of the forming and shaping operations. For these materials, the surface smut was first removed by immersion in 20 g/l NaOH at 60° C for 30 seconds. The

samples were then wiped clean and washed in flowing water. This process was repeated three times or until the smut was removed.

2) The samples were wiped with hexanes and then degreased by immersion in boiling hexanes for 15 minutes. Following the hexane bath, the samples were air dried.

3) The samples were cleaned in a commercial silicate cleaner (Ridoline 53,Parker+Amchem Corporation) at 66° C for 10 minutes. The primary ingredients of the cleaner are tetrasodium pyrophosphate and sodium metasilicate. Following the cleaning, the samples were washed in running water for 5 minutes.

4) Deoxidizing was done in a commercial deoxidizing bath (Diversey Wyandotte 560, Parker+Amchem Corporation) for 40 minutes. The primary ingredients of the deoxidizer are sulphuric acid, nitric acid and hydrofluorosilic acid. The samples were washed in a water bath for 5 minutes after deoxidizing.

After preparation of the surface, the samples were dried and one side of the samples was masked with tape. For anodizing, the sample in preparation was mounted parallel to an AA6061 plate with a separation of 2.5 cm. The samples were immersed in a solution of 15 weight percent sulphuric acid. Anodizing is an exothermic process (24). In addition, the passing of electrons and charged ions across the barrier layer during the anodizing process will produce joule heating.

Sulphuric acid anodizing is a competitive process between formation of oxide and the dissolution of the oxide by the electrolyte (6) with the dissolution rate increasing with temperature. A cooling bath around the electrolyte and stirring of the solution were used to maintain the solution near 20° C. A current of 1 amp was applied with the sample as the anode and the second aluminum plate serving as the cathode. This gives a current density of approximately 1.5 amps/decimeter^2 (15 mA/cm^2). Anodizing was done for 40 minutes. A multimeter was connected between the anode and the cathode to allow monitoring of the voltage during anodizing. After anodizing, the samples were neutralized in a solution of 5% by weight $CaCO_3$ and washed in a water bath. These procedures are representative of those required to meet MILSPEC MIL-A-8625 for type II (Sulphuric Acid) anodized coatings. The procedure used here and the recommended procedure (24,85) are summarized in Table 4.3.

Table 4.3-Anodizing Procedure

Parameter	Anodizing Procedure	Recommended Procedure
Electrolyte	15 weight percent	10-15 weight percent
Temperature	20° C	21±1° C
Time	40 minutes	30-60 minutes
Current density	1.5 A/dm^2	1-2 A/dm^2

4.2.1.1 Hot Water Sealing

Samples were sealed by either hot water sealing or dichromate sealing. Hot water sealing was done for 40 minutes in boiling, deionized water. Anodized samples of AA6061 were also sealed for times ranging from 30 to 75 minutes to investigate the effect of sealing time.

4.2.1.2 Dichromate Sealing

Dichromate sealing was carried out in a boiling dichromate solution. Dichromate sealing is a compromise between the sealing effects, which are best accomplished at neutral pH, and the incorporation of chromium in the oxide, which is best accomplished at more acidic pHs (6,20,22,30). Three different solutions were used as shown in Table 4.4. Procedure 1 is an accelerated, optimized procedure

Table 4.4 Dichromate Sealing Procedure

Procedure	1 (6,25)	2	3 (85)
Solution	100 g/l $K_2Cr_2O_7$ + 13 g/l NaOH	100 g/l $K_2Cr_2O_7$	5 wt % $Na_2Cr_2O_7$
Sealing Time (minutes)	5	5	40

after Tomashov and Tyukina performed in a neutral solution (6,25). Procedure 2 is the same accelerated process without NaOH to neutralize the solution. Procedure 2 uses an acidic solution, so less sealing, but more incorporation of chromium is expected compared to procedure 1. Procedure 3 is a standard procedure recommended in the Metals Handbook (85) and is an acidic solution.

4.2.2 Chromate Conversion Coatings

Chromate conversion coatings were applied using an optimized procedure developed by Mansfeld (39-40) for AA7075-T73 based on a statistical testing procedure to determine the optimum parameters for coating. This follows earlier work by Bailin et al. (41).

Conversion coatings were prepared in a solution based on Alodine 600 (Parker+Amchem Corporation), a commercial conversion coating product. Alodine 600 is composed of approximately 30-40% by weight chromic acid, 40-50 % sodium fluoborate and 10-15 % potassium fluozirconate. Conversion coatings are frequently catalyzed with ferricyanide. However, coatings with ferricyanide have been found to have too high an electrical resistance for aerospace applications (41). Alodine 600 is a non-catalyzed conversion coating developed specifically for applications requiring a low electrical resistance coating.

The surfaces to be conversion coated were degreased, cleaned and deoxidized using the same procedure as with anodizing. The coating solution composition was 15 g/l Alodine 600, 4 volume percent Toner 22 (Parker+Amchem Corporation, approximately 5 wt % Sodium Hydroxide and 20 wt % Sodium Nitrate) and the remainder deionized water. The pH of the solution was adjusted to 1.7 to 1.8 through the addition of nitric acid. The solution was maintained at 38° C. The samples were immersed in the solution for 15 minutes, followed by a water bath and drying in air for 24 hours.

4.2.3 Polymer Coatings

Polymer coatings based on Araldite 985 (Ciba-Geigy) were applied. Araldite 985 is a thermosetting epoxy resin system recommended for protection of light metals. Araldite 985 was previously used for corrosion protection of magnesium with excellent results (86-87).

The procedure for applying Araldite 985 was provided by a metal finishing firm (88). Prior to application of the coating, the surfaces were degreased, cleaned and deoxidized as for anodizing. The samples were then placed in an oven at 200 °C for 30 minutes. The parts were cooled for 5 minutes, dipped in the resin for 30 seconds with mild agitation, the parts were dried in air for 20 minutes and then cured for 30 minutes in a 200 °C oven. The cooling, dipping, and air drying were then repeated to apply a second coat. The final cure was for 1 hour at 200°C. Coatings produced by this procedure had a thickness of approximately 30 μm.

4.3 Potentiodynamic Polarization Curves

Potentiodynamic polarization curves were measured in 0.5 NaCl. The measurement system consisted of a Princeton Applied Research Potentiostat Model 173 with a Model 376 Interface controlled by an IBM compatible computer using the Model 342 software from Princeton Applied Research.

The cathodic polarization curves were measured with the solution open to air. The anodic polarization curves were measured in 0.5 N NaCl deaerated by bubbling N_2 through the solution for at least 20 minutes or until the open-circuit potential stabilized. The anodic measurements were performed in a deaerated solution to allow an accurate determination of the pitting potential. The pitting potential of aluminum is very close to the open circuit potential in neutral, aerated solution (23). Determining the pitting potential in aerated solutions is problematic due to the close proximity of the two potentials. The samples were prepared by polishing with progressively finer polishing paper down to 1200 grit. The anodic curves were measured from a potential 20 mV cathodic (negative) to the open circuit potential to 500 millivolts positive to the open circuit potential. The cathodic measurements were made from the corrosion potential to a potential 300 mV more negative. For both curves, the polarization sweep rate was 1 mV/sec.

4.4 EIS

Electrochemical Impedance Spectroscopy (EIS) was used to provide in situ monitoring of the properties of the anodized films, conversion coatings and polymer coatings during immersion in 0.5 N NaCl. The impedance measurements were made using a Schlumberger Model 1250 Frequency Response Analyzer and a Schlumberger Model 1286 Electrochemical Interface controlled by an IBM compatible personal computer using the ZPLOT software package (Scribner and Associates, Charlottesville, Va). The experimental arrangement is shown in Figure 4.1. The samples were placed into the cell with an area of 20 cm^2 exposed to the electrolyte. The cell design is shown in Figure 4.2. The working electrode (WE) was the exposed area on the sample. The counter electrode (CE) was a 316L stainless steel disk which was passivated in concentrated HNO_3. The reference electrode (RE) was a saturated calomel electrode. A platinum wire connected to a 5 nF capacitor was placed parallel to the tip of the reference electrode and hooked in parallel with the reference electrode. This was done to mimimize the phase shift introduced by the potentiostat and the reference electrode at high frequencies (89).

Measurement parameters were set using the ZPLOT software. The FRA analyzer generated the perturbing signal which was a sine wave of 10 mV amplitude for most samples. For polymer coatings, the high impedance at low frequency required a higher amplitude signal. In this case, an amplitude of 100 mV was used. Measurements for polymer coatings were made for the frequency range from 65 kHz to 10 mHz. For the other systems, measurements were made from 65 kHz to 1 mHz. In general, ten data points per decade of frequency were collected. For some measurements at low frequencies, fewer points per decade were used to keep the measurement times reasonable. The measurement time used was ten seconds at frequencies above 1 Hz and 3 cycles below 1 Hz. For maximum sensitivity, the current measuring resistor in the electrochemical interface was matched to the measured impedance. The maximum measuring resistor in the 1286 Electrochemical Interface is 10^5 ohms. For polymer coatings and anodized samples, the impedance at low frequency frequently exceeds the maximum measuring resistor. On high impedance samples, the result was an increase in scatter at low frequencies.

4.5 Scanning Electron Microscopy/Energy Dispersive Spectroscopy

Scanning Electron Microscopy (SEM) was performed on selected samples using a Cambridge Model Stereoscan 360. Energy Dispersive X-ray Spectroscopy (EDS) using a Link Analytical Model 10000 Analyzer was used in conjunction with the SEM. Samples were examined from the top and in cross-section. Cross-sectional samples were prepared by cutting the samples using a wafering machine with an alumina blade. The samples were then cleaned using an ultrasonic cleaner with acetone. The samples were not polished in order to minimize damage to the surface. The cross-sectional samples were imaged to determine the thickness of the oxide layers for both conversion coating and anodizing. EDS was used in a point mode to identify SiC particles in the oxide films. In addition, the EDS was used in a scanning mode (90). By scanning the electron beam across the surface, maps of the relative Al, Si and O composition were produced. Combining the composition map with the image allowed determination of the oxide thickness and the distribution of the SiC particles in the oxide layer.

5. EXPERIMENTAL RESULTS

Electrochemical Impedance Spectroscopy (EIS) was used to study the response of as-received and protected samples to immersion in 0.5 N NaCl (open to air) for extended periods of time. The EIS results were supplemented by observation of the surfaces after immersion with optical microscopy and visual observations of the surfaces during immersion. Potentiodynamic polarization measurements were recorded to determine the pitting potential and the cathodic reaction kinetics of the as-received materials. In addition, Scanning Electron Microscopy (SEM) with Energy Dispersive X-ray Spectroscopy (EDS) was used for selected samples. In this chapter, the experimental results will be presented.

5.1 As-received Al Alloys and Al MMCs

Corrosion of Al alloys and Al MMCs was investigated with potentiodynamic polarization measurements, EIS and SEM.

5.1.1 Potentiodynamic Polarization Measurements

Polarization measurements were made for the 6061, A356 and 2009 series materials in 0.5 N NaCl with the anodic measurements performed in a deaerated solution and the cathodic measurements in a solution open to air. Figures 5.1-5.3 show the cathodic results for the 6061, A356 and 2009 composites, respectively. For each matrix alloy, the corrosion potential is independent of the reinforcement concentration as shown in Table 5.1. The maximum deviation is 16 mV from the value for the unreinforced matrix. In all cases, the polarization curves show a cathodic limiting current. In addition, the trend for the 6061 and A356 samples is for a higher current density with increasing reinforcement concentration. In order to compare the current densities as a function of reinforcement concentration, the current density at -900 mV was used. The results for 6061 and A356 are plotted in figure 5.4. The 2009 series composites do not show an increasing current density with reinforcement concentration, however the types of reinforcement are different and the current density is greater than on AA6061. The 15% sample is reinforced with whiskers, while the 20% sample has particulate reinforcement.

Table 5.1 Summary of Polarization Measurements

Matrix alloy	Reinforcement	E_{corr} (aerated) (mV)	Current density @ -900 mV (μA/cm^2) (Aerated)	Current density @ -800 mV (μA/ cm^2) (Deaerated)	E_{pit} (mV)
6061	0% SiC_p	-730	-8	9	-734
	15%	-730	-10	5	-744
	25%	-743	-19	10	-751
	40%	-728	-39	24	-726
A356	0% SiC_p	-732	-7	1	-716
	10%	-741	-16	4	-727
	15%	-748	-15	3	-733
	20%	-746	-23	2	-737
2009	15% SiC_w	-701	-19	28	-678
	20% SiC_p	-708	-14	11	-698

The anodic measurements were made in a deaerated solution to allow determination of pitting potentials, E_{pit}. Figures 5.5 to figure 5.7 show the measurements for the 6061, A356 and 2009 series composites, respectively. As expected, the anodic curves show a passive region of nearly constant current density. The magnitude of the passive current density at -800 mV is shown in Table 5.1. There does not appear to be a noticable pattern. The current densities for a given alloy are relatively close with the exception of the 6061/40% sample which has a much higher current density than the other 6061 samples. The 2009 series MMCs showed higher passive current densities than the 6061 or A356 MMCs.

A large increase in current density is noted as the samples are polarized anodically. This is the pitting potential, Epit, which is listed in Table 5.1. The pitting potentials for a particular matrix material are very similar with a maximum spread of only 25 mV. The 6061 series composites have pitting potential values clustered in the range -726 to -751 mV, the A356 alloys have values between -716 and -737 mV and values for the 2009 composites are between -678 and -698 mV. The pitting potential appears to be independent of the reinforcement concentration, but dependent on the matrix alloy.

5.1.2 EIS Results

Samples of the composite materials and the matrix alloys were exposed to 0.5 N NaCl in the as-received condition. EIS was performed at frequent intervals to monitor the corrosion process in situ. In addition, the samples were visually observed in conjunction with the EIS measurements. The samples were exposed until substantial corrosion was noted, at which point the tests were concluded. The samples were then observed in an optical micrscope at a magnification of 30 times. Crevice corrosion occurred under the O-ring used to seal the cell (figure 4.1) on a number of the samples, particularly the A356 and 2014 samples. The results of the visual observations are summarized in Table 5.2. All samples showed pitting with the degree of pitting generally increasing with the reinforcement concentration. Individual pits were observed to form during the first day of exposure. After a few days, most samples showed large area fractions with white corrosion products on the surface.

Impedance measurements of the as-received samples revealed characteristic impedance spectra for pitting. Figure 5.8 is the spectrum for a 6061/10% Al_2O_3 sample after 7 days in 0.5 N NaCl. The spectrum is similar to that found by Mansfeld and co-workers (73-75) and fits their pitting model (Figure 3.3). At high frequencies, R_s, the solution resistance, occurs followed by a linear region in the modulus plot (log |Z| vs log f) at intermediate frequencies. This linear region is attributed to the capacitance of the passive oxide film and the capacitance of the corroding area in parallel. The phase angle minimum and the rise in the phase angle at low frequencies are typical for the pitting processes (73-75). Fitting of the experimental data to the pitting model shows an excellent correlation (figure 5.8). The fit parameters for figure 5.8 are shown in Table 5.3.

Table 5.2-Observations of As-received Samples after Exposure to NaCl

Material	Days to visual observation of first pit	Total Exposure time (days)	Observations after immersion
6061	1	21	75% of surface covered with corrosion products
6061/20% SiC_p	1	2	50% of surface covered with corrosion products
6061/25% SiC_p	1	3	80% of surface covered with corrosion products
6061/10% Al_2O_3	2	7	Numerous pits clustered along the O-ring, 10% of surface covered with corrosion products
6061/20% Al_2O_3	2	7	50% of surface covered with corrosion products
2014	5	5	4 pits, crevice corrosion under the O-ring
2014/10% Al_2O_3	4	7	numerous small pits, crevice corrosion under the O-ring
2009/15% SiC_w	16 hours	2	Heavily pitted, 80% of the area covered with corrosion products

Table 5.2 (cont.)

A356	1	91	Corrosion products over 50% of the surface, crevice corrosion under the O-ring
A356/10% SiC_p	1	5	2 pits, nearly entire surface oxide discolored, crevice corrosion under the O-ring
A356/15% SiC_p	5	5	Numerous pits, corrosion products deposited along the O-ring, crevice corrosion under the O-ring
A356/20% SiC_p	2	5	Numerous pits, nearly the entire surface is discolored, crevice corrosion under the O-ring

Table 5.3 Fit parameters for 6061/10% Al_2O_3 after 7 days of exposure

$R_p/(1-F)$	1.3×10^4 ohm
C_t	1.5×10^{-4} F
K/F	7.0×10^3 ohm
n	-0.7
R_{pit}/F	2.7×10^3 ohm

In figure 5.9, the impedance spectra for A356 MMCs after 1 day are compared to that for the A356 alloy. The impedance for the MMCs is lower than the alloy throughout the entire spectrum. Fit parameters for the spectra in figure 5.9 are shown in Table 5.4.

Table 5.4 Fit parameters for A356 MMCs after 1 day of exposure

Parameter	A356	A356/10% SiC	A356/20% SiC
$R_p/(1\text{-}F)$ (kΩ)	13	2.3	2.8
C_t (μF)	72	400	400
K/F (MΩ)	1.4	0.16	0.21
n	-0.74	-0.7	-0.89
R_{pit}/F (kΩ)	6.5	0.75	1.8

In addition to a new impedance element at low frequencies, Mansfeld and co-workers (73-75) noted an increase in the capacitance, C_t, upon the initiation of pitting due to the contribution from C_{pit}. This result was verified for some of the samples tested in this work, but not for all. Figure 5.10 shows the capacitance, C_t, versus time for the EIS data in figure 5.9. There clearly is an increase of the capacitance in the first few days. Figure 5.11 shows the impedance spectra as a function of exposure time for 6061/10% Al_2O_3. Close examination of the data shows that the highest impedance in the capacitive region occurs for the longest exposure time, 7 days. The capacitance, C_t, for this MMC as a function of exposure time is shown in figure 5.12. The capacitance shows an initial increase, but this is followed by a decrease. This pattern was also noted for A356/15% SiC, 6061/25% SiC and a 6061 sample. It is apparently characteristic to have some instability in the capacitance during pitting. The results here indicate that C_t may increase or decrease following pit initiation.

During this work, it was noted that the pitted area exhibited capacitances far in excess of the theoretical double layer capacitance of 20 μF/cm^2. Similar results have been noted by other authors (91-93). In order to determine the response of an active aluminum surface of known area, a 1 cm^2 disk of AA6061 was cleaned in 20 g/l NaOH for 30 minutes, polished to 1200 grit, immersed in a commercial deoxidizer (Diverssey 560 from Parker+Amchem Corporation) and the impedance measurement performed. The impedance spectrum is shown in figure 5.13. The impedance at high frequencies shows a solution resistance for frequencies above 10 kHz, a capacitive region, an inductance near 10 Hz, and another capacitance at low frequencies. This impedance spectrum is similar to that reported by Frers et al. (76) and Bessone et al. (94). The model used by Frers et al. (76) is shown in Figure 3.4. Table 5.5 compares capacitance values obtained by fitting the spectrum in figure 5.13 to the Frers model and the results of Frers et al. The capacitances are in excellent agreement. The capacitance at low frequencies is approximately 10000 μF/cm^2 in both cases. Capacitance values this large have been noted previously for actively corroding surfaces (91-93), but no satisfactory physical explanation for this result has been found.

Table 5.5 Fit results for spectra in Figure 5.13 compared to data reported by Frers et al. (76)

Parameter	Frers et al. (76)	This work
C (mF/cm^2)	9.6	9.1
C* (μF/cm^2)	6.58	6.9

5.1.3 SEM of Composite Surfaces

The surface of an as-received 6061/20% SiC$_p$ was examined in the SEM to determine the distribution of SiC particles at the surface. Figure 5.14 shows a typical view of the composite surface. Numerous white particles with an average size of approximately 5 μm on a side protrude from the surface. Typical SiC particles used in the manufacture of this composite are 5 μm on a side (95). Using the EDS detector, these particles were confirmed to be SiC. Apparently, the surface of the as-received MMCs contains reinforcement particles extending through the aluminum oxide.

5.2 Sulphuric Acid Anodizing

Sulphuric Acid Anodizing (SAA) was performed on both unreinforced alloys and MMCs. Sealing was performed in both hot water and dichromate solutions.

5.2.1 AA6061

SAA was performed on AA6061 samples. The process was validated by measuring the coating weight after anodizing in accordance with ASTM B137 and MILSPEC 8625 for SAA. For the anodizing procedure described in chapter 4, the coating weight was determined to be approximately 4.5 mg/cm^2 which is approximately seven times the minimum MILSPEC weight of 0.65 mg/cm^2. To investigate the effects of sealing, samples were prepared without sealing, sealed in hot water for various times, and dichromate sealed using three different procedures. The corrosion resistance was determined by exposure to 0.5 N NaCl.

5.2.1.1 Unsealed SAA AA6061

An unsealed sample was used for comparison with the sealed samples. It was exposed for 63 days after which no pits were noted visually. The impedance spectra for the unsealed surface are shown in Figure 5.15. The initial spectrum at 2 hours shows the solution resistance at high frequencies and a capacitive response in the remainder of the impedance spectrum. The experimental capacitance corresponds to the barrier layer capacitance. The capacitance of the unsealed sample as a function of exposure time is shown in Figure 5.16. The capacitance can be evaluated using the equation for a parallel plate capacitor,

$$C=\varepsilon\varepsilon_o A/d \qquad (5.1).$$

The dielectric constant for Al_2O_3 has been reported as approximately 8-12 (6,18,78,96-97). Using an average value of 10 for ε with the permittivity constant of free space (ε_o) of 8.85×10^{-12} F/m and an area (A) of 20 cm^2, a thickness (d) of approximately 180 Å is calculated. The anodizing voltage was approximately 18 volts which yields an anodizing ratio of 10 Å/V in good agreement with reported values of the anodizing ratio of 10-14 Å/V (6,21,24). The capacitance is stable over the entire test period. The resistance of the barrier layer is too high to be detected in the frequency range tested. This is most clearly seen by the phase angle remaining at a maximum down to the lowest frequency measured.

During exposure to NaCl, a new time constant appears at high frequencies. After 2 hours of exposure, the pores are not sealed and the solution resistance in the cell occurs at high frequencies. With increasing exposure time, pore sealing begins to be seen in the high-frequency impedance and phase angle. After 63 days, the impedance follows the model for the sealed oxide shown in Figure 3.8. Figure 5.17 and 5.18 show the time dependence of the pore impedance transmission line coefficient (K) and the pore impedance exponent (n). The initial values correspond to the solution resistance, but then rise toward values similar to those of the sealed oxides. With the rising impedance in the pores, the porous layer capacitance, C_{po}, begins to appear in the high frequency impedance. After 28 days, the high frequency phase angle shows a rise due to C_{po}. This rise is more pronounced after 63 days of exposure. C_{po} is plotted versus time in Figure 5.19. C_{po} for the unsealed oxide after extended exposure time is the same as for the sealed oxide. Without sealing, C_{po} is shorted by the low pore impedance. The combination of the rising pore impedance and the emergence of the porous layer capacitance in the spectrum indicate that self-sealing is occurring during the exposure.

5.2.1.2 Hot Water Sealing

Samples were prepared with sealing times of 30, 40, 60 and 75 minutes to determine the effect of sealing time. The samples were exposed to 0.5 N NaCl for at least 28 days. The sample sealed for 75 minutes was exposed for 63 days. No pits were noted on any of the samples after exposure. In figure 5.20, the impedance spectra after two hours are shown for the various sealing times. The impedance spectra for 40, 60 and 75 minutes are nearly identical. The spectrum for 30 minutes of sealing shows a lower impedance at the high and intermediate frequency ranges. In figure 5.21, the spectra for a sample which was sealed for 40 minutes are shown for 2 hours, 14 days and 35 days of exposure. The spectra show very little change with exposure time across the entire frequency range, which is typical for the hot water sealed samples.

The impedance spectra for hot water sealed samples were analyzed using the model for anodized aluminum in figure 3.8. The fitting results are summarized in figures 5.16-5.19. The barrier layer capacitance, C_b, can be used to estimate the thickness of the barrier layer and the anodizing ratios. The results of these calculations assuming a dielectric constant, ε, of 10 are summarized in Table 5.6. The anodizing ratios all fall within the expected range of 10-14 Å/V. Using the calculated thicknesses, an estimate of the barrier layer resistance can be made according to:

$$R=\rho d/A \quad (5.2),$$

Table 5.6 Barrier Layer Thickness and Anodizing Ratios

Sealing Time (minutes)	Initial Capacitance (μF)	Calculated Barrier Layer Thickness (Å)	Final Voltage (volts)	Anodizing Ratio(Å/V)
Unsealed	10.1	180	18	10
30	8.8	201	18.9	10.6
40	7.2	246	18.8	13.8
60	7.5	236	19	12.4
75	7.5	236	19.6	12

where ρ is the resistivity of aluminum oxide, d is the thickness of the barrier layer and A is the immersed area. The resistivity of alumina is 10^{11} to 10^{14} ohm-cm (83,32). Using a $\rho=10^{14}\ \Omega$–cm, d=200 Å and A=20 cm^2, the resistance of the barrier layer, R, is estimated as 10 MΩ. Since the impedance of the barrier layer capacitance in the frequency range shown in figures 5.15, 5.21 and 5.22 is less than the barrier layer resistance , the impedance spectra do not show the barrier layer resistance. Measurements to sufficiently low frequencies, where the impedance of the capacitance exceeds the barrier layer resistance, would allow the barrier layer resistance to be detected in the spectra. Figures 5.17 and 5.18 show the exponent, n, and coefficient of the transmission line term, K, describing the impedance of the pores. The exponents for the transmission line elements are in the range 0.15 to 0.22 for the sealed samples. The coefficient of the pore impedance in figure 5.18 has a nearly constant value of K=600 MΩ–cm^2 for the samples sealed for 40 minutes or more. The unsealed sample and the sample sealed for only 30 minutes show a much lower K. Therefore, a sealing time of 40 minutes was chosen for use with the anodized and hot water sealed composites.

In figure 5.19, $C_{p\infty}$ is plotted versus exposure time in NaCl for the various sealing times. $C_{p\infty}$ is similar for samples sealed for 40 minutes or longer. The capacitances are between 0.6 to 0.7 nF/cm^2. The sample sealed for 40 minutes was examined in the Scanning Electron Microscope in cross-section and the porous layer thickness was determined to be approximately 20 μm. Using the initial $C_{p\infty}$ of 14 nF (0.7 nF/cm^2) and equation 5.1, ε for the porous layer was calculated as 16.

5.2.1.3 Dichromate Sealing

In comparison to hot water sealing where the primary variable is sealing time, dichromate sealing may be accomplished in solutions of different composition and for varying times. The porous layer will have different properties as a function of the particulars of the sealing process. For this investigation, three different procedures were employed (Table 4.4). Procedure 1 is a neutral, dichromate solution with a pH of 7.6 and a sealing time of 5 minutes. Procedure 2 is identical to procedure 1 with the exception that NaOH is not added to the sealing bath to neutralize the solution. The sealing bath in procedure 2 has a pH of 3.6. Procedure 3 also uses a solution of pH 3.6, but with a sealing time of 40 minutes. Samples produced with the three procedures were exposed to 0.5 N NaCl for 71, 64 and 28 days respectively for procedures 1, 2 and 3. No pits were noted after exposure on any of the samples.

The impedance spectra for the three types of samples were quite different. Figure 5.22 shows the impedance spectra for all three procedures after 2 hours of exposure to NaCl. Procedures 2 and 3, which are acidic solutions, produced impedance spectra which were dominated by a capacitance, which is seen in the phase angle maximum near 90° from 10^3 Hz to 0.1 Hz and is due to the barrier layer. The initial spectra do not show the barrier layer resistance and are similar to those for the unsealed sample in Figure 5.15. The sample produced using the neutral sealing solution (procedure 1) showed spectra similar to those for hot water sealed samples. The two-layer structure is clearly seen in the phase angle with a maximum at high frequencies due to the porous layer capacitance and another maximum at low frequencies due to the barrier layer capacitance. In figure 5.23, spectra for the same samples are shown after 28 days of immersion. The sample produced with the neutral sealing solution (procedure 1) still shows the characteristic spectrum for sealed aluminum oxide. The other two samples have begun to show the same characteristic spectra with an additional time constant visible in the modulus and phase angle at frequencies above 10 Hz. Note that the impedance in the intermediate frequency range, 10 Hz to 1 kHz, is lowest for the sample sealed for 40 minutes in an acidic sealing solution (procedure 3). Solution 2 is also an acidic solution, but sealing was done for only 5 minutes. The fit results for these samples are shown in figures 5.24 to 5.27. The barrier layer capacitance is lowest for the sample sealed in the neutral solution. Calculation of the anodizing ratio was done as for the hot water sealed samples (Table 5.7).

Table 5.7-Barrier Layer Thickness and Anodizing Ratio for Dichromate Sealing

Sealing Method	Calculated Thickness (Å)	Anodizing Ratio (Å/V)
Procedure 1 (5 minutes in a neutral dichromate solution)	201	10.4
Procedure 2 (5 minutes in an acidic dichromate solution)	142	9.6
Procedure 3 (40 minutes in an acidic dichromate solution)	188	9.4

As was noted for hot water sealing, the anodizing ratio calculated after sealing is a function of the sealing process. Sealing in acidic dichromate solutions yields lower anodizing ratios than hot water sealing. The ratio decreases with increasing sealing time in acidic solutions. Comparing the anodizing ratios with the results for hot water sealing in Table 5.6, the anodizing ratio for procedure 1 is slightly larger than the ratio for the unsealed oxide, but slightly less than the ratio for hot water sealing for 30 minutes.

The capacitance of the porous layer, C_{po}, as a function of exposure time is shown in figure 5.25. For the samples sealed in acidic solutions, C_{po} is initially not seen due to the low impedance of the pores (19). As the pore impedance increases with time, the porous layer is seen in the measured frequency range. For procedure 3, the capacitance could only be detected after 28 days. For procedure 2, the capacitance was seen after 21 days and there was good agreement between C_{po} for procedures 1 and 2. The most obvious difference in the fitted parameters is in the transmission line term describing the pore impedance. The coefficient of the transmission line term, K, increases with time for all three cases (figure 5.26). It is largest for the neutral sealing solution with the lowest value for the longer time, acidic sealing solution. The exponent, n, is between 0.15 and 0.25 (figure 5.27) for all the samples after 15 days. This is similar to the results obtained for hot water sealing.

Sealing solutions 2 and 3 are acidic sealing solutions, but are slightly different in composition. To investigate the effect of sealing time on the oxide film, samples were anodized and sealed in sealing solution 2 for 5, 10, 20 and 30 minutes. The impedance spectra for the 5, 10 and 30 minute samples after 2 hours, 5 days and 62 days (64 days for the 5 minute sample) are shown in figures 5.28 to 5.30. After 2 hours of exposure (figure 5.28), the impedance spectra for all three samples are dominated by the barrier layer capacitance. After 5 days (figure 5.29), some self-sealing of the porous layer is evident. The impedance at high frequencies decreases with increasing sealing time. After more than 60 days of exposure, the self-sealing effect is more pronounced for the 5 minute sample than the 10 and 30 minute samples (figure 5.30). Fit results are shown in figures 5.31 to 5.34. The barrier layer capacitance, C_b, (figure 5.31) is stable and similar for all sealing times. The porous layer capacitance, C_{po}, (figure 5.32) shows an increase with increased sealing time. The pore impedance terms again show an exponent, n, between 0.15 and 0.25 after 15 days (figures 5.34), but the coefficient of the pore impedance, K, for 5 minutes of sealing is larger than the terms for longer sealing times (figures 5.33).

5.2.2 Metal Matrix Composites

Samples of the MMCs were anodized and sealed using the same procedures as for the AA6061 alloys. During the anodizing process, the current density was maintained at approximately 1.5 amps/dm^2 and the voltage was recorded as a function of time. A difference in the anodizing behavior of the composites versus the unreinforced alloys was noticed immediately in the voltage versus time behavior. Pure aluminum and aluminum with low concentrations of alloying elements will show a sharp rise in the voltage as anodizing begins. This rise will be followed by a small drop and then a constant voltage for the remainder of the anodizing period. The steep initial rise usually occurs in 25 seconds or less and corresponds to the formation of the barrier layer. A small drop is then seen as the barrier layer is breached by the first pores. At this point, a steady state is reached with the acid solution creating pores in the barrier layer and then reforming a new barrier layer (6,22,24). The MMCs show a much different voltage-time behavior. The initial rise in voltage is slower, a drop in the voltage is not seen and a final steady-state voltage is reached which is substantially higher than for the alloy. Figure 5.35 shows a typical plot of the voltage-time behavior for an AA6061 alloy and for two 6061/SiC$_p$ composites. The cell voltage for the MMCs is much higher than for the unreinforced alloy. The voltage rise is also slower as the reinforcement concentration is increased and the final voltage is higher as the reinforcement concentration increases. Since the initial voltage rise is due to the formation of the barrier layer, it is apparent that the barrier layer formation is different for MMCs as compared to AA6061. A voltage-time behavior similar to the MMCs was also noted for the A356 alloy without reinforcement which contains about 7% Si (Table 4.2). In figure 5.36, the voltage time behavior is shown for A356 and A356 with 15 % and 20% SiC_p. The cell voltage shows a slower rise than for AA6061 and the final voltage is much higher. Again, the final voltage is seen to be higher with increasing reinforcement concentration.

After anodizing, the MMC samples were sealed in either hot water or dichromate and exposed to 0.5 N NaCl as for AA6061.

5.2.2.1 Hot Water Sealing

Based on the results for AA6061 samples, a standard sealing time of 40 minutes was selected for the anodized MMCs. Table 5.8 is a summary of the results from exposure tests in 0.5 N NaCl for different MMCs with sulphuric acid anodizing and hot water sealing. In comparison to AA6061 alloys, the corrosion resistance of anodized alloys with higher alloying contents such as A356 and 2014 is lower.

The addition of composite reinforcement adversely affects the pitting resistance of the anodized MMCs. The number of pits observed visually after exposure to NaCl generally increases with reinforcement concentration.

Table 5.8 Exposure test results for anodized and hot water sealed MMCs

Matrix/Reinforcement	Exposure Time (days)	Number of pits
AA6061 Unsealed	63	0
AA6061 HWS	79	0
6061/15% SiC	28	2
6061/20% SiC	28	15
6061/40% SiC	28	11
6061/10% Al_2O_3	78	3
6061/20% Al_2O_3	28	15
AA2014	78	2
2014/10% Al_2O_3	79	4
A356	43	5
A356/10% SiC	28	15
A356/15% SiC	21	14
A356/20% SiC	21	20
2009/20% SiC_p	28	5

The anodized samples were monitored during exposure using EIS. The unreinforced AA6061 alloys showed the characteristic impedance spectrum for a two-layer structure. The impedance spectra for the MMCs did not have the same characteristics. Figure 5.37 shows impedance spectra for 6061/SiC MMCs as a function of SiC concentration after 7 days of immersion. A comparison of these spectra to those for AA6061suggests that the structure of the anodized layers on MMCs is different from that of the matrix alloy. The impedance of the MMCs is less than that of the matrix alloy in the entire frequency range and decreases with increasing reinforcement concentration. For AA6061, the capacitance of the porous layer, C_{po}, is seen at high frequencies followed by the pore impedance at intermediate frequencies. For the 15% and 20% MMCs, the porous layer impedance can be represented by a Constant Phase Element (CPE). The spectra can be analyzed with the model for anodized aluminum, but a CPE must be substituted for C_{po} in figure 3.8. A CPE may be expressed as:

$$Z_{CPE}=K(jw)^{-n} \quad (5.3).$$

The exponent n for the 15% and 20% MMCs is shown as a function of exposure time in figure 5.38. For the 15% sample after 2 hours of exposure, n is 0.84, which approaches the value of 1 expected for an ideal capacitor. However, for longer exposure times, n decreases. The 20% sample shows a slight initial drop in n before stabilizing near 0.6. The impedance spectra for the 40% sample are similar to those for bare aluminum (figure 5.9). The spectra are now dominated by a CPE with n equal to 0.8. There is no evidence in the spectra of more than one phase angle maximum as would be expected for the two-layer structure of anodized aluminum.

The impedance at low frequencies for AA6061 does not show the barrier layer resistance, R_b, in the measured frequency range. The MMC samples, however, show R_b at low frequencies. R_b for these samples (figure 5.39) is much lower than for AA6061 and decreases with increasing reinforcement concentration. Figure 5.40 shows R_b as a function of reinforcement concentration after 2 hours of exposure to NaCl.

In figure 5.41, the impedance spectra for an anodized and sealed 6061/15% SiC MMC are shown for exposure times of 2, 14 and 28 days. For the 2 day sample, there are shallow phase angle maxima near 10 kHz and 10 mHz. These maxima give evidence of a two layer structure. However, the lack of definitive maxima as in AA6061 (figure 5.21) clearly indicates a difference in the structure of the anodized layer for the MMC. With increasing exposure time, degradation was indicated throughout the impedance spectra and the high- and low-frequency maxima were absent. After 28 days, an additional phase angle maximum occurs at low frequencies. The Nyquist plot shows an increase in the imaginary component at low frequencies, which is similar to the response seen in pitting of as-received Al. A low-frequency phase angle increase was noticed shortly before pits were detected visually. The increase in the imaginary component can be clearly seen in figure 5.42, where the imaginary component, Z", is plotted versus frequency . For a sample with a continuous barrier layer, the low-frequency impedance will tend toward the barrier layer resistance and the imaginary component will decrease to zero. Z" shows a rapid decrease for the two day sample. After 14 days, Z" levels off at 10 mHz, while after 28 days it is clearly rising. The impedance spectra can be analyzed with the model shown in figure 5.43, which is a modification of the anodized aluminum model shown in figure 3.8. The porous layer capacitance, C_{po}, has been replaced with a CPE and an additional RC element has been added in series with the barrier layer resistance to account for the impedance of the corroding interface. The polarization resistance of the corroding interface, R_p, was found to be 35.5 kohm and the capacitance, C, to be 1.3 mF for anodized and hot water sealed 6061/15% SiC.

Figure 5.44 shows impedance spectra for A356 after anodizing and hot water sealing. The spectra for two hours of exposure show two shallow phase angle maxima near 50 mHz and near 100 Hz. These phase angle maxima and minima are not as distinct as for AA6061 (figure 5.21). Fitting of the spectra to the anodized aluminum model of figure 3.8 shows that the porous layer is characterized by a CPE with n=0.65. Degradation of the porous layer can be seen in the decrease in the impedance with exposure time at the intermediate frequencies. The distinct phase angle minimum seen with AA6061 and the initial A356 spectrum, corresponding to the pore impedance, is not seen in the spectra for 9 days and 35 days. After two hours of exposure, the barrier layer resistance is being approached at low frequencies as indicated by the decrease of the phase angle. With increasing exposure time, there is a large drop in the resistance. The decrease in the barrier layer resistance can be seen in the steep drop of the phase angle at low frequencies and the decrease of the low-frequency impedance. The barrier layer resistance as a function of exposure time (figure 5.45) shows a decrease of more than an order of magnitude. The barrier layer capacitance is still seen at low frequencies. The initial capacitance is approximately 19 μF (0.95 $\mu F/cm^2$). Using $\varepsilon=10$ for the barrier layer, a thickness of approximately 94 Å is calculated, which is far less than the values of 200 Å seen for AA6061 under similar conditions (see Table 5.6).

Figure 5.46 shows the spectra for A356 with 0, 15 and 20% SiC after anodizing, sealing and exposure to NaCl for 2 hours. As for the AA6061-based MMCs, the

A356-based MMCs show a lower impedance in the entire frequency range. The distinctive phase angle maxima and minima for wrought anodized aluminum alloys are absent. The barrier layer resistance, R_b, decreases with increasing reinforcement concentration. R_b for A356 is compared to A356/15% SiC in figure 5.45. As was the case with 6061-based MMCs, increasing additions of the reinforcing phase decreases R_b.

In figure 5.47, impedance spectra for 2009/20% SiC_p after anodizing, sealing and exposure to NaCl for 2,17 and 28 days are shown. As noted previously, the spectra for the MMCs are different from the spectra for anodized wrought aluminum alloys. The barrier layer capacitance, C_b, is seen in the phase angle maximum near 100 mHz after 2 days of immersion. By fitting the spectra to the model in figure 3.8, C_b was calculated as 49 μF and a barrier layer thickness of approximately 36 Å was estimated. The calculated barrier layer thickness for AA6061, A356 and 2009/20% SiC are compared in Table 5.9 which clearly shows that the thickness of the barrier layer is greatly decreased in A356 and 2009/20% SiC compared to the model AA6061 system.

The 2009/20% SiC sample showed a pit visually after 17 days, which was also detected in the impedance spectra after 17 days (figure 5.47). As noted previously for 6061/SiC MMCs, pitting leads to an increase in the imaginary

Table 5.9 Calculated Barrier Layer Thickness for AA6061, A356 and 2009/20% SiC_p

Material	Calculated Thickness (Å)
AA6061	246
A356	94
2009/20% SiC_p	36

component of the impedance at low frequencies. This increase in the imaginary component was observed as a small bump in the phase angle spectra near 10 mHz after 17 and 28 days. The increase in the imaginary component can be seen directly in the Nyquist plot (figure 5.47c).

The results presented so far have involved MMCs with SiC as a reinforcing phase. Since anodizing produces Al_2O_3, the use of Al_2O_3 reinforcement was investigated in an attempt to determine the effect of the reinforcement composition. Figure 5.48 shows impedance spectra after 2 hours exposure to NaCl for 6061 MMCs reinforced with 10 and 20% Al_2O_3 as well as the spectra for 6061/20% SiC for comparison. Comparison of the spectra for the Al_2O_3 samples in figure 5.48 with the spectra for AA6061 in figure 5.21 demonstrates that the characteristic two-layer impedance spectra for AA6061 are not found on the Al_2O_3 MMCs. The spectra for the 6061/Al_2O_3 MMCs are similar to those for the other MMCs with the spectra being dominated by a CPE. The barrier layer resistance shown by the low frequency limit of the impedance is much less for the

6061 MMC than for the unreinforced alloy. This is similar to the SiC reinforced MMCs. The impedance also decreases throughout the entire impedance spectrum with increasing reinforcement concentration as noted previously for 6061 and A356 MMCs. As shown in figure 5.48, the impedance for the 20% Al_2O_3 sample was lower over the entire frequency range than that for a 20% SiC sample.

In figure 5.49, the impedance spectra for AA2014 and 2014/10% Al_2O_3 are shown for two hours exposure to NaCl. The AA2014 sample shows an impedance spectrum similar to the spectrum for 6061 with phase angle maxima at high and low frequencies and a minimum at intermediate frequencies. As noted for the other MMCs, the addition of a reinforcing phase causes the impedance spectra to be altered. The minima and maxima of the phase angle are not as pronounced for the MMC. The barrier layer resistance is lowered and therefore occurs in the measured frequency range. Increasing additions of the reinforcing phase also cause a noticable decline in the high-frequency impedance, where the porous layer capacitance is seen in the spectrum for anodized AA6061.

5.2.2.2 Dichromate Sealing

Selected MMC samples were anodized and sealed using a neutral dichromate sealing solution (Procedure 1 in Table 4.4) or an acidic dichromate sealing solution (Procedure 2 in Table 4.4). The concentration of dichromate added to the sealing solution was identical in both cases, but NaOH was not added to the sealing bath in procedure 2 yielding an acidic solution. In both cases, a sealing time of 5 minutes was used. Samples of AA6061 were a yellow color after dichromate sealing. All MMCs sealed in dichromate were gray-green after sealing.

The effectiveness of the two different dichromate sealing procedures in preventing pitting was evaluated for the 6061/SiC MMCs (Table 5.10). Based on the increased effectiveness of Procedure 2 for the 20% SiC samples, procedure 2 was chosen as the standard procedure for the remainder of the MMCs. Exposure test results for MMC samples sealed with Procedure 2 dichromate sealing are shown in Table 5.11. Fewer pits were found on the MMCs with dichromate sealing than on samples sealed with hot water sealing (see Table 5.8).

In figure 5.50, the spectra for anodized and dichromate sealed 6061/SiC MMCs after 2 hours of exposure are shown. For comparison, the spectrum for similarly prepared AA6061 is also plotted. The impedance for the MMCs is lower than for the AA6061 sample throughout the frequency range of measurement. The phase angle maximum is lower for the MMCs than for the AA6061 sample. The barrier layer resistance is also lower for the MMC than the AA6061 sample. In figure 5.51, the fit results for the barrier layer resistance, R_b, and capacitance, C_b, versus volume percent of reinforcement are shown for 2 hours of exposure to NaCl. R_b decreases and C_b increases with increasing reinforcement concentration. In figure 5.52, R_b is plotted for 0, 15, 20 and 25% SiC as a function of exposure time. R_b is much lower for the MMCs and decreases with increasing reinforcement concentration. In figure 5.53, R_b for 20% SiC is plotted versus time for hot water sealing and dichromate sealing. R_b is significantly higher for dichromate sealing.

Table 5.10 Comparison of Exposure Test Results for Sealing Procedures 1 and 2

Material	Sealing Procedure	Exposure Time (days)	Number of Pits
6061/20% SiC	# 1	32	2
		28	1
	# 2	32	0
		28	0
6061/25% SiC	# 1	28	0
	# 2	28	0

Dichromate sealed AA6061 undergoes self-sealing during exposure testing. This can be clearly seen by comparing the spectrum after 2 hours in figure 5.22 with the spectrum in figure 5.23 after 28 hours. The high frequency impedance after 2 hours shows only the solution resistance, but after 28 days the spectrum resembles that for hot water sealing with the porous layer capacitance and pore impedance visible in the spectra. This sealing effect is much lower on the MMCs. Figure 5.54 shows the impedance spectra for a dichromate sealed 2009/15% SiC_w after 4 hours, 17 days and 28 days. The self-sealing effect is seen in a very small increase of the high frequency impedance, but this increase is much less than the increases of more than an order of magnitude for AA6061. In

Table 5.11 Exposure Test Results for Dichromate Sealed MMCs

Material	Exposure Time (days)	Number of Pits after immersion
6061/15% SiC	28	0
20%	32	0
25%	28	0
A356/15% SiC	28	0
2009/15% SiC_w	28	1
20% SiC_p	28	3
6061/20% Al_2O_3	28	7

addition, the phase angle does not show the clearly defined two layer structure with two phase angle maxima and a phase angle minimum. The spectrum in figure 5.54 also demonstrates the changes due to pitting. As was noted for hot water sealed samples, an increase in the imaginary component at low frequencies was observed for those dichromate sealed samples which showed pits after exposure. Pits were noted visually on this sample after 17 days and the imaginary component at low frequencies increased after 17 days of exposure. This can be seen by comparing the phase angles at low frequencies or directly by examining the Nyquist plots. In figure 5.55, the frequency dependence of the imaginary component, Z", is shown. The plot for 4 hours shows a maximum for Z", while after 17 days Z" shows an increase at the low frequencies. The imaginary component shows a further increase after 28 days.

5.2.2.3 SEM/EDS Results

Scanning Electron Microscopy (SEM) was used determine the thickness of the oxide layers formed on selected Al alloys and MMCs. Energy Dispersive X-ray Spectroscopy (EDS) was used in conjunction with the SEM to determine the distribution of reinforcement particles in the oxide.

The thickness of the oxide layer on an AA6061 sample after anodizing and hot water sealing was found with the SEM to be approximately 20 μm. Figures 5.56 and 5.57 show cross-sectional views of a 6061/25% SiC sample and an A356/20% SiC sample, respectively. An oxide layer thickness of approximately 22 μm for 6061/25% SiC and 25 μm for A356/20% SiC was measured. These oxide thicknesses are similar to those observed for AA6061.

In order to determine the distribution of reinforcement particles in the oxide, anodized and sealed samples were examined in the SEM in conjunction with the EDS detector. The electron beam was scanned across the surface and the relative composition of selected elements versus position was recorded. In figure 5.58, an image of the oxide formed on an A356/10% SiC sample is shown opposite the composition maps of aluminum, oxygen and silicon. The composition is scaled to the color with white indicating high concentrations of the element and black indicating absence of the element. By comparing the oxygen and aluminum maps with the silicon map, it can be seen that there are voids in the aluminum oxide in the same locations where Si is present. A356 has a concentration of 7% Si in the alloy, so the observed Si signal may be due to SiC reinforcement particles or elemental Si in the alloy. Si is distributed throughout the porous layer. The oxide-metal interface can be identified from the aluminum and oxygen maps.

The barrier layer is located at the oxide-metal interface. Comparison of the Si concentration map with the interface as determined from the oxygen concentration map shows that there are particles breaching the barrier layer. Figure 5.59 shows a composition map for an anodized 6061/25% SiC sample. As was seen in figure 5.58, there is Si in the porous layer and breaching the barrier layer. For AA6061, the amount of elemental Si in the alloy is negligible. Therefore, the observed Si signal is due to the SiC reinforcement. The SEM/EDS results show that the oxide layers formed on MMCs are of approximately the same thickness as on the matrix alloy and that the reinforcement particles are distributed throughout the porous layer and across the barrier layer.

5.3. Chromate Conversion Coatings

Chromate conversion coatings were applied to a selection of MMCs and to AA6061and AA7075-T73. Conversion coatings were applied followed by exposure testing in 0.5 N NaCl. EIS measurements were made during exposure. The coated surfaces were examined under an optical microscope after exposure testing. Selected samples were examined in the SEM from both top views and cross-sectional views.

5.3.1 Al Alloys and MMCs

Chromate conversion coatings were applied using Alodine 600 (Parker+Amchem Corporation). The coating procedure employed was based on an optimized procedure developed by Mansfeld (39-40) for AA7075-T73. To validate the procedures, the coating was done on AA7075-T73 first. In the study by Mansfeld, properly prepared conversion coatings on Al were found to follow the one time constant model shown in figure 3.9. They developed a quality control test based on scatter bands for the impedance modulus and phase angle. AA7075-T73 samples were prepared, exposed to 0.5 N NaCl and the impedance spectrum compared to the results of Mansfeld. The measured impedance spectrum fit into the scatter bands. In addition, the capacitance was calculated as 5.4 $\mu F/cm^2$ which is similar to the values measured by Mansfeld of 5-8 $\mu F/cm^2$. In addition, samples of AA6061, 6061/20% SiC and 6061/25% SiC were conversion coated and then stripped in an HNO_3 solution to determine the coating weight (28). The coating weight was calculated as 200 mg/ft^2, 260 mg/ft^2 and 320 mg/ft^2 for the AA6061, 6061/20% SiC and 6061/25% SiC samples, respectively. These coating weights are substantially larger than the 75 mg/ft^2 measured by Mansfeld (40).

After verifying the procedure, samples of the MMCs, AA6061 and AA7075 were conversion coated and exposed to 0.5 N NaCl. The conversion coated AA6061 and AA7075 samples were dull yellow in color. After conversion coating, the MMCs were green. The coated AA6061 sample was immersed for 12 days and the coated AA7075 for 24 days without developing pits. All of the MMCs, however, developed pits in 12 days of exposure. Most of the samples showed 20 or more small pits spread across the surface. The 6061 based MMCs were typical. The exposure test results for AA6061 and the 6061 based MMCs are shown in Table 5.12. EIS was used to monitor the samples during exposure to NaCl. For AA6061 and AA7075, the impedance spectra fit the one-time-constant-model (figure 3.9) for the entire exposure period.

Table 5.12 Exposure Test Results for 6061-based MMCs

Material	Exposure Time (days)	Number of Pits
AA6061	12	0
6061/15% SiC	28	30
20% SiC	12	20
40%	12	>20

In Figure 5.60, the impedance spectra for conversion coated AA6061 and 6061/SiC MMCs after 1 day of exposure to NaCl are shown. The impedance was lower over the entire frequency range for the MMCs and decreased with increasing reinforcement concentration. The impedance of the coating capacitance, C_c, dominates the impedance spectra from 1 kHz to 100 mHz. C_c increases with increasing reinforcement concentration as shown in Figure 5.61, where C_c determined after 2 hours of exposure is plotted versus reinforcement concentration.

As was noted with the anodized MMCs and the as-received materials, pitting on the conversion coated samples was accompanied by an increase in the imaginary component at low frequencies. After one day in NaCl, the impedance spectra for AA6061 and 15% SiC MMC follow the one-time-constant-model with the phase angle tending to 0° at low frequency (figure 5.60). The impedance spectra for 20% and 40% samples show deviations from the one-time-constant-model at low frequencies after only one day of exposure to NaCl. The phase angle shows a short plateau in both cases near 10 mHz. The Nyquist plot shows a deviation from the semi-circle expected for the one-time-constant-model. The increase in the imaginary component at low frequencies can be seen directly in Figure 5.62, where the imaginary component of the impedance is plotted versus frequency. After 2 hours, both the 20% and 40% MMCs show a decrease in the imaginary component as the impedance approaches the resistance of the coating. After 1 day, the imaginary component shows an increase at low frequencies in both cases.

The impedance spectra were analyzed using the one-time-constant-model shown in Figure 3.9 for those cases where the imaginary component reached a maximum and then monotonically decreased at low frequencies. When the imaginary component showed an increase at low frequencies as is characteristic of pitting, the impedance spectra was fit to the coating model shown in Figure 3.10. C_c increased with increasing reinforcement concentration as shown in Figure 5.63. In addition, C_c decreased slightly with exposure time. The coating resistance, R_c, was also a function of the reinforcement concentration. In figure 5.64, R_c is plotted versus time for a series of reinforcement concentrations. R_c decreased with increasing reinforcement concentration. For a given reinforcement concentration, R_c showed a slight increase with exposure time.

Pitting of the MMCs was accompanied by an increase in the imaginary component at the low frequencies. The impedance spectra for conversion coated 6061/20% SiC MMC for 2 hours, 6 days and 12 days of exposure to NaCl are shown in figure 5.65. The spectrum after 2 hours shows the typical spectrum for the one-time-constant-model with the low frequency phase angle tending to 0°. As noted in Figures 5.60 and 5.62, the spectra for this MMC began to show deviation from the one-time-constant-model after only 1 day. After 6 days, the changes in the modulus and phase angle at low frequencies are obvious. The additional circuit elements corresponding to the corrosion process are clearly seen in the Nyquist plot. The imaginary component is shown as a function of frequency in figure 5.67 and an increase can be clearly seen at low frequencies.

During pitting of the MMCs, an additional RC element was observed in the low frequencies. Using the coating model (Figure 3.10), these elements were calculated. The capacitance of the corroding area increased with increasing reinforcement concentration, while the polarization resistance of the interface decreased with reinforcement concentration. The capacitance and resistance of the corroding area are shown as a function of reinforcement concentration for 6061/SiC MMCs in figure 5.68.

5.3.2 SEM/EDS Results

Chromate conversion coated AA6061 and 6061/20% SiC samples were examined in the SEM from the top view as well as a cross-sectional view. In Figure 5.69, the top view of a coated AA6061 alloy is shown. The cellular structure with "mud cracking" between the cells is typical of thick chromate conversion coatings (6,28). In Figure 5.70, the structure of coated 6061/20% SiC is shown. The "mud cracked" structure is seen in the background. The large white particles seen in the foreground are SiC particles extending through the conversion coating. EDS was used to verify that these were SiC particles. Cross-sectional views of conversion coated AA6061 and 6061/20% SiC are shown in Figures 5.71 and 5.72, respectively. The thickness of the conversion coating is essentially identical for both the alloy and the MMC is approximately 3.3 μm.

5.4 Polymer Coatings

Polymer coatings are frequently used to protect metals from corrosion. Typically, polymer films are between 10 and 50 μm thick and have very high electrical resistances. The spectra for epoxy coated AA6061 after 2 days and 34 days of exposure to NaCl are shown in figure 5.73. These spectra are typical of spectra for protective films without defects. Both the impedance modulus and phase angle plots are very stable over long time periods for coatings without defects. Typical spectra are dominated by the coating capacitance, C_c. The typical spectrum for a protective coating can be fit to the One-Time-Constant-Model (OTCM) shown in figure 3.9.

The Schlumberger Model 1286 Electrochemical Interface and Model 1250 Frequency Response Analyzer used in this study are designed to measure a maximum impedance of about 10 MΩ with an input signal of 100 mV (98). In this work, samples with an area of 20 cm^2 were used. The coating resistances frequently exceeded 10 MΩ for an area of 20 cm^2. As expected, the data for impedances above 10 MΩ frequently show considerable scatter. Since the design range of the instruments is being exceeded, accurate determination of the coating resistance is not possible. For protective coatings without defects, the coating capacitance is the primary information which can be determined from EIS.

All of the coated MMCs showed the typical capacitive spectrum after two hours of exposure. The coating capacitance is related to the thickness, d, and dielectric constant, ε, of the coating according to equation 5.1. A micrometer was used to measure the thickness of the samples before and after coating to determine the coating thickness. Since the coating capacitance is linearly related to the inverse of the coating thickness, 1/d, a plot of C_c versus 1/d should be a straight line. These results are plotted in Figure 5.74 and an approximately linear relationship is observed. The result for the 6061/15% SiC MMC shows a significant deviation. There was a significant variation in the measured thickness of this MMC prior to coating. The agreement is excellent for the other samples. The slope of the C versus 1/d line is equal to $\varepsilon\varepsilon_o A$, from which ε was calculated as approximately 6.5. This value correlates very well with previous findings of 6.7 for this coating (87). Using equation 5.1, ε=6.5 and C_c calculated from the spectra after two hours, unknown coating thicknesses can be estimated.

Protective coatings have an impedance spectrum dominated by the coating capacitance, C_c. Coatings with defects will show decreases in both the modulus and phase angle. The decrease in the impedance is due to the formation of conductive paths in the coating. 2009/20% SiC, A356/10% SiC and A356/20% SiC MMCs with two coats of polymer, approximately 35 μm thick, showed failure in short exposure times. These samples were removed, polished and a third coat of polymer applied. After the application of a third coat, the samples remained capacitive for 34 days of exposure. Figure 5.75 shows the spectra for 2009/20% SiC with two and three coats of polymer. After two hours, the spectra for both 2 and 3 coats are dominated by C_c. After 3 days, the two coat sample has obviously failed. The high impedance of the two hour spectrum is not seen. The spectrum for the sample with 3 coats was still capacitive after 34 days of exposure.

Mansfeld and Tsai (99) have proposed the use of damage functions to provide a measure of coating damage. This damage function is based on a ratio of the impedance at two frequencies. For an ideal coating in the capacitive region, the capacitance is inversely proportional to the frequency as seen in Table 3.1. Accordingly, the impedance increases by one order of magnitude for an order of magnitude decrease in the frequency. Mansfeld and Tsai were able to correlate the degree of coating delamination to the ratio of the impedance of two frequencies in the capacitive region. The damage function is given as

$$D=\log(Z_{1\,\mathrm{Hz}}/Z_{100\,\mathrm{Hz}}) \quad (5.4).$$

An ideal coating without degradation would have a damage function of 2. Mansfeld and Tsai found that D was most sensitive for coating delamination of less than 0.1% of the coating area and was suitable for monitoring the initial stages of coating deterioration. In this work, the formula was modified to use the impedance at 100 Hz for the initial spectrum as the denominator for all times, while Mansfeld and Tsai used the impedance at 100 Hz determined at the time for which the damage function was being calculated. As seen in figure 5.75, coating damage was seen throughout the spectrum for some samples. Since the impedance spectra were stable for protective coatings (see for example Figure 5.73), D for an ideal protective coating is 2. The damage functions for the spectra in figure 5.75 are shown in Figure 5.76. The rapid degradation with application of only two coats is reflected in the rapid drop of the damage function. With application of three coats, the damage function is stable for 34 days of immersion. A356 MMCs and 2009 MMCs showed similar behavior. The damage functions for A356 MMCs are shown in Figure 5.77. Degradation was detected after only a few days with application of only two coats. With the addition of a third coat to bring the coating thickness to approximately 50 μm, degradation of the coating did not occur. A 6061/10% Al_2O_3 MMC was coated with approximately 45 μm of polymer coating. The damage function shows that degradation has not occurred (figure 5.78).

Two coats were applied to a series of 6061/SiC MMCs to compare the effect of reinforcement concentration on coating effectiveness. The resulting coatings were from 30 to 40 μm thick. The impedance spectra after 34 days of exposure are shown in Figure 5.79. Degradation is seen in the deviation from capacitive behavior for the MMCs. The degradation is most easily observed in the phase angle. The phase angle for the MMCs shows a maximum in the high frequencies, but a decrease is noted at frequencies as high as 10 kHZ for the 25% SiC sample. The degradation as a function of reinforcement concentration can be seen in Figure 5.80, where the damage function versus time is plotted for the MMCs. The damage function for AA6061 stays constant near 2, while the MMCs show a steady decline with immersion time. The damage function shows the greatest decline for the 25% and 40% samples. Hack and Scully (100) have proposed that the lower breakpoint frequency be used to monitor the early stages of coating delamination. The lower breakpoint frequency is the frequency at which the phase angle equals 45° at low frequencies. At this frequency, the imaginary component of the impedance, due to C_c, is equal to the real component from the sum of R_{po} and R_p (figure 3.10). With increasing damage to the coating, the lower breakpoint frequency is expected to rise and this is in fact noted for the 25% and 40% samples (figure 5.81). With increasing damage, another breakpoint frequency will be noted at high frequencies (99,100). The upper breakpoint frequency was not detected on these samples due to the relatively small amount of damage.

Loss of adhesion is a major failure mechanism for polymer coated metals. Adhesion loss leads to disbonding of the coating from the metal and an increase in the corroding area laterally on the surface. Cathodic sites develop a high (alkaline) pH in neutral solutions due to the cathodic reaction (44):

$$1/2\ O_2 + H_2O + 2e^- \text{------>}\ 2OH^- \quad (5.5).$$

Alkaline solutions are believed to have a detrimental effect on adhesion (46). To test the adhesion of the coating in the presence of an alkaline solution, holes of

0.05" (1.3 mm) in diameter were drilled in the coated surfaces. The coated MMCs with the artificial defect were then exposed to 0.5 N NaCl and polarized at -1250 mV with respect to the saturated calomel electrode. This potential is approximately 500 mV cathodic (negative) to the open circuit potential of Al. The predominant reaction at this potential is given in equation 5.5. Therefore, at the defect site, the solution will be highly alkaline. After 24 hours, the samples were removed from the solution and dried. The coatings were then scribed in an X pattern and a knife point check for delamination was performed as described in ASTM Standard G8 (101). The coatings were adherent in all cases with no delamination noted.

6. DISCUSSION OF RESULTS

6.1 Composites without Protection Methods

Aluminum alloys exhibit good corrosion resistance due to their protective oxide films. Corrosion of aluminum occurs predominantly through localized corrosion due to breakdown of the protective films (5). Exposure test results for aluminum alloys and aluminum composites in 0.5 N NaCl are summarized in Table 5.2. Pitting was detected visually on all samples in 5 days or less. For most of the samples, pitting was detected after only 1 day. Pitting attack was more severe on the MMCs than on the matrix and the pitting was more severe as the reinforcement concentration increased. The increase in the intensity of pitting for the MMCs has previously been noted by others (7-8,11-14). A number of authors have measured the open circuit potential and the pitting potential of MMCs (7, 10-15). and found that in general the pitting potential is nearly identical for MMCs and the matrix alloy. In addition, the open circuit potential is also nearly identical for the MMC and the matrix alloy and is very close to the pitting potential. The polarization results obtained in this work show similar results (Table 5.1). The anodic polarization curves are shown in figures 5.5 to 5.7. For a given matrix, the curves for the matrix alloy and the MMCs are very similar with no apparent pattern as a function of reinforcement volume fraction. The pitting potentials were within a few millivolts of open circuit potential and there was little variation in the open circuit potential for the materials from a given matrix alloy. This is the expected result if the pitting process is due to the localized attack of the aluminum oxide, since the oxide on the composite is expected to be the same as on the matrix. This result has been confirmed by McCafferty et al.(11) with a model composite surface. A number of authors (7,11-15,54) have reported that pits do not initiate preferentially at reinforcement particles. To verify this, McCafferty et al. fabricated a composite surface with an exposed SiC particle, immersed the surface and polarized above the pitting potential. Pits developed in the aluminum away from the interface. Apparently, the increased pitting noted on MMCs is not due to the anodic reaction. The behavior is a function of the matrix alloy, however. This is seen in the variation in the pitting potential and passive current density between the 2009 based composites and the A356 and 6061 based composites. The higher pitting potential and increased passive current densities are consistent with previous findings (5) on Al alloys with copper as a major alloying element. This is believed to be due to a less resistive oxide film due to the incorporation of some Cu in the oxide (5) and to galvanic coupling between the Cu and Al (22).

Cathodic polarization curves are shown in figures 5.1 to 5.3. The curves show a limiting current density in the range of measurement. For the A356 and 6061 matrix MMCs, the current density increased with increasing reinforcement concentration as seen in figure 5.4. SiC particles are present on the surface of the as-received MMC (figure 5.14). Increasing reinforcement would increase the SiC area fraction on the surface. For the 2009 series materials, a higher current density was seen for 15% SiC whiskers than for 20% SiC particles. Whisker particles would be expected to align themselves in the direction of working during mechanical forming. The aspect ratio of the whiskers used in this MMC is 15:1 (83), so it is possible that the exposed area of reinforcement is greater for a 15% whisker than a 20% particle sample.

The increasing cathodic current density with reinforcement seems to indicate that the reinforcement particles act as a cathode site; however, it is unlikely that the SiC is acting as a cathode site. Pure SiC is an insulator (18). The SiC used in the 6061 MMCs is a commercial grade with a purity of greater than 98% (95). If the surface were composed of only alumina and high quality SiC particles, the current density would be expected to be very low due to the highly resistive outer layer. However, in MMCs, an interface forms between the reinforcement and the aluminum matrix during manufacturing. A number of studies (2,47-48,50-53) have shown that the interface in MMCs commonly contain impurities. Segregation of alloying elements, the formation of Al_4C_3 and the formation of intermetallic precipitates have been found to occur at the interface. These impurities will prevent the formation of a continuous, resistive aluminum oxide-SiC outer layer across the entire surface. The presence of a more conductive phase will provide an easier path for the electron exchange necessary for oxygen reduction to occur. Due to the less resistive current path, a higher current density is seen. Trazskoma (14) has noted that pits do not preferentially initiate at the interface, but appear to occur at defects in the oxide film, particularly where there are Cu precipitates. The interface is acting as a preferential cathode site and is driving the anodic reaction at a higher rate in MMCs versus Al alloys.

The increased cathodic limiting current with volume fraction combined with the anodic curve being nearly independent of reinforcement concentration explains the nearly constant open circuit potential and pitting potential for MMCs. Figure 6.1 shows a schematic of the situation. The anodic half reaction has a sudden increase in current density at the pitting potential. The cathodic half reaction is superimposed upon this reaction to determine the open circuit potential and the current density. At open circuit, the anodic and cathodic current will be exactly equal. Since the cathodic reaction is in a limiting current region where the current density-voltage curve is nearly vertical and the anodic curve is essentially horizontal, the intersection of the two lines is at the same potential regardless of reinforcement. The current density at the intersection of the anodic and cathodic curves is the corrosion current and this increases greatly with reinforcement concentration.

Mansfeld et al. (73-75) noted that there is a characteristic impedance spectrum for aluminum undergoing pitting. According to Mansfeld et al., the spectrum shows an increase in capacitance, a change in the frequency dependence at low frequencies, and an additional maximum of the phase angle at low frequencies. Al MMCs show the characteristic phase angle and impedance behavior at low frequencies (figures 5.8, 5.9 and 5.11). An increase of the capacitance, C_t, with time was not seen in all cases. The time dependence of C_t for A356 MMCs is shown in figure 5.10. C_t increases greatly after one day of exposure in accordance with the findings of Mansfeld et al. In figure 5.12, C_t is plotted versus time for a 6061/10% Al_2O_3 sample. C_t shows an initial increase at 2 days. After 7 days, C_t has decreased to a value below that of the initial C_t. It should be noted that Mansfeld et al. used the increase in C_t as an indicator of the initiation of pitting. In the 6061/10% Al_2O_3 sample and a number of other samples, pitting was noted and C_t initially increased followed by a decrease in C_t. Use of the capacitance measure alone as an indicator of pitting is dangerous in these cases. Making a measurement on samples following this trend after C_t had decreased could lead to the conclusion that pitting was not occurring when in fact it had initiated. However, the characteristic response at low frequencies reported by Mansfeld et al. (73-75) was noted in all cases.

The source of this capacitance should also be considered. Bessone et al. (94) and later Oltra and Keddam (92-93) considered this capacitance to be related to the surface oxide film. They used the formula for a parallel plate capacitor,

$$C = \frac{\varepsilon\varepsilon_o A}{d} \qquad (6.1),$$

to interpret changes in the value of this capacitance as changes in oxide thickness. In equation 6.1, ε is the dielectric constant of the oxide, ε_o is the dielectric constant of free space (also known as the vacuum permittivity) and is equal to 8.85×10^{-12} F/m, A is the area of the dielectric material (in this case, the oxide film) and d is the oxide thickness. ε and ε_o are constant for a given oxide, A should not change much unless there is alot of pitting, so changes in the capacitance were attributed to changes in the thickness. Frers et al. (76) attributed this capacitance to a series combination of the double layer capacitance and the oxide layer capacitance. Frers et al. do not explain why the oxide layer should be in series with the double layer. The double layer is expected to be present only in those places where the oxide was not present on the aluminum surface. If this is the case, then the oxide and double layer capacitances should be in parallel rather than series. Mansfeld et al. consider the capacitance to be due to the oxide and capacitance of the pit, C_{pit}, being in parallel according to:

$$C_t = FC_{pit} + (1-F)C_{oxide} \qquad (6.2).$$

F is the fraction of the surface area which is pitted. C_{pit} is expected to be of the order of an ideal double layer capacitance with a value of 10-40 μF/cm^2 (62,64,102-103). Assuming a typical air formed oxide thickness of approximately 50 Å (5) and a typical dielectric constant for aluminum oxide of approximately 10 (18,96-97), C_{oxide} may be estimated as approximately 1.5 μF/cm^2. Since C_{pit} is about an order of magnitude greater than the oxide capacitance, increases in F are expected to increase the total capacitance. This implicitly assumes that the oxide thickness remains constant. In addition, the assumption is made that F only increases. Were the fraction F to decrease due to repassivation of the surface, the capacitance could decrease. Based on the results of Bessone et al. and Mansfeld et al., the capacitance changes noted here are due to a combination of changes in the pitted area and the oxide thickness.

C_t was much higher for the MMCs than the matrix materials. In figure 5.9 the impedance spectra are shown for 3 reinforcement concentrations of an A356 MMC. The impedance of the MMCs is lower in the capacitive region indicating a higher capacitance. C_t versus time is plotted in figure 5.10. At first glance, it would appear possible that the increased capacitance is due to the presence of reinforcement particles in parallel with the oxide layer. The reinforcement particles would displace the oxide on the surface. This does not explain this result, however. SiC has a dielectric constant of approximately 10 (104) or approximately the same as the aluminum oxide. The particles are approximately 5 μm by 5 μm by 12 μm in size (95). Using equation 6.1, ε and ε_o are constant and the area of oxide displaced is equal to the area of the oxide particles. The thickness of the reinforcement particles is much greater than the oxide thickness. Since capacitance is inversely proportional to the thickness, a reinforcement particle would have a much lower capacitance than an equivalent area of oxide and reinforcement particles would be expected to lower the capacitance. The rise in capacitance may be due to a decrease in the oxide thickness. An alternate explanation, using the model of Mansfeld et al. (73-75), is that the pit area has increased. An increase in the pit area on the MMCs versus the matrix is consistent with the observation that the number of pits and the pitted area on the MMCs is greater than on the matrix.

In all the samples used in this study, the impedance spectra at low frequencies showed the response described by Mansfeld et al. for pitting. The response was noted after exposure for only two hours (for an example see Figure 5.11). The spectra showed an excellent fit to the model of Mansfeld et al. (73-75) as seen in Figure 5.8. In the model of Mansfeld, the low frequency impedance is fit to a resistor in series with a constant phase element of the form $W=K(jw)^n$ with values of n near -0.5 (73,75). In this work, values of n varied between -0.7 and -1. In table 5.3 and table 5.4, typical fit parameters are shown. A value of -1 for n would indicate a pure capacitor. The high values of n found here indicate that the low frequency element approaches a capacitor.

Other authors have noted that large capacitances appear in the impedance spectra of corroding surfaces at low frequencies. (76,91-93). To attempt to determine the nature of a corroding aluminum surface without an oxide layer, a sample was deoxidized, polished and placed in a commercial deoxidizer for EIS testing. The results are shown in Figure 5.13. The impedance at high frequencies shows a capacitance of approximately 9 $\mu F/cm^2$. This is similar to the capacitance results of Frers et al. (76). The capacitance is slightly less than the expected double layer value indicating there may still be a thin oxide film in places on the surface. The intermediate frequencies show an inductive reaction. This is most clearly seen in the Nyquist plot (figure 5.13c) where a loop is seen separating the high and low frequency time constants. Similar inductive impedances have been noted by Frers et al.(76), Bessone et al. (94), and Keddam and Oltra (92-93). An inductance in the spectra was theoretically predicted by Armstrong and Edmondson (105) for metals in the transition region between passive behavior and pitting. This inductance was not seen in the testing of samples with the air formed oxide. This is likely due to the higher impedance of the oxide layer. In the model of Frers et al. (figure 3.4), the inductance is in series with a resistor and in parallel with a resistor. For a metal with an oxide coating, the area of exposed metal is much lower. Since resistance is inversely proportional to area, a decreased area would increase the resistances and the inductance may not be seen in favor of the resistances.

At low frequencies, another capacitive loop is seen in the Nyquist plot. In the work of Frers et al. and in this work, capacitances of approximately 10 mF/cm^2 were noted. These values are three orders of magnitude greater than the values expected for an ideal double layer. Oltra and Keddam (92-93) attributed these large capacitances to a diffusion controlled process, while Frers et al. (76) attributed the capacitances to the formation of a soluble aluminum-chloride salt.

The large capacitance of the corroding surface in the low frequency region leads to the exponents of -0.7 to -1 in the transmission line element of the Mansfeld pitting model. Using the results of Frers et al. (76) and the result found here, a capacitance of the order of 10 mF/cm^2 may be expected for corroding aluminum surfaces.

6.2 Sulphuric Acid Anodizing

Sulphuric acid anodizing and sealing was performed for both Al alloys and MMCs. The results for Al alloys will be presented first to develop the foundation for a discussion on the results for the MMCs.

6.2.1 Hot Water Sealing of Anodized Al Alloys

The effect of sealing the anodized aluminum surface can be clearly seen by comparing figure 5.15 to figures 5.20 and 5.21. The initial impedance spectra for the unsealed anodized surface shows a capacitive response for the frequency range below 10 kHz. The sealed surfaces show an additional time constant at high frequency corresponding to the porous layer (66,77-78). With extended exposure time, an additional time constant corresponding to the impedance of the porous layer is seen at high frequencies for the unsealed sample. This self-sealing behavior with time is due to the lower free energy of the hydrated, sealed oxide as given by (26):

$$Al_2O_3 + H_2O \text{------>} 2AlO(OH), \quad \Delta G' = -1.54 \text{ kcal/g-mol} \quad (6.3).$$

The use of high temperatures for sealing increases the speed of the sealing process (6,26). The sealing effects can also been seen in the fit parameters in figures 5.17 to 5.19. The initial C_{po} for the samples sealed for 40 minutes or longer are between 0.6 to 0.7 nF/cm^2 with a slowly decreasing trend with exposure time. This slow decrease is likely due to increased sealing of the porous layer with a corresponding volume increase. C_{po} for the sample sealed for 30 minutes is much higher initially and decreases with increasing exposure time to values similar to the longer sealing times. The unsealed sample does not show the C_{po} initially. The low impedance of the pores acts as a short circuit and the impedance is dominated by the pores. After 21 days of exposure, the pore impedance has increased sufficiently that C_{po} can be seen at high frequencies and C_{po} is similar to the sealed samples.

The dielectric constant of the porous layer was calculated for the sample sealed for 40 minutes. The thickness of the sample was measured using the SEM. The dielectric constant, ε, was calculated as 16 using equation 5.1 and C_{po} (figure

5.19). Other authors have reported the dielectric constant of the porous layer as 33-40 (79), 20.5 (106) and 55 (78). The value of 55 was reported by Hitzig et al. (66,77-78) in a series of papers, where impedance data were used to determine the capacitance in conjunction with eddy current measurements to determine the layer thickness. These authors reported that after 60 days of exposure to air, the dielectric constant of the porous layer had decreased to 23. They attributed this decrease to the dehydration of the porous layer. The apparent change may also be due to an inadequacy in their experimental procedure. They only measured to 10 kHz for a sealing time of 30 minutes even though there own simulations (78) show that the breakpoint frequency (the frequency at which the real and imaginary components are equal) is greater than 1 kHz and the phase angle maximum due to C_{po} is not reached until 100 kHz. As can be seen in figure 5.20, for a sealing time of 30 minutes, the impedance at 10 kHz is not yet in the capacitive region. The phase angle is still increasing with increasing frequency indicating that the impedance at 10 kHz is a combination of the pore impedance and the porous layer capacitance. Hitzig et al.(66,77-78) found the capacitors to be highly non-ideal with α=0.75 (equation 3.6). After 60 days of exposure to air, the pore impedance had increased greatly so that the porous layer capacitance dominated the impedance at 10 kHz allowing the true capacitance to be determined. The value of 55 reported for the initial data is likely a the result of inadequate high frequency data. An estimate of the dielectric constant can be made using the dielectric constant of water, approximately 80, and the dielectric constant of aluminum oxide, approximately 10 (6). The composition of the porous layer is approximately 72% aluminum oxide hydrated with approximately 15% water (6). The water and oxide can be considered to be in parallel electrically, so that a weighted average of the dielectric constants can be used to estimate the dielectric constant of the hydrated layer (65). Using this method, the dielectric constant is estimated as 19, in good agreement with the value of 16 calculated here.

The sealing effects on the pore impedance can be seen in the variation of the transmission line exponent, n, and coefficient, K, in figure 5.17 and 5.18. All sealed samples show a slight decrease in the pore impedance after 2 hours of immersion. This can be seen in figure 5.21 by comparing the impedance in the range from 10 to 100 Hz for the 2 hour and 14 day samples. For the samples sealed for 40 or more minutes, n (see figure 5.17) shows a slight increase with K remaining nearly constant. The increase in the exponent causes a small decrease in the impedance. For the sample sealed for 30 minutes, much greater changes in the impedance are noted. K decreases by more than an order of magnitude after the initial testing before rising again. The decrease of the pore impedance during the initial immersion may be due to the re-hydration of the pores and establishment of lower impedance paths through the pores. A sealing time of 40 minutes was chosen for use with the MMCs. Sealing for more than 40 minutes did not provide an appreciable increase in the pore sealing as measured by the pore impedance. Sealing for only 30 minutes provides a much lower pore impedance than sealing for 40 minutes or more. In addition, the sample sealed for 30 minutes showed a large degradation of the pore impedance in the first few days of immersion.

The impedance measured for the initially unsealed sample corresponds to the barrier layer capacitance,C_b. C_b for the unsealed sample was higher than for the sealed samples. This result yielded lower calculated values of the barrier layer thickness for the unsealed sample than for the sealed samples. The anodizing ratio is the thickness of the barrier layer oxide formed per volt. The voltage is a function of the resistance across the barrier layer during formation. The anodizing ratio calculated based on the thickness determined from the barrier layer capacitance is lowest for the unsealed sample followed by the sample sealed for only 30 minutes (see table 5.6). The samples sealed for 40 minutes or longer all show substantially higher anodizing ratios than the unsealed and 30 minute samples. The anodizing ratios calculated are all within the values of 10-14 Å/V found in the literature (6,21,24), but the increase of the anodizing ratio and the capacitance decrease indicate that the barrier layer thickness is a function of both the anodizing voltage and the sealing process. An anodizing ratio of 10 Å/V appears correct for unsealed oxides. The increase above 10 Å/V is due to sealing. The decreased C_b values and increased anodizing ratios can be attributed to an increase in thickness of the barrier layer which is likely due to a combination of sealing of the base of the pores and an increase in hydration of the barrier layer which leads to a volume increase (24).

The barrier layer resistance, R_b, for the anodized samples can not be detected in the frequency range measured. As R_b is approached in the plot of the impedance versus frequency, the phase angle will decrease toward 0°. The measured phase angle did not decrease from the maximum in the measured range indicating that the impedance is still dominated by the capacitance of the barrier layer. The resistance of the barrier layer must exceed the low frequency impedance of 20 $M\Omega$–cm^2. The barrier layer resistance is estimated as greater than 200 $M\Omega$–cm^2.

6.2.2 Dichromate Sealing of Anodized Al Alloys

Dichromate sealing (DS) is a combination of the adsorption of chromate and the closing of the pores as occurs in hot water sealing (6). Chromate provides corrosion protection by providing a reservoir of oxidizing species to passivate flaws which may develop in the film (27). Analysis of dichromate sealed films show that the sealed films contain a greater concentration of chromium than would have been present from the solution in the pores. This indicates that the chromium is adsorbed in the porous layer and in the pore walls during sealing (21,30,91). Chromate adsorption occurs most readily in low pH solutions, while sealing occurs most rapidly in neutral pH solutions (6).

Dichromate sealing was accomplished using three different sealing procedures. Procedure 1 is an optimized sealing procedure after Tomashov and Tyukina (6). It uses a neutral pH solution, so the sealing is expected to be greater than with acidic sealing solutions, however the chromate adsorption will be lower (22,30). Procedures 2 and 3 use acidic sealing solutions and a low degree of porous layer sealing can be expected, but more chromate will be incorporated into the oxide film. This is the result seen in the impedance results. The initial spectra after 2 hours of exposure are shown in figure 5.22. The spectrum for procedure 1 shows a visible pore impedance and porous layer capacitance, while procedures 2 and 3 do not show the pore impedance and porous layer capacitance. This is similar to the results of Mansfeld and Kendig (39) who found that for an acidic sealing solution the pores were not sealed and concluded that the dichromate was covering the pore walls. Anodizing and sealing with any of the dichromate sealing procedures provided effective corrosion protection for extended exposure times in 0.5 N NaCl.

Analysis of the impedance spectra for the DS samples show that self-sealing, as predicted by the decrease in the free energy change for the formation of the hydrated oxide, occurs similar to the unsealed sample and the sample sealed for 30 minutes with hot water. Initially, the pore impedance is very low for the acidic sealing solutions, but a rapid rise is seen. This is clearly shown by the coefficient, K, of the pore impedance in figure 5.26. All samples show a rise of K with exposure time as the pores sealed. K rose by more than two orders of magnitude in 28 days for procedures 2 and 3. After 60 days of immersion, the sample sealed in a neutral DS solution has values of K and n similar to those for hot water sealing. The sample sealed for only five minutes in an acidic solution has a slightly lower K and a similar n. The sample sealed for 40 minutes in an acidic solution shows a lower K. The degree of sealing as indicated by the pore impedance was greatest for the neutral sealing solution and decreased with increasing sealing time for acidic dichromate solutions.

As for hot water sealing, the anodizing ratios indicate that the sealing procedure have some effect on the barrier layer produced. As reported earlier in this chapter, the anodizing ratio for an unsealed sample is approximately 10 A/V. As shown in table 5.7, the anodizing ratio for sealing in a neutral dichromate solution compared to the unsealed sample is slightly larger. Sealing with acidic sealing solutions for increasing times produced decreasing anodizing ratios. Apparently, the acidic DS procedure results in some thinning of the barrier layer oxide with the thinning increased with increasing sealing time.

To investigate further the effect of extended sealing times in acidic solutions, samples were sealed in the solution used for procedure 2 for 5, 10, 20 and 30 minutes. The spectra (figures 5.28, 5.29 and 5.30) clearly show the sealing of the porous layer in the high frequency impedance. It is notable also that the sealing effect as measured by the increase in high frequency impedance is more pronounced on the samples sealed for shorter times. Analysis of the pore impedance (see figures 5.33 and 5.34) confirms this conclusion. K is highest and n is lowest for the sample sealed for 5 minutes. Increases in K and decreases in n both lead to higher impedance values and indicate a higher degree of sealing.

The porous layer capacitance, C_{po} (see figure 5.32), shows an increase with sealing time. C_{po} for the sample sealed for only 5 minutes is similar to the value for the sample sealed for 5 minutes in a neutral DS solution (see figure 5.25) and to the hot water sealed samples (see figure 5.19). Acidic DS for longer than 5 minutes resulted in an increase in C_{po} most likely due to thinning of the porous layer during extended sealing times. This is similar to the degradation seen for the barrier layer.

For all dichromate sealed samples, the barrier layer resistance was too large to be detected in the frequency range tested. As seen in figures 5.28 and 5.30, the phase angle has begun to decrease between 10 mHz and 1 mHz indicating that R_b is being approached. The impedance is near 200 $M\Omega$–cm^2 and still increasing. As for hot water sealing, the barrier layer resistance exceeds 200 $M\Omega$–cm^2.

Dichromate sealing results in the incorporation of dichromate in the porous layer and sealing of the oxide. The degree of sealing increases with pH. Decreasing pH thins the porous layer with extended sealing times. A small decrease in the barrier layer thickness for acidic sealing solutions is seen with increasing sealing times. For use with MMCs, procedures 1 and 2 were chosen. Procedure 1 uses a neutral sealing solution and resulted in the greatest degree of sealing. Procedure 2 is an acidic sealing solution and is expected to increase the dichromate incorporation, while minimizing the negative effects of extended acidic sealing.

6.2.3 Formation of Anodized Layers on Aluminum MMCs

The anodizing behavior of MMCs and high alloy Al alloys is different from AA6061. This can be seen in the voltage versus time behavior in figures 5.35 and 5.36. The exposure test results for anodized MMCs (see Table 5.8) indicate that anodizing is less effective than on AA6061. The impedance spectra for anodized MMCs are also very different from those for AA6061. This can be seen by comparing the spectrum in figure 5.37 for AA6061 with the spectra for 6061 MMCs. In addition, a comparison of the calculated barrier layer thicknesses as shown in Table 5.9 indicates that the oxide formed under similar circumstances for MMCs and high alloy Al materials may be very different from that on pure Al or low alloy Al materials.

The SEM micrographs in figures 5.56 and 5.57 show that the total oxide layer thickness (porous layer plus barrier layer) is nearly identical for MMCs and AA6061. However, the impedance spectra shows that the structure is very different. The composition maps in figure 5.58 and 5.59 demonstrate that the porous layer contains reinforcement particles and that the barrier layer is breached by reinforcement particles. To understand the effect of reinforcement particles on the anodized layers, the anodized structure on pure Al must be considered.

Anodized Al is known to form a two-layer structure. The inner layer is a dense, highly resistive layer. This layer is referred to as the barrier layer. The outer layer is a porous layer which is formed in solutions such as sulphuric acid, where the oxide is soluble in the electrolyte. The solubility of the oxide is necessary for continued formation of the porous layer (6). Aluminum oxide, Al_2O_3, is an insulator with a resistivity of 10^{11}-10^{14} Ω-cm (18,29). The voltage necessary for anodizing is used to move the anions and cations across the highly resistive barrier layer. If the oxide were not soluble, the oxide would grow to a limiting thickness based on the voltage drop across the barrier layer and then would stop growing (24). Use of an electrolyte which dissolves the oxide leads to the continual dissolution of the barrier layer to form the porous layer and to the formation of a new barrier layer. The voltage-time behavior during anodizing is related to this process. During anodizing at constant current, the initial, rapid rise of the voltage corresponds to the formation of the barrier layer. A slight decrease is seen due to the formation of pores. The voltage remains nearly constant for the remainder of the anodizing time (6,22,24).

The porous layer forms a hexagonal cell structure with a central pore in each cell. The pores are parallel and perpendicular to the surface of the metal (5,6). Figure 6.2 shows a schematic diagram of the top view of an anodized aluminum sample. The dimensions are representative dimensions for Al (107). Figure 6.3 shows the cross-sectional view of typical anodized aluminum oxide layers. The SEM/EDS results for the anodized MMCs (figure 5.58-5.59) indicate that reinforcement particles are incorporated into the oxide layers. In figure 6.4, the same structure is shown with reinforcement particles incorporated. The relative sizes of the cells and the reinforcement particles should be emphasized. Typical reinforcement particle dimensions are 5 μm by 5 μm by 12 μm. A reinforcement particle with an area of 25 μm^2 perpendicular to the pores would block approximately 300 pores. As noted, the pores are necessary to allow continued growth of the oxide layer. The pores carry the electrolyte which is necessary for mass transport of the anion and for dissolution of the barrier layer for further growth. With the blockage caused by the introduction of reinforcement particles, the well-spaced pores, perpendicular to the metal substrate, will be disturbed. The electrolyte will be forced to go around the reinforcement particles which will substantially lengthen the diffusion path for the anion and will increase the porosity of the oxide. At the barrier layer, reinforcement particles will block sites for the formation of pores. The reinforcement particles will act as large, insoluble resistors in place of the thin barrier layer. The resistance of a particle can be calculated as:

$$R=\rho l/A \qquad (6.3).$$

In equation 6.3, ρ represents the resistivity, l is the thickness of theparticle and A is the area of the particle. The resistivity of pure SiC is of the same order of magnitude as the barrier layer oxide (18,29). The thickness of the barrier layer on AA6061 is approximately 250 Å (see Table 5.9), but the thickness of the reinforcement particle is 5 μm or approximately 200 times as thick. Substitution of an equal area of reinforcement particles for barrier layer will increase the resistance of the layer due to the increased thickness found in the particles. The reinforcement will have the net effect of increasing the effective resistance of the metal-oxide interface for a given barrier layer thickness. As the reinforcement concentration is increased, the resistance will be increased. This explains the increase in the anodizing voltage seen in figures 5.35 and 5.36. A similar increase in the anodizing voltage was noted for A356. This is likely due to a similar increase in the interfacial impedance due to the elemental Si in the alloy.

The increase in the voltage at constant current is pertinent for practical applications of anodizing to MMCs. The rule of thumb for anodizing ratios is that the barrier layer formed will be approximately 10-14 Å/V (6,21,24). These calculations assume that the voltage drop is due to the barrier layer of aluminum oxide only. Because of the increased resistance of the interface due to the reinforcement, a higher voltage will be required with MMCs to achieve the same thickness of the barrier layer.

The impedance spectra for anodized MMCs are much different from those for AA6061. This is likely due to the changes in the impedance caused by the incorporation of the reinforcement particles during the anodizing process. As shown by figure 6.4, the pore structure will be disturbed by the reinforcement particles. The decreased impedance at high frequencies, where the porous layer capacitance and pore impedance are normally seen, indicates that the structure is not as dense. In addition, the distinctive contributions of the capacitance and pore impedance to the impedance are not seen. This can be explained by the schematic in figure 6.5. The individual pore current paths in parallel seen in figure 3.7 are now formed into a network by the additional pores around the exterior of the reinforcement particles. The columns of oxide forming a continuous, capacitive layer have been broken down by the additional pores. Circuit elements R1 in figure 6.5 correspond to the resistance of the additional pores formed around the exterior of the reinforcement particles. These pores connect the vertical pore paths and yield an impedance spectrum for a branched network.

The impedance behavior of pores has been studied by a number of authors. Delevie (81), who has published an extensive study of pore impedance, found that the impedance of a single pore or a porous electrode with parallel pores may be approximated by a transmission line impedance. The transmission line impedance is named after the impedance of electrical transmission lines, where there are distributed capacitances and resistances along the length of the line. The transmission line impedance is usually expressed as a constant phase element (CPE) with the impedance expressed as:

$$Z=K(jw)^{-n} \qquad (6.4).$$

Keiser et al. (108) extended the work of Delevie and showed that the impedance was a function of the shape of the pore. The impedance of a branched network of the type shown in figure 6.5 has been found to fit a transmission line impedance with the exponent n depending on the degree of branching (60-62,69). The constant phase behavior indicative of this type of impedance dominates the high-frequency impedance of the anodized MMCs (see for example figure 5.41). The CPE in the spectrum is attributed to the breakdown of the regular pore structure and columns of aluminum oxide by the reinforcement particles. The particles cause the parallel pore network to become a network of pores with a more open structure and a lower impedance.

The increase in porosity of the anodized MMCs compared to AA6061 can also be seen in the self-sealing behavior of the porous layer after acidic, dichromate sealing. For AA6061, the spectrum after two hours of immersion (see figure 5.22) does not show any evidence of the porous layer. After 28 days of exposure to NaCl, substantial sealing has taken place, the impedance in the high frequency region has risen by more than an order of magnitude and the phase angle shows the maximum indicative of the porous layer capacitance and the minimum indicative of the pore impedance. In figure 5.54, a typical spectrum for a dichromate sealed MMC is shown. The effect of self-sealing is seen in a slight increase in the high frequency impedance, but the rise in impedance is much less than an order of magnitude. In addition, the phase angle behavior of a sealed anodized layer on Al alloys or the CPE behavior of sealed layers on MMCs is not seen.

The effect of the reinforcement can also be seen in the barrier layer. The barrier layer resistance is much lower on the composites than on AA6061 as shown in figures 5.39, 5.45, 5.51 and 5.52. The resistance decreases with increasing reinforcement which is likely due to the interface between the particles and the barrier layer oxide. Both the oxide and the particles are highly resistive (18,29). If there were a perfect resistive interface between the two, the resistance of the barrier layer would be expected to rise due to the greater thickness and therefore resistance of the reinforcement particles. The interface between the reinforcement particles and the matrix has been shown by a number of authors (2,47,50-53) to include second phase particles, precipitate free zones, and solute enrichment or depletion. The inhomogeneous nature of the interface is likely to lead to development of an interface of much lower resistance than the dense barrier layer and the reinforcement particles. Increasing reinforcement concentration increases the interface area between the particles and the oxide which should decrease the barrier layer resistance and this is the effect seen. Evidence that the interface is the culprit are also found in the results for MMCs produced with Al_2O_3. Since the barrier layer and the reinforcement for these MMCs are the same chemical composition, the layer should have a high resistance assuming a perfect interface. In fact, the impedance spectra for Al_2O_3

reinforced MMCs are similar to those for the SiC reinforced composites as seen in figures 5.48 and 5.49. The pitting resistance of these materials is less than the unreinforced alloy indicating that the use of Al_2O_3 reinforcement has a similar effect as SiC. The effect of the reinforcement on the corrosion protection provided by anodizing does not appear to be a function of the type of reinforcement. The decrease in the impedance and the barrier layer resistance as well as the increase in the number of pits with increasing reinforcement concentration indicate that the critical factor is the volume percent of reinforcement.

The capacitance of the barrier layer decreases for high alloying element Al alloys like A356 and for MMCs. This is shown in the thicknesses calculated from the capacitances in Table 5.9 and in the capacitances shown in figure 5.51. Higher capacitance may be a result of thinning of the barrier layer. Thicker layers could be due to the increased resistivity occurring as a result of the reinforcement particles or alloying elements at the metal-oxide interface. The barrier layer formed on AA6061 or on pure Al is dense with little change seen during sealing which indicates a very stable oxide. The oxide formed on the high alloying element Al alloys and the MMCs may not be as dense due to the inhomogeneities caused by the particles and interface segregation. A less dense oxide would contain more water during immersion. Since water has a dielectric constant of 80 (29) versus a dielectric constant of 10 (6) for aluminum oxide, the incorporation of additional water would increase the capacitance. The rise in capacitance with reinforcement concentration is likely the result of both thinning and the incorporation of more water in the barrier layer.

The corrosion resistance of the anodized film on the A356 and 2014 alloys were less than on AA6061 as seen in Table 5.8. This is likely due to the alloying elements. The A356 alloy has 7% Si. The impedance spectra for anodized A356 are shown in figure 5.44. The typical impedance spectrum for AA6061 is degraded and a constant phase element is seen at high frequency. The barrier layer resistance is much lower on A356 than the 10^8 Ω–cm^2 or more seen for AA6061. Similar results have been reported by Tanaka et al. (109) who attributed failure of an anodized, high Si content Al alloy to the elemental Si introducing defects in the oxide film. They viewed the anodized layer in the SEM and noted that the oxide failed to cover the Si particles. The AA2014 alloy contains 4.4% Cu. Studies of bare Al-Cu alloys have shown that they have an increased tendency to pit compared to pure Al. This has been attributed to an increased conductivity of the oxide due to the incorporation of Cu (5) or to galvanic coupling between Cu and Al (22).

For those samples where pitting occurred, the onset of pitting was accompanied by an increase in Z" at low frequencies (figures 5.41, 5.42, 5.47, 5.54 and 5.55). The increase of Z" can be seen in the modulus plot as an increase or in the phase angle plot as a plateau or increase. With these type of plots, the increase in the imaginary component may not be immediately apparent. For instance, in figure 5.41, the impedance spectrum for an anodized 6061/15% SiC MMC is shown after 14 days exposure to NaCl. The modulus plot is a logarithmic plot, so small changes in the impedance may not be readily apparent. The phase angle shows a slower drop towards zero, but an additional circuit element is not obvious. The Nyquist plot for 14 days does not show the plot returning to the real axis, but rather has a plateau. By plotting Z" in figure 5.42, the evidence for the beginning of pitting is seen clearly. After two days, Z" reaches a maximum and begins to decrease as the barrier layer resistance is approached at low frequencies and the impedance tends toward a pure resistance. The imaginary component shows a very different shape after 14 days with the imaginary component decreasing and then leveling off. An additional circuit element with an imaginary component is necessary to describe this behavior. After 28 days, the increase of Z" is obvious in all types of plots. Analysis of the impedance spectrum using the model in figure 5.43, yields a capacitance of 1.3 mF and a resistance of 35.5 kΩ for the corroding area. Assuming that these are the polarization resistance and the capacitance of the corroding interface, the corrosion rate can be estimated. The capacitance is much larger than the ideal double layer capacitance of approximately 20 $\mu F/cm^2$ (106) would allow, since this would indicate a corroding area greater than the total immersed area of 20 cm^2. Using an estimate of the capacitance of an actively corroding surface of 10 mF/cm^2 (Table 5.5), the corroding area is estimated as 0.13 cm^2. The corrosion rate is inversely proportional to the polarization resistance (15):

$$i=B/R_p \qquad (6.5).$$

The constant B is approximately 25 mV. The experimental value of the polarization resistance is normalized by multiplying by the corroding area to yield R_p=4.6 $k\Omega$-cm^2. The corrosion rate is then calculated as about 5 $\mu A/cm^2$ or a penetration rate of 60 μm/year.

6.2.4 Sealing of Anodized MMCs

Sealing of MMCs was done in both hot water and dichromate solutions. The results for exposure testing in NaCl are summarized in Table 6.1. Dichromate sealing was more effective on composites than hot water sealing in preventing pittings of the anodized MMCs.

Table 6.1 Comparison of Exposure Test Results for Hot Water Sealing and Dichromate Sealing

Matrix/Reinforcement	Exposure Time (days) in 0.5 N NaCl Hot Water/Dichromate	Number of Pits Hot Water/Dichromate
AA6061	79/64	0/0
6061/15% SiC	28/28	2/0
6061/20% SiC	28/32	15/0
6061/20% Al_2O_3	28/28	15/7
A356/15% SiC	21/28	14/0
2009/20% SiC_p	28/28	5/3

Anodizing and hot water sealing provide corrosion protection by forming a dense, inner barrier layer and a sealed outer oxide layer. The oxide structure protects the metal from oxidation (6). The MMC barrier layer is less resistive, apparently thinner and has inhomogeneities due to the interface between the particles and the oxide. The outer layer is also more porous on the MMC allowing the electrolyte more access to the oxide. The increased porosity and decreased resistance reduce the corrosion protection provided by hot water sealing. Anodizing followed by dichromate sealing provides not only the oxide structure to protect the metal, but also incorporates a strong oxiding species, Cr^{6+}, into the oxide. Hexavalent chromium provides an oxidizing agent that can passivate flaws in the oxide (27). Chromate ions chemisorb on the surface of the anodized film. When aluminum is exposed due to flaws, the Cr^{6+} forms an oxide to repair the flaw (22). Support for this mechanism of protection by Cr^{6+} was provided by Wainwright et al. (27) who proposed that the metal surface is screened from the oxidizing potential of the Cr^{6+} and the oxidizing potential of other oxidants by the resistive film. For less resistive films, electron transfer can occur across the oxide. Wainwright et al. reported that Cr^{3+} was found at the oxide surface of thin films and at repaired flaws in the oxide. Cr^{6+} was found in thicker films, where the insulating oxide better screened the metal from the oxidizing potential of the chromium. The ability of the Cr^{6+} to repair defects in the oxide, an advantage not provided by hot water sealing, provides better and longer lasting protection than hot water sealing. The repair of defects in the barrier layer can be seen in the increased barrier layer resistance (figure 5.53) for dichromate sealing over hot water sealing. The color of the sealed oxide also provides more evidence of the sealing by dichromate. Upon reduction of Cr^{6+} in a dichromate solution to Cr^{3+}, a color change is seen from orange or yellow to green (20). Dichromate sealed AA6061 samples have a bright yellow color, while MMCs are green in color. The change in color due to reduction of the chromate ion is likely occuring while repairing defects in the oxide film on the MMCs.

Dichromate sealing in an acidic solution was found to be more effective than in neutral solutions. Dichromate sealing is a combination of the adsorption of chromate ions and the closing of the pores as occurs in hot water sealing. The adsorption of chromate occurs best at low pH, but closing of the pores is best accomplished at neutral pH values (6,22,30). A neutral dichromate sealing solution is recommended for Al alloys to get the best combination of sealing of the pores and chromate adsorption. For MMCs, the more porous structure prevents closing of the pores. The oxidizing action of Cr^{6+} is greatest in acid solutions (20). Since the pore sealing is less effective with MMCs and the oxidizing action for sealing defects is greatest in acid solutions, acid dichromate sealing solutions should be more effective than neutral dichromate sealing solutions.

6.3 Chromate Conversion Coatings

Chromate conversion coatings are amorphous protective coatings containing hexavalent chromium (28). They have the ability to be self-healing due to the incorporation of hexavalent chromium in the coating. When defects form in the surface oxide film, chromium is reduced from the 6+ valence to 3+. Since hexavalent chromium is a stronger oxidizing agent than oxygen, an Al-Cr-O compound is formed to repair the oxide rather than the $Al(OH)_3$ corrosion products formed in the absence of the chromium (28). The trend for R_c to increase with immersion time and for C_c to decrease with immersion time are consistent with self-healing. C_c and R_c versus time for AA6061 are shown in figure 6.6. R_c increases with time indicating a sealing of defects, while C_c decreases with time. Since C_c is inversely proportional to thickness (see equation 6.1), the decrease in C_c can be attributed to a thickening of the oxide layer.

The thickness of the oxide layer on conversion coated aluminum can be estimated from the capacitance. Using equation 6.1 with a dielectric constant of 10. the approximate value for aluminum oxide (6), and the initial C_c for AA6061 of 89 μF (4.45 $\mu F/cm^2$), the thickness is estimated as approximately 20 Å. After 12 days of immersion, C_c has decreased to 72 μF (3.6 μF/cm^2) and the thickness is estimated as 25 Å. These thicknesses are much thinner than those found on anodized film, but are of the same order of magnitude as the oxide films naturally formed in air (5,20,21). The SEM micrographs in Figures 5.71 and 5.72 show that the total oxide film formed is over 3 μm thick, however. The micrographs in Figures 5.69 and 5.70 help to explain the discrepancy. Thick conversion coatings tend to form a crazed or "mud cracked structure" (6,28). Conversion coatings form by precipitation of spherical particles, 2-4 μm in diameter, which form successive layers (110). The spherical particles can be plainly seen in figure 5.69. Conversion coated surfaces have a thin layer of aluminum oxide at the metal interface which is covered by a thicker, hydrated chromium oxide (6,31). The chromium oxides have a low resistance (31) and there are current paths between the particles, so C_c and R_c are likely the properties of the thin, inner layer of aluminum oxide. Hexavalent chromium retained in the coating serves as a passivating agent to repair any flaws which form. Hawkins et al. (33) studied the concentration of hexavalent chromium as a function of oxide film thickness. They found that trivalent chromium predominated in thin, air formed oxide films. The trivalent chromium concentration decreased and the hexavalent chromium content increased as the oxide film thickness increased. Hawkins et al. (33)

concluded that the thinner, air formed films have more defects and at the defects, the hexavalent chromium is reduced to trivalent chromium oxide.

The effectiveness of conversion coating can be seen by comparing the exposure test results for conversion coated Al alloys to the as-received exposure test results in Table 5.2. The as-received AA6061 material showed pits after only 1 day in 0.5 N NaCl while the conversion coated alloy did not pit in 12 days. The conversion coatings were also effective on the MMCs in reducing the corrosion damage. The MMC conversion coatings were pitted after 12 days, but the damage was much less severe than on the as-received surface. The color of the conversion coatings formed on the alloy versus the MMC is significant also. Dichromate solutions containing hexavalent chromium are a orange or yellow. Upon reduction to the trivalent state, a color change to green is seen (20). The AA6061 and AA7075 samples were a dull yellow, while the conversion coated MMCs were green indicating that a substantial amount of the hexavalent chromium had been reduced in the formation of the coating. The increase in the dichromate reduction can be explained using the flaws model of Hawkins (33). The MMCs have a more aggressive cathodic reaction (figures 5.1 and 5.2). A higher corrosion current density results and more defects are formed in the oxide film. Due to the increase in defects, there are more sites for chromium reduction.

Even after formation of the conversion coatings, reinforcement particles can be seen in figure 5.70 extending through the oxide. As discussed for the unprotected MMCs, the interface of the particles with the oxide and matrix will provide a lower resistance current pathway. More extensive pitting on the conversion coated MMCs is likely due to the combined effect of a lower hexavalent chromium concentration and the improved current pathways provide by the MMC interfaces.

Pitting on the conversion coated MMCs was accompanied by the detection of an additional RC time constant in the impedance spectrum at low frequencies. In figure 5.68, the capacitance, C_{corr}, seen with pitting is shown to increase and the resistance ,R_{corr}, to decrease with reinforcement concentration. In Table 6.2, the fitting parameters for 6061/SiC MMCs after 12 days of immersion are compared.

Table 6.2 Fitting Parameters for Low Frequency Pitting Time Constant

Percent Reinforcement	R_{corr} (kΩ)	C_{corr} (mF)	Estimated Corrosion Rate (mm/yr)
15% SiC	6.1	5.8	0.08
20% SiC	4.9	6.1	0.09
40% SiC	2.2	8.08	0.16

Using an estimate of the specific capacitance of the corroding area as 10 mF/cm^2 (76), the corroding area may be estimated. The resistance is then converted to a specific resistance by multiplying by the area. Using equation 6.5, the corrosion rate was then calculated. The corrosion rate is seen to rise with reinforcement percentage (figure 6.7). The corrosion rates calculated here are slightly greater than the 0.06 mm/year seen on anodized and hot water sealed 6061/15% SiC.

6.4 Polymer Coatings

Leidheiser (111) correlated effective corrosion protection with polymeric coatings to a high impedance, 10^8 Ω-cm^2 or more, at low frequencies over extended exposure times. Less protective coatings will show a decrease in the low frequency impedance. The coating resistance after two hours of immersion exceeded 10^8 Ω-cm^2 for all of the MMCs. Using the conditions in this study, coating thicknesses of 30 μm or more and an area of 20 cm^2, the impedance spectra should be dominated by the coating capacitance, C_c. For coatings which do not show degradation, the spectrum should continue to be dominated by the coating capacitance. This is the case for AA6061 (figure 5.73).

C_c is linearly related to the inverse coating thickness (figure 5.74) from which the dielectric constant was calculated as 6.5. This is slightly higher than the typical dielectric constant of 2 to 4 for a polymer coating. The increased dielectric constant may be due to water uptake in the coating.

The impedance spectra for all of the polymer coated MMCs were capacitive after two hours, but degradation was noted for the A356, 6061/SiC and 2009 MMCs with increasing exposure to NaCl. This is clearly seen in the damage functions (figures 5.76, 5.77 and 5.80). The damage function for AA6061 may be compared to the damage functions for 6061/SiC in figure 5.80. The damage function for 15% SiC shows only a slight decrease, but with increasing reinforcement concentration (25% and 40%) and increasing exposure time, the damage function shows more degradation. The degradation of the 25% and 40% SiC MMCs can also be seen in the breakpoint frequency (figure 5.81) which increases with reinforcement concentration. The breakpoint frequency is not visible in the AA6061 spectra even after 34 days of immersion, yet the samples are all of similar thicknesses. The degree of degradation increases with increasing reinforcement concentration.

The A356 and 2009 MMCs showed a rapid drop in the damage function (figures 5.76 and 5.77). The addition of a third coat of polymer greatly improved the corrosion resistance. The damage function for three coats show that the sample remained capacitive even after 34 days. The use of a thick coating, on the order of 50 μm, is appropriate for these materials. The matrix alloys for A356 and AA2009 contain greater concentrations of alloying elements than AA6061 (Table 4.2). The greater damage on these MMCs implies that the amount of degradation is a function of the alloy as well as the reinforcement concentration.

Early theories suggested that polymer coatings inhibited corrosion by acting as an impermeable barrier to water and oxygen. Permeability studies have shown that coatings are permeable to water and oxygen to some extent (43). Mansfeld and Kendig (46) reviewed the use of polymeric coatings and emphasized that in coating design, the adhesive and cohesive properties of the coating on the metal must be considered as well as the transport of corrodents. The pore resistance of a coating on a metal generally decreases. Using a free polymer film, Mansfeld and Kendig measured the pore resistance of the film in the absence of a substrate. The pore resistance was found to be a constant over time. They attributed the decreasing pore resistance on the metal to mechanical damage caused by stresses due to the formation of corrosion products under the coating. In this study, increasing the reinforcement concentration was found to increase the degradation of the coating system. The increased corrosion rate of the MMC with increasing reinforcement concentration would predict that the degradation should increase with reinforcement concentration and this was confirmed. In addition, a similar result is expected and is noted for alloys with greater concentrations of alloying elements such as A356 and 2009.

The adhesion of the coating to the substrate is critical for effective long term corrosion protection. Adhesion of the coating adjacent to a corroding site will prevent the spread of the delamination and corrosion laterally. The adhesion of the surface at an artificial defect after 24 hours of cathodic polarization indicate good adhesion. This is similar to the results of Lin et al. (112). Using a polymer coating system on a 6061/SiC MMC, Lin et al. found minimal delamination at an artificial defect after 83 days of exposure to 0.5 N NaCl.

The effectiveness of polymer coatings is a function not only of the coating parameters, but also the surface preparation. The polymer coatings in this study were applied to cleaned and deoxidized surfaces. Frequently, polymer coatings are applied in conjunction with anodizing or conversion coatings to maximize the adhesion or to provide a passivating layer at the metal-coating interface. For example, Lin et al. (112) found that corrosion protection provided by polymer coatings was enhanced by the use of a $CeCl_3$ surface passivation prior to applying the polymer. Since the corrosion protection is a function of both adhesion and passivation of the surface, a systematic study is needed to optimize the coating and surface treatment system. An example of such a study to determine the optimum coating and surface treatment system has been performed at USC on magnesium materials (86-87).

6.5 Additional Weight of Protection Systems

The major advantage of MMCs versus aluminum alloys is the increased strength available per unit weight (1). The methods for corrosion protection discussed here all add to the weight of the piece. It is standard industrial practice to apply a corrosion protection system to aluminum alloys. Due to the increased tendency to pit in MMCs, it is likely that a more protective coating system would be required with an MMC. Table 6.3 summarizes the weight penalty incurred for using a number of different protection systems on sheets of 2 mm thick AA6061 and a 6061/15% SiC MMC assuming that the protection system will be applied to one side only. If both sides must be protected, the percentage increase in weight must be doubled. The percentage increase in weight is also a function of the thickness of the workpiece, which in turn is a function of the application. With a thicker workpiece, the percentage increase in weight will decrease. To optimize the protection system for a given application, the weight increase would have to be factored against the corrosion protection and wear resistance necessary. It is interesting to note that the weight gain from the use of a conversion coating with a thick (50 μm) polymer coating is less than that from anodizing alone. Further investigation is necessary to determine the relative corrosion protection provided by anodizing as compared to a conversion coating-polymer coating system.

Table 6.3 Weight of Corrosion Protection Systems

Protection Method	Weight/surface area (mg/cm^2)	Percent increase in weight
Bare AA6061	280	---
Bare 6061/15% SiC	280	---
Anodizing (20 μm)	4.5	0.8
Chromate Conversion Coating	0.28	0.05
Polymer Coating (50μm)	3.7	0.65
Anodizing and Polymer Coating	8.2	1.45
Conversion Coating and Polymer Coating	4	0.7

7. CONCLUSIONS

The corrosion protection of aluminum metal matrix composites using sulphuric acid anodizing, conversion coatings and polymer coatings was studied using electrochemical techniques and SEM/EDS. The results are summarized here.

7.1 Polarization Behavior of MMCs

Anodic cathodic polarization measurements were made for both Al and Al MMCs in 0.5 N NaCl. The anodic polarization behavior was independent of the reinforcement concentration for a given matrix alloy. From this, it was concluded that pitting occurs by the same mechanism on the MMCs and the Al alloys. Pitting is the result of the localized breakdown of the aluminum oxide layer for both the MMC and the alloy. The corrosion potential in aerated solutions and the pitting potential are nearly identical for the MMCs of a given matrix, yet MMCs have been shown to be more susceptible to pitting. The cathodic polarization behavior for the MMCs was found to be a function of the reinforcement concentration. A limiting current was seen in the cathodic curves which increased with increasing reinforcement concentration. The increase in current density with reinforcement concentration yields a higher current density at the same pitting potential. The increase in cathodic current density was attributed to the matrix-reinforcement interface, which increases in area with reinforcement concentration, acting as a site at which oxygen reduction could occur.

7.2 Anodizing and Sealing of Aluminum Alloys

A new model for anodized aluminum has been proposed. The pore resistance was replaced by a pore impedance represented by a transmission line element. The new model was found to fit the EIS spectra for hot water sealed samples very well. Hot water sealing was found to be most effective for a minimum sealing time of 40 minutes. Sealing with dichromate produced different spectra depending on the pH of the sealing solution. Neutral sealing solutions produce a spectrum similar to hot water sealing. Acidic sealing solutions did not produce sealing of the porous layer, but the oxide was still very protective and self-sealing was found to occur with increasing exposure to NaCl.

7.3 Anodizing of MMCs

Anodizing of MMCs is less effective than for Al alloys. The structure resulting from anodizing on MMCs is much more porous than that formed on Al alloys.

The distinctive two-layer structure found for Al alloys is disturbed by the reinforcement particles in MMCs. The protective and high-resistance barrier layer formed on Al alloys is breached by reinforcement particles. The interface between the reinforcement particles and the matrix lowers the resistance of the layer and acts as a cathodic site. In addition, the presence of the reinforcing particles increases the anodizing voltage required for MMCs.

Hot water sealing of anodized MMCs is substantially less effective in preventing corrosion than for Al alloys. The use of an acidic dichromate seal produced substantially better results than hot water sealing for MMCs. This is due to the passivating effect of hexavalent chromium ions which are deposited in the pores of the outer oxide layer.

7.4 Chromate Conversion Coating

Chromate conversion coatings increased the corrosion resistance of MMCs, although it was to a lessor degree than for Al alloys. The conversion coating formed on MMCs was as thick as on Al alloys. On MMCs, however, reinforcement particles breached the coating. The interface associated with the reinforcement is believed to provide a more effective cathodic site on the MMCs, thereby lowering the corrosion resistance.

7.5 Polymer Coatings

Polymer coatings on AA6061 showed no evidence of degradation after exposure to NaCl for 34 days. However, on MMCs degradation occurred in 34 days with the highest degradation for the highest reinforcement concentrations. A356 and 2009 MMCs with a two-coat polymer system showed damage after a few days. Three coats of the polymer provided excellent protection over a 34 day immersion. Polymer coatings of 50 μm are recommended for MMCs. The use of anodizing or conversion coating pretreatments could possibly reduce the thickness of polymer coating required in duplex coating systems.

7.6 Electrochemical Impedance Spectroscopy

EIS was demonstrated to be an effective and sensitive technique for monitoring the efficiency of different corrosion protection methods for MMCs. The impedance at low frequencies showed characteristic changes during degradation. For as-received, anodized and conversion coated samples, the imaginary component provides a very sensitive indicator of pitting. An increase in the imaginary component at low frequencies was indicative of pitting.

7.7 Corrosion Protection of MMCs

Standard protection methods for Al alloys are less effective for MMCs. Therefore, simply transferring protection methods from Al will not be effective. The effectiveness of all methods studied decreases with increasing reinforcement concentration. The effectiveness of corrosion protection methods is also a function of the matrix alloy. The results for Al_2O_3 reinforced MMCs were similar to SiC reinforcement indicating that the effectiveness is not a function of the nature of the reinforcing particle.

The inhomogeneous structure of the MMC must be considered in designing corrosion protection systems. An obvious solution to corrosion protection of MMCs appears to be the application of a face sheet of the matrix alloy to the outside of the MMC followed by treatment of the face sheet. MMCs are desirable for the excellent mechanical properties available with decreased weight. Application of a face sheet is undesirable, since the cost as well as the weight will increase. The optimum corrosion protection for the MMC will undoubtedly be a combination of different techniques. Both anodizing and conversion coating are frequently used as pretreatments for polymer coatings. Polymer coatings applied over a conversion coating or an anodized layer are likely to produce better protection than any of these techniques alone. Anodized oxides should be sealed with dichromate or a similar passivating agent. A comparison of the candidate combinations should be made to determine the optimum combination.

8. RECOMMENDATIONS FOR FURTHER RESEARCH

8.1 Alternatives to the Use of Hexavalent Chromate Ions

Dichromate sealing was found to be the most efficient method of sealing for anodized MMCs. In addition, chromate conversion coating was effective for reducing corrosion on MMCs. Unfortunately, both of these methods involve hexavalent chromium ions which produce toxic waste. Its use is facing increasing government regulation and will likely be prohibited in the near future. There are a number of on-going programs to develop alternatives. Molybdates and tungstates have been proposed as alternatives in sealing of anodized aluminum (6). Hinton et al. (113) and Mansfeld et al. (114,115) have proposed the use of rare earth elements as alternatives to chromate conversion coatings. These techniques are believed to modify the oxide films on the as-received surface. With MMCs, the inhomogeneous oxide due to the protruding reinforcement particles will make the application of these techniques more difficult. Ion implantation of Mo, Cr, and W has been proposed as another alternative to modify the surface of aluminum (116). Increasing the concentration of these ions is believed to inhibit the adsorption of agressive ions and inhibit pitting.

Selective alloying to modify the interfaces in MMCs might improve the corrosion resistance.

8.2 Electrochemical Behavior of MMC Interfaces

From the mechanical properties literature, the interfaces in MMCs are known to contain impurities. There has been no research into the electrochemical behavior of these interfaces. It is apparent from the polarization results that the interfaces play an important role in the corrosion of MMCs. The nature of the interface, the elements present and their effects on the corrosion resistance are not known. With knowledge of the behavior of the interface, modification of the interface during processing to increase the electrical resistance and decrease the cathodic current density might be possible.

8.3 Analysis of Pitting Impedance

An increase in the imaginary component is seen at low frequencies when pitting occurs. This increase has been noted phenomenologically by Mansfeld et al. (73-75) and has been modeled by a transmission line term in their pitting model.

The origin of the capacitance leading to a transmission line response has not been identified. Frers et al. (76) propose that the source of the capacitance is the formation of a soluble aluminum chloride salt, while Oltra and Keddam (92,93) suggest that it may be due to a diffusion controlled process. Neither group produced conclusive evidence to support their thesis. Since the increase in the imaginary component appears to be indicative of pitting, it is of great theoretical interest. It is also of great practical interest for developing better methods for identifying and quantifying the start of pitting on aluminum alloys and MMCs.

8.4 Optimization of Protection Systems

In this study, various methods of corrosion protection for MMCs were applied and evaluated separately. In industrial practice, these methods are frequently combined. In order to optimize the protection system, the work presented here should be used as the starting point for an evaluation of specific combinations of polymer coating of various thicknesses with anodizing or conversion coating. This testing should include exposure of samples with artificial defects for extended times to measure delamination for various pretreatments. In addition, the weight penalty of the various treatments must be evaluated against the degree of corrosion protection required.

9. REFERENCES

1. H.J. Rack, in "Metal Matrix Composites: Processing and Interfaces", edited by R.K. Everett and R.J. Arsenault. Academic Press, 83-101 (1991).

2. W. C. Harringan Jr. , in "Metal Matrix Composites: Mechanisms and Properties", Edited by R. K. Everett and R. J. Arsenault, Academic Press, 383-404 (1991).

3. D.J. Lloyd, in "Advanced Structural Materials", edited by D.S. Wilkinson, Pergamon Press, 1-21 (1989).

4. R. T. Foley, Corrosion, 42, 277-288 (1986).

5. H. Kaesche, "Metallic Corrosion", National Association of Corrosion Engineers (1985).

6. S. Wernick, R. Pinner and P.G. Sheasby, "The Surface Treatment and Finishing of Aluminum and its Alloys", 5th edition, ASM International (1987).

7. P.P. Trzaskoma, in "Metal Matrix Composites: Mechanisms and Properties", edited by R.K. Everett and R.J. Arsenault, Academic Press, 383-404 (1991).

8. D. M. Aylor and P. J. Moran, Paper no. 202, Corrosion '86, National Association of Corrosion Engineers (1986).

9. L.H. Hihara and R.M. Latanision, "Galvanic Corrosion of Aluminum Metal Matrix Composites", Technical Report no. 2 to ONR, Grant no. 14-89-J-1588 (1991).

10. H. Sun, E.Y. Koo and H.G. Wheat, Corrosion, 47, 741-753 (1991).

11. E. McCafferty, P.P. Trzaskoma and P.M. Natishan, in "Advances in Localized Corrosion", edited by H.S. Issacs, U. Bertocci, J. Kruger and S. Smialowski, National Association of Corrosion Engineers, 181-190 (1990).

12. P.P. Trzaskoma, Corrosion, 46, 402-409 (1990).

13. P.P. Trzaskoma and E. McCafferty, in "Proceedings of the Symposium on Aluminum Surface Treatment Technology" , edited by R. S. Alwitt and G.E. Thompson, The Electrochemical Society, Proceedings volume 86-11, 171-180 (1986).

14. P.P. Trzaskoma, Corrosion, 46, 402-409 (1990).

15. Y. Shimizu, T. Nishimura and M. Tamura, Corrosion, 40, 489-498 (1991).

16. S. Lin, "Corrosion of Aluminum Metal Matrix Composites", Ph. D Dissertation, University of Southern California (1990).

17. F. Mansfeld and S.L. Jeanjaquet, Corrosion Science, 26, 727-734 (1986).

18. N. Ichinose, "Introduction to Fine Ceramics", John Wiley (1987).

19. F. Mansfeld and M.W. Kendig, J. Electrochem. Soc., 135, 828-833 (1988).

20. M. Pourbaix, "Atlas of Electrochemical Equilibria in Aqueous Solutions", National Association of Corrosion Engineers (1974).

21. J. W. Diggle, T.C. Downie and C.W. Goulding, Chem Rev, 69, 365-405 (1969).

22. G. E. Thompson and G.C. Wood, Treatise on Materials Science and Technology, 23, 205-329 (1983).

23. J.R. Galvele, Treatise on Materials Science and Technology, 23, 1-53 (1983).

24. S. Tajima, in "Advances in Corrosion Science and Technology", edited by M.G. Fontana and R. W. Staehle, Plenum Press, 1, 229-362 (1970).

25. D. Thomas, Metal Finishing, 88(1A), 417-432 (1990).

26. T.P. Hoar and G.C. Wood, Electrochimica Acta, 7, 333-353 (1962).

27. J. S. Wainwright, O.J. Murphy and M. R. Antonio, Corrosion Science, 33, 281-293 (1992).

28. K. A. Korinek, in "Metals Handbook", 9th Edition, volume 13, 389-395 (1982).

29. "CRC Handbook of Chemistry and Physics", 71st Edition, edited by D.R. Lide (1990).

30. G. C. Wood and V. J.J. Marron, Trans. Inst. Metal Fin., 45, 17-26 (1967).

31. J. A. Treverton and N. C. Davies, Metals Technology, 4, 480-489 (1977).

32. J. A. Treverton, A. Bosland and J. M. Brown, Corrosion Science, 30, 1159-1175 (1990).

33. J. K. Hawkins, H.S. Isaacs, S.M. Heald, J. Tranquada, G.E. Thompson and G.C. Wood, Corrosion Science, 27, 391-399 (1987).

34. K. Asami, M. Oki, G.E. Thompson, G.C. Wood and V. Ashworth, Electrochimica Acta, 32, 337-343 (1987).

35. J. A. Treverton and M.P. Amor, Trans. Inst. Metal Fin., 60, 92-96 (1982).

36. J. A. Treverton and M.P.Amor, J. Materials Science, 23, 3706-3710 (1988).

37. G. P. Halada and C.R. Clayton, J. Electrochem. Soc. 138, 2921-2927 (1991).

38. Y. Zuzhan, N. Hongbin and . Guanshen, unpublished work, Fudan University, Shanghai, PRC.

39. F. Mansfeld, "Development of an Electrochemical Quality Control Test for Chromate Conversion Coatings on Aluminum Alloys", Report to Sandia National Laboratories, contract no. 02-5212, December 1987.

40. F. Mansfeld, "Optimization of Chromate Conversion Coatings on Al7075-T73", final report to Sandia National Laboratories, contract no. 57-2928, Dec. 1989.

41. L.J. Bailin, P. Fitzpatrick and M.J. Joyce, presented at the Electrochemical Society Meeting, San Diego, CA, October 1986.

42. W. Funke, in "Corrosion Protection by Organic Coatings", edited by M.W. Kendig and H. Leidheiser, The Electrochemical Society, Proceedings vol. 87-2, 1-7 (1987).

43. G.W. Walter, Corrosion Science, 26, 27-38 (1986).

44. H. Leidheiser Jr., in "Advances in Localized Corrosion", edited by H.S. Isaacs, U. Bertocci, J. Kruger and S. Smialowska, National Association of Corrosion Engineers, 339-342 (1990).

45. H. Leidheiser Jr., W.Wang and J.V. Standish, Polymer News, 6, 208-214 (1980).

46. M. Kendig and F. Mansfeld, Mat. Res. Soc. Symp. Proc., 125, 293-320 (1988).

47. S. R. Nutt, Treatise on Materials Science and Technology, 31, 389-409, (1989).

48. M. Skibo, P.L. Morris and D. J. Lloyd, in "Cast Reinforced Composites", edited by S.G. Fishman and A. K. Dhingra, ASM International, 257-261 (1988).

49. J.E. Hatch, "Aluminum: Properties and Physical Metallurgy", American Society for Metals (1984).

50. C. M. Friend, I. Horsfall, S.D. Luxton and R. J. Young, in "Cast Reinforced Composites", edited by S.G. Fishman and A.K. Dhingra, ASM International, 257-261 (1988).

51. D. Lee, M. Vaudin, C. Handwerker and U. Kattner, Mat. Res. Soc. Symp Proc, 120, 357-365 (1968).

52. M. Strangwood, C.A. Hippsley and J.J. Lewandowski, Scripta Metallurgica, 24, 1483-1487 (1990).

53. L.M. Dignard-Bailey, T.F. Malis, J.S. Boyd and J.D. Embury, in "Advanced Structural Materials", edited by D.S. Wilkerson, Pergamon Press, 87-95 (1989).

54. R. C. Paciej and V. S. Agarwala, Corrosion, 42, 718-729 (1986).

55. S. Lin, H. Greene, H. Shih and F. Mansfeld, Corrosion. 48, 61-67 (1992).

56. F. Mansfeld, S. Lin, S. Kim and H. Shih, Electrochimica Acta, 34, 1123-1132 (1989).

57. H.H. Uhlig and R.W. Revie, "Corrosion and Corrosion Control", John Wiley, Third edition (1985).

58. F. Mansfeld and W. J. Lorenz, in "Techniques for Characterization of Electrodes and Electrode Processes", edited by R. Varma and J.R. Selman, John Wiley, 581-647 (1991).

59. C. Gabrielli, " Use and Applications of Electrochemical Impedance Techniques", Schlumberger Technologies, Billerica, Ma (1990).

60. D.D. Macdonald, Corrosion, 46, 229-242 (1990).

61. D.D. Macdonald, in "Techniques for Characterization of Eletrodes and Electrochemical Processes", edited by R. Varma and J.R. Selman, John Wiley, 515-580 (1991).

62. J.R. MacDonald. "Impedence Spectroscopy", John Wiley (1987).

63. F. Mansfeld, Corrosion, 44, 558-559 (1988).

64. A.J. Bard and L.R. Faulkner, "Electrochemical Methods, Fundamentals and Applications", John Wiley (1980).

65. B.K.P. Scaife, "Principals of Dielectrics", Clarendon Press (1989).

66. K. Juttner, W.J. Lorenz and W. Paatsch, Corrosion Science, 29, 279-288 (1989)

67. W. D. Kingery, H. K. Bowen and D.R. Uhlman, "Introduction to Ceramics", John Wiley (1976).

68. K. Juttner, Electrochimica Acta, 35, 1501-1508 (1990).

69. W. Scheider, J.Phys. Chem., 79, 127-136 (1975).

70. K. Juttner, W.J. Lorenz, M.W. Kendig and F Mansfeld, J. Electrochem. Soc., 135, 332-339 (1988).

71. A.K. Jonscher, Phys. Stat. Sol. A, 32, 665-676 (1975).

72. F. Mansfeld, H. Shih,H Greene and C.H. Tsai, "Analysis of EIS-Data for Common Corrosion Processes", ASTM Committee G01-EIS Symposium, ASTM, in press.

73. F. Mansfeld, S. Lin, S. Kim, and H. Shih, J. Electrochem. Soc., 137, 78-82 (1990).

74. H. Shih and F. Mansfeld, Corrosion, 45, 610-614 (1989).

75. F. Mansfeld and H. Shih, J. Electrochem. Soc., 135, 1171-1172 (1988).

76. S.E. Frers, M.M. Stefenel, C. Mayer and T. Chierchie, J. Appl. Electrochem., 20, 996-999 (1990).

77. J. Hitzig, K. Juttner, W. J. Lorenz and W. Paatsch, J. Electrochem Soc., 133, 887 (1986).

78. J. Hitzig, K.Juttner, W.J. Lorenz and W. Paatsch, Corrosion Science, 24, 945-961 (1984).

79. M. Koda, H. Takahashi and M. Nagayama, in "Aluminum Surface Treatment Technology", edited by R.S. Alwitt and G.E. Thompson, The Electrochemical Society, Proceedings vol. 86-11, 394-405 (1986).

80. F. Mansfeld and M.W. Kendig, Corrosion, 41, 490-492 (1985).

81. R. Delevie, in "Advances in Electrochemistry and Electrochemical Engineering", Volume 6, edited by P. Delahay, John Wiley , 329-397 (1967).

82. B.A. Boukamp, " Equivalent Circuit Users Manual", Second Edition, Department of Chemical Technology, University of Twente, The Netherlands (1989).

83. A. Greer, Advanced Composite Materials Corporation, Greer, SC, private communication.

84. R. G. King, "Surface Treatment and Finishing of Aluminum", Pergamon Press (1988).

85. J. Pernick, in "Metals Handbook", vol 13, 396-398 (1987).

86. F. Mansfeld, S. Lin, S. Kim and H. Shih, J. Coat, Tech., 61, 22 (1989).

87. F. Mansfeld and H. Greene, "Evaluation of Coatings on Magnesium AZ31", Report to Magnesium Elektron Inc., Corrosion and Environmental Effects Lab, University of Southern California (1990).

88. Araldite 985 Sealing Worksheet, Colonial Coatings Corp., Milford, CT (1991).

89. F. Mansfeld, S. Lin, Y.C. Chen and H. Shih, J. Electrochem. Soc. 135, 906-907 (1988).

90. J. I. Goldstein, D.E. Newbury, P. Echlin, D.C. Joy, C. Fiori, and E. Lifshin, "Scanning Electron Microscopy and X-Ray Microanalysis", Lenum Press (1981).

91. M. Kendig and S. Jeanjaquet, in "Proceedings of the Symposium on Transient Techniques in Corrosion Science and Engineering", edited by W.R. Smyrl, D.D. MacDonald and and W.J. Lorenz, The Electrochemical Society, Proceedings volume 89-1, 378-389 (1989).

92. R. Oltra and M. Keddam, Electrochimica Acta, 35, 1619-1629 (1990).

93. R. Oltra and M. Keddam, Corrosion Science, 28, 1-18 (1988).

94. J. Bessone, C. Mayer, K. Juttner and W.J. Lorenz, Electrochimica Acta, 28, 171-175 (1983).

95. W. Harrigan, DWA Composites, Chatsworth, CA private communication.

96. R.S. Alwitt, C. Ortega, N. Thorne and J. Siejka, in "Aluminum Surface Treatment Technology", edited by R.S. Alwitt and G.E. Thompson, The Electrochemical Society, Proceedings vol. 86-11, 394-405 (1986).

97. T. A. Libsch and O.F. Devereux, J. Electrochem. Soc., 122,1654-1660 (1975).

98. F. Clayton, Schulumberger Instruments, Billerica, Ma, private communication.

99. F. Mansfeld and C.H. Tsai, "Determination of Coating Deterioration with EIS; II. Development of a Method for Field Testing of Protective Coatings", submitted to Corrosion.

100. H. P. Hack and J.R. Scully, J. Electrochem. Soc, 138, 33-40 (1991).

101. ASTM Standard G8, "ASTM Annual Book of Standards", ASTM (1987).

102. D.C. Grahame, Chem Review, 41, 441-501 (1947).

103. D.C. Grahame, J. American Chem. Soc., 63, 1207-1215 (1941).

104. "Gmelin Handbook of Inorganic Chemistry, Si", vol B2, Springer-Verlag, 153 (1984).

105. R.D. Armstrong and K. Edmondson, Electrochimica Acta, 28, 171-175 (1983).

106. R. S. Alwitt, Oxides and Oxide Films, 4, 169-254 (1976).

107. E.T. Englehart and D.J. George, Materials Protection, 3, 24-30 (1964).

108. H. Keiser, K. D. Beccu and M. A. Gutjahr, Electrochimica Acta, 21, 539-543 (1976).

109. S. Tanaka, Y. Isobe and F. Hine, Corrosion Engineering, 39, 479,488 (1990).

110. D. J. Arrowsmith, J.K. Dennis and P.R. Sliwinski, Trans, Inst. Metal Finish., 62, 117-120 (1984).

111. H. Leidhiser, Extended Abstracts, Fall Meeting, Electrochemical Society, 1991.

112. S. Lin, H. Shih and F. Mansfeld, "Corrosion Protection of Aluminum Alloys and Metal Matrix Composites by Polymer Coatings", submitted to Corrosion Science.

113. B.R.W. Hinton, D.R. Arnott and N.E. Ryan, Mater. Forum, 9, 162-173 (1986).

114. F. Mansfeld, S. Lin, S. Kim and H. Shih, Corrosion, 45, 615-631 (1981).

115. H. Shih and F. Mansfeld, in "New Methods for Corrosion Testing of Aluminum Alloys". ASTM STP 1134, edited by V.S. Agarwala and G.M. Ugianksy, ASTM, 180-195 (1992).

116. P.M. Natishan, E. McCafferty and G.K. Hubler, Corrosion Science, 32, 721-731 (1991).

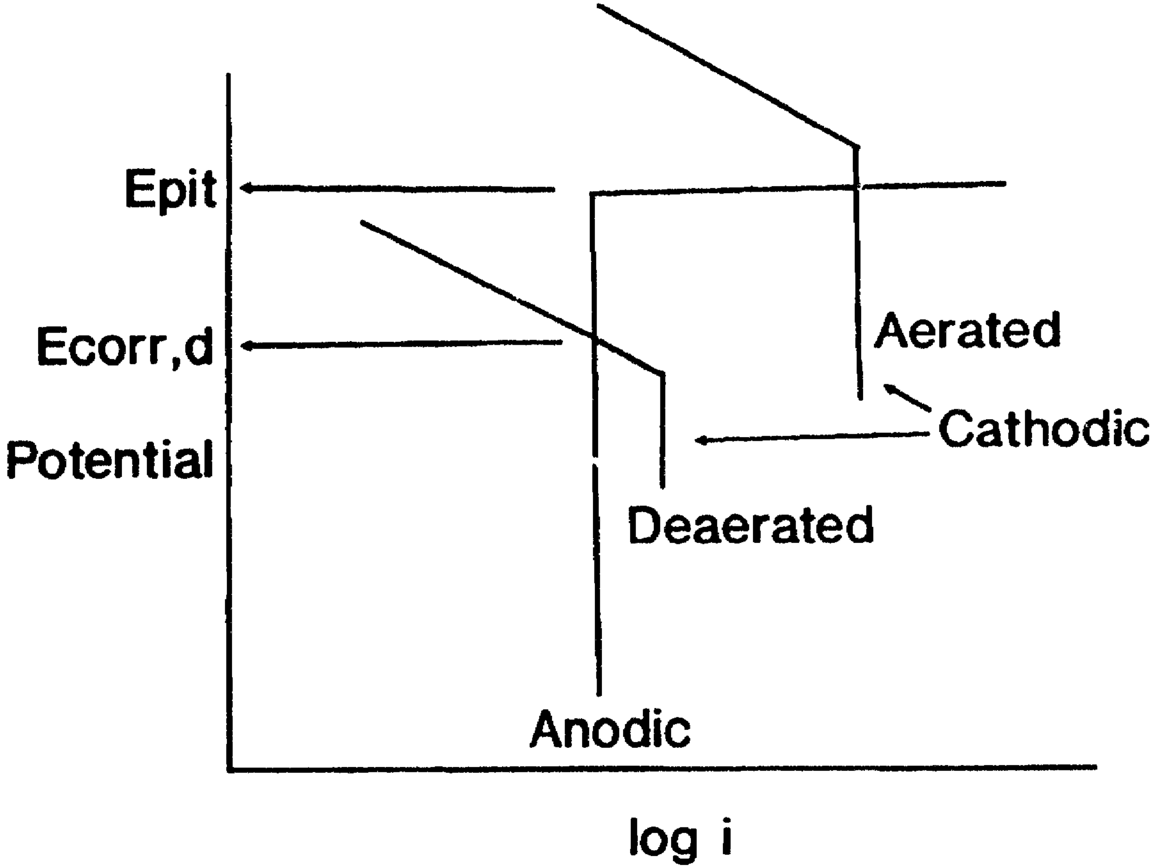

Figure 3.1 Schematic anodic and cathodic polarization curves for aluminum. Cathodic curves for both aerated and deaerated solutions are shown. E_{pit} is the pitting potential and is also the corrosion potential in an aerated solution. $E_{corr,d}$ is the corrosion potential in a deaerated solution.

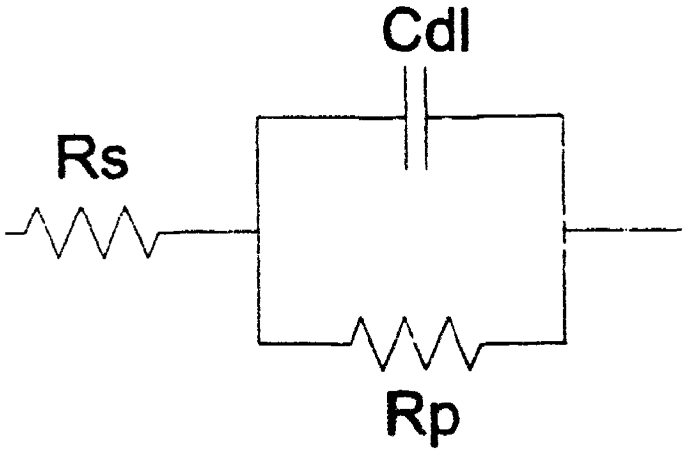

Figure 3.2 Equivalent circuit for a system under charge transfer control.

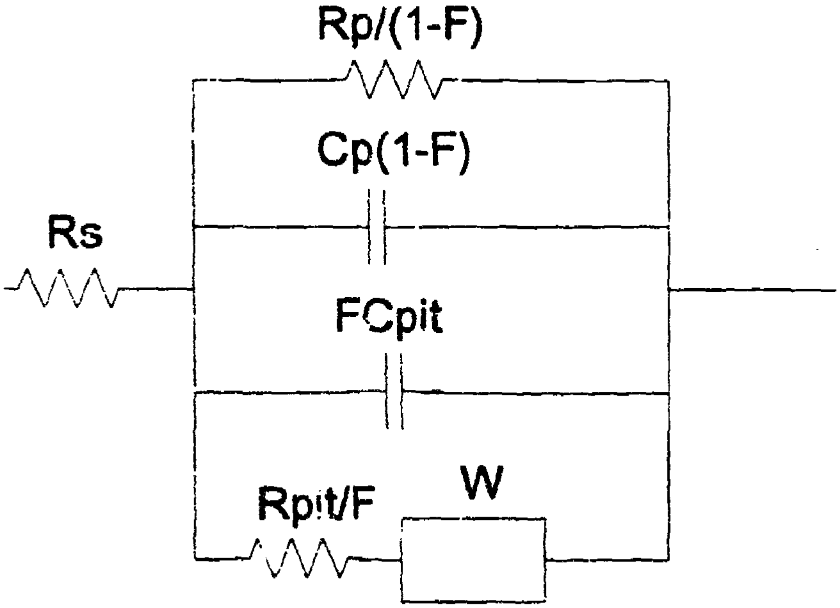

Figure 3.3 Equivalent circuit model for pitting of aluminum.

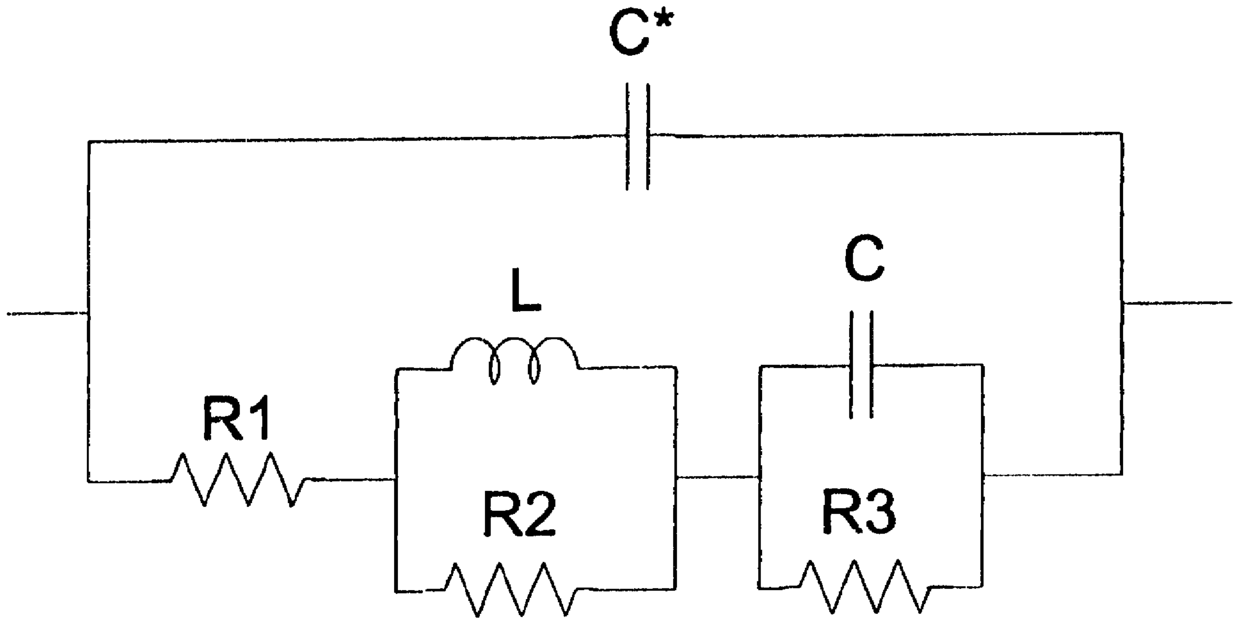

Figure 3.4 Equivalent circuit model for aluminum in Frers et al. (76).

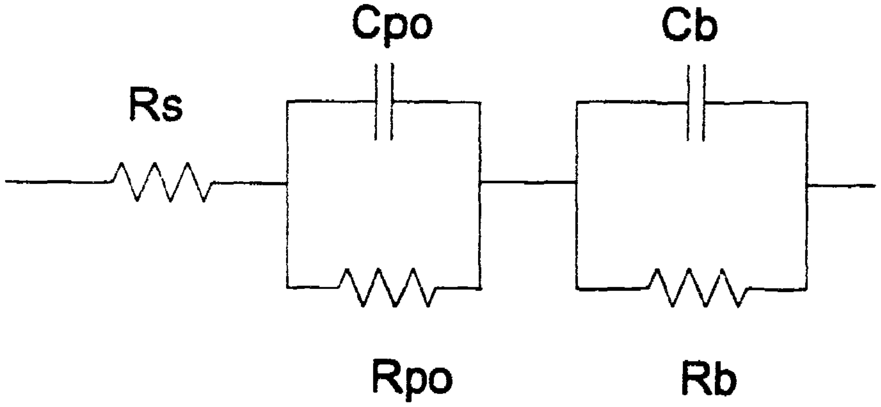

Figure 3.5 Equivalent circuit model for anodized aluminum.

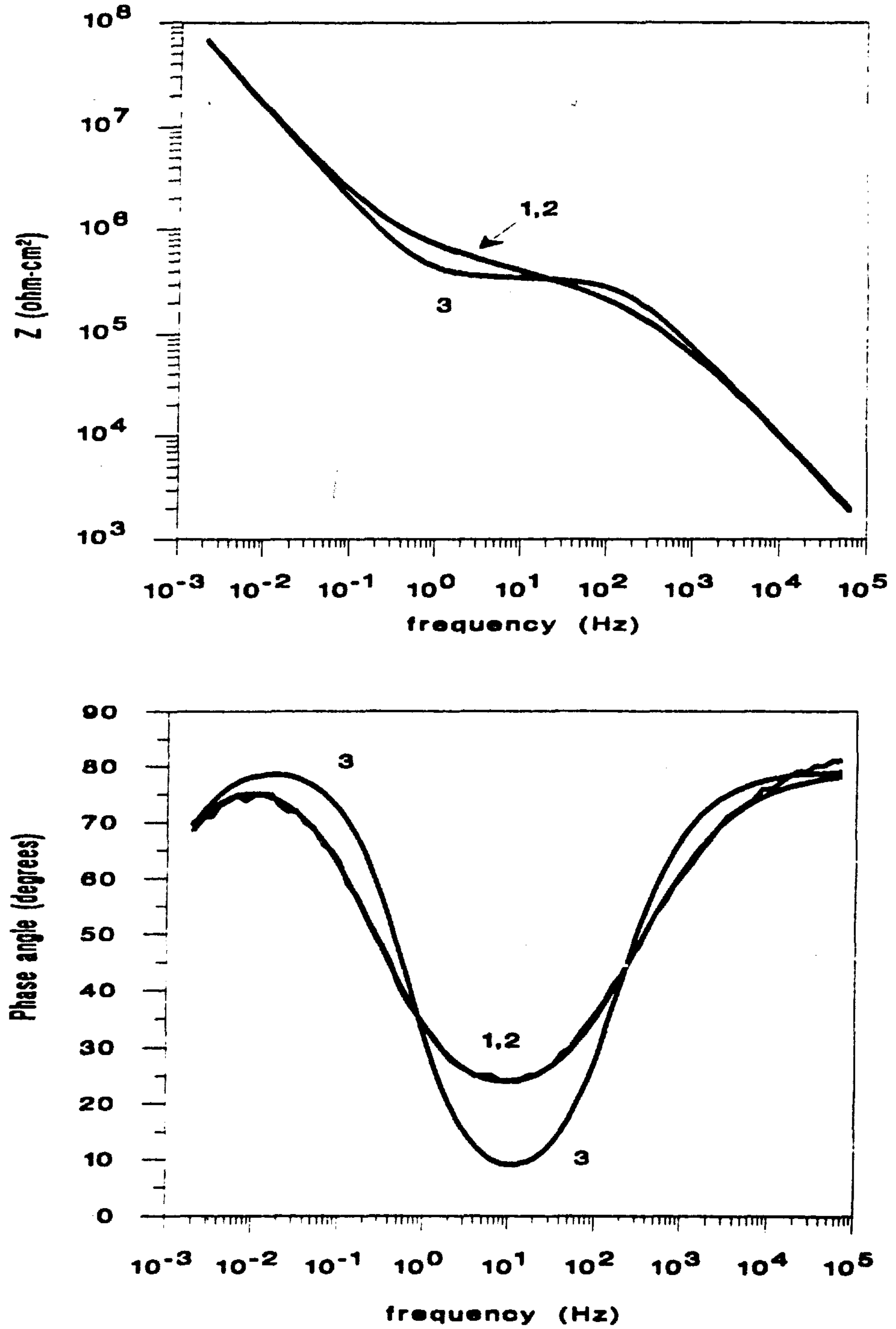

Figure 3.6 Bode plots for anodized aluminum. Experimental results (curve 1), result from fitting with new model (curve 2) and results from fitting with previous model (curve 3).

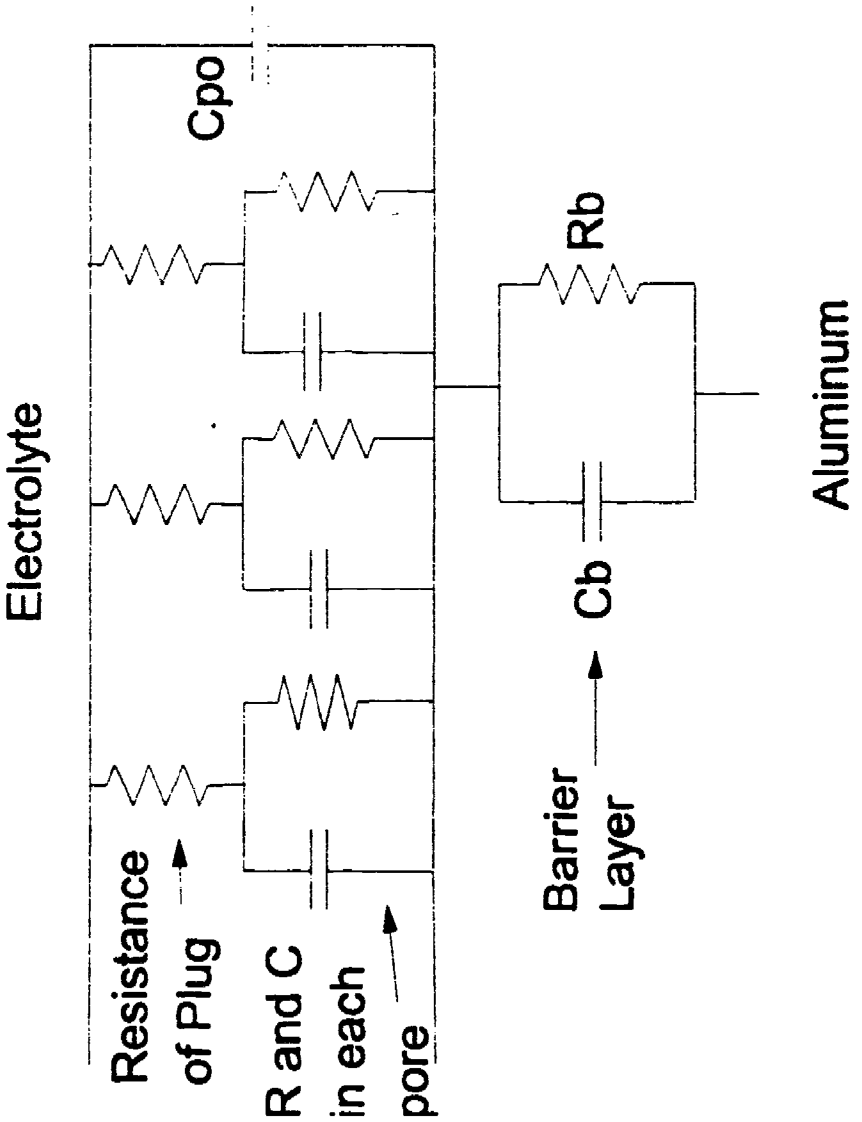

Figure 3.7 Schematic of the electrical network of the anodized film.

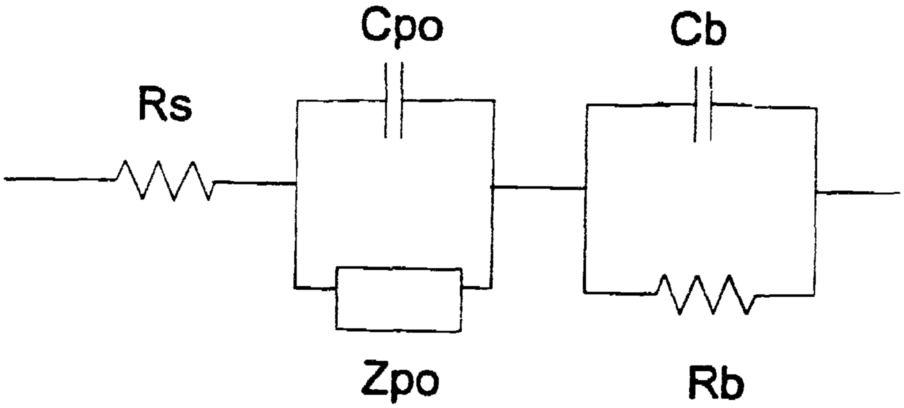

Figure 3.8 New equivalent circuit model for anodized aluminum.

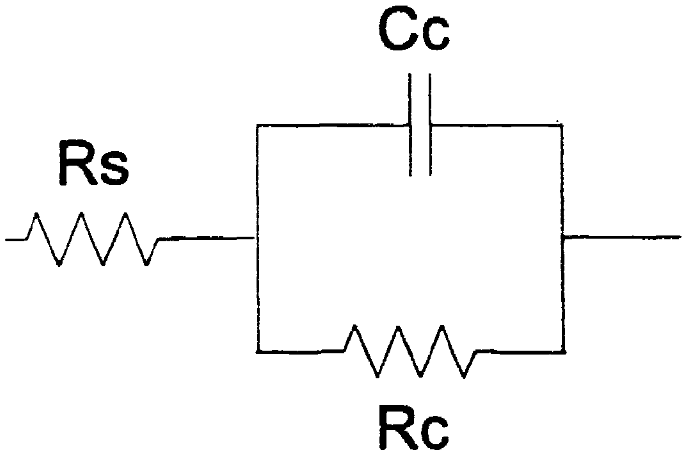

Figure 3.9 Equivalent circuit model for chromate conversion coating.

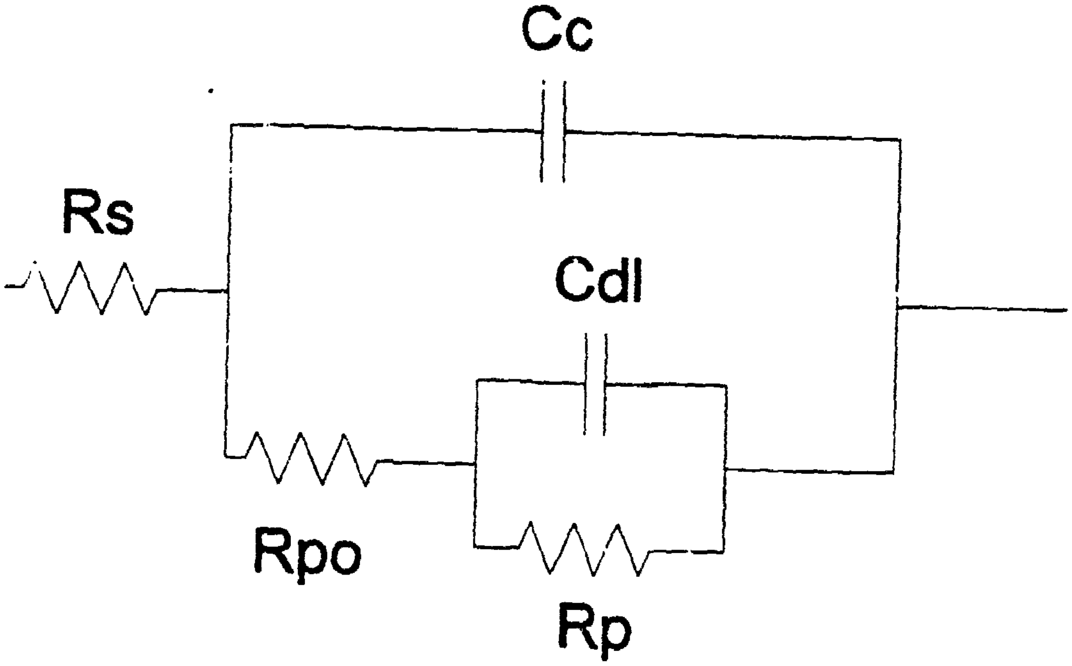

Figure 3.10 Equivalent circuit model for polymer coated metals.

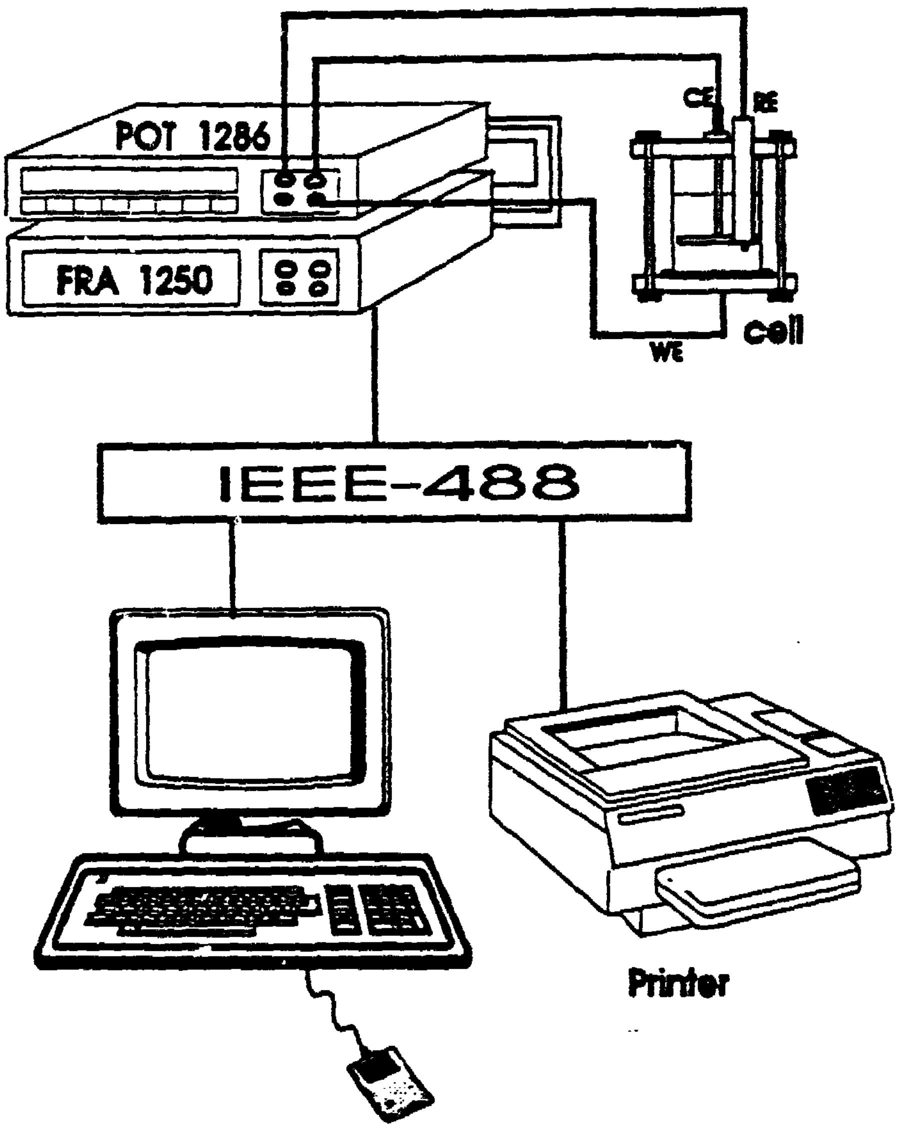

Figure 4.1 Experimental arrangement for EIS.

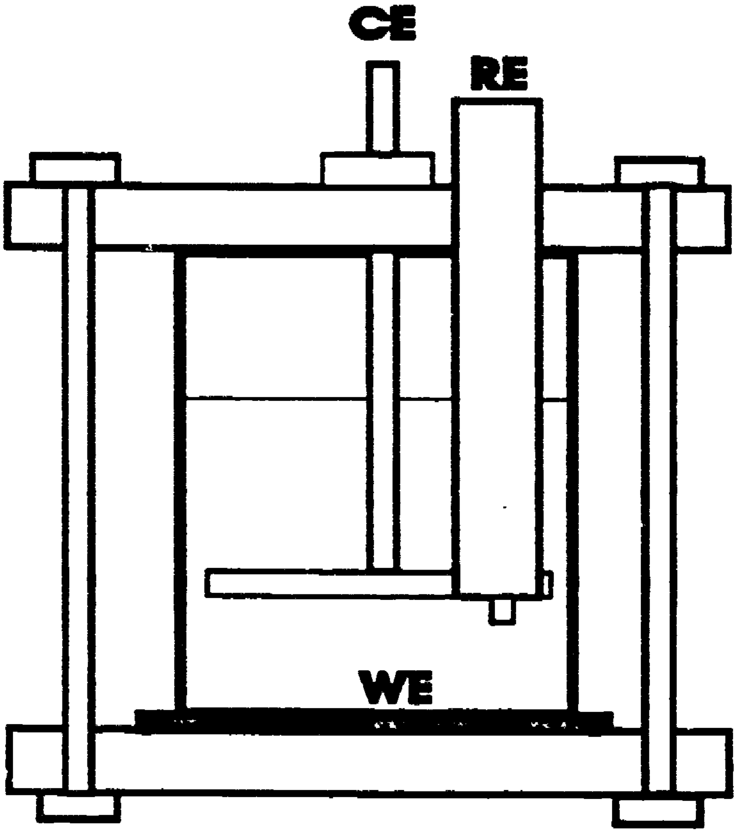

Figure 4.2 Cell design for EIS.

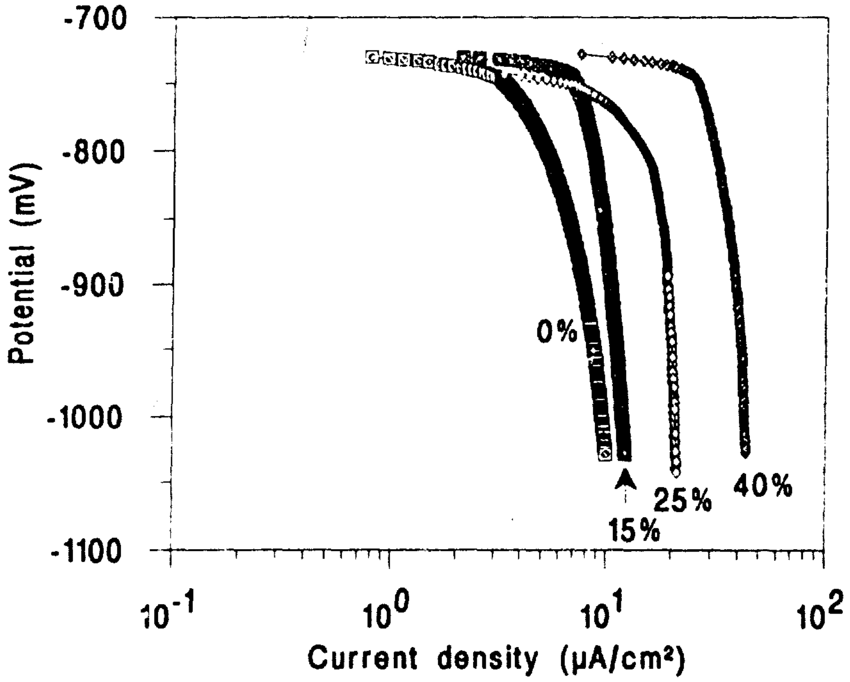

Figure 5.1 Cathodic polarization curves for 6061/SiC MMCs in 0.5 N NaCl open to air as a function of SiC concentration.

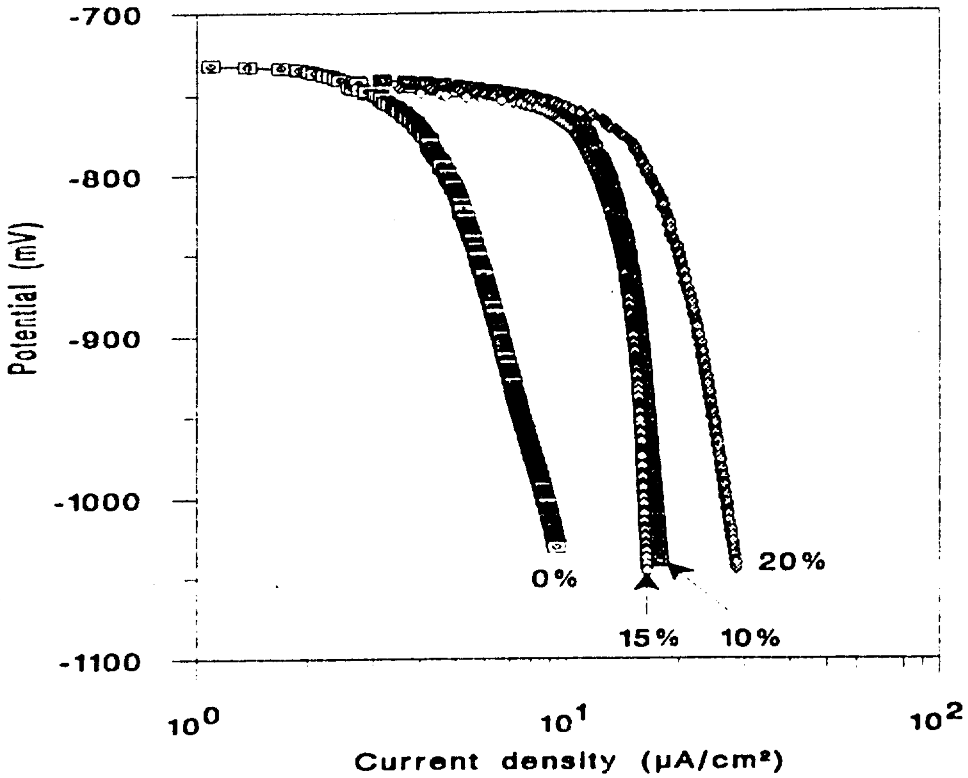

Figure 5.2 Cathodic polarization curves for A356/SiC MMCs in 0.5 N NaCl open to air as a function of SiC concentration.

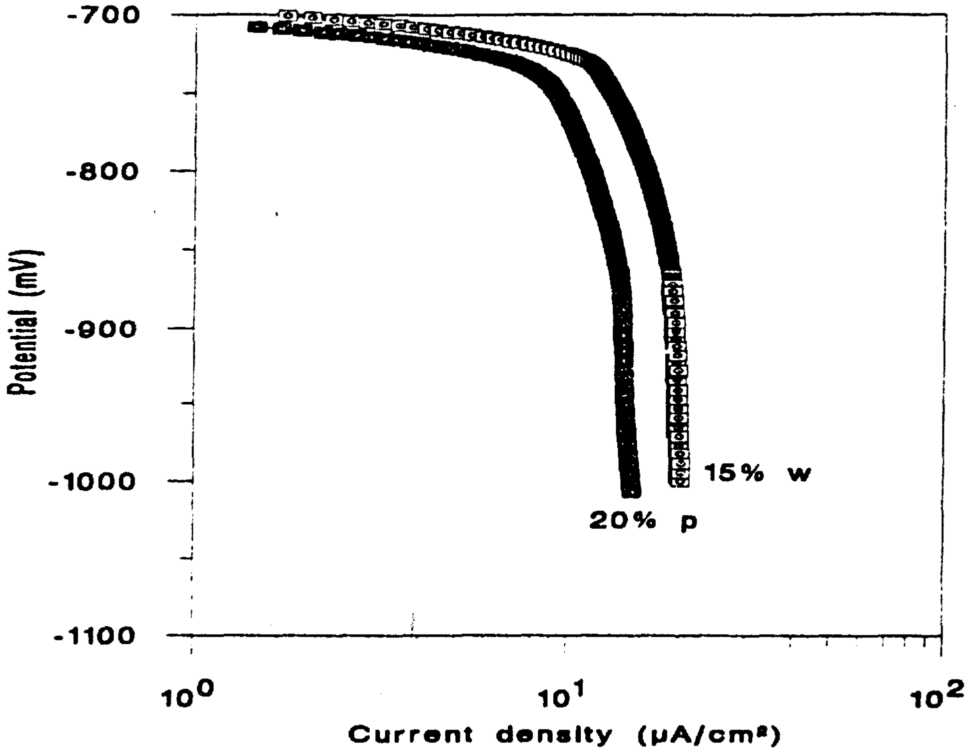

Figure 5.3 Cathodic polarization curve for 2009/15% SiC_w and 20% SiC_p MMCs in 0.5 N NaCl open to air.

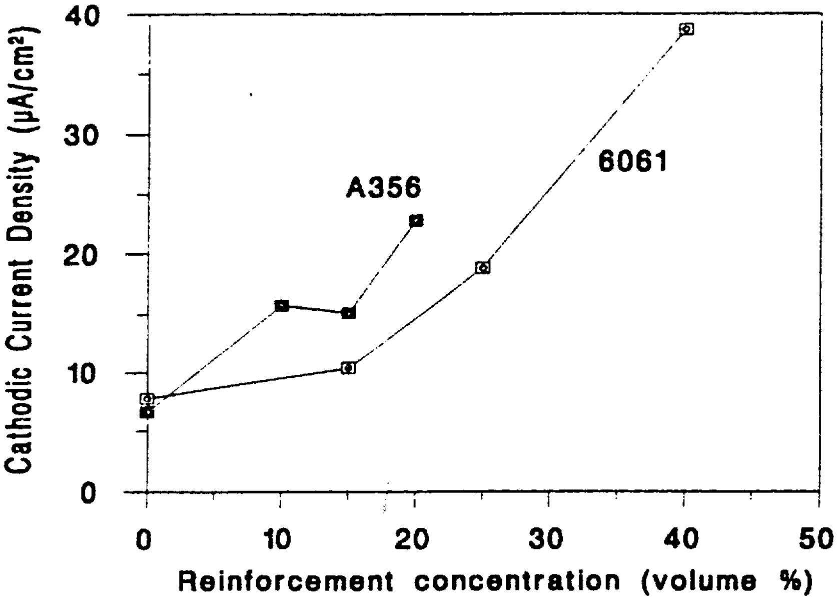

Figure 5.4 Cathodic current density at -900 mV for 6061/SiC and A356/SiC MMCs as a function of reinforcement concentration.

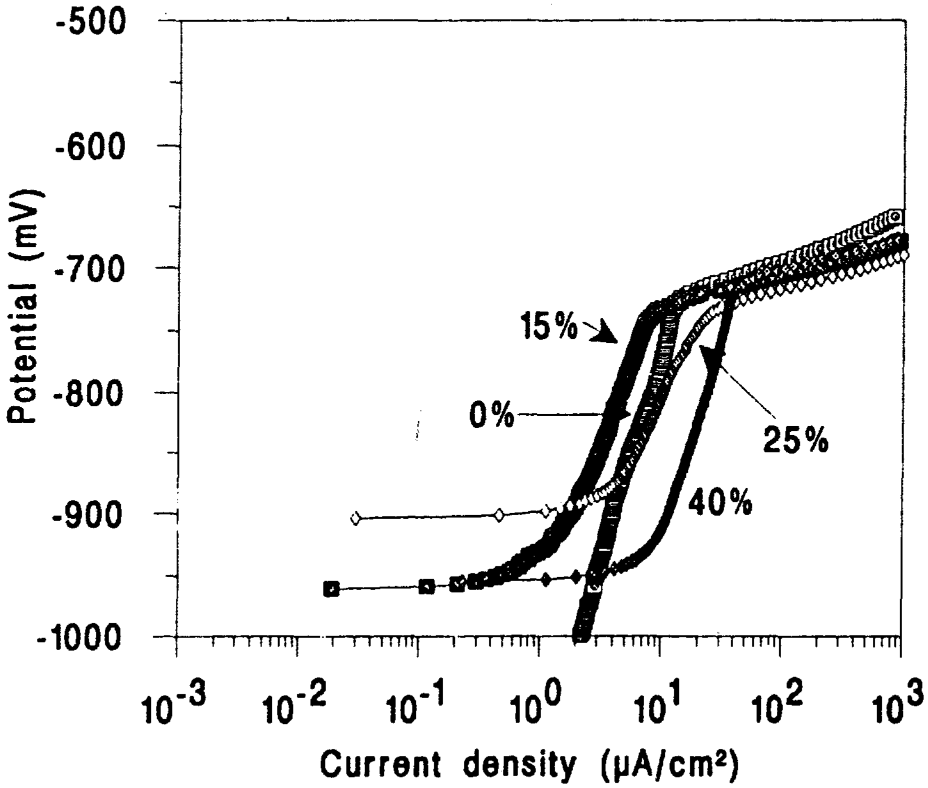

Figure 5.5 Anodic polarization curves for 6061/SiC MMCs in deaerated 0.5 N NaCl as a function of reinforcement concentration.

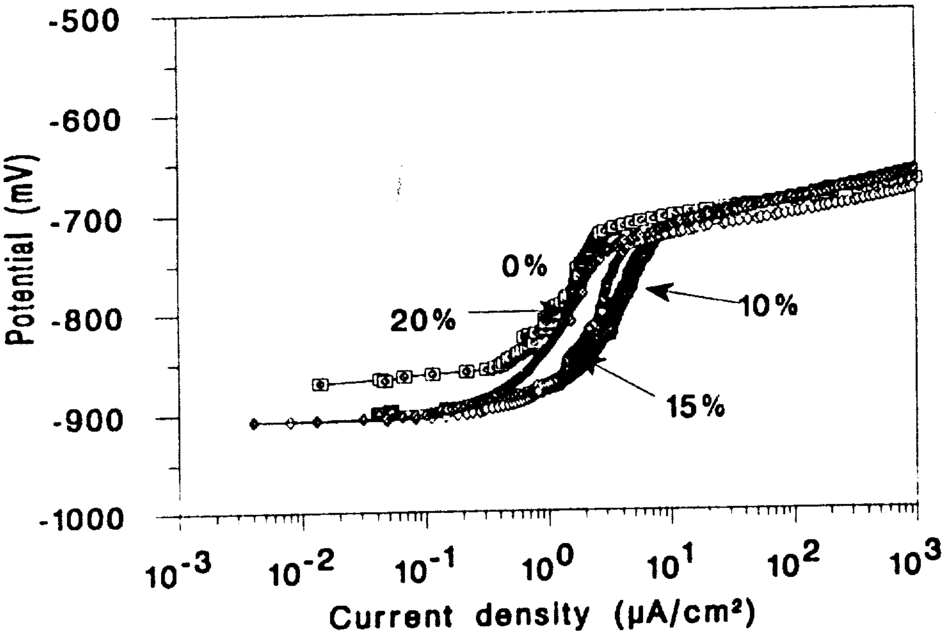

Figure 5.6 Anodic polarization curves for A356/SiC MMCs in deaerated 0.5 N NaCl as a function of reinforcement concentration.

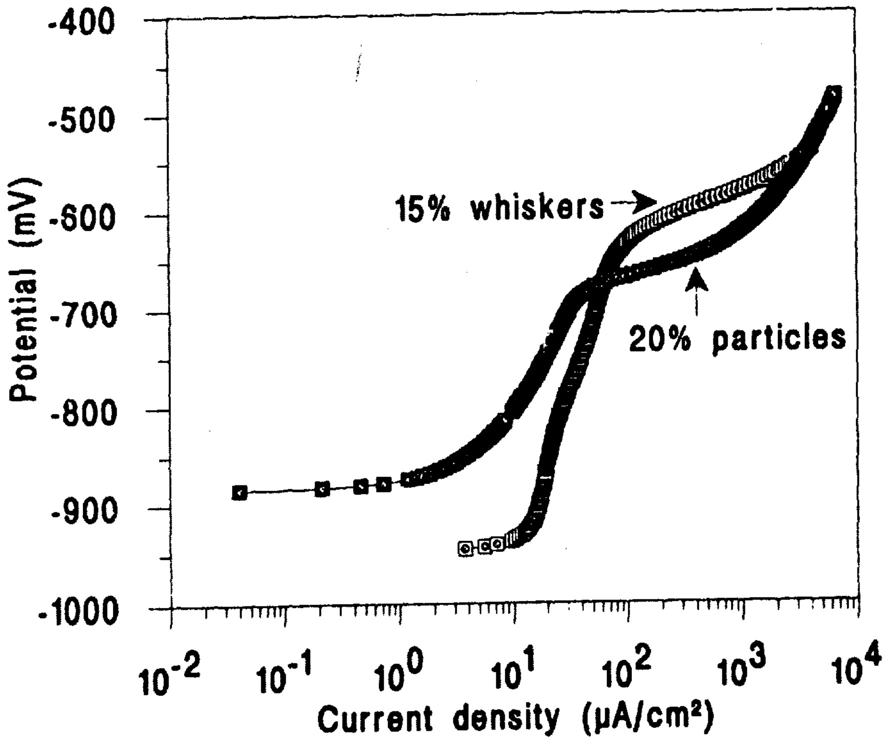

Figure 5.7 Anodic polarization curves for 2009/15% SiC_w and 20% SiC_p MMCs in deaerated 0.5 N NaCl.

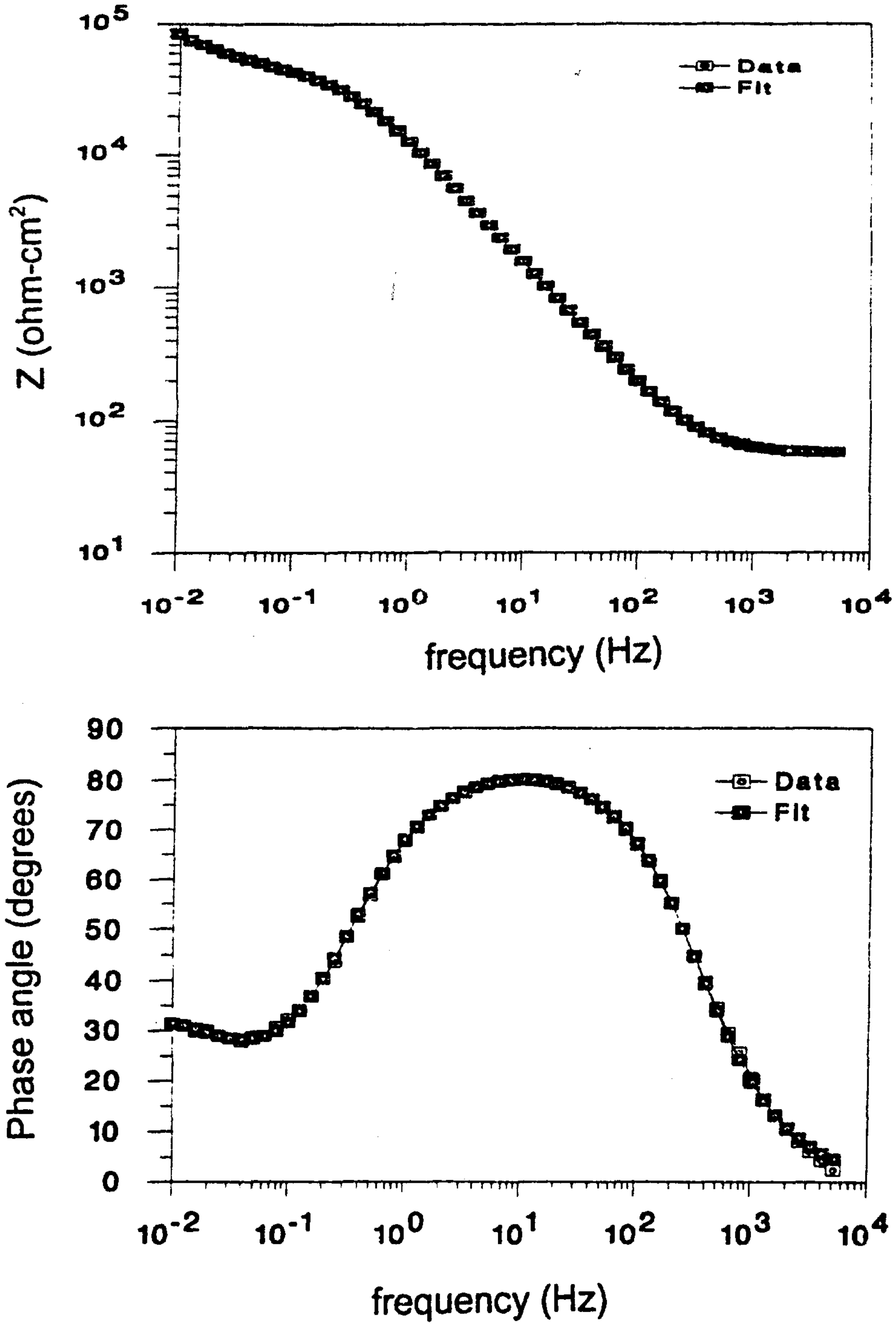

Figure 5.8 Bode plots for 6061/10% Al_2O_3 after 7 days in 0.5 N NaCl showing experimental data and fit results.

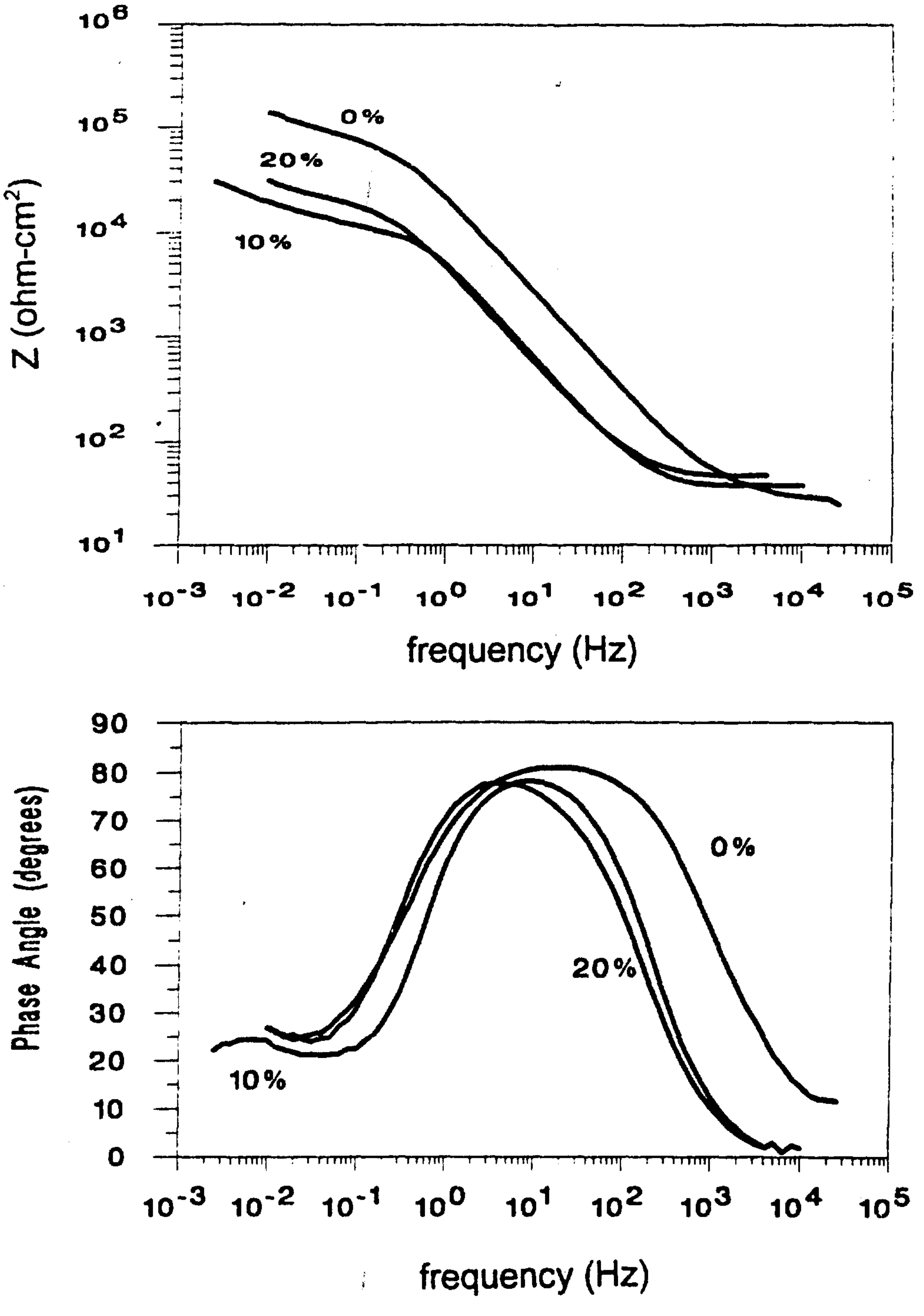

Figure 5.9 Bode plots for A356 after 2 days and for A356/10% and 20% SiC after 1 day in 0.5 N NaCl.

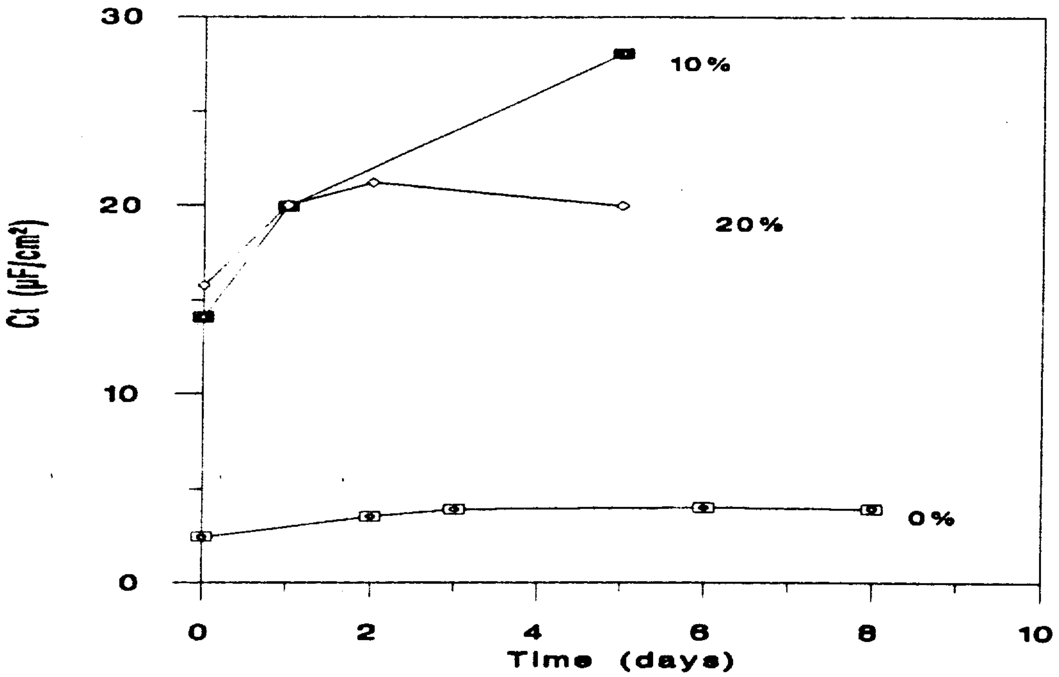

Figure 5.10 C_t as a function of exposure time for A356/SiC MMCs.

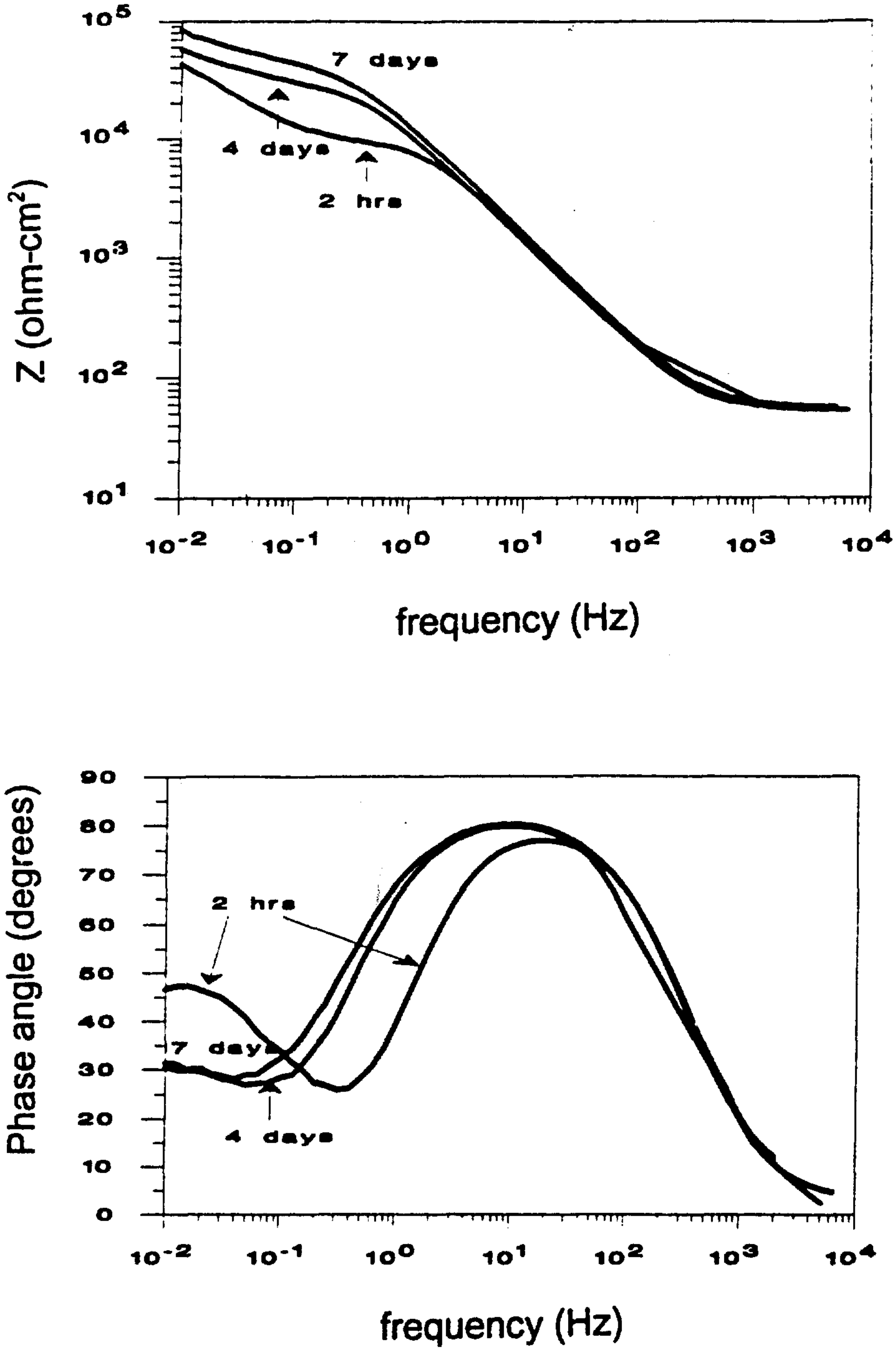

Figure 5.11 Bode plots for 6061/10% Al_2O_3 after 2 hours, 4 days and 7 days in 0.5 N NaCl.

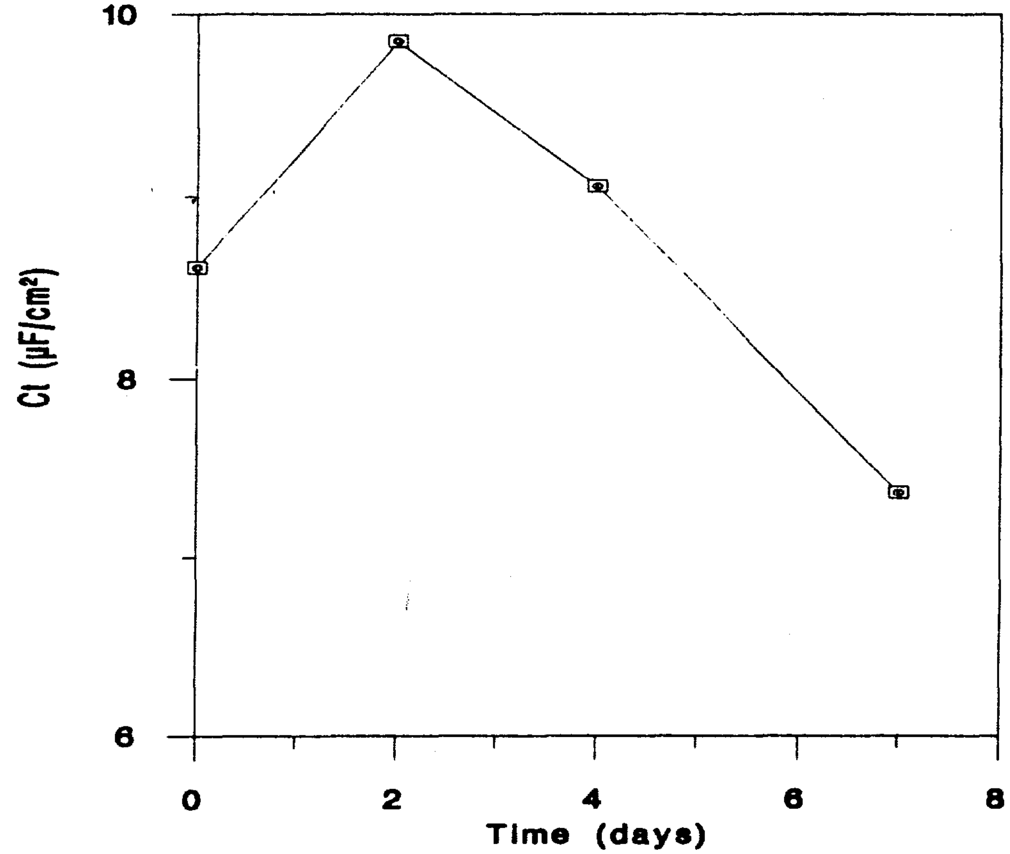

Figure 5.12 C_t versus time for 6061/10% Al_2O_3.

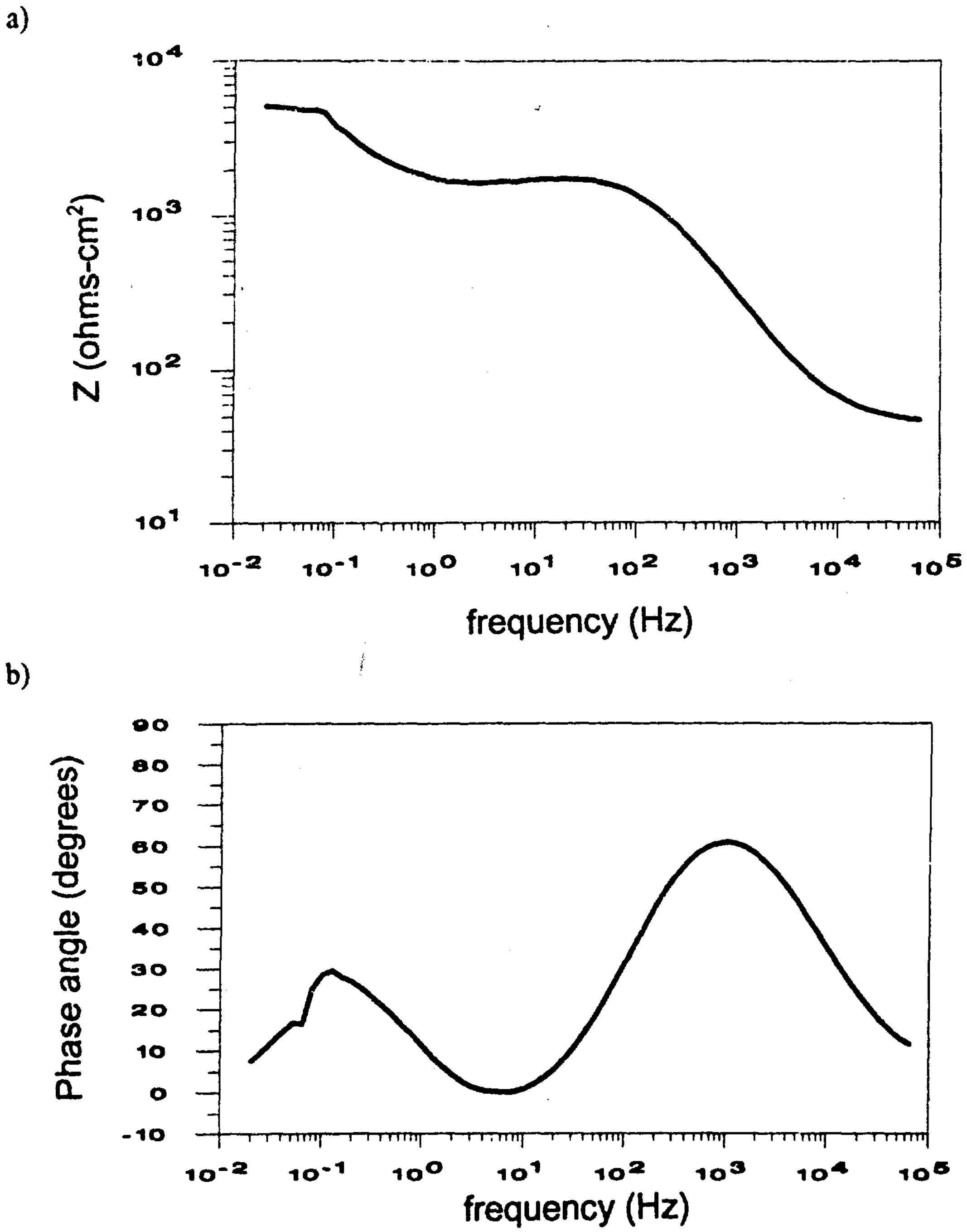

Figure 5.13 Bode plots (a and b) and Nyquist plot (c) for AA6061 after deoxidizing and polishing. Measurement conducted in Diverssey 560 Deoxidizer (Parker+Amchem Corporation).

Figure 5.13 (continued)

c)

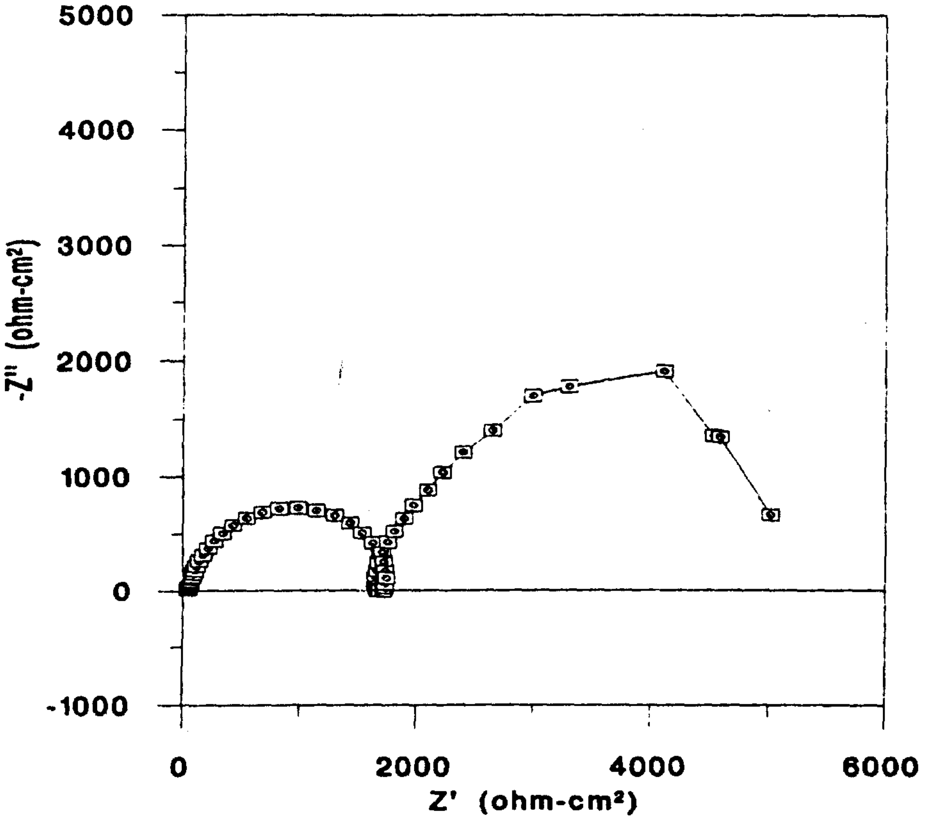

Figure 5.14 SEM micrograph of the as-received surface of a 6061/20% SiC MMC.

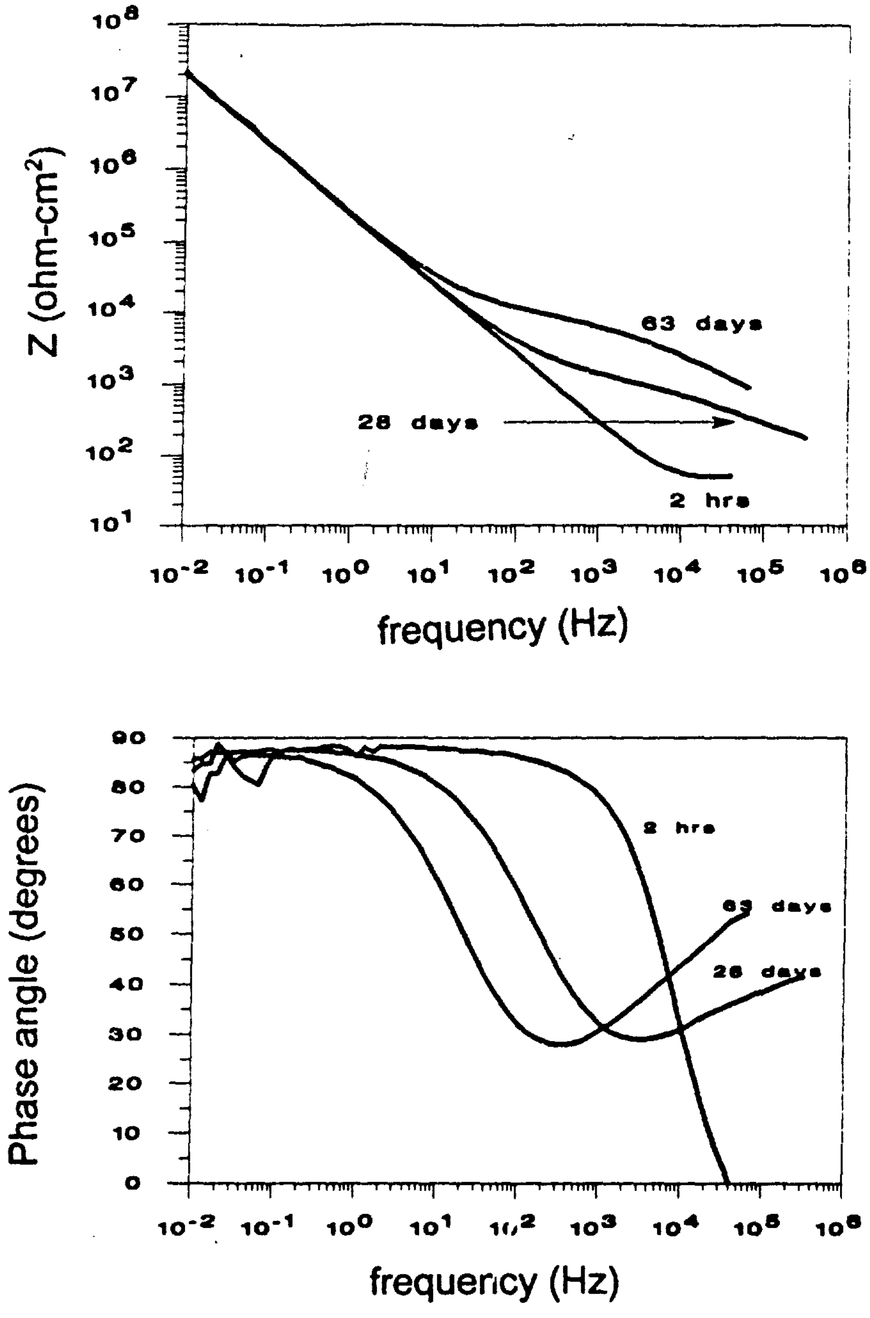

Figure 5.15 Bode plot of sulphuric acid anodized AA6061 after immersion in 0.5 N NaCl for 2 hrs, 28 days and 63 days. Sample was not sealed prior to immersion.

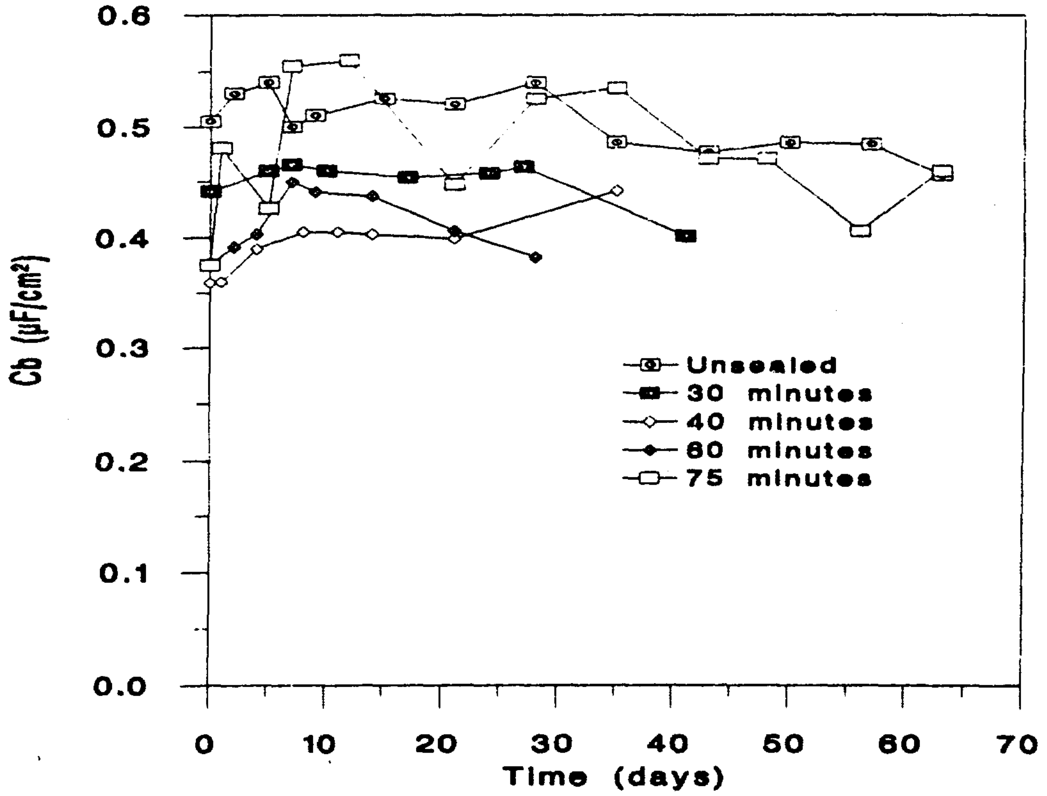

Figure 5.16 Barrier layer capacitance, C_b, as a function of exposure time in 0.5 N NaCl for sulphuric acid anodized AA6601 for sealed and unsealed samples.

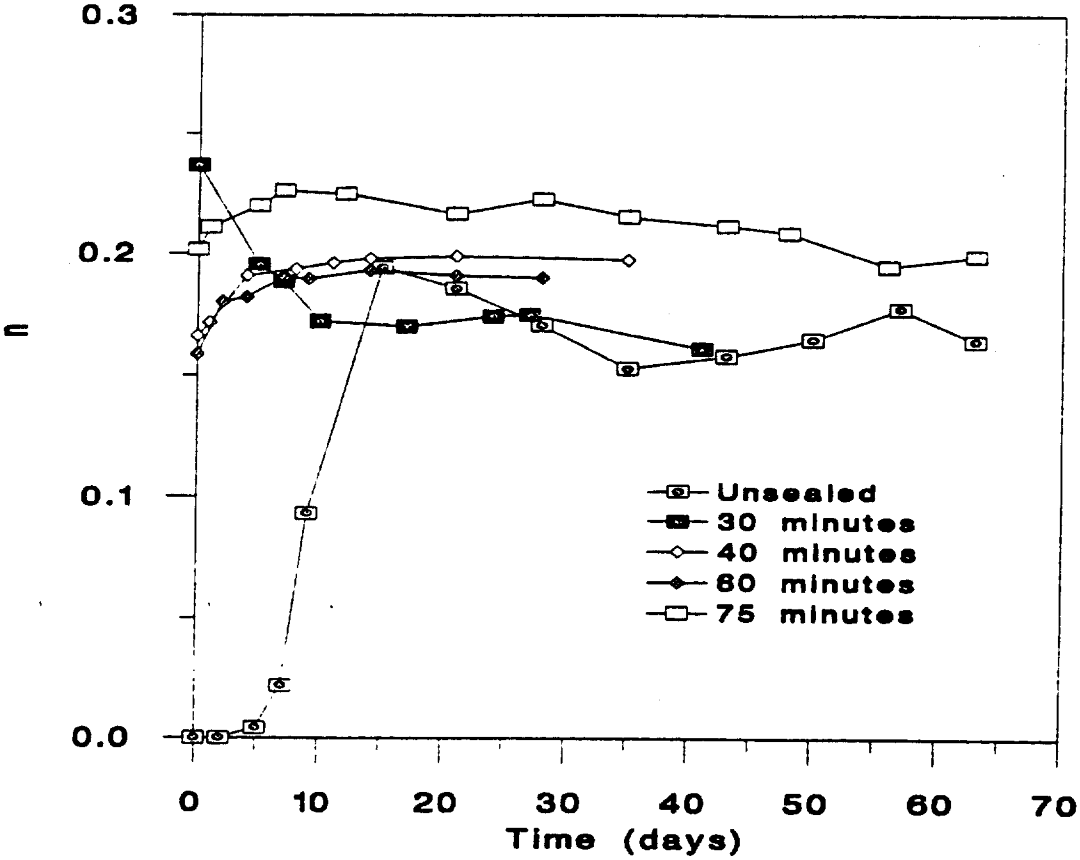

Figure 5.17 Transmission line exponent, n, of pore impedance versus exposure time for hot water sealed and unsealed AA6061.

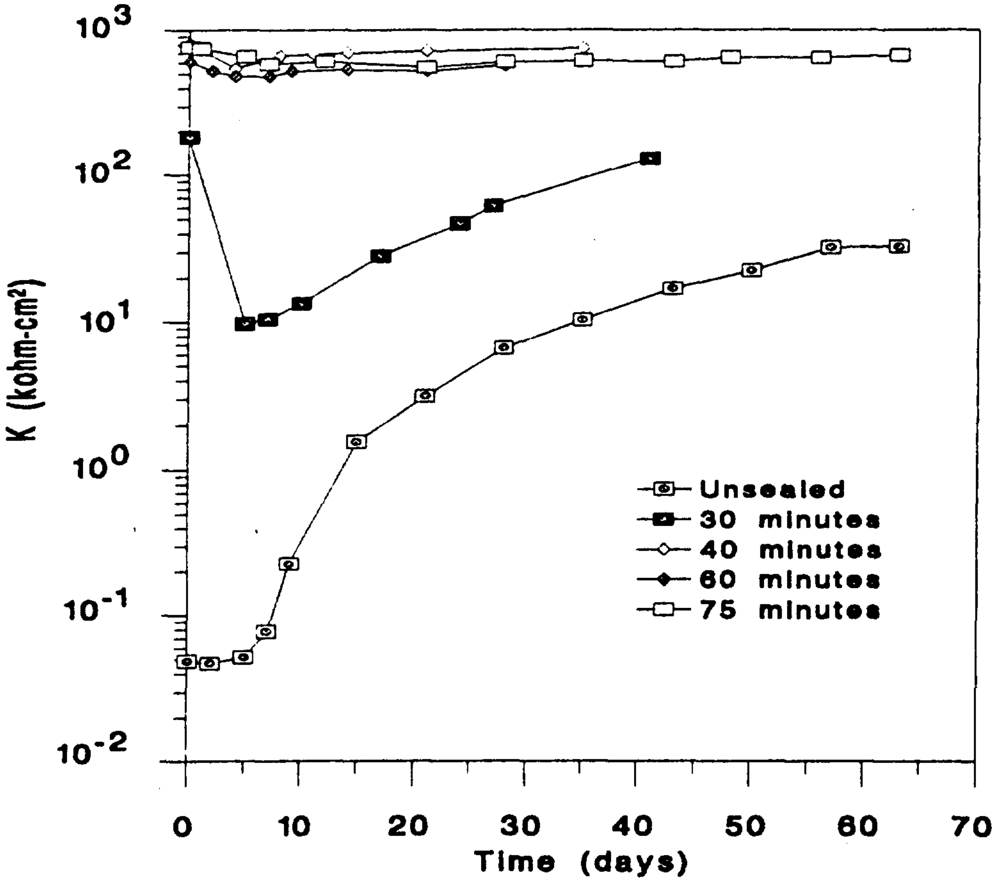

Figure 5.18 Transmission line coefficient, K, of pore impedance versus exposure time for hot water sealed and unsealed AA6061.

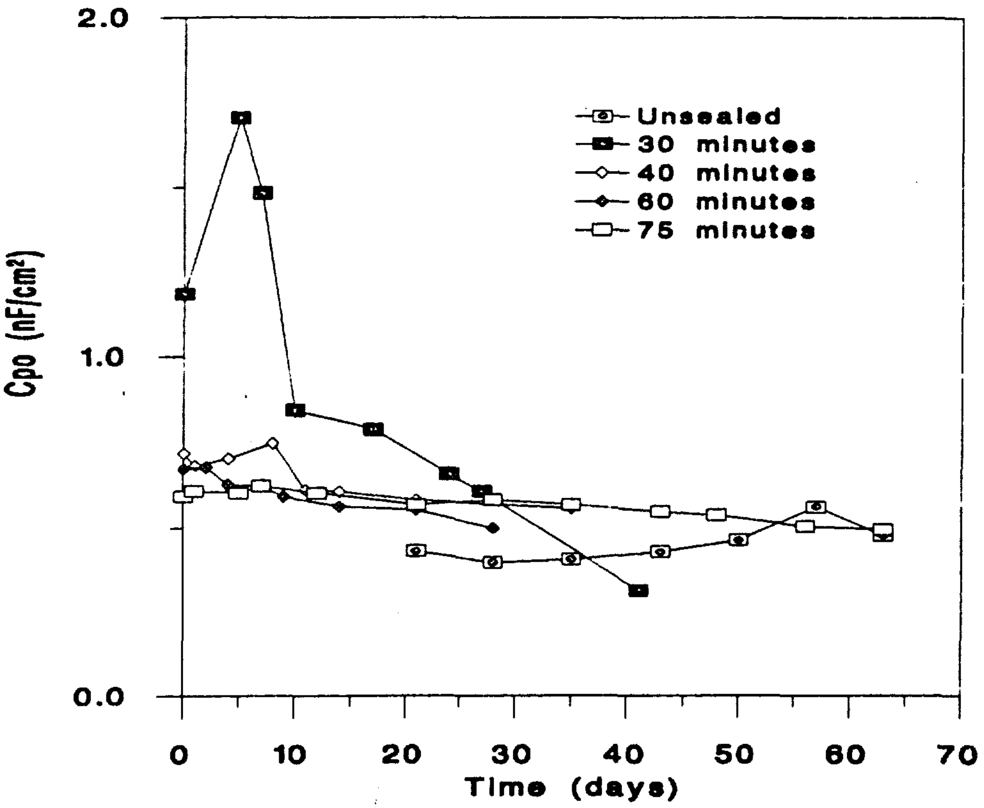

Figure 5.19 Porous layer capacitance, C_{po}, versus exposure time for hot water sealed and unsealed AA6061.

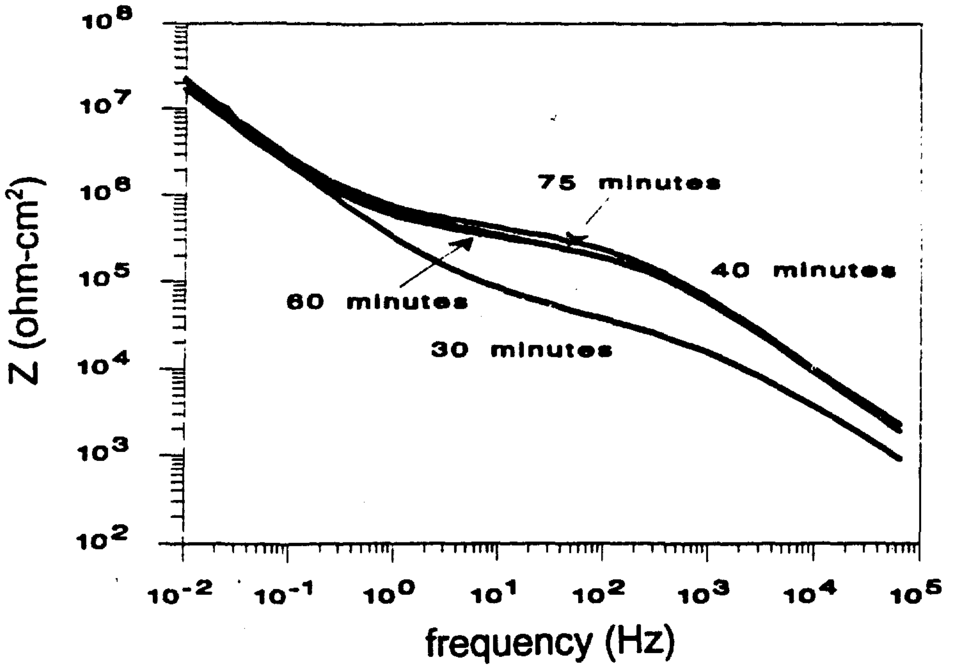

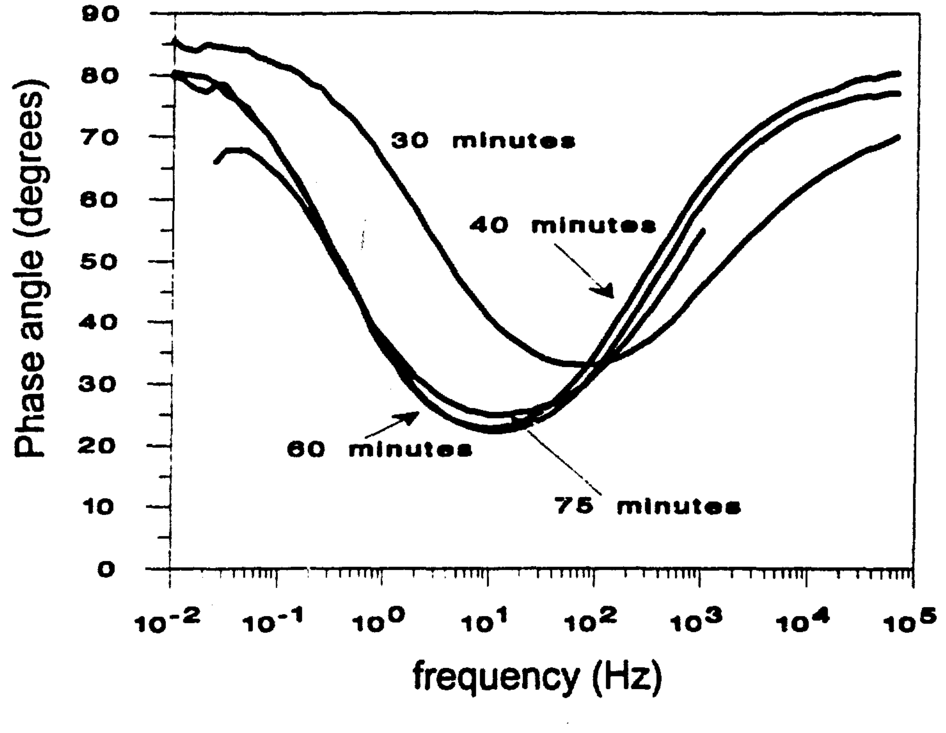

Figure 5.20 Bode plots for sulphuric acid anodized and hot water sealed AA6061 after two hours of exposure to 0.5 N NaCl; results for sealing times of 30, 40, 60 and 75 minutes.

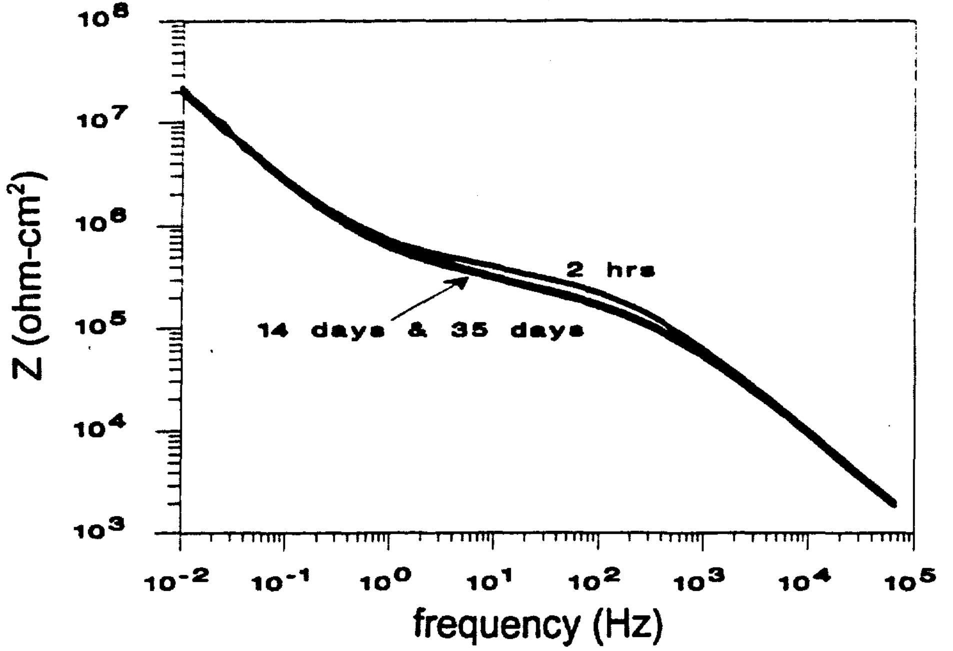

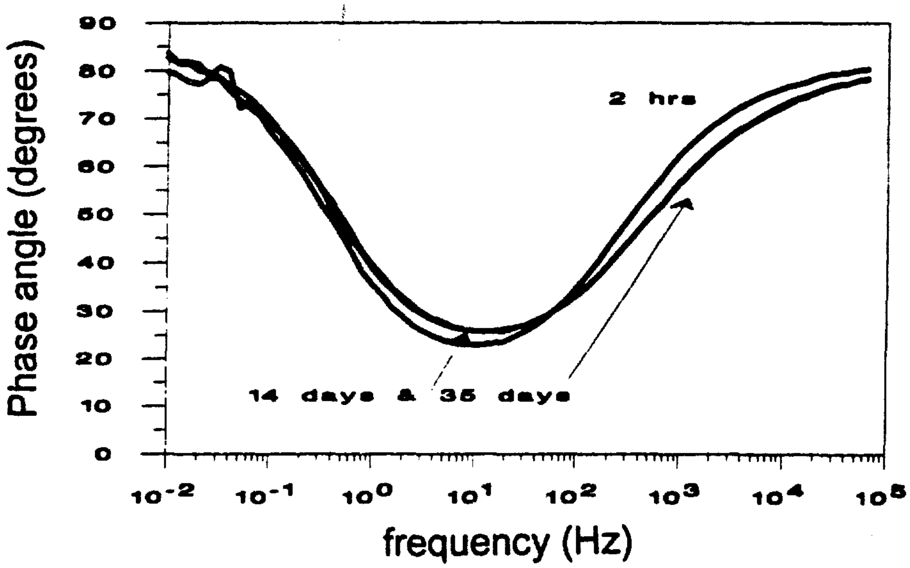

Figure 5.21 Bode plots for sulphuric acid anodizing and hot water sealing for 40 minutes on AA6061 after 2 hrs, 14 days and 35 days of exposure to 0.5 N NaCl.

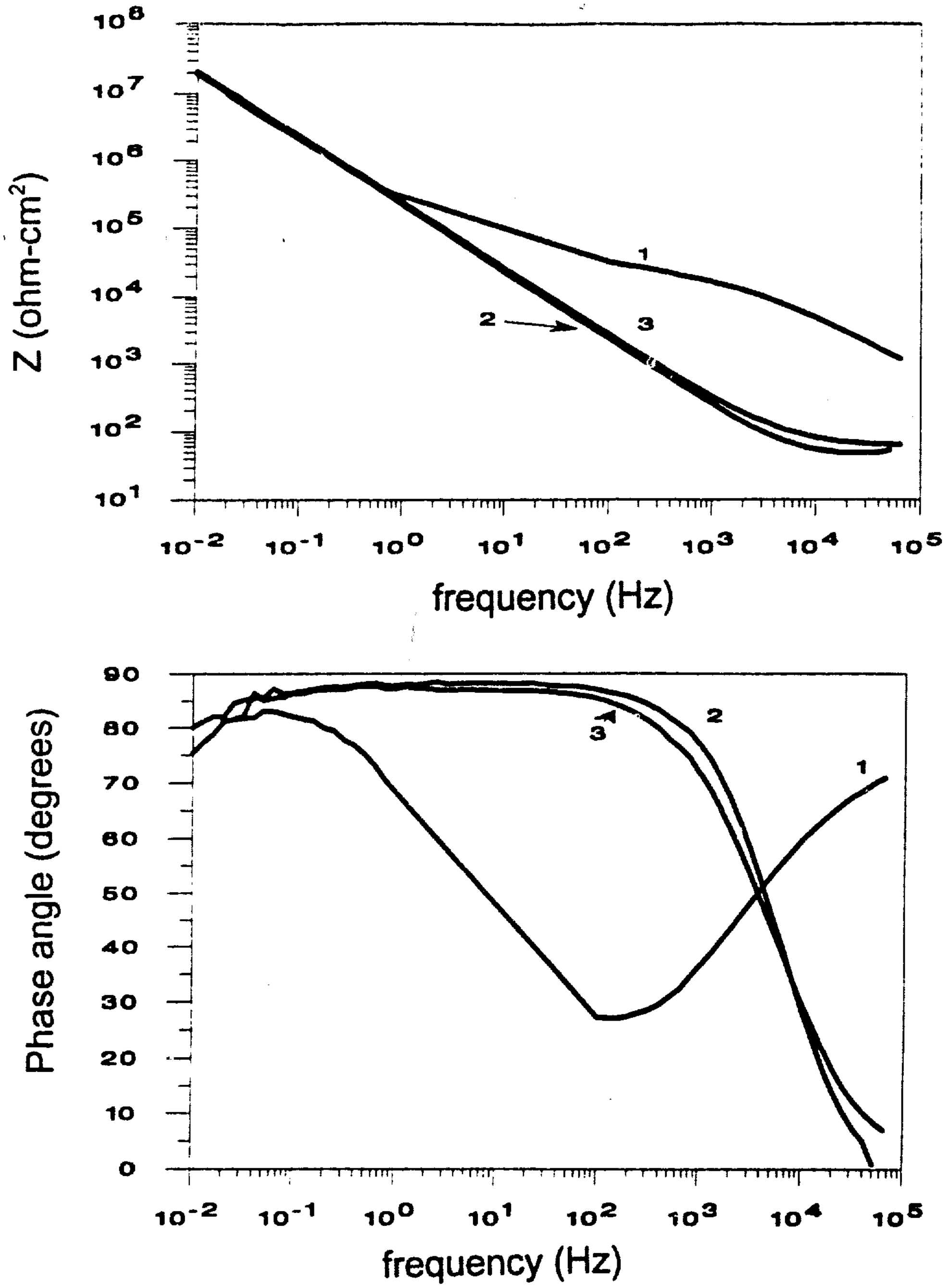

Figure 5.22 Bode plots for sulphuric acid anodizing and dichromate sealing of AA6061 using procedures 1, 2 and 3 after 2 hours of exposure to 0.5 N NaCl.

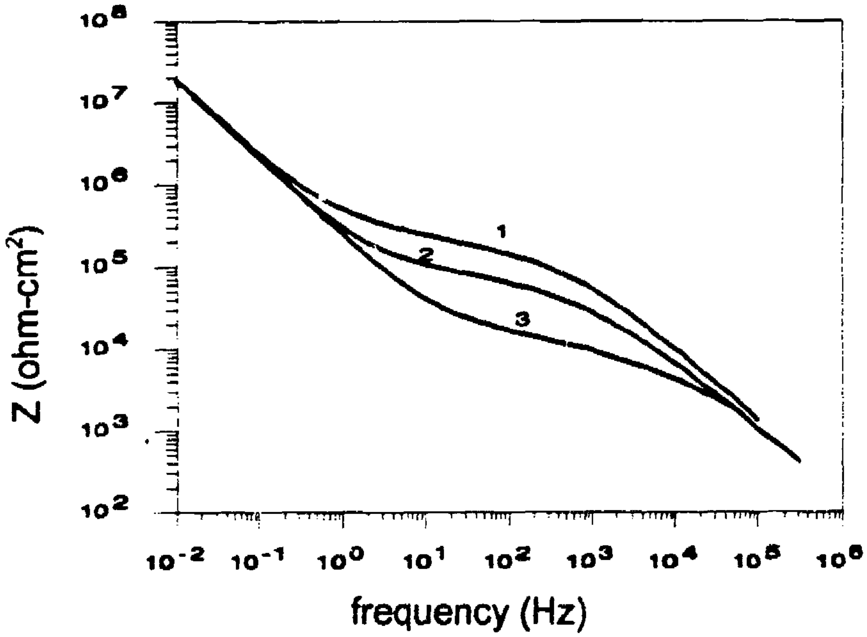

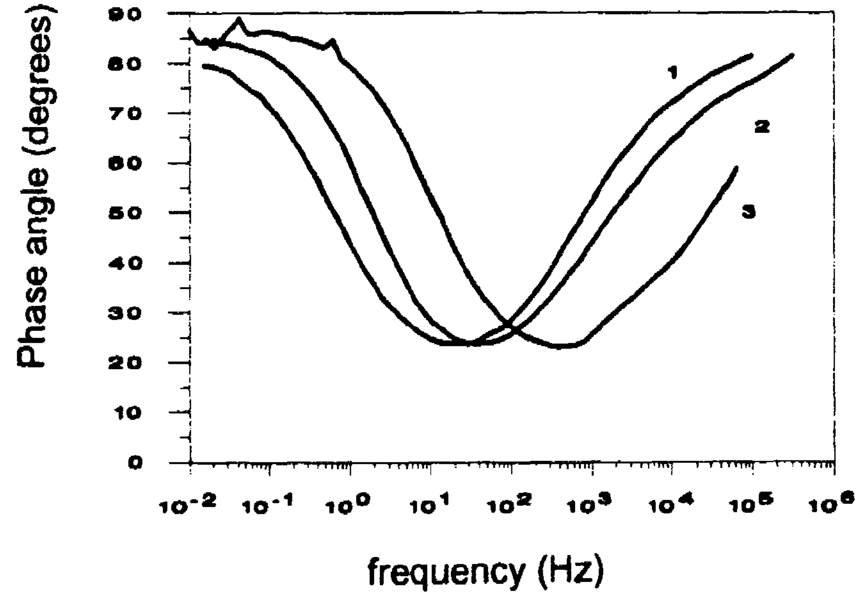

Figure 5.23 Bode plot for sulphuric acid anodizing and dichromate sealing of AA6061 using procedures 1,2 and 3 after 28 days in 0.5 N NaCl.

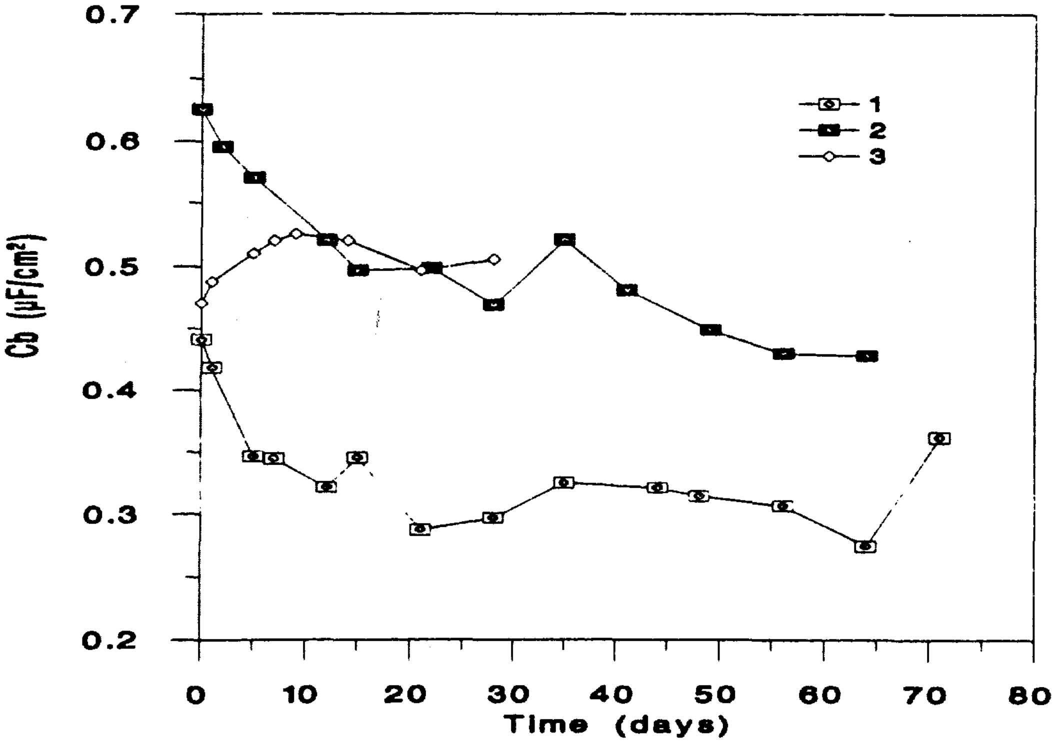

Figure 5.24 Barrier layer capacitance, C_b, versus exposure time for anodized and dichromate sealed AA6061 . Results are shown for sealing procedures 1, 2 and 3.

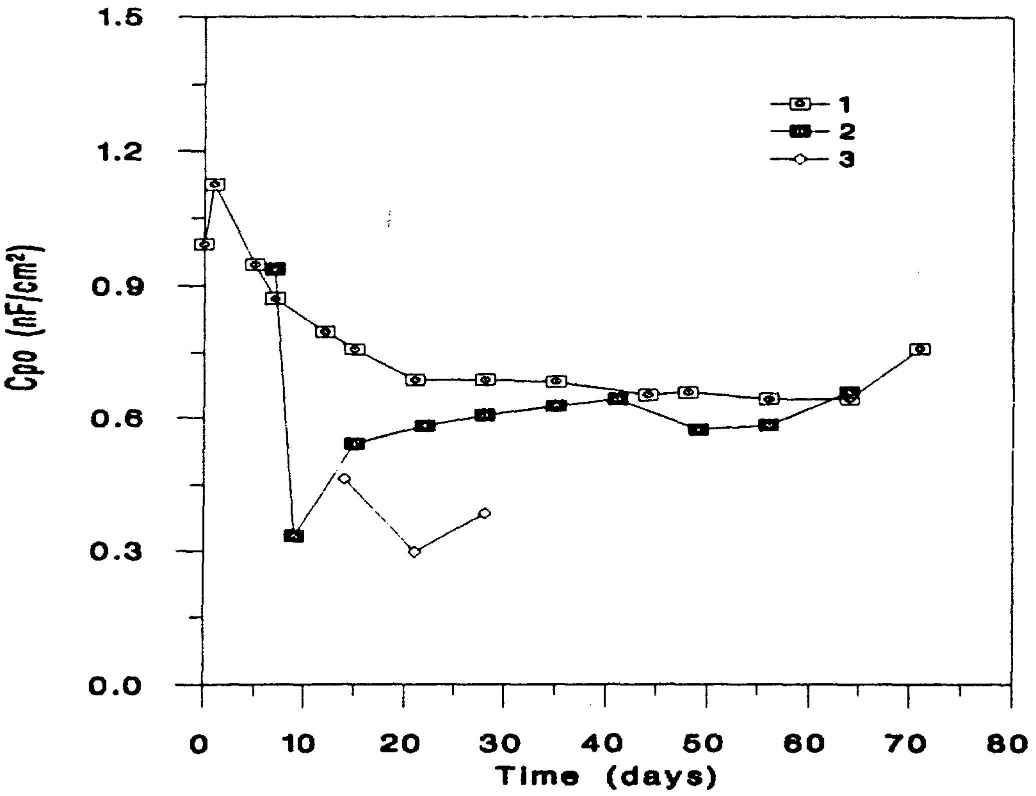

Figure 5.25 Porous layer capacitance, C_{po}, versus exposure time for anodized and dichromate sealed AA6061 . Results are shown for sealing procedures 1, 2 and 3.

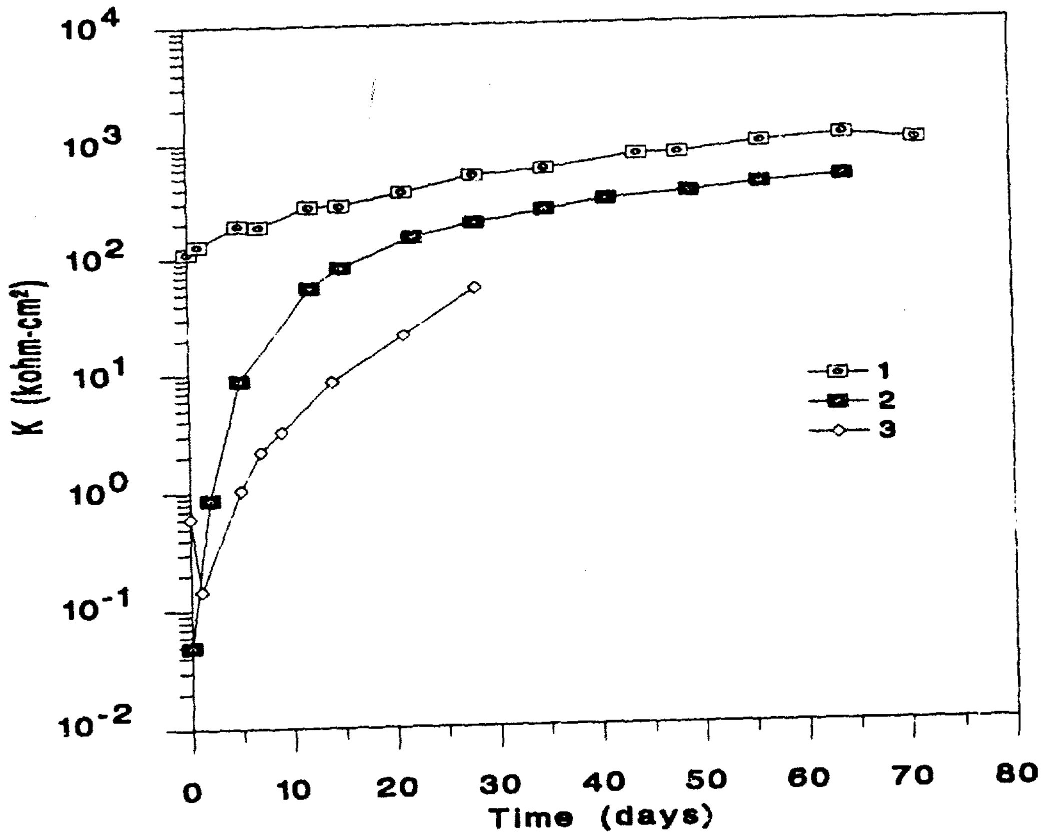

Figure 5.26 Transmission line coefficient, K, of pore impedance versus exposure time for dichromate sealing on AA6061 using procedures 1, 2 and 3.

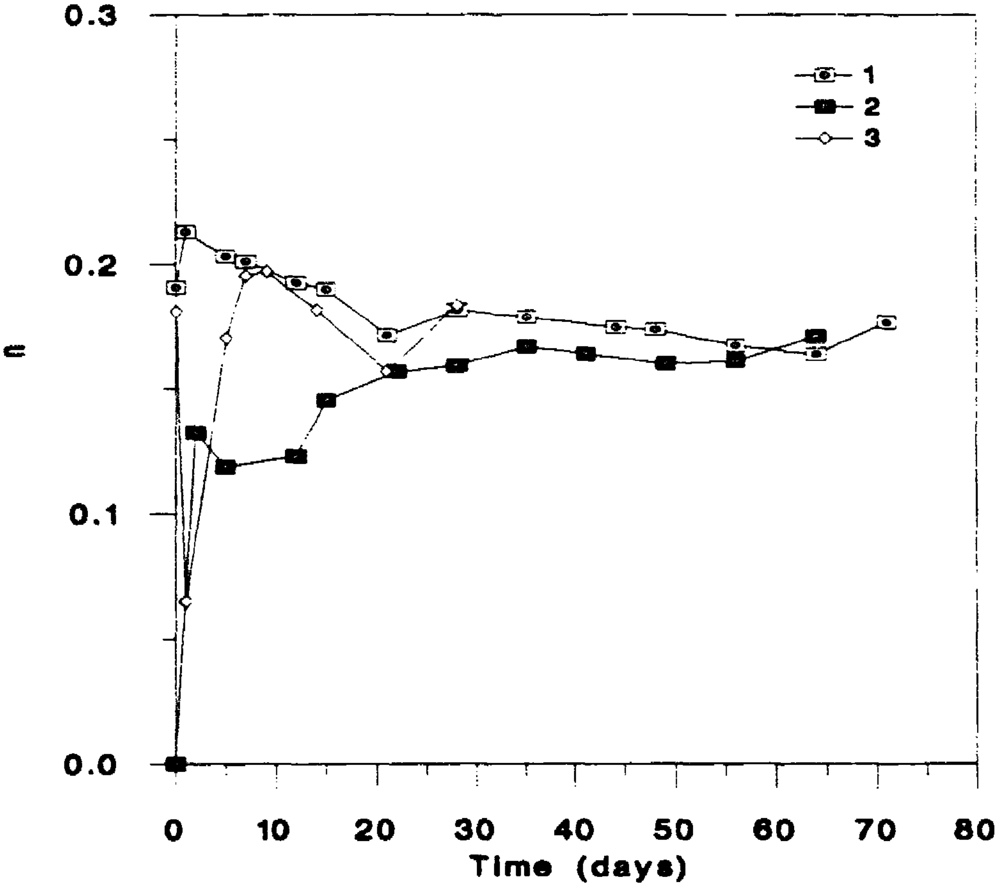

Figure 5.27 Transmission line exponent, n, of pore impedance versus exposure time for dichromate sealing on AA6061 using procedures 1, 2 and 3.

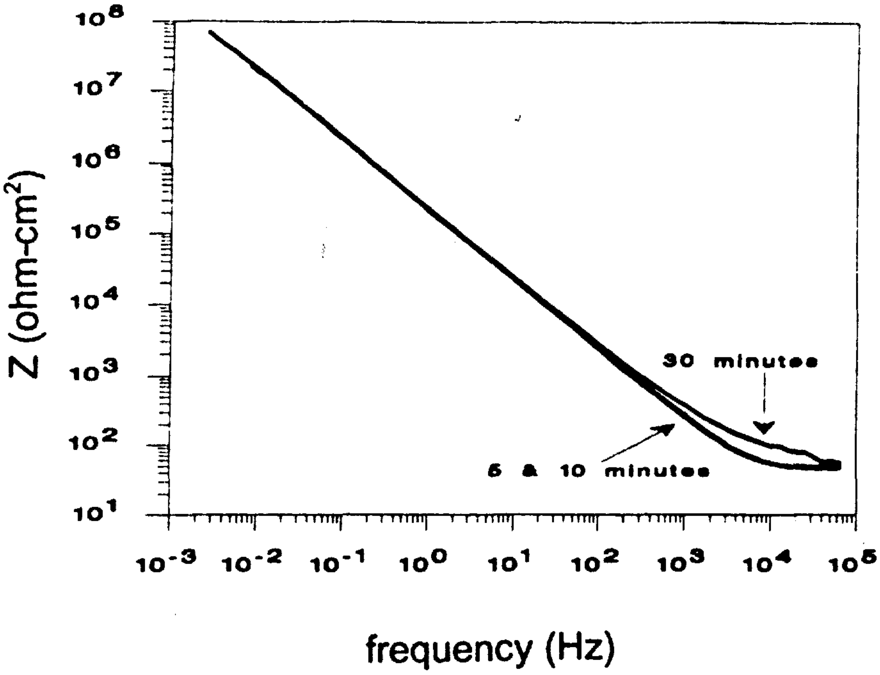

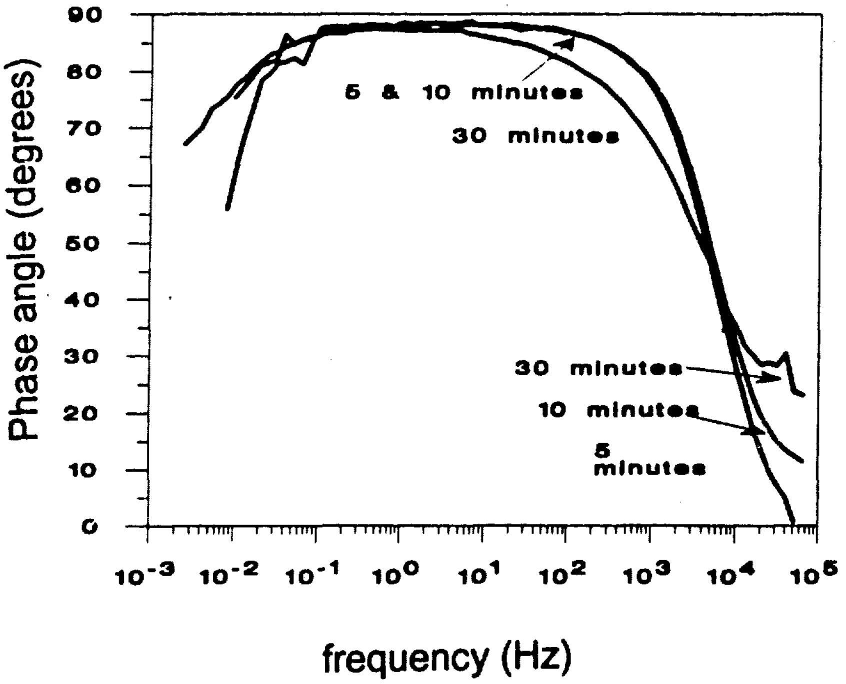

Figure 5.28 Bode plots for anodized AA6061after 2 hours of exposure to 0.5 N NaCl. Dichromate sealed for 5,10 and 30 minutes.

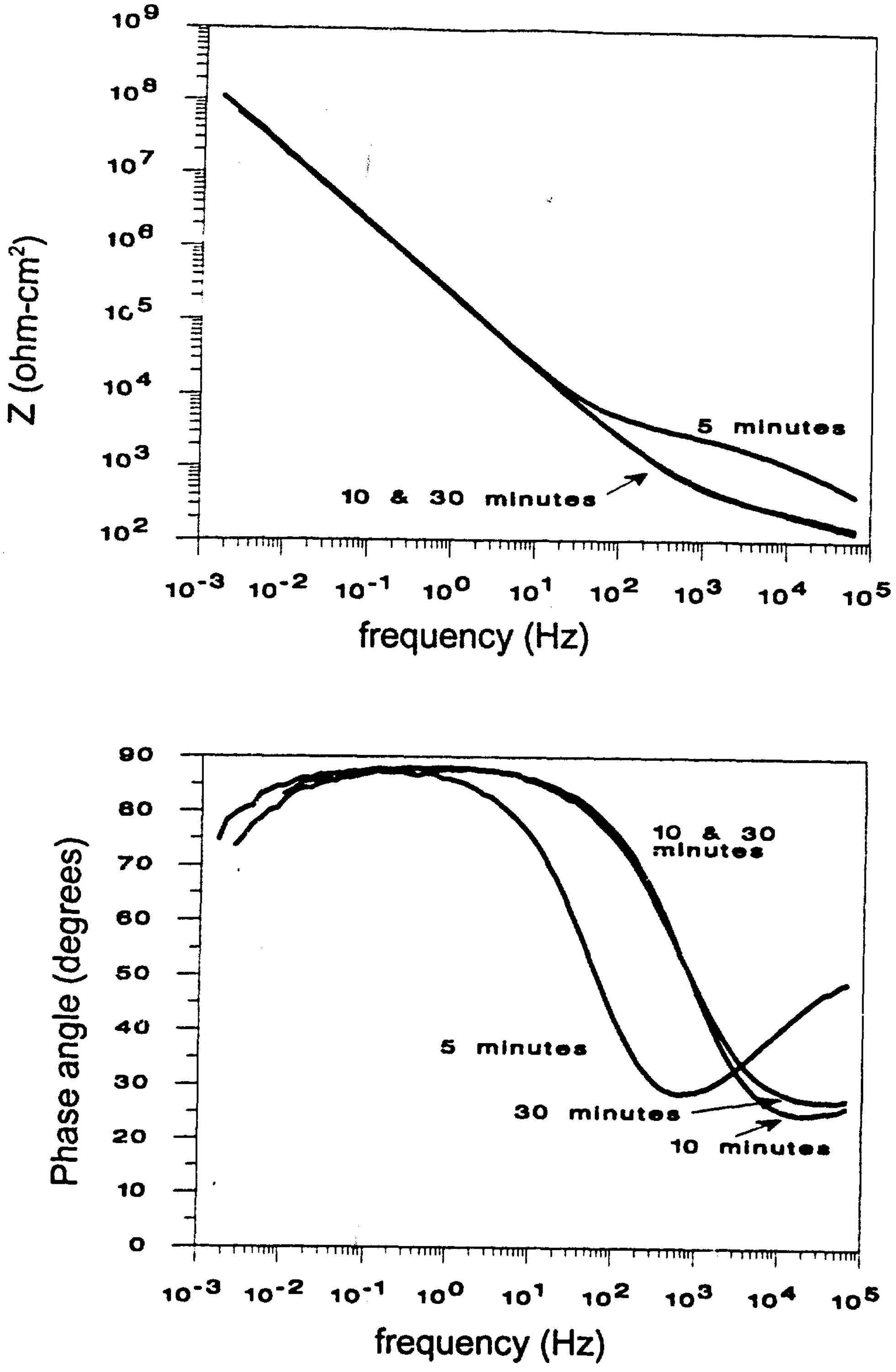

Figure 5.29 Bode plots for anodized AA6061after 5 days in 0.5 N NaCl. Dichromate sealed for 5,10 and 30 minutes.

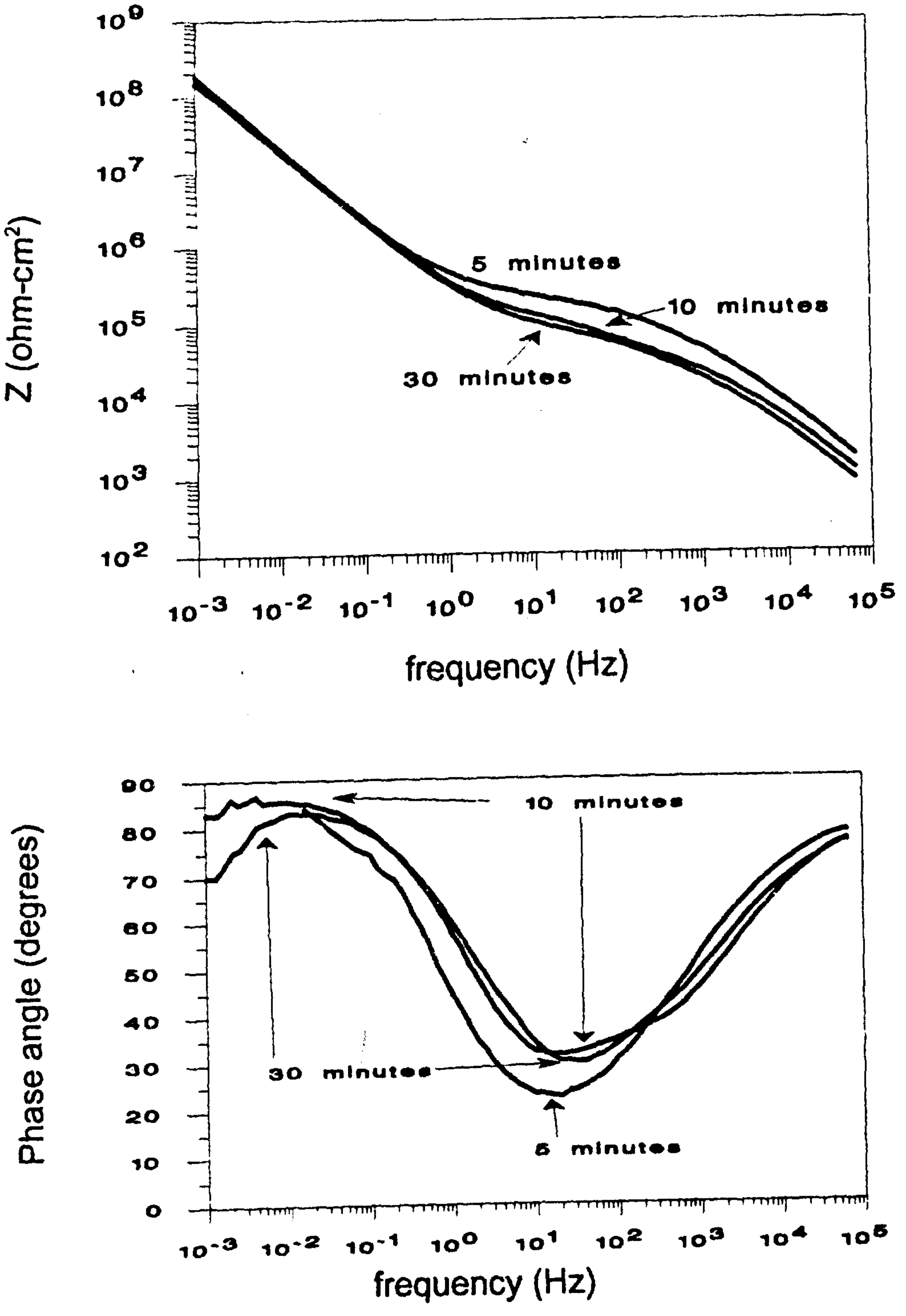

Figure 5.30 Bode plots for anodized AA6061 in 0.5 N NaCl. Dichromate sealed for 5,10 and 30 minutes. Exposure time of 64 days for sealing for 5 minutes and 62 days for the 10 and30 minute sealing.

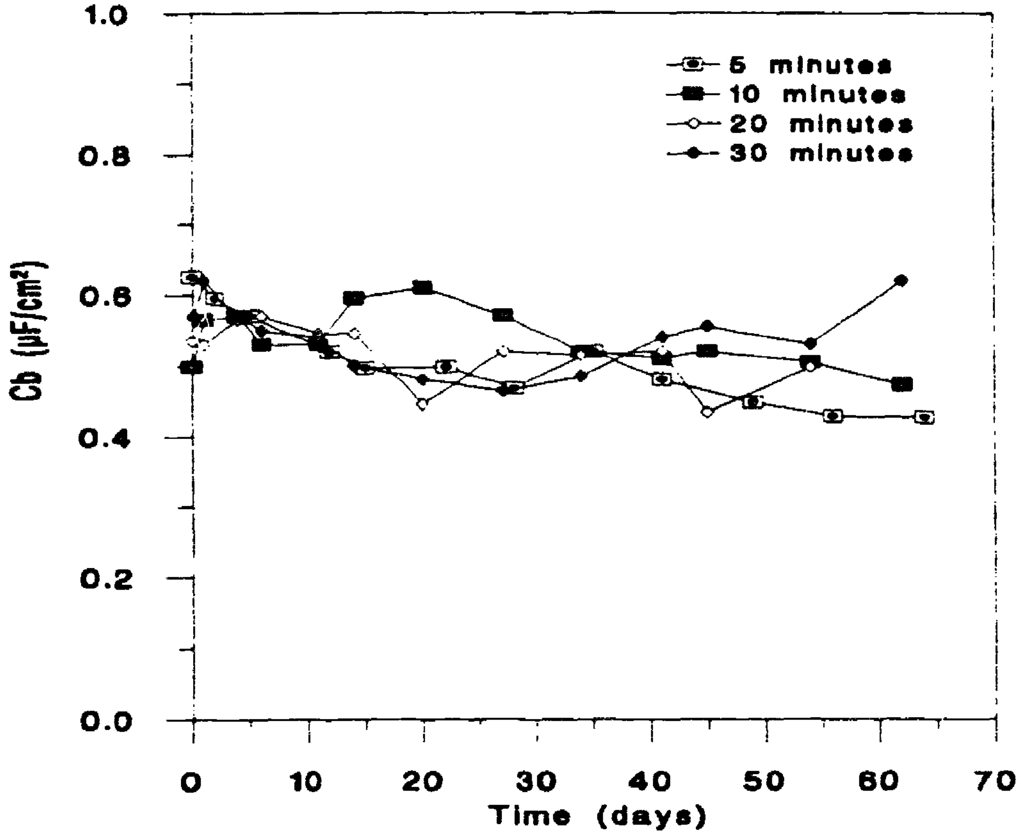

Figure 5.31 Barrier layer capacitance, C_b, versus exposure time for anodized AA6061. Dichromate sealed for 5, 10, 20 and 30 minutes.

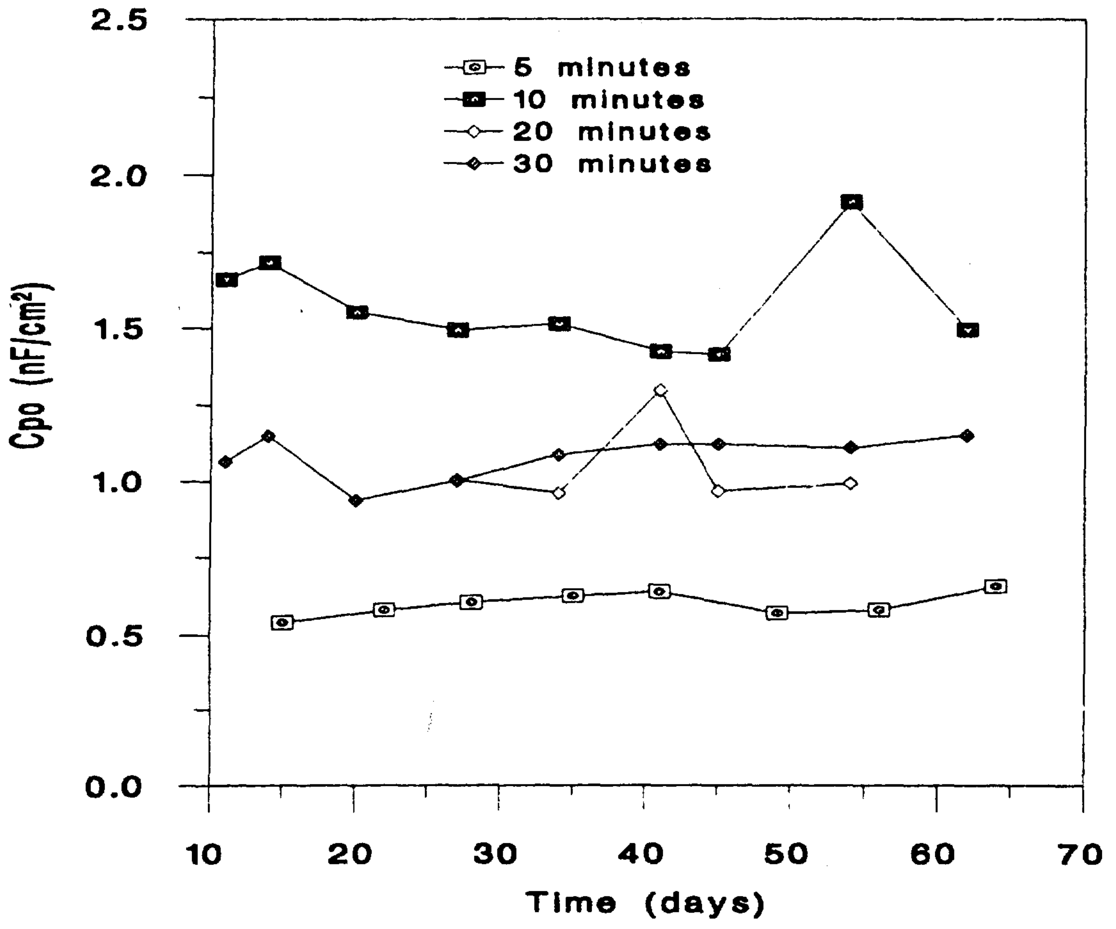

Figure 5.32 Porous layer capacitance, C_{po}, versus exposure time for anodized AA6061. Dichromate sealed for 5, 10, 20 and 30 minutes.

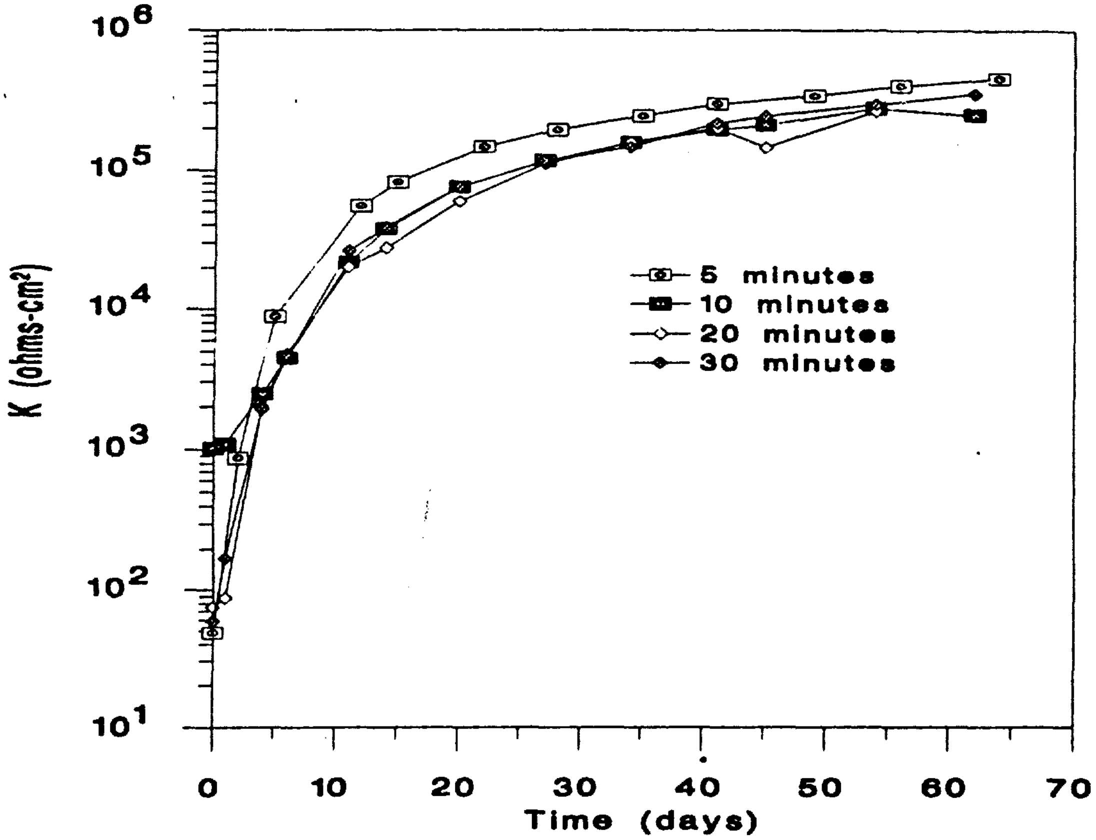

Figure 5.33 Transmission line coefficient, K, of pore impedance versus exposure time for anodized AA6061. Dichromate sealed for 5, 10, 20 and 30 minutes.

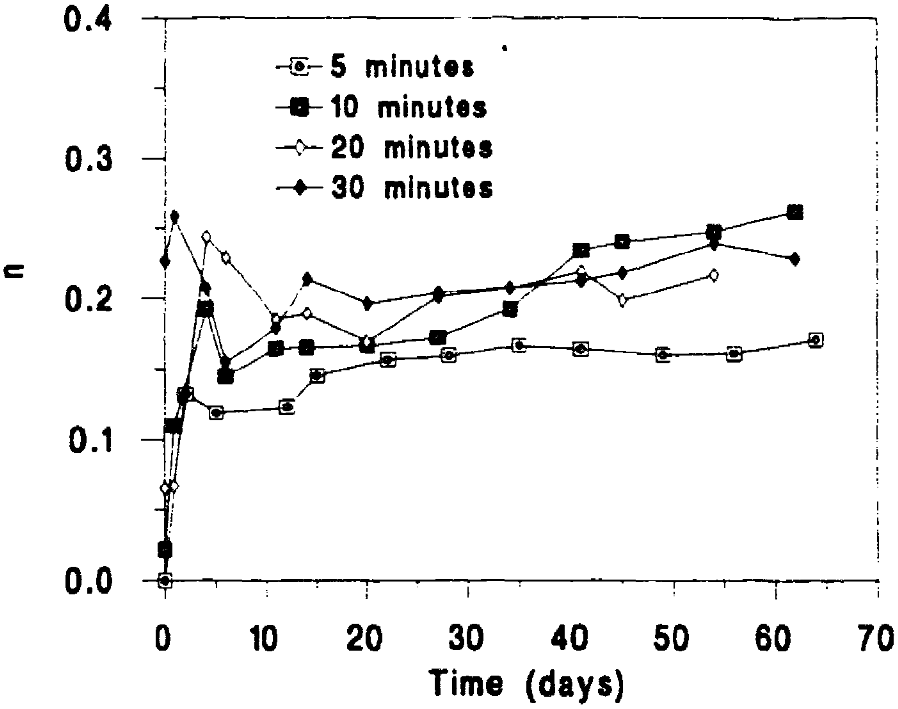

Figure 5.34 Transmission line exponent, n, of pore impedance versus exposure time for anodized AA6061. Dichromate sealed for 5, 10, 20 and 30 minutes.

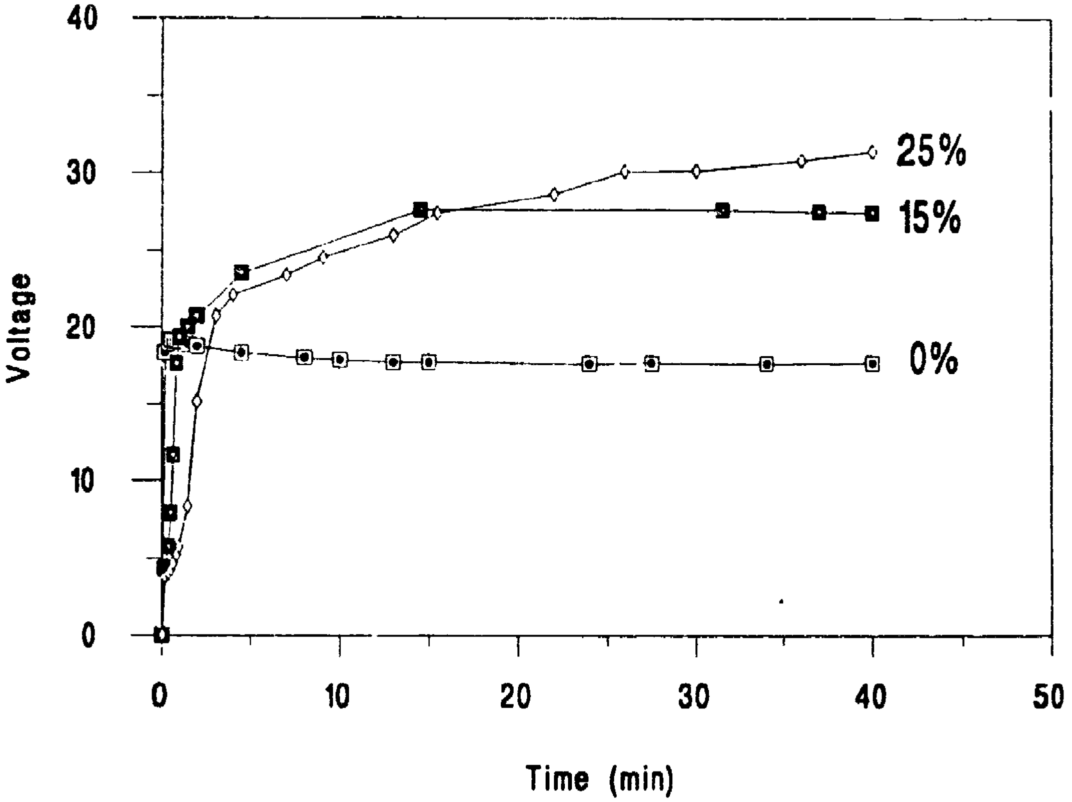

Figure 5.35 Anodizing voltage versus time for AA6061 and 6061/15% and 25% SiC MMCs.

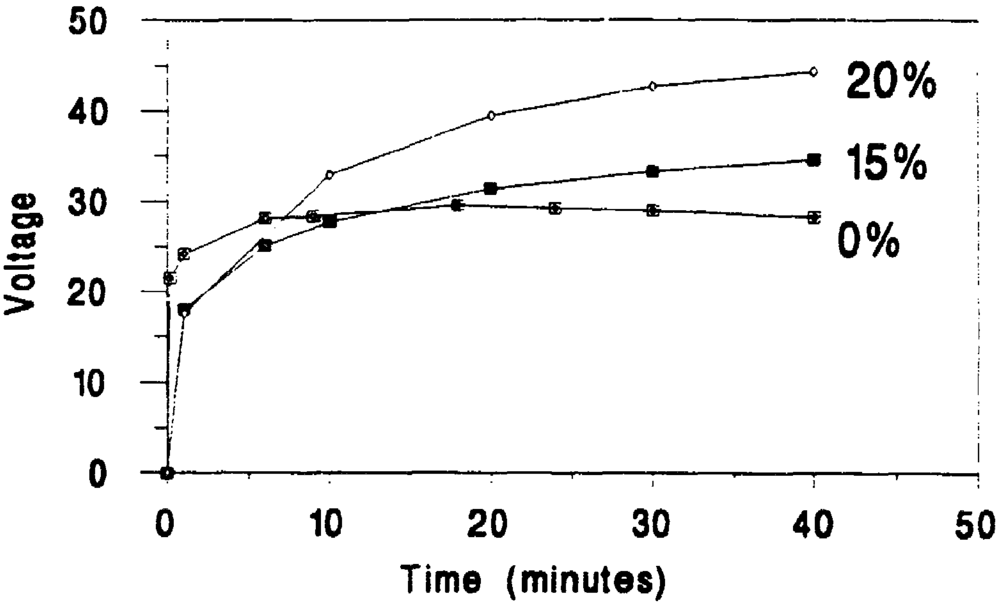

Figure 5.36 Anodizing voltage versus time for A356 and A356/15% and 20% SiC MMCs.

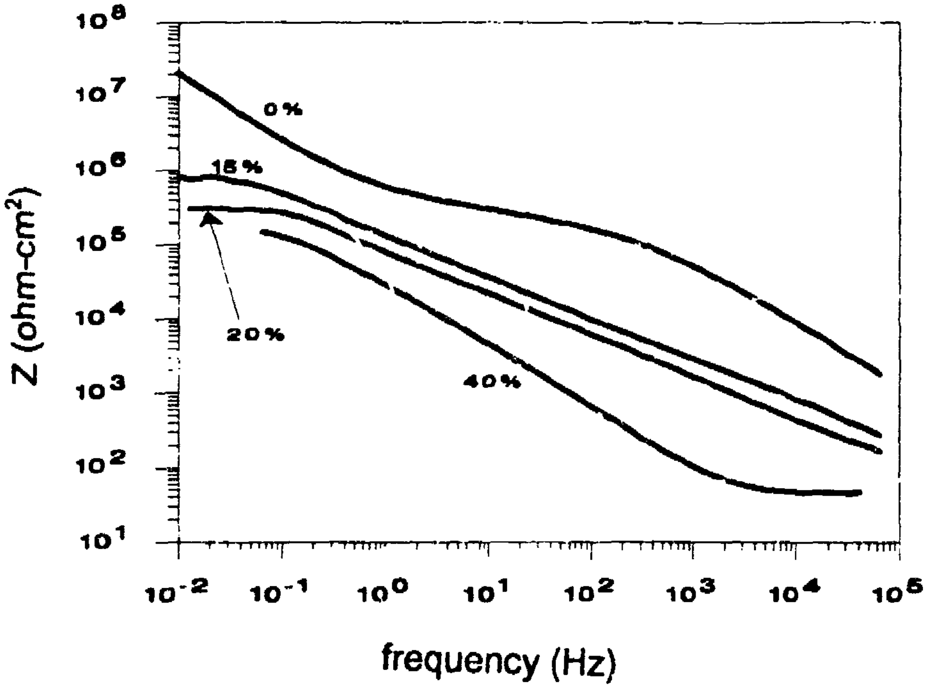

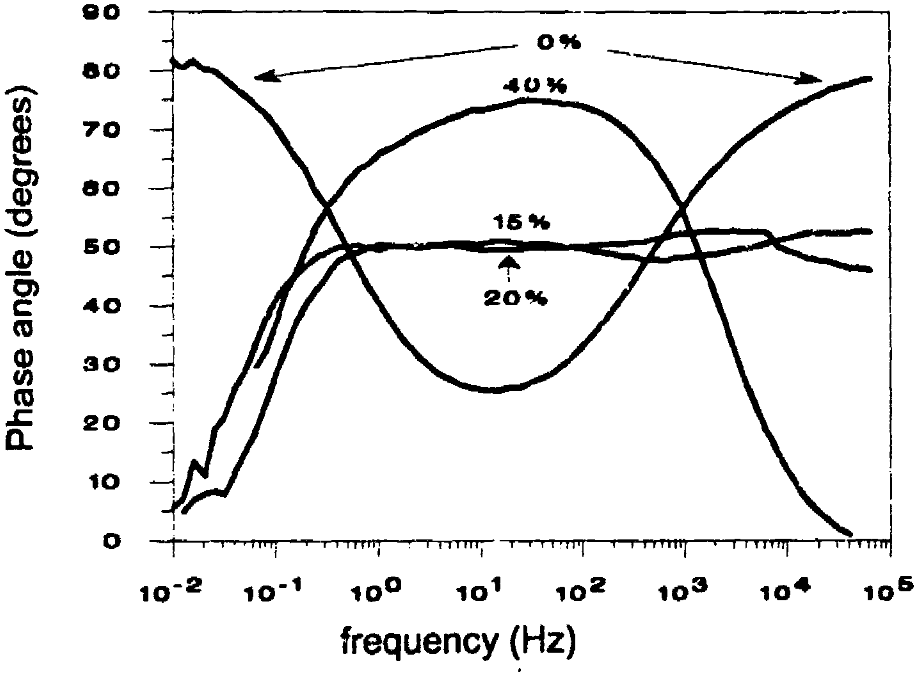

Figure 5.37 Bode plot for sulphuric acid anodizing and hot water sealing on 6061/SiC MMCs after 7 days in 0.5 N NaCl.

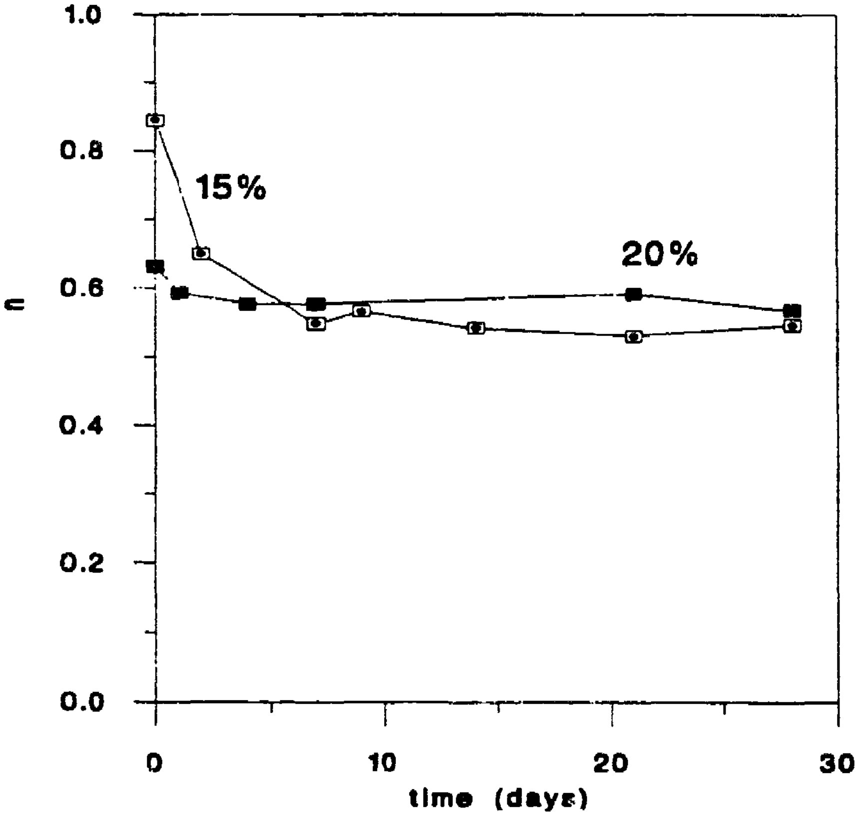

Figure 5.38 Exponent of Constant Phase Element for anodized and hot water sealed 6061/15% SiC and 20% SiC versus exposure time.

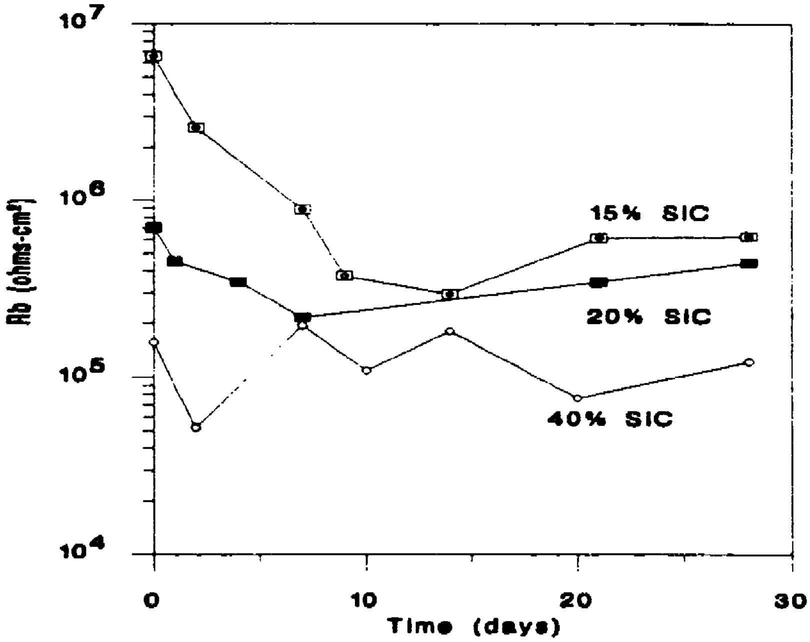

Figure 5.39 Barrier layer resistance versus immersion time for anodized and hot water sealed 6061/SiC MMCs.

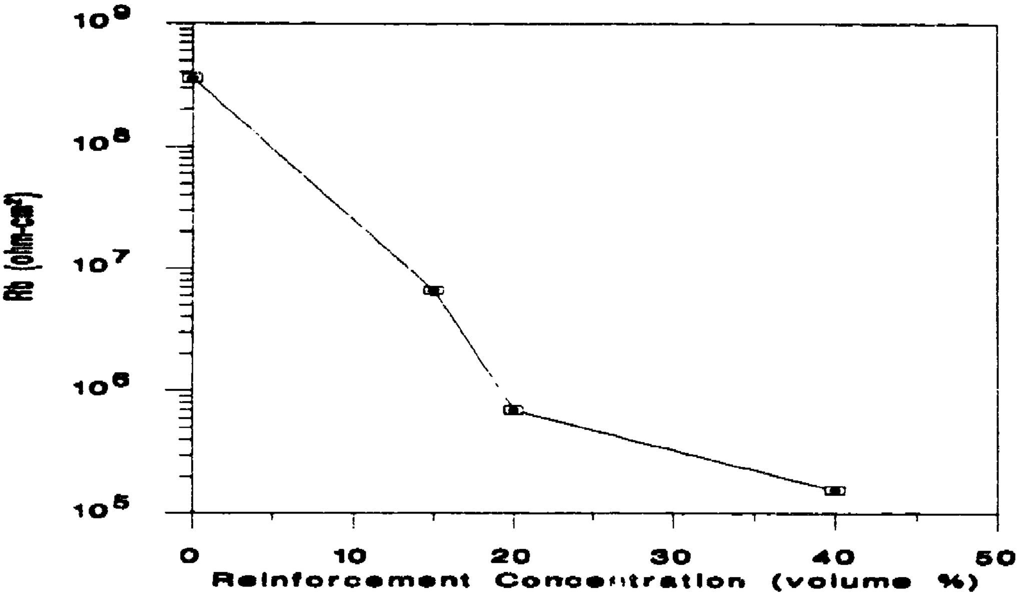

Figure 5.40 Barrier layer resistance of anodized 6061/SiC MMCs versus percent reinforcement after 2 hrs of exposure to 0.5 N NaCl.

a)

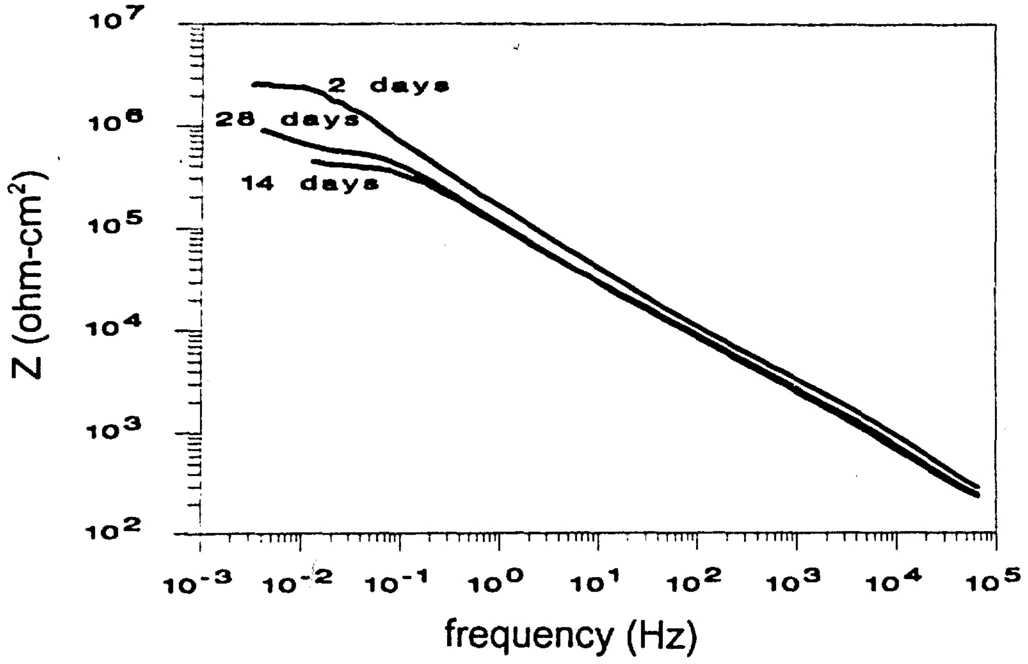

b)

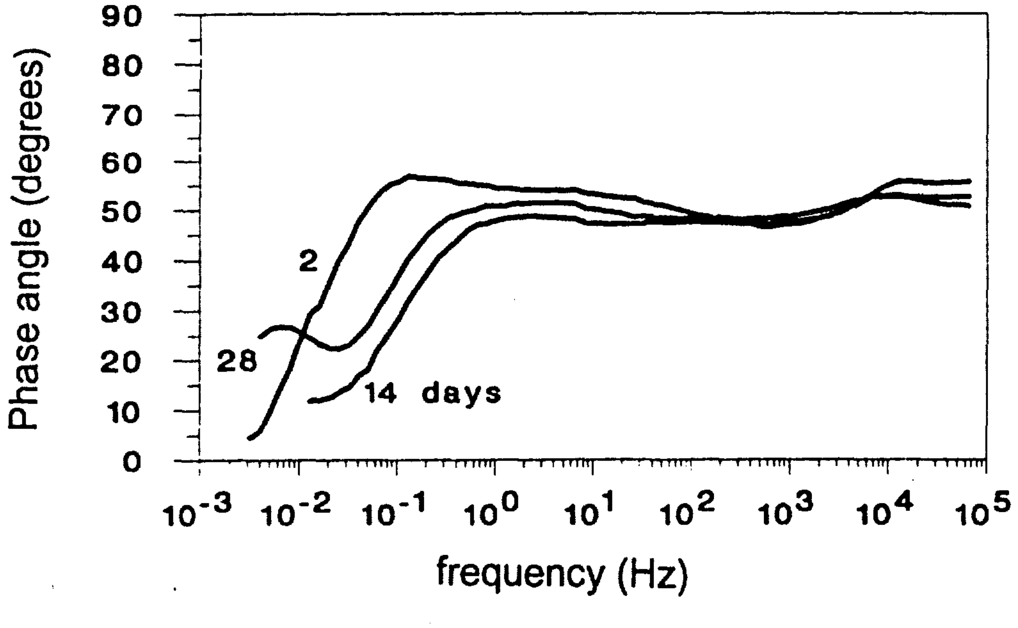

Figure 5.41 Bode plots (a and b) and Nyquist plot (c) for anodized and hot water sealed 6061/15% SiC after 2, 14 and 28 days of exposure to 0.5 N NaCl.

Figure 5.41 (continued).

c)

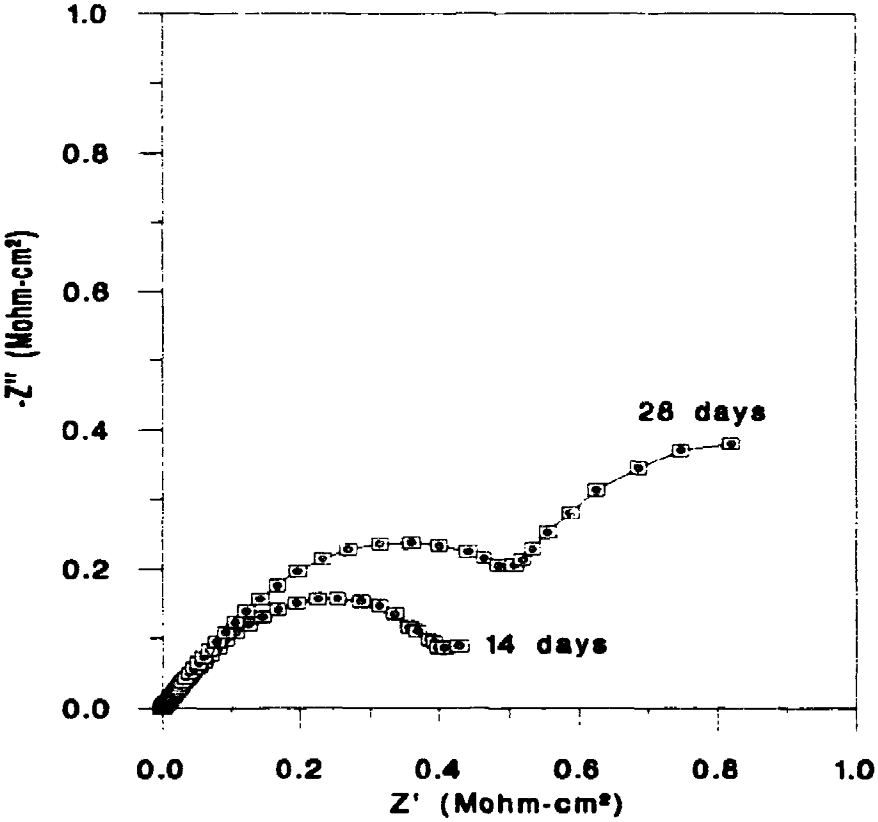

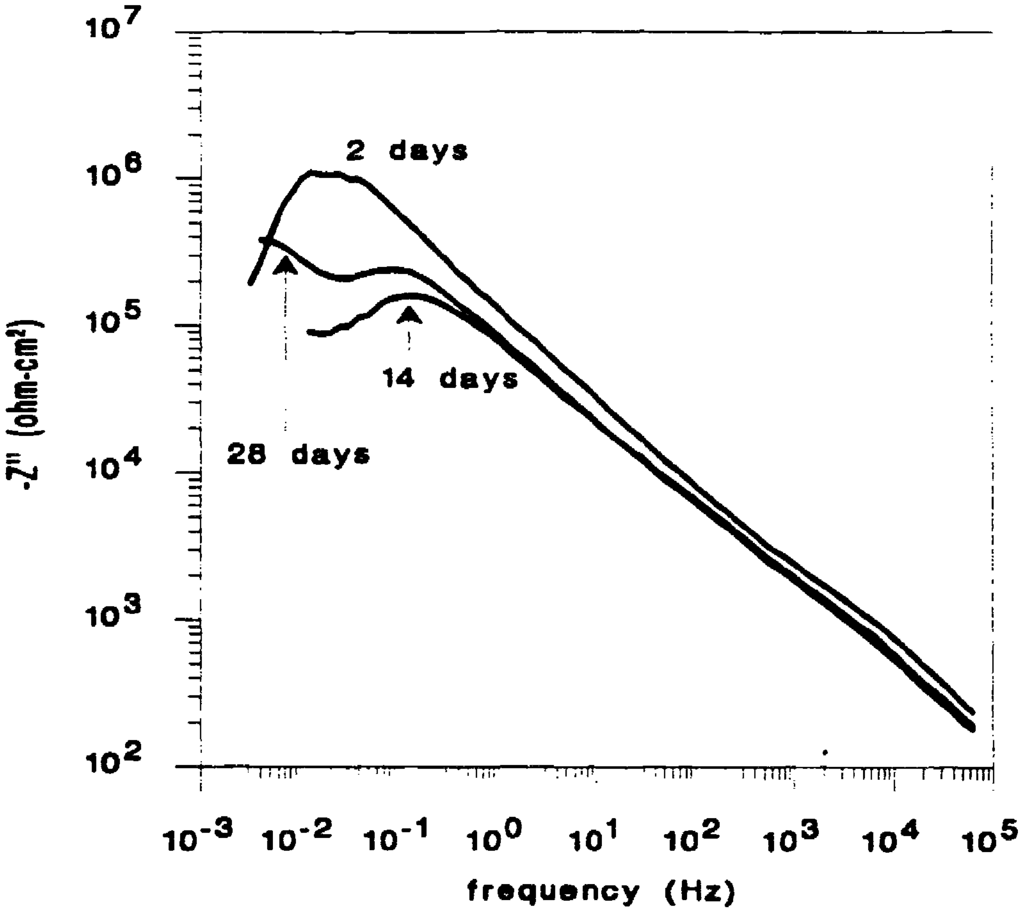

Figure 5.42 Imaginary component of the impedance versus frequency for 6061/15% SiC after 2, 14 and 28 days of exposure to 0.5 N NaCl.

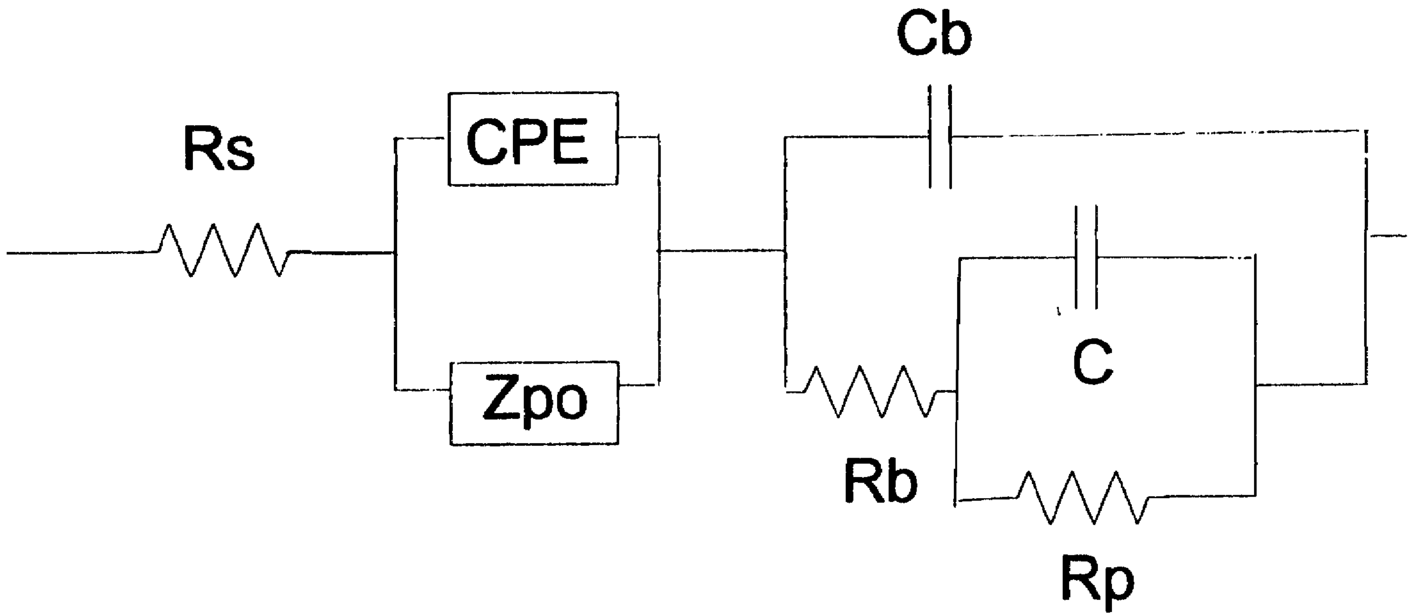

Figure 5.43 Modified anodized aluminum equivalent circuit for MMCs with corrosion damage.

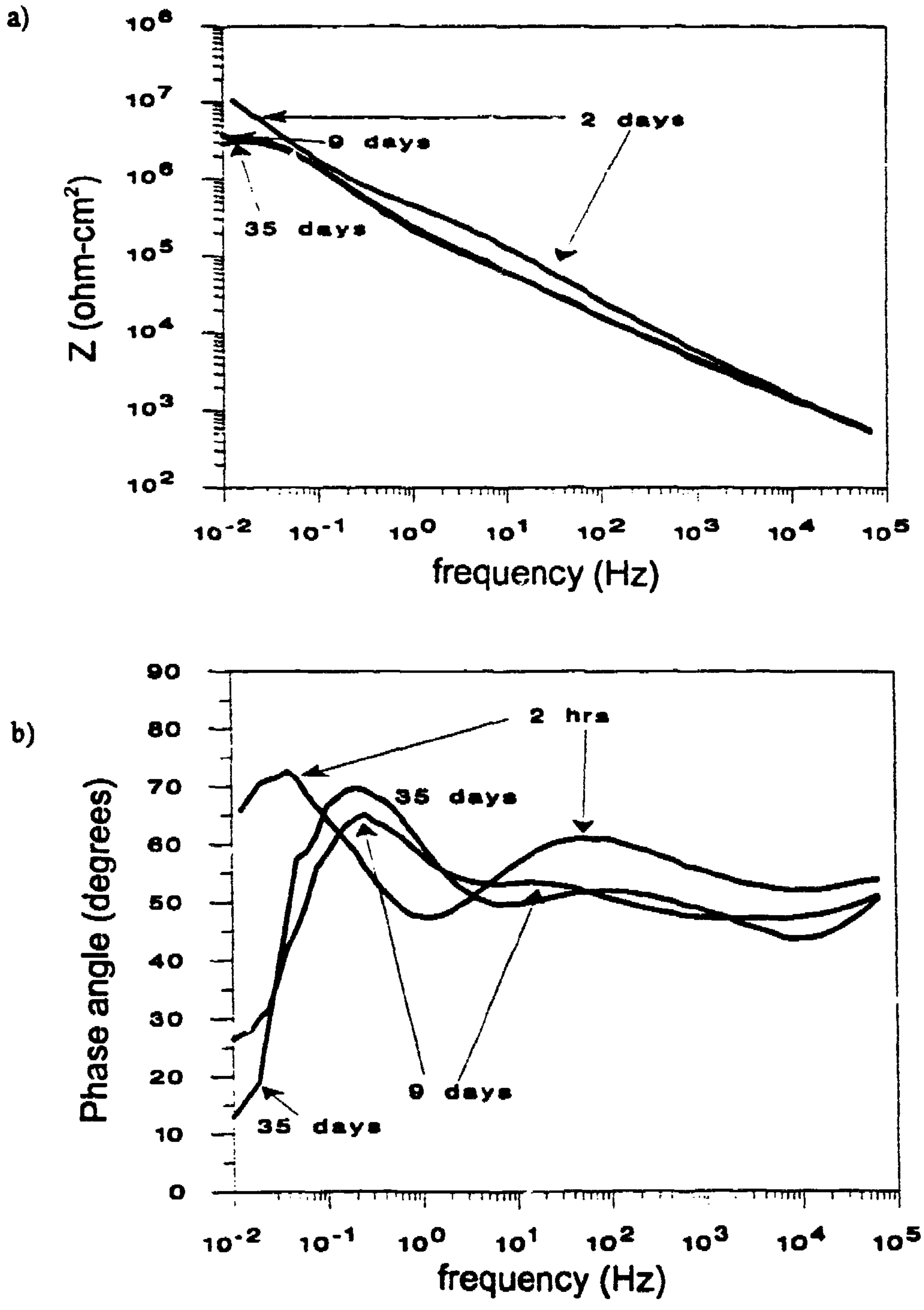

Figure 5.44 Bode plots (a and b) and Nyquist plot (c) for anodized and hot water sealed A356 after 2 hrs, 9 days and 35 days in 0.5 N NaCl.

Figure 5.44 (continued)

c)

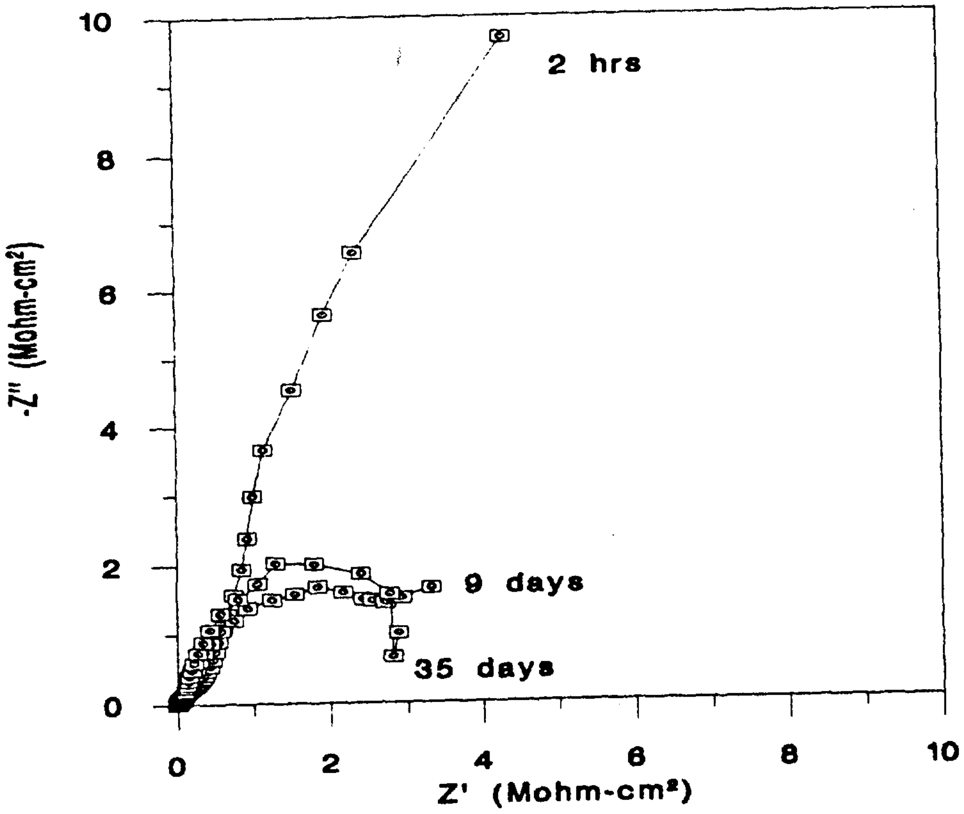

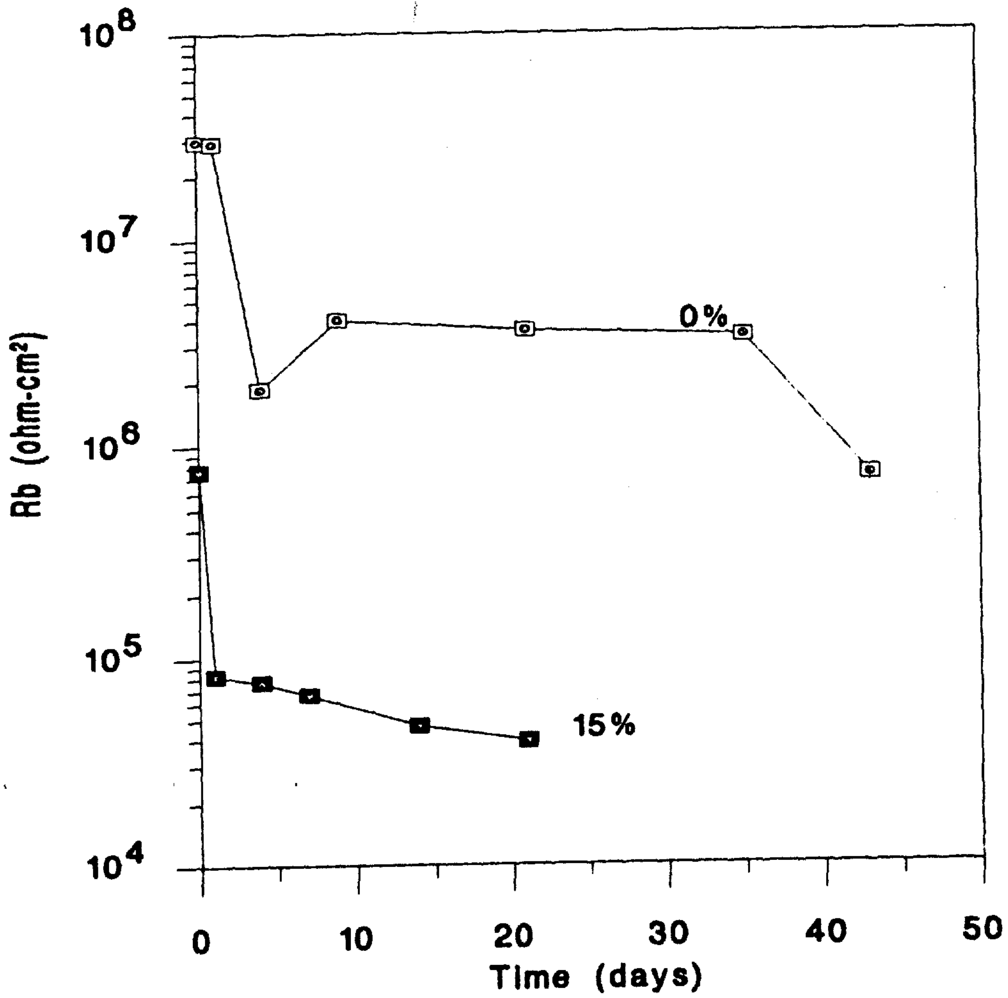

Figure 5.45 Barrier layer resistance versus exposure time for anodized and hot water sealed A356 and A356/15% SiC.

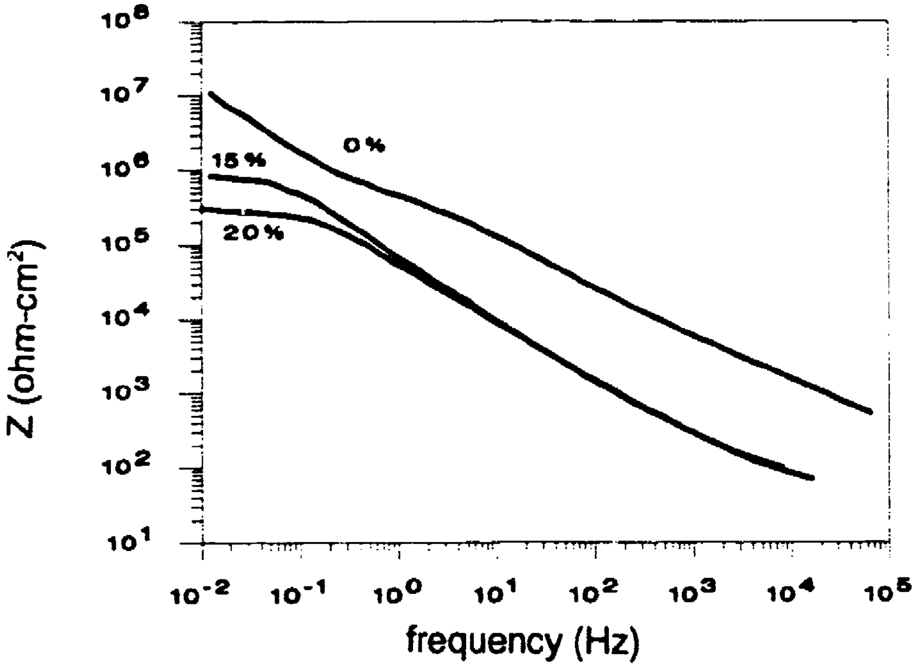

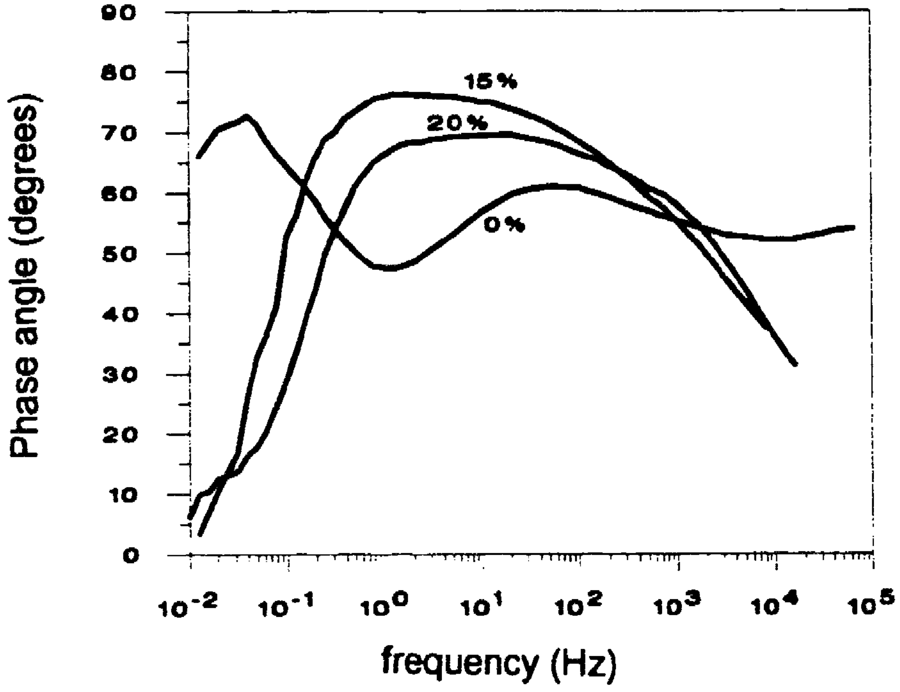

Figure 5.46 Bode plots for anodized and hot water sealed A356 and A356/SiC MMCs after 2 hrs in 0.5 N NaCl.

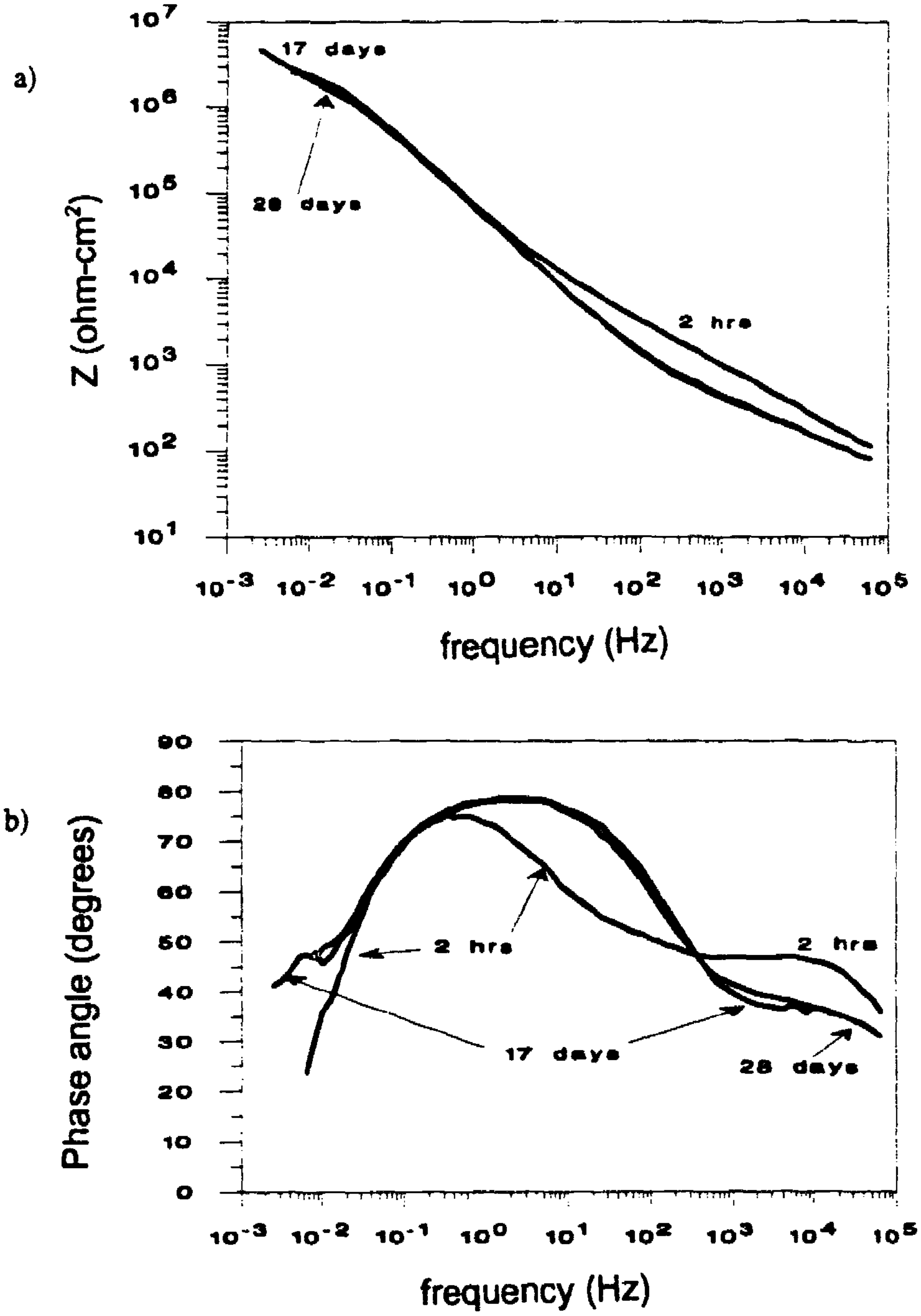

Figure 5.47 Bode plot (a and b) and Nyquist plot (c) for anodized and hot water sealed 2009/20% SiC_p after exposure to 0.5N NaCl for 2 hrs, 17 days and 28 days.

Figure 5.47 (continued)

c)

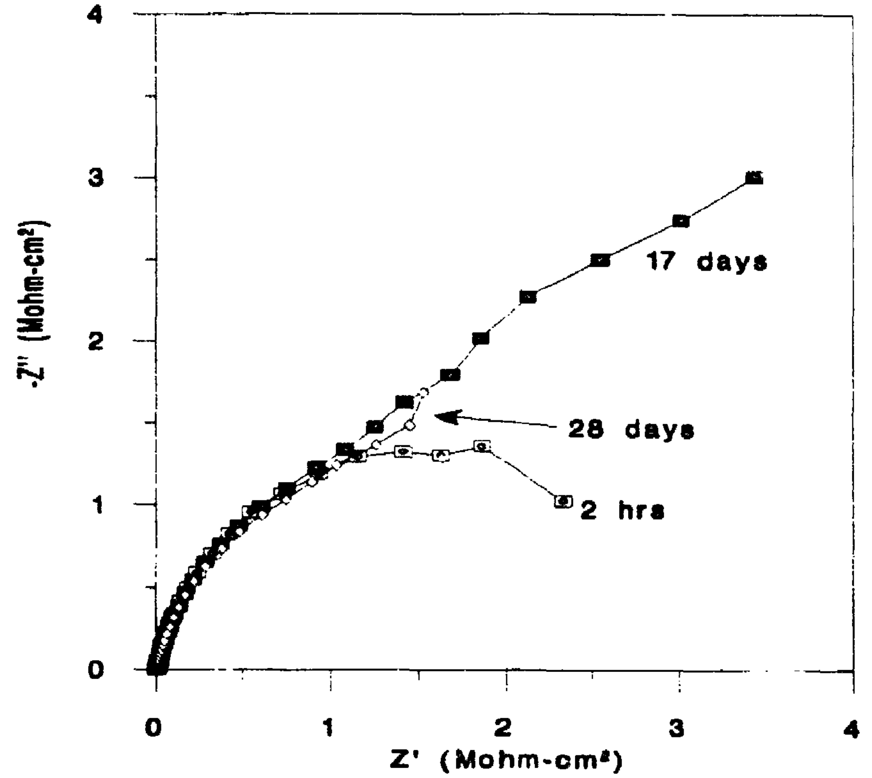

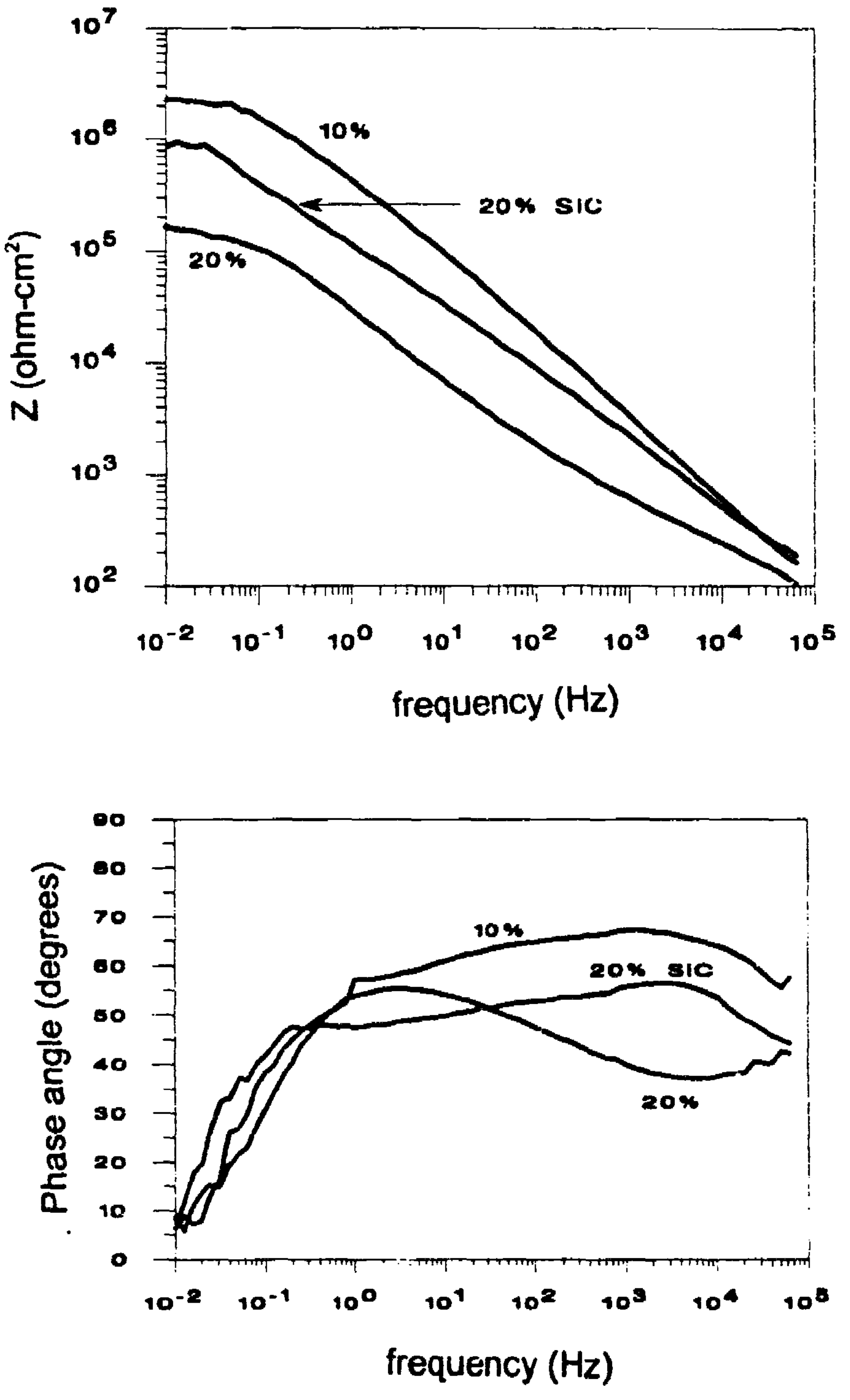

Figure 5.48 Bode plot for anodized and hot water sealed 6061/10% and 20% Al_2O_3 and 6061/20% SiC after 2 hrs in 0.5 N NaCl.

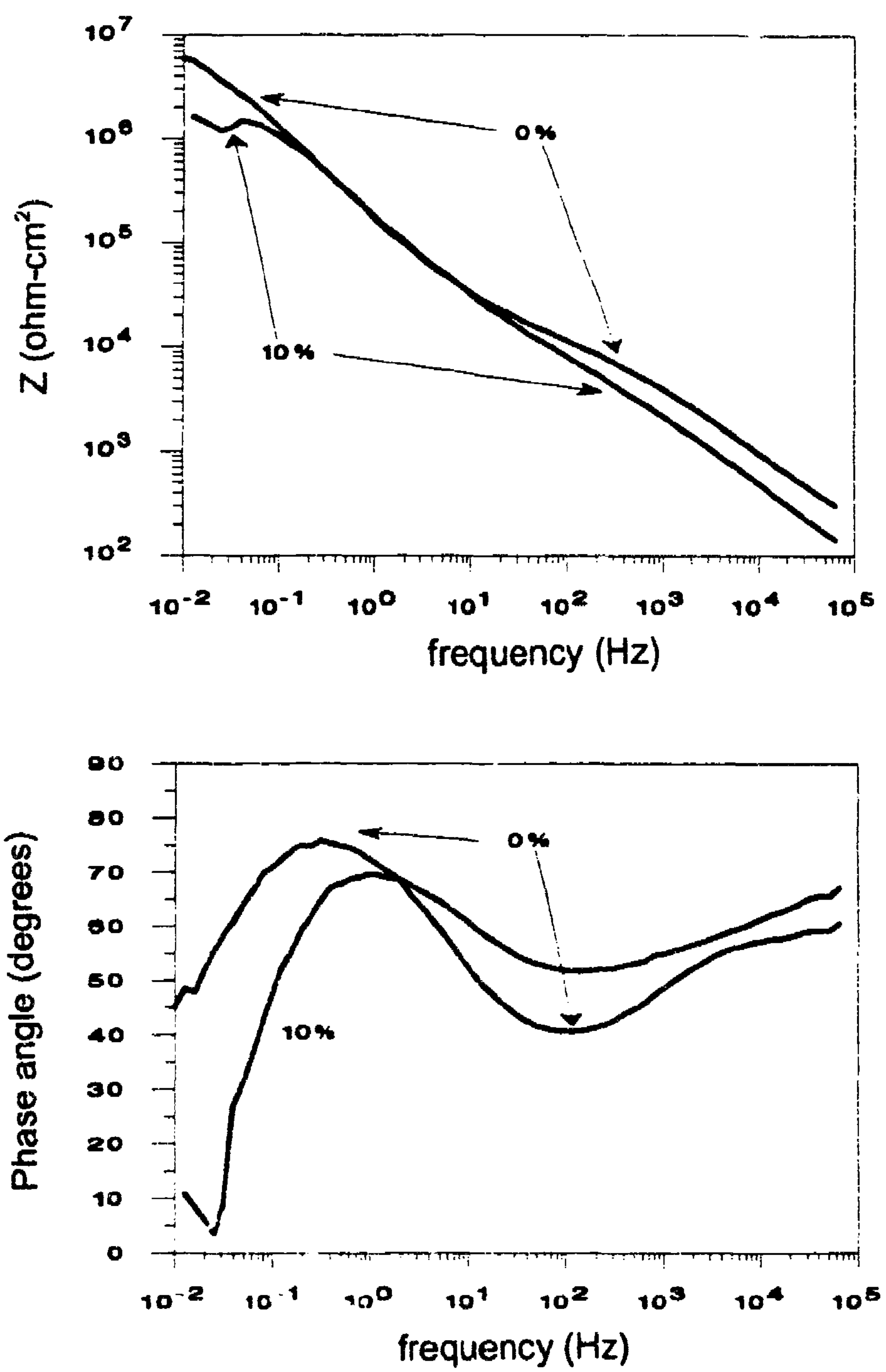

Figure 5.49 Bode plot for anodized and hot water sealed AA2014 and 2014/10% Al_2O_3 after 2 hrs in 0.5 N NaCl.

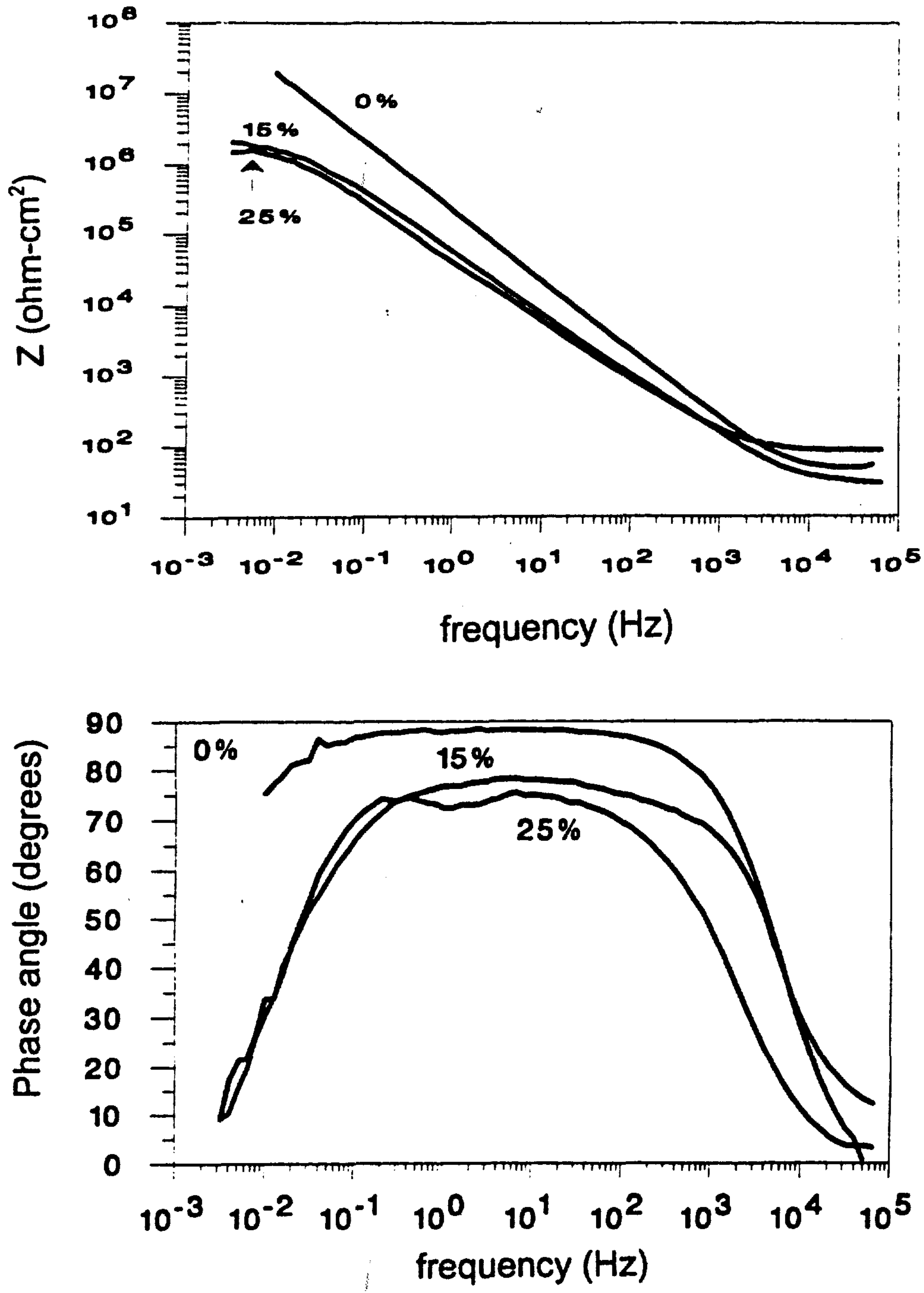

Figure 5.50 Bode plots for anodized and dichromate sealed AA6061 and 6061/SiC MMCs after 2 hrs of exposure to 0.5 N NaCl.

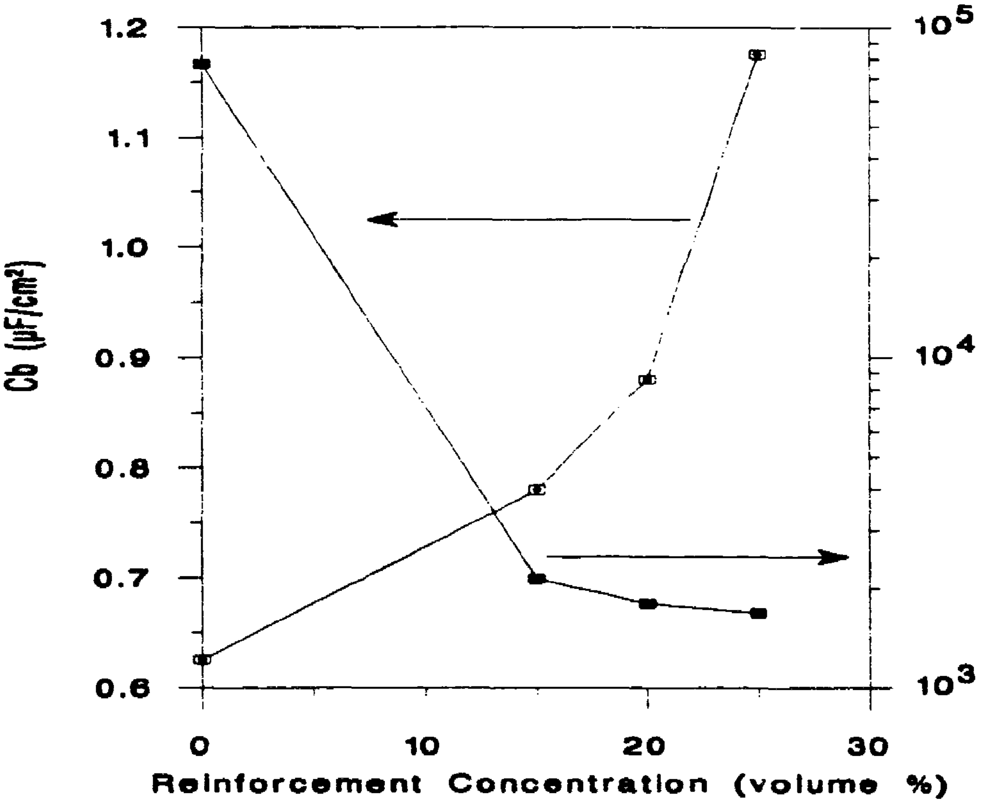

Figure 5.51 Barrier layer resistance, R_b, and barrier layer capacitance, C_b, versus volume percent of SiC reinforcement for anodized and dichromate sealed 6061/SiC MMCs after 2 hrs of exposure.

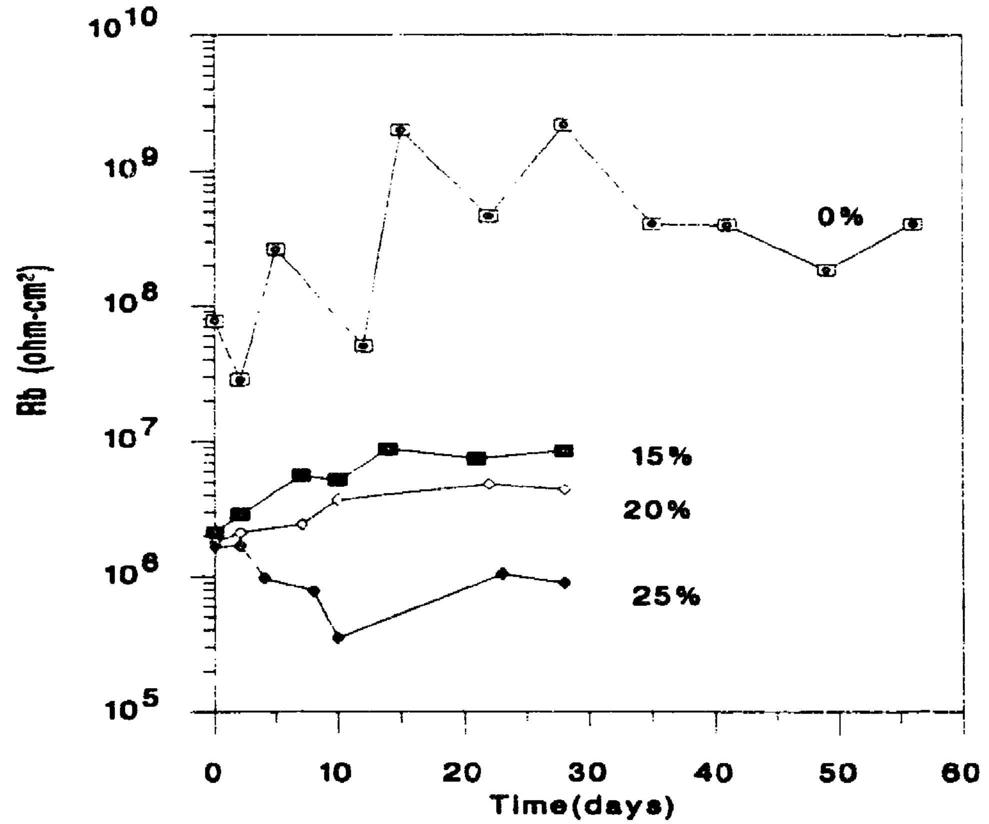

Figure 5.52 Barrier layer resistance, R_b, versus exposure time for anodized and dichromate sealed 6061/SiC MMCs.

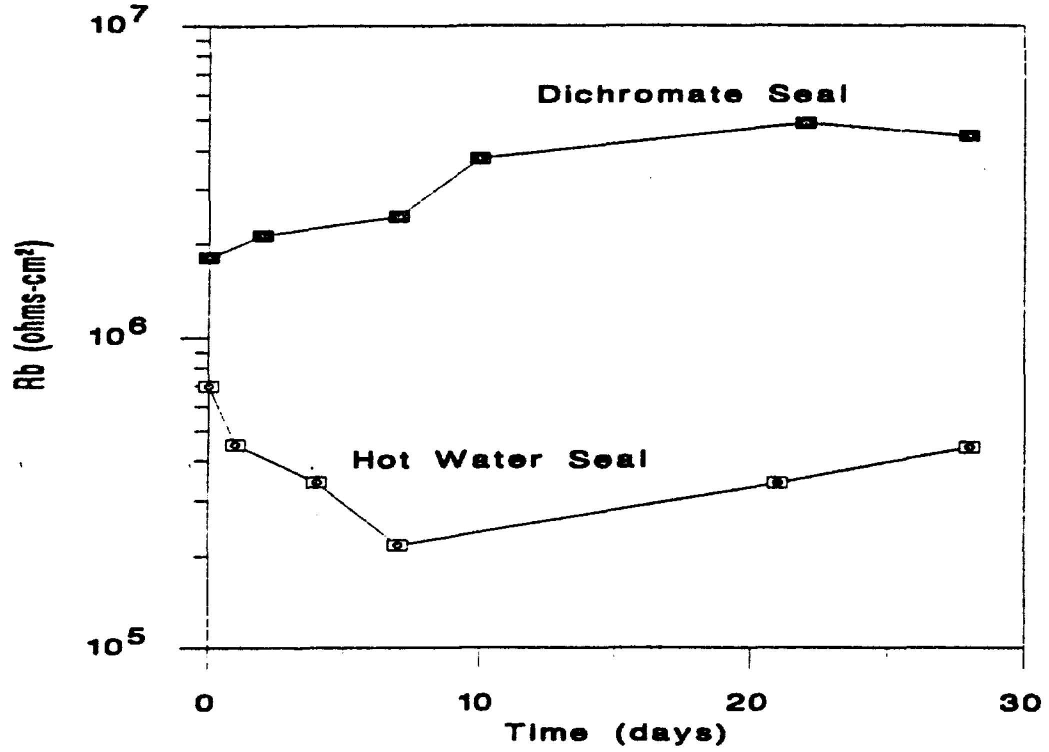

Figure 5.53 Barrier layer resistance, R_b, versus exposure time for anodized 6061/20% SiC MMC for hot water sealing and dichromate sealing.

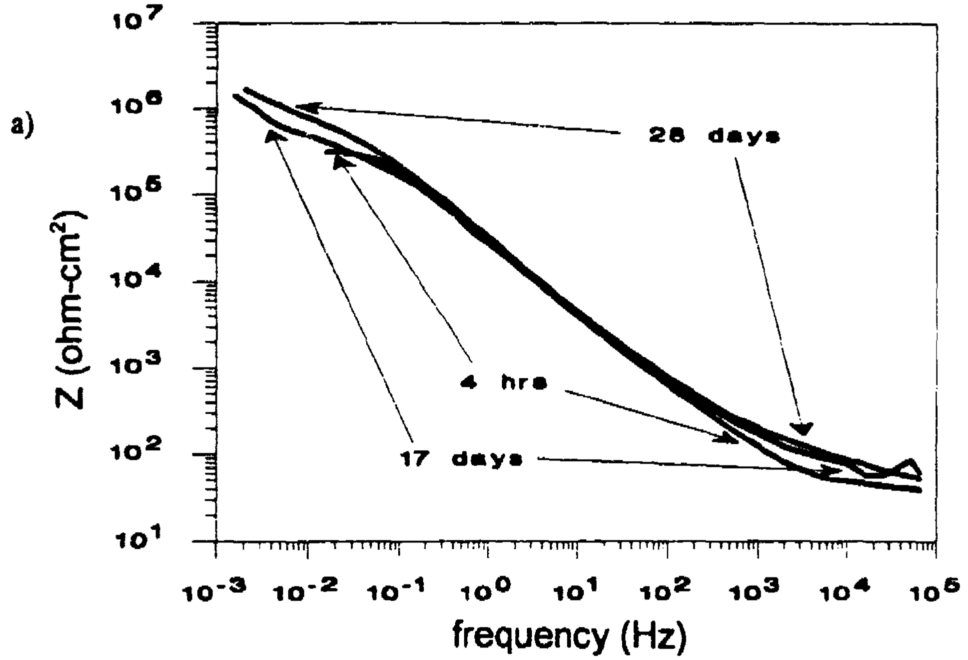

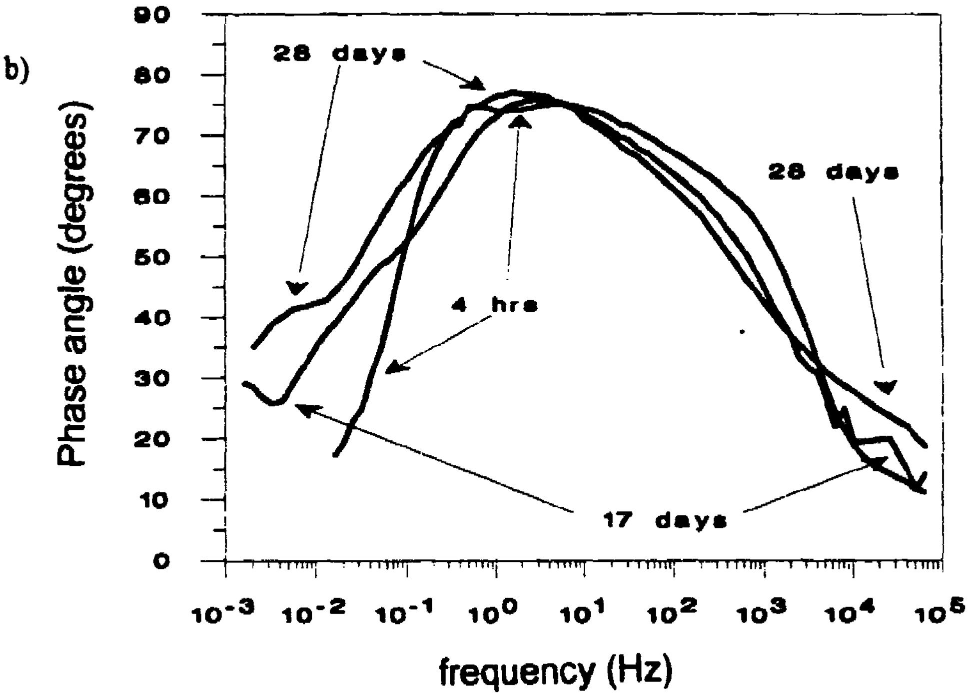

Figure 5.54 Bode plot (a and b) and Nyquist plot (c) for anodized and dichromate sealed 2009/15% SiC_w after 4 hrs, 17 days and 28 days of exposure to 0.5 N NaCl.

Figure 5.54 (continued)

c)

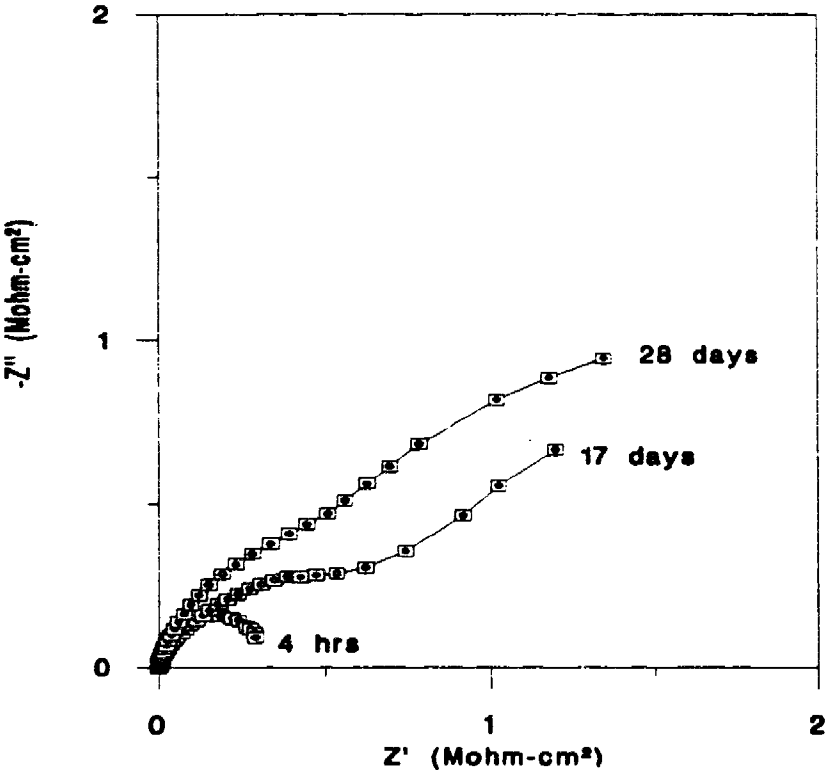

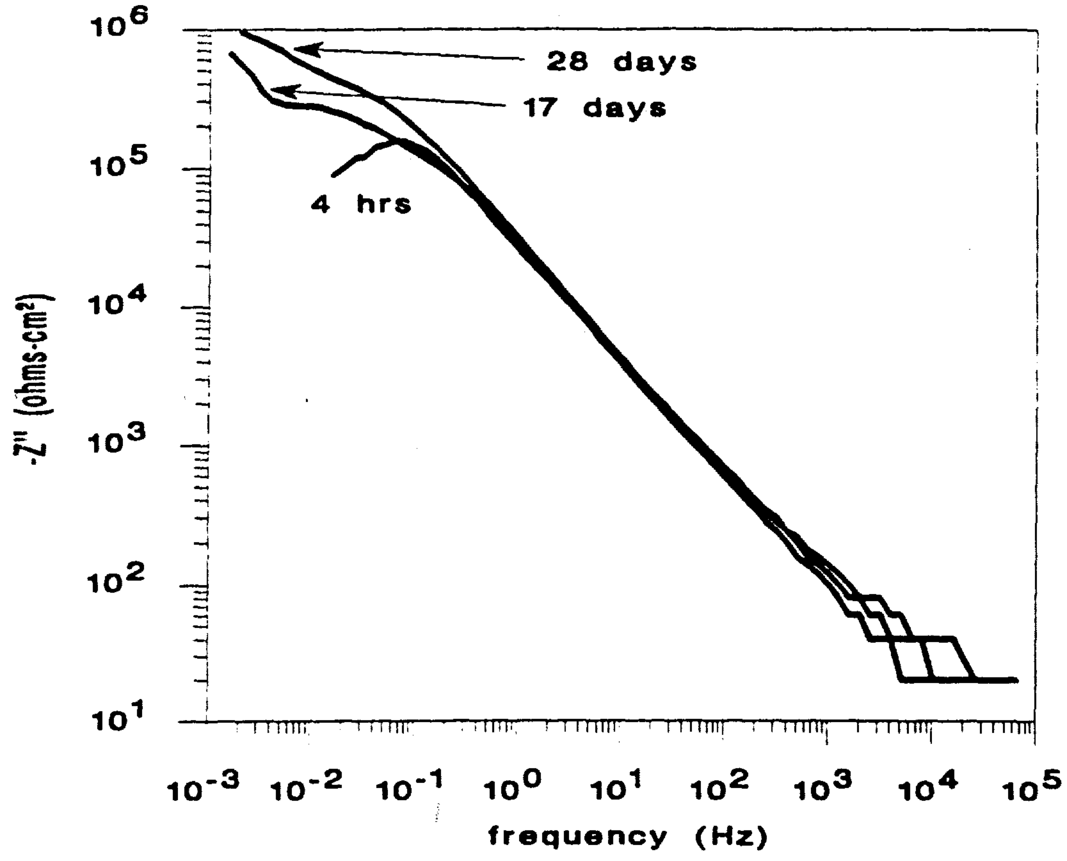

Figure 5.55 Imaginary component of the impedance versus frequency for anodized and dichromate sealed 2009/15% SiC_w after 4 hrs, 17days and 28 days of exposure to 0.5 N NaCl.

Figure 5.56 SEM micrograph of the cross-section of an anodized and hot water sealed 6061 25% SiC MMC.

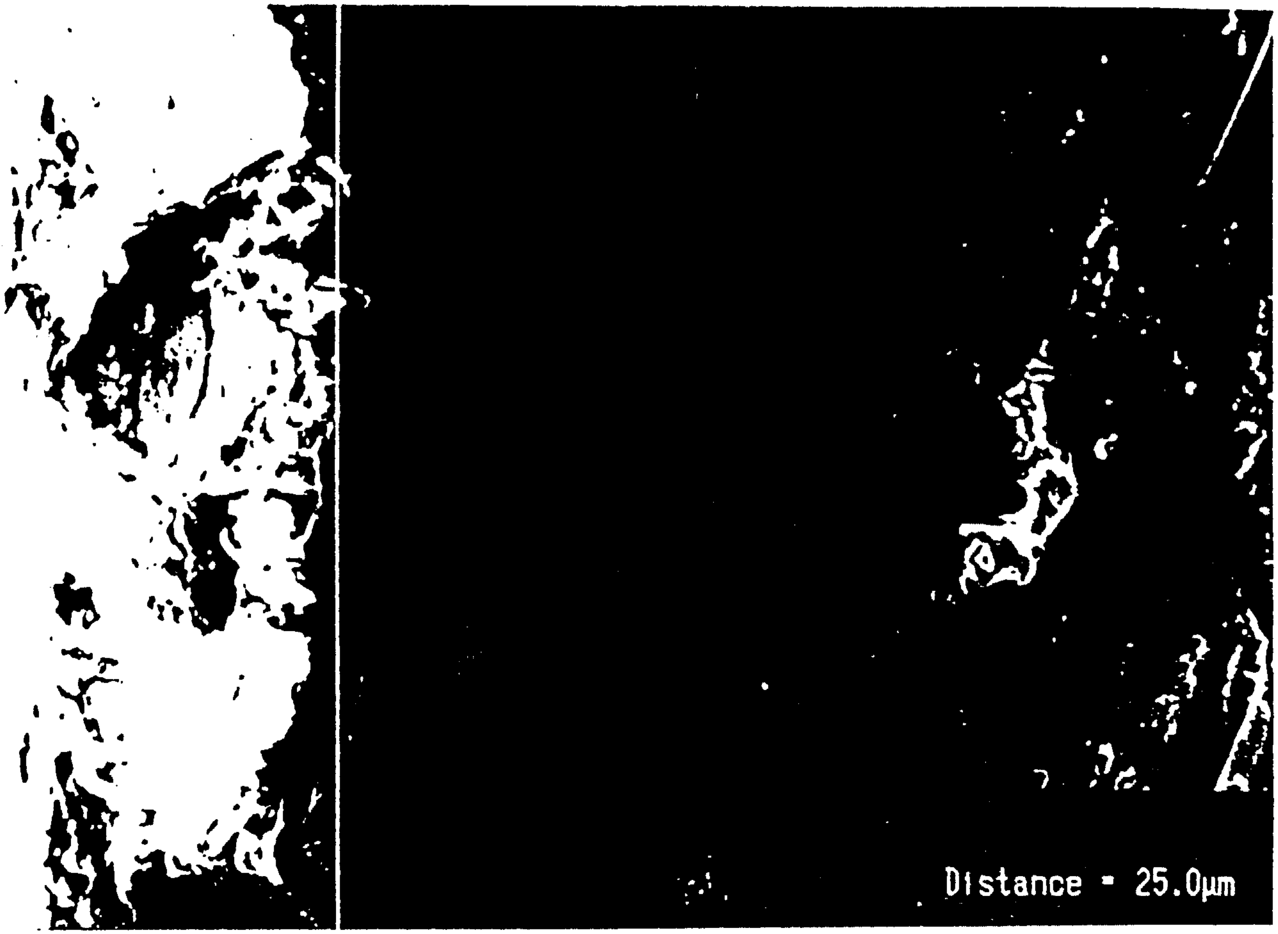

Figure 5.57 SEM micrograph of the cross-section of an anodized and hot water sealed A356/20% MMC.

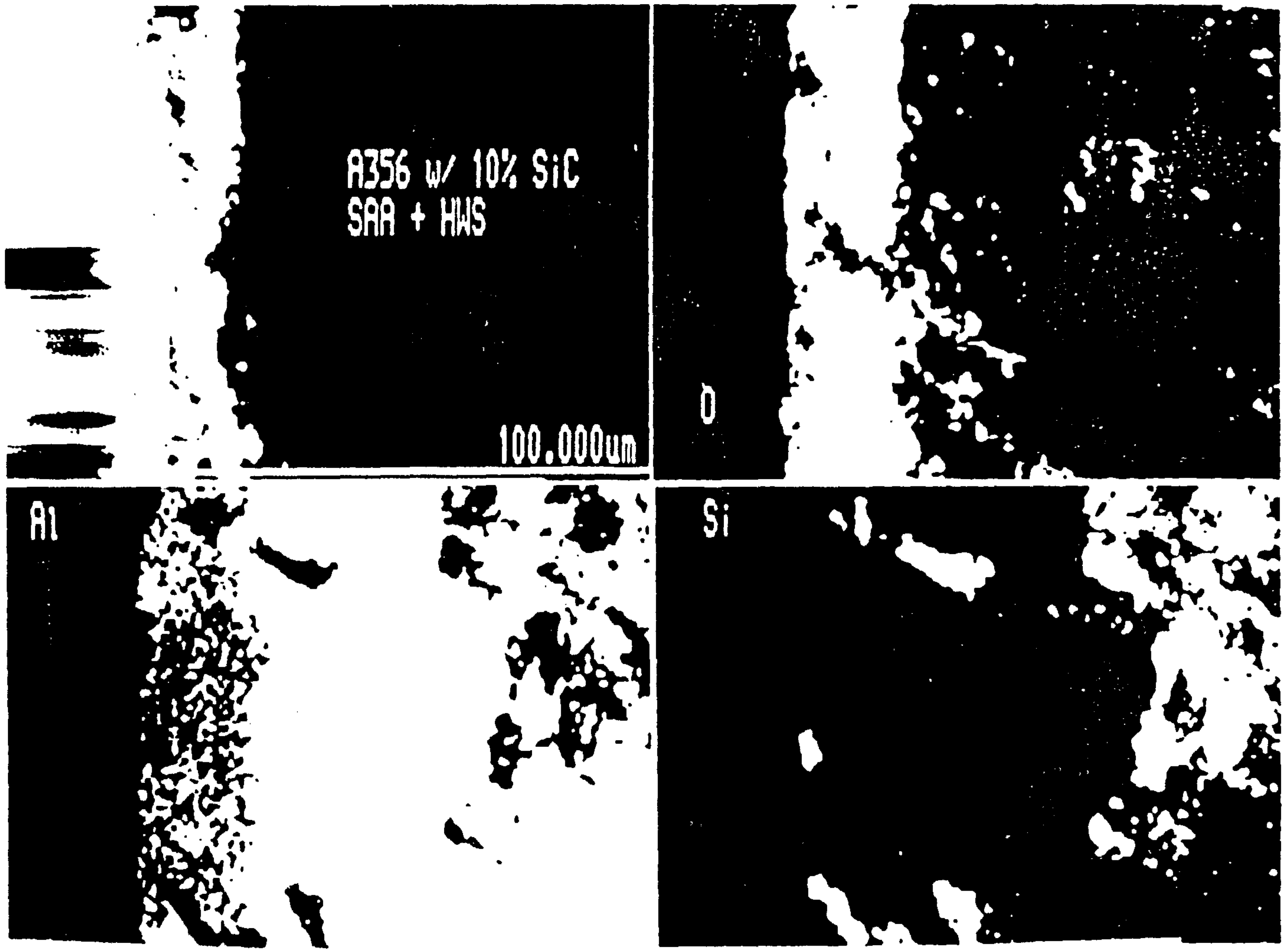

Figure 5.58 SEM image and EDS composition maps for O, Al and Si on an anodized and hot water sealed A356/10% SiC MMC.

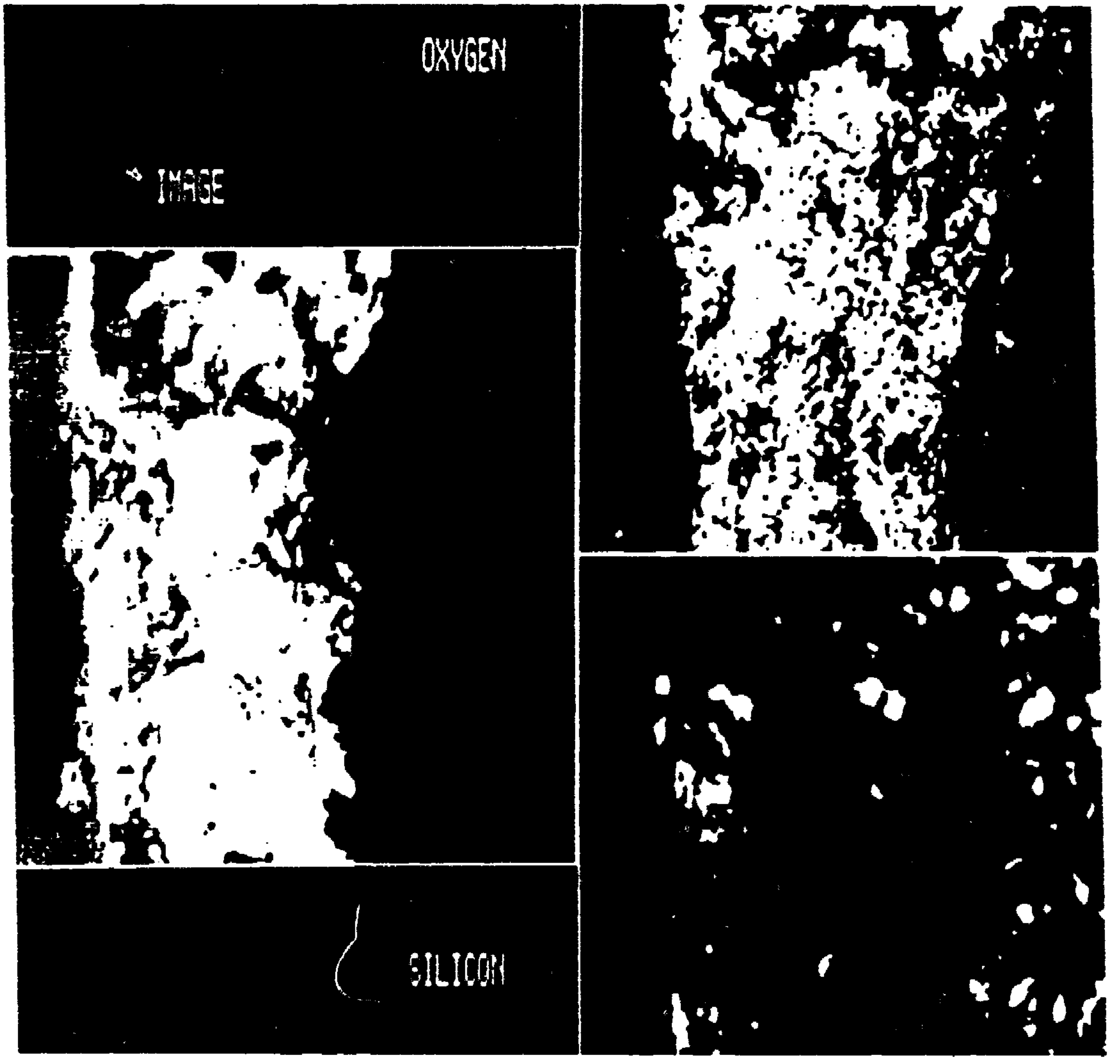

Figure 5.59 SEM image and EDS composition maps for O and Si on an anodized and hot water sealed 6061/25% SiC MMC.

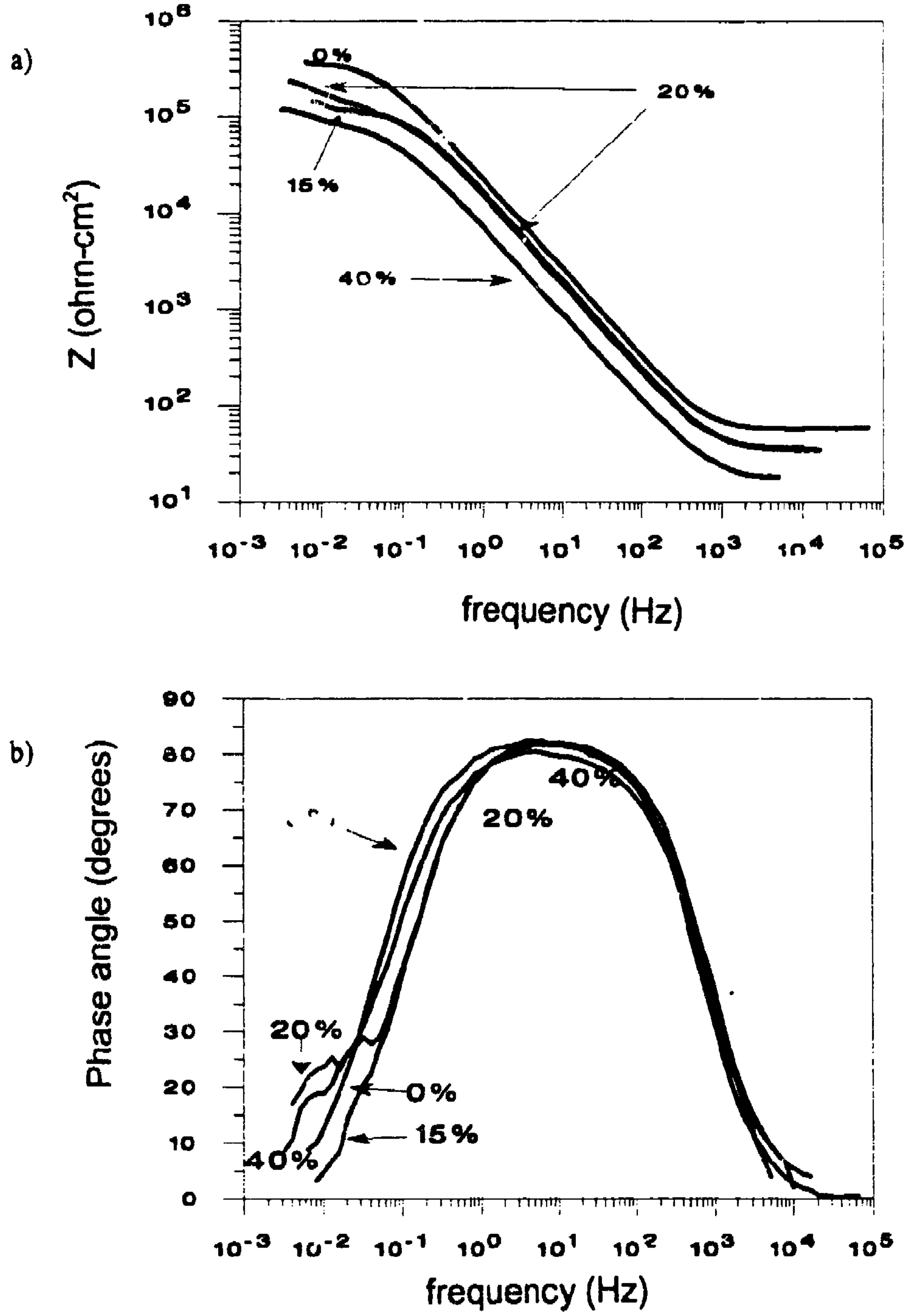

Figure 5.60 Bode plot (a and b) and Nyquist plot (c) for Alodine 600 chromate conversion coating on AA6061 and 6061/SiC MMCs after 1 day in 0.5 N NaCl.

Figure 5.60 (continued)

c)

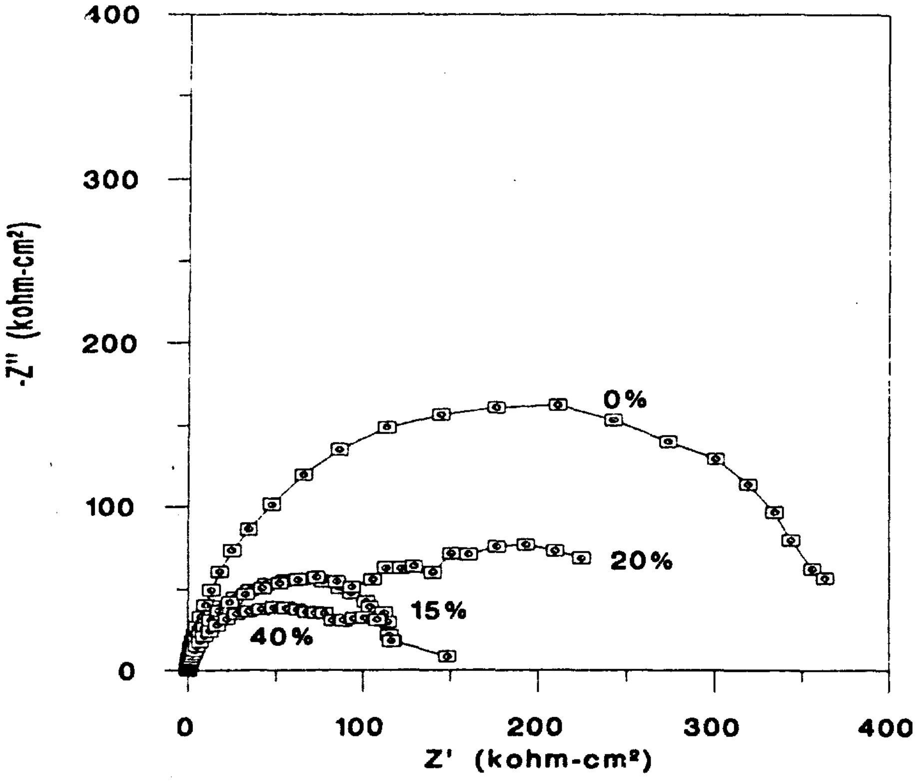

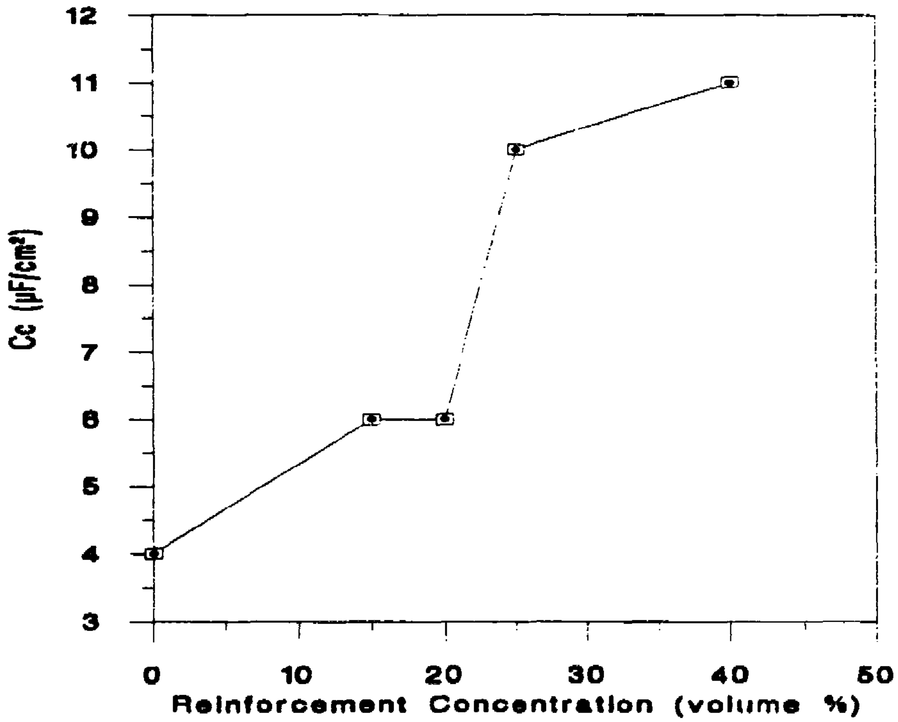

Figure 5.61 Coating capacitance versus volume percent reinforcement for 6061/SiC MMCs after 2 hrs of exposure to 0.5 N NaCl.

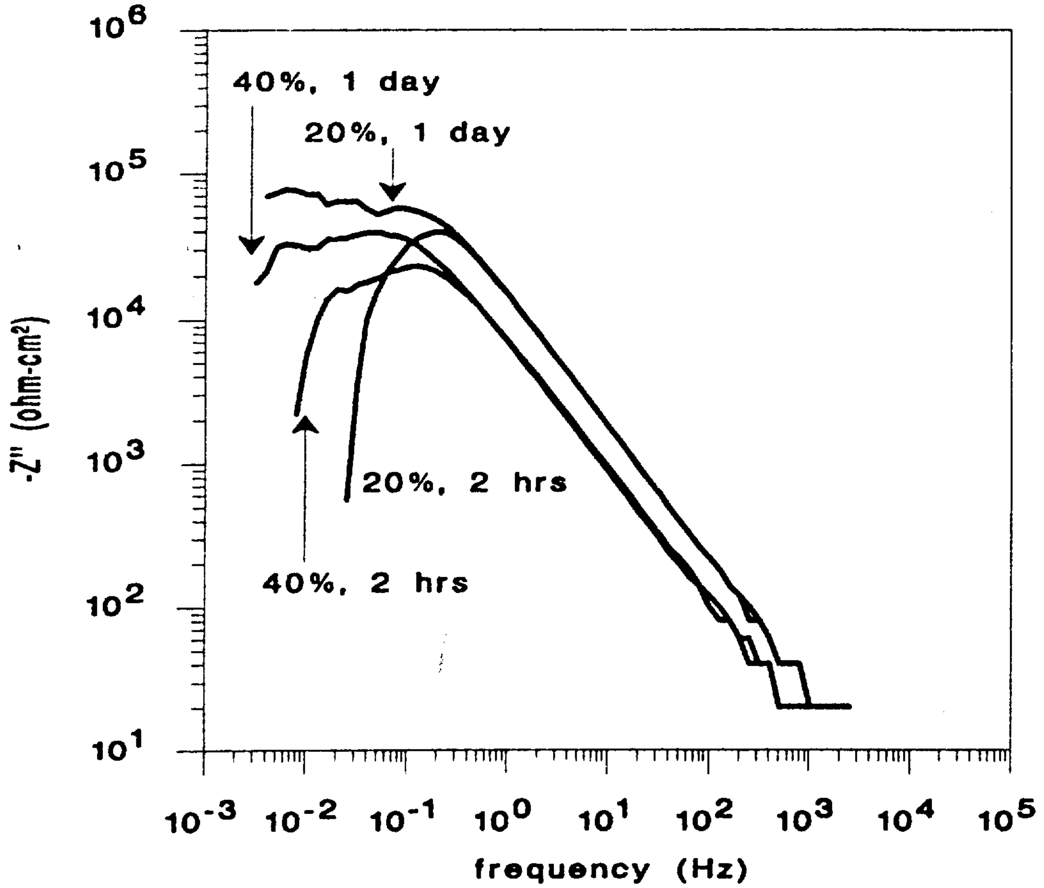

Figure 5.62 Imaginary component of the impedance versus frequency for conversion coated 6061/20% SiC and 6061/40% SiC MMCs for 2 hrs and 1 day of exposure.

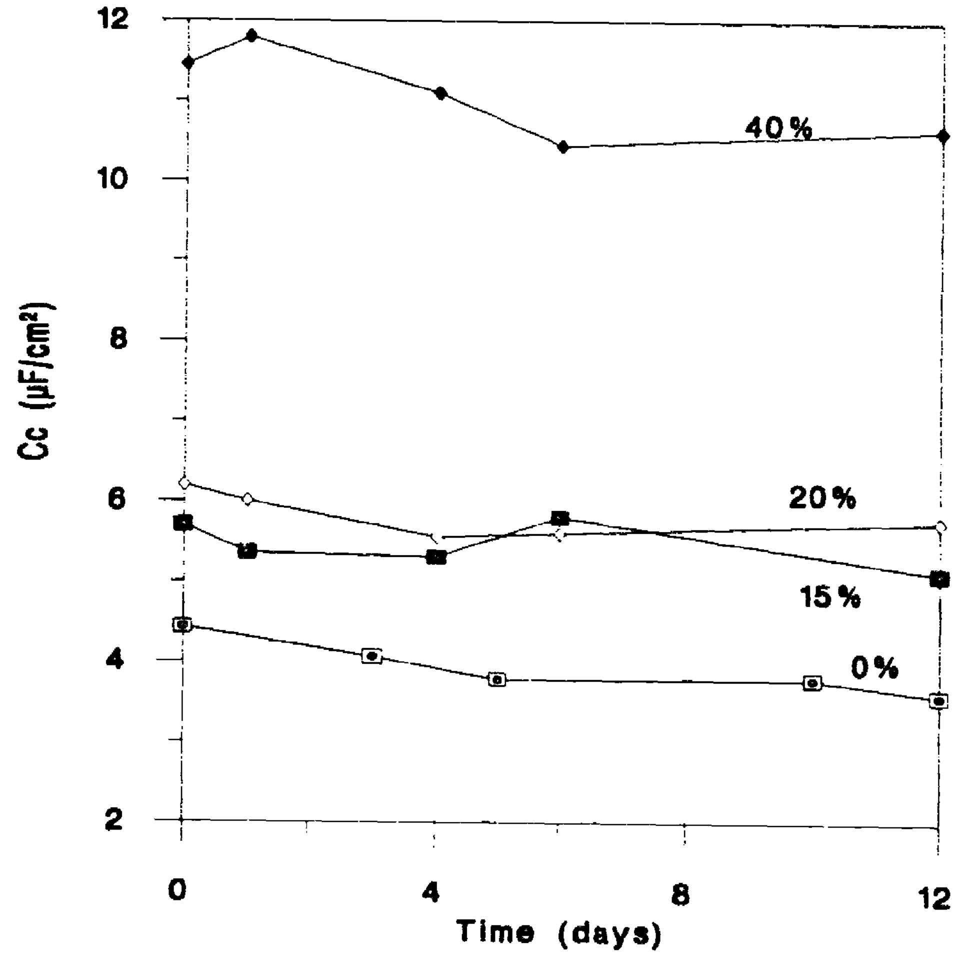

Figure 5.63 Coating capacitance, C_c, versus exposure time in 0.5 N NaCl for conversion coated 6061/SiC MMCs.

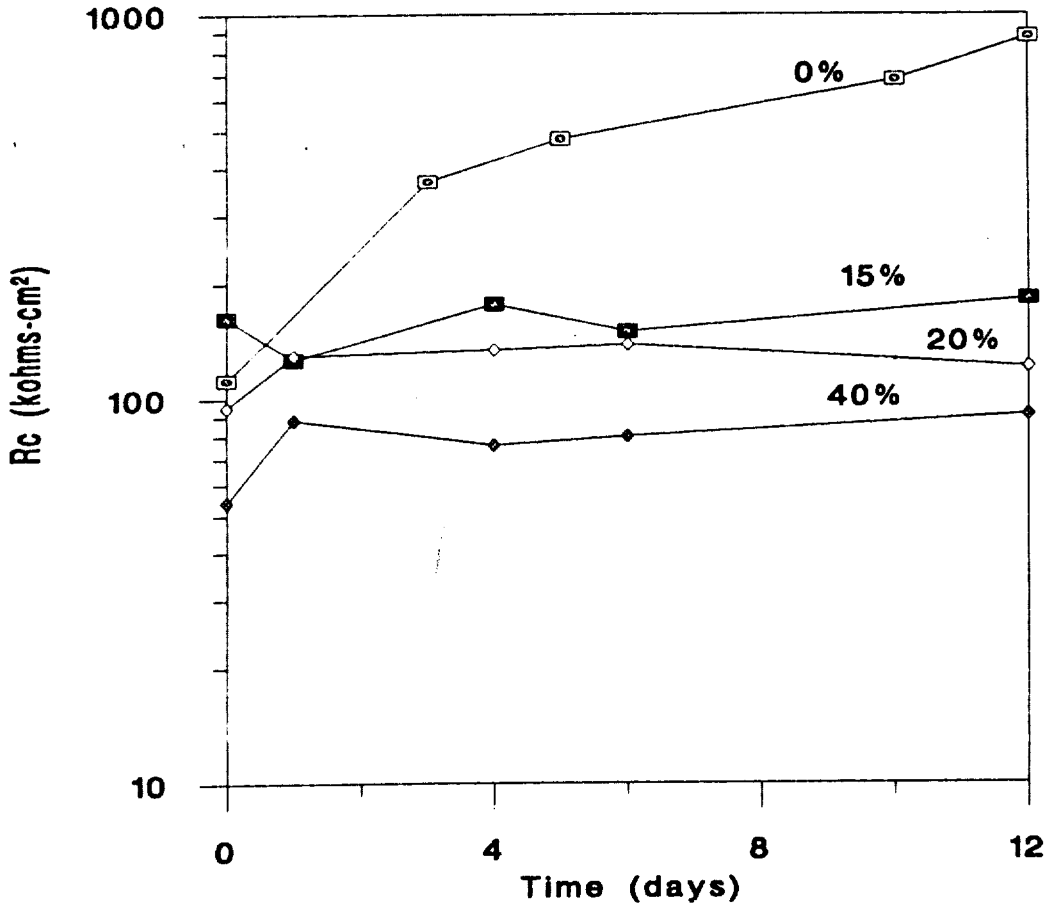

Figure 5.64 Coating resistance, R_c, versus exposure time in 0.5 N NaCl for conversion coated 6061/SiC MMCs.

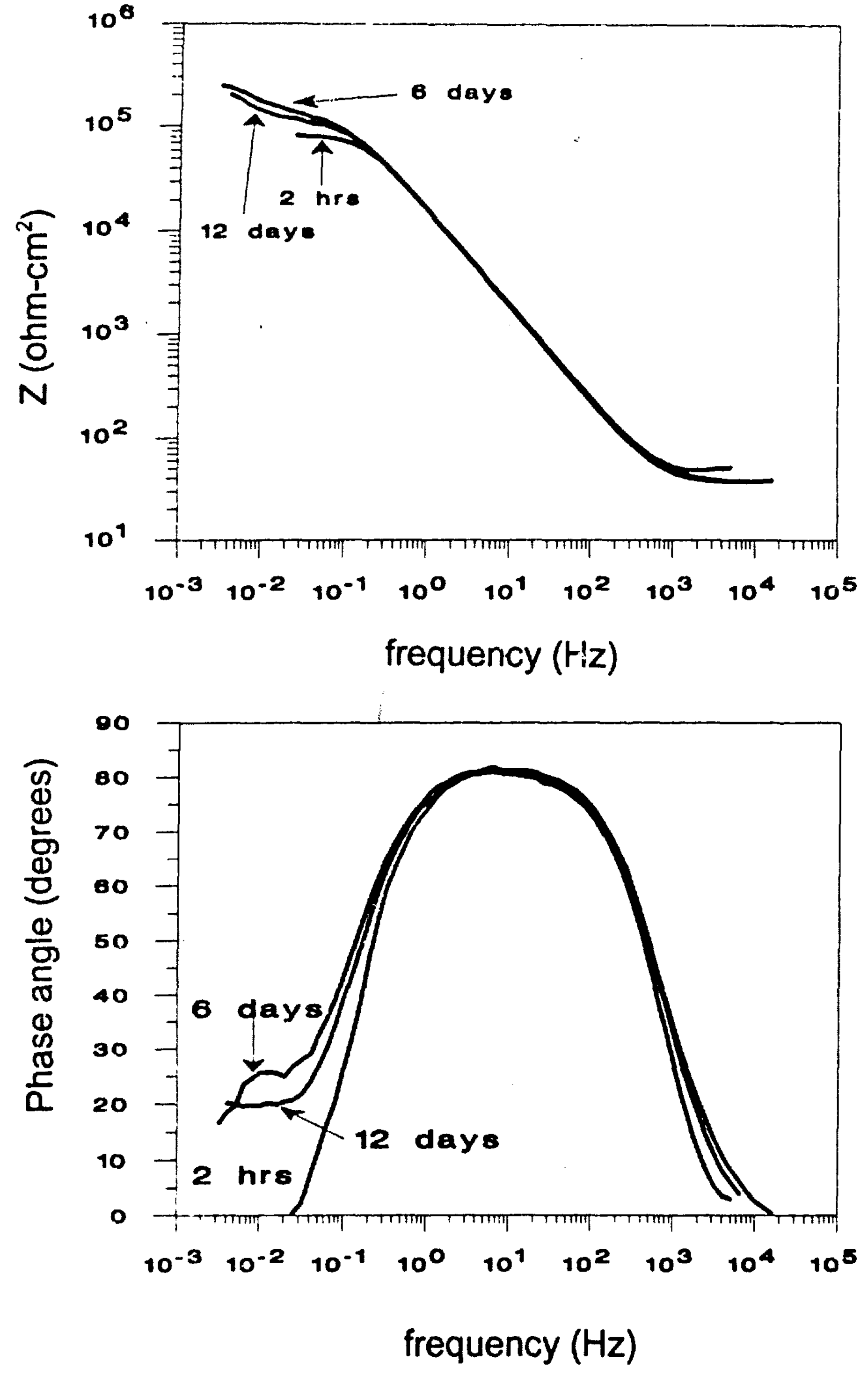

Figure 5.65 Bode plot for conversion coated 6061/20% SiC after 2 hrs, 6 days and 12 days of exposure to 0.5 N NaCl.

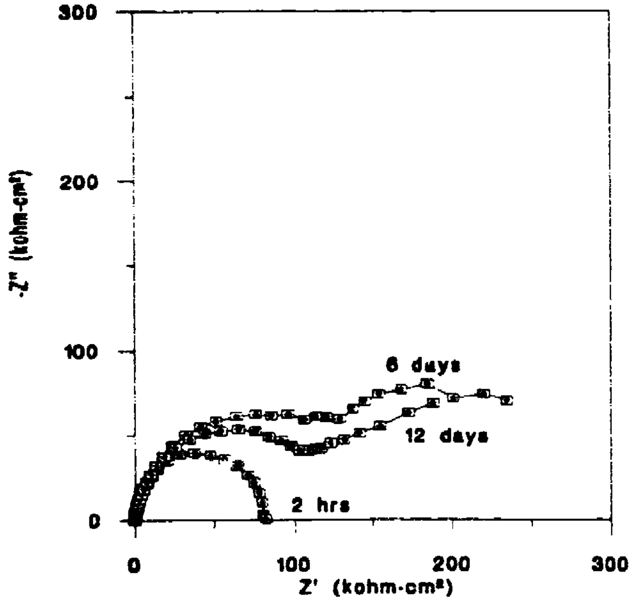

Figure 5.66 Nyquist plot for conversion coated 6061/20% SiC after 2 hrs, 6 days and 12 days of exposure to 0.5 N NaCl.

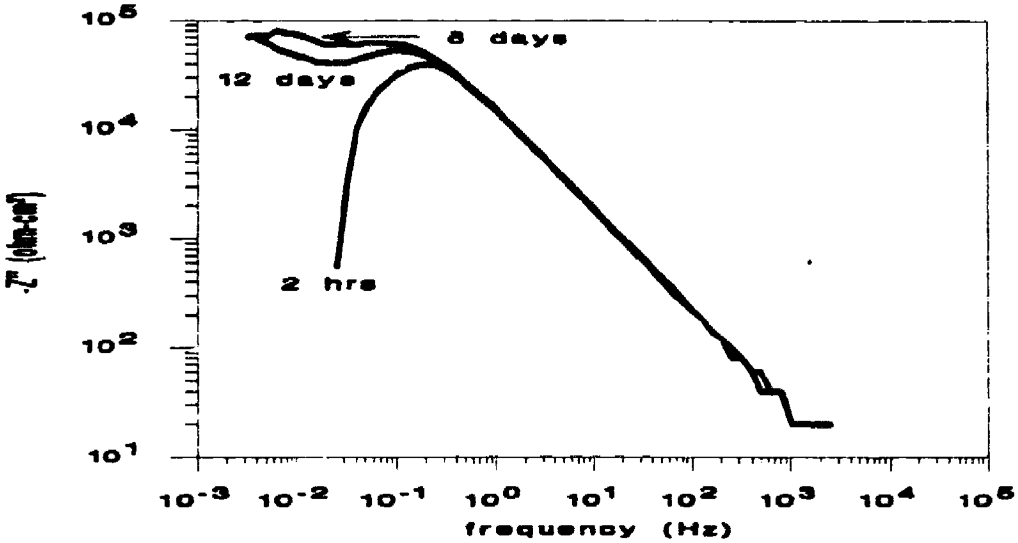

Figure 5.67 Imaginary component of the impedance for conversion coated 6061/20% SiC after 2 hrs, 6 days and 12 days of exposure to 0.5 N NaCl.

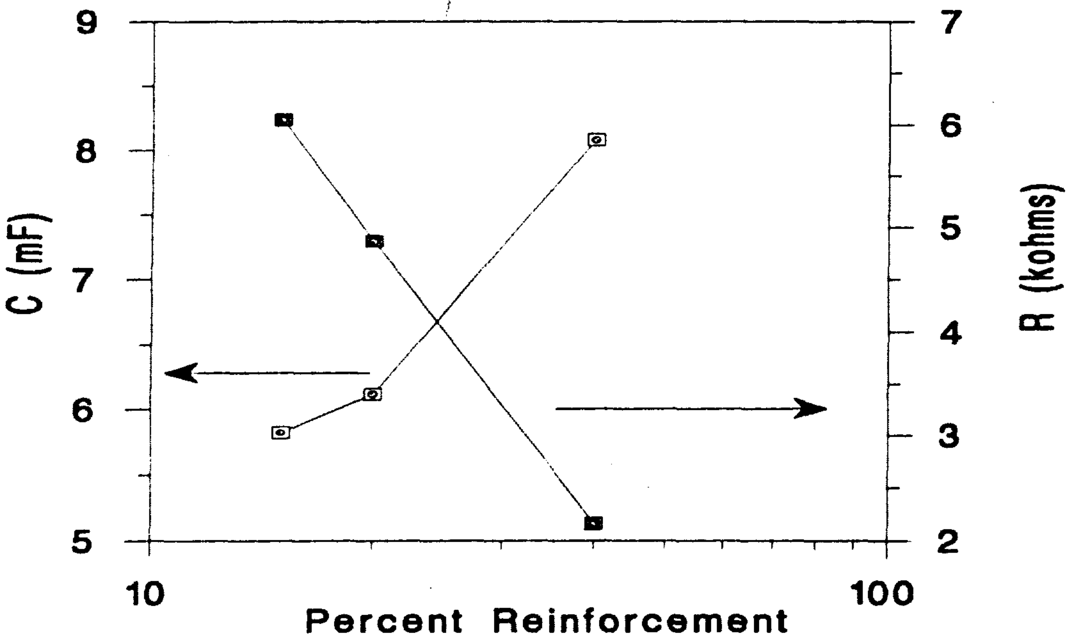

Figure 5.68 Capacitance and resistance of pits versus percent reinforcement for conversion coated 6061/SiC MMCs after 12 days of exposure.

Figure 5.69 SEM micrograph of the top view of conversion coated AA6061.

Figure 5.70 SEM micrograph of the top view of conversion coated 6061/20% SiC MMC.

Figure 5.71 SEM micrograph in cross-section of conversion coated AA6061.

Figure 5.72 SEM micrograph in cross-section of conversion coated 6061/20% SiC MMC.

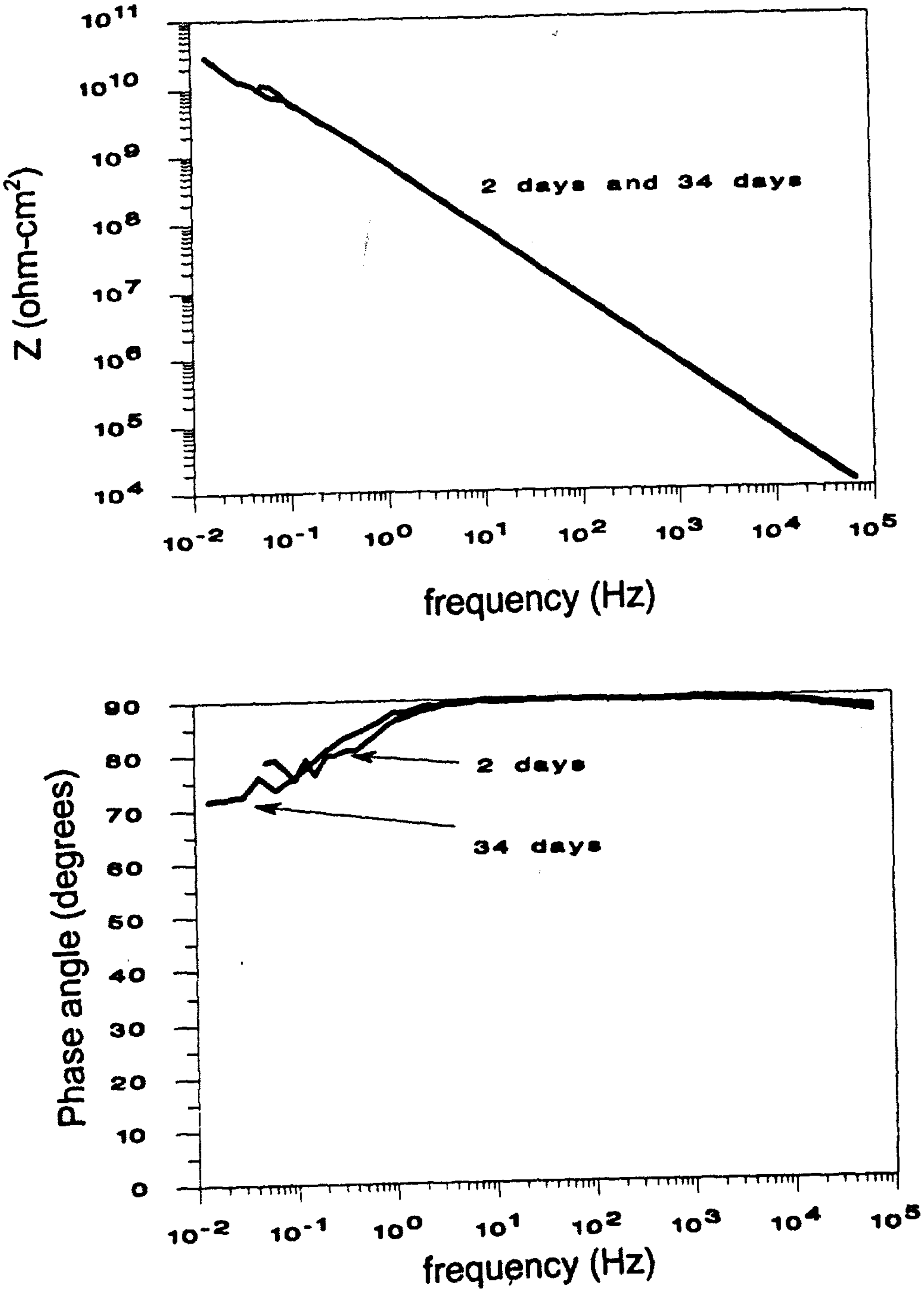

Figure 5.73 Bode plot for AA6061 coated with Araldite 985 after 2 days and 34 days of exposure to 0.5 N NaCl.

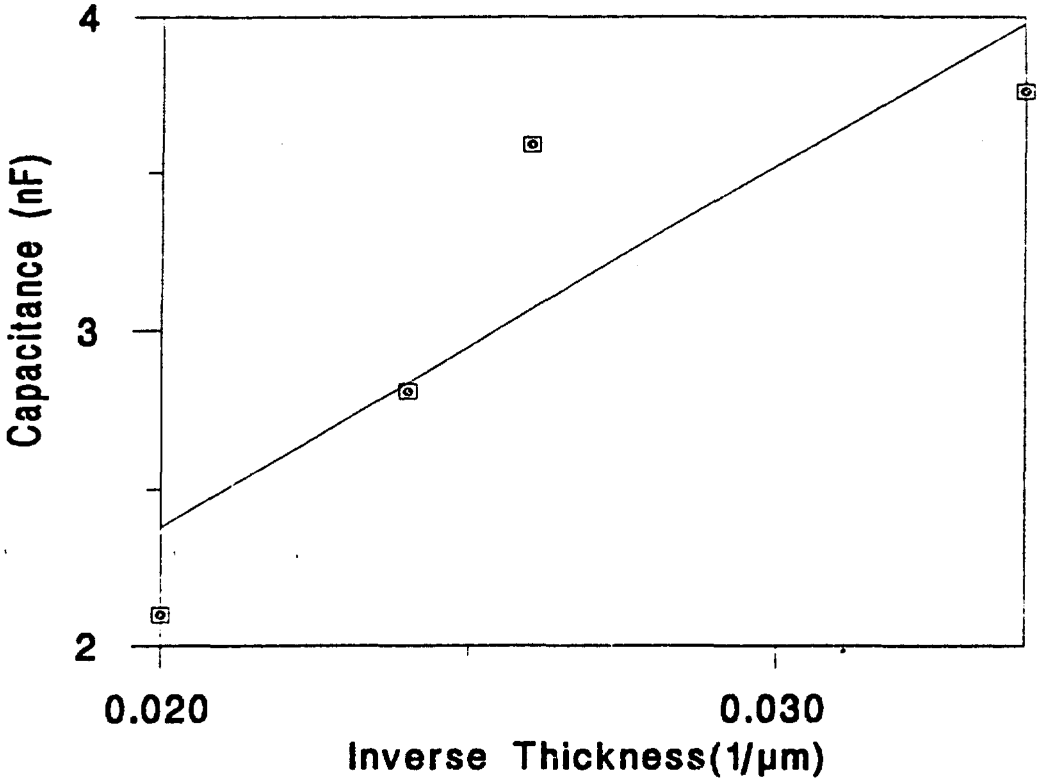

Figure 5.74 Coating capacitance versus inverse thickness for Araldite 985 polymer coatings.

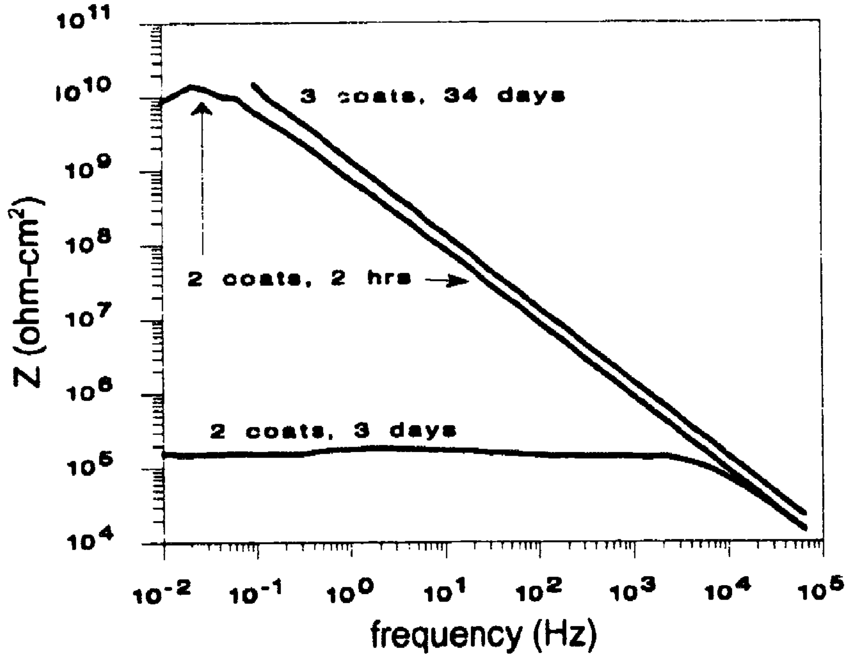

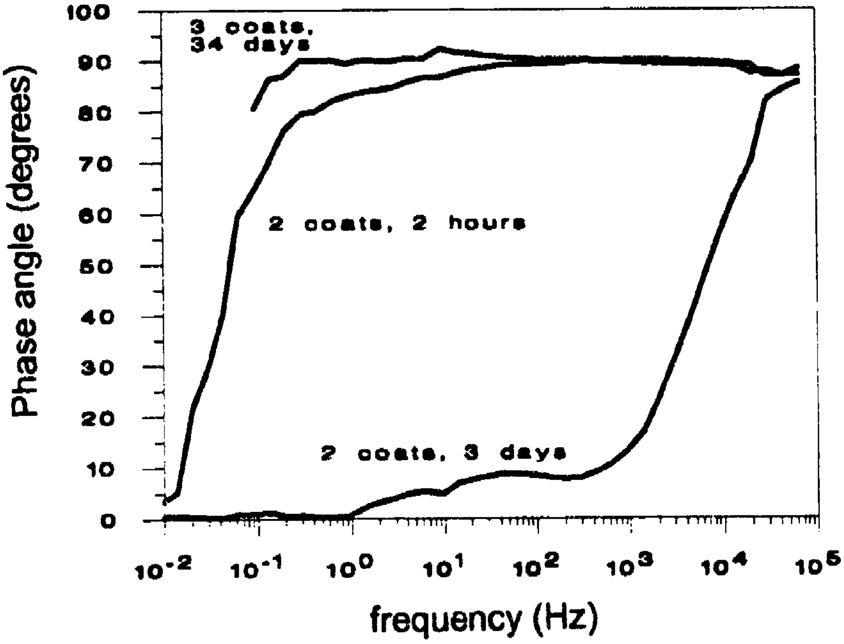

Figure 5.75 Bode plot for 2009/20% SiC with two coats of Araldite 985 after 2 hrs and 3 days and three coats after 34 days of exposure to 0.5 N NaCl.

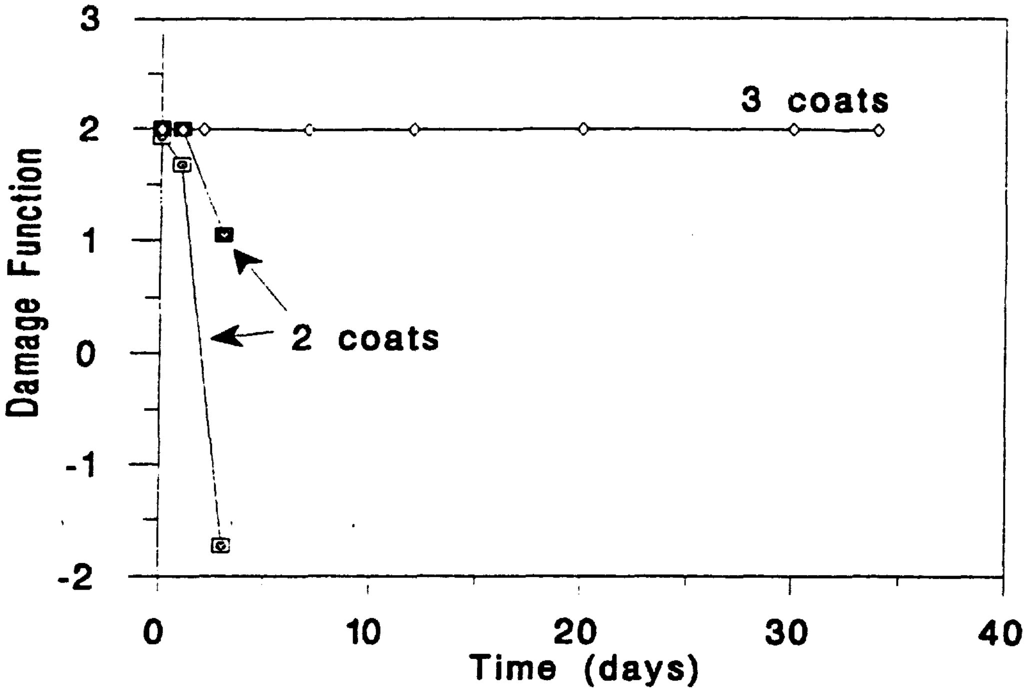

Figure 5.76 Damage function for 2009/20% SiC with two and three coats of Araldite 985 versus exposure time.

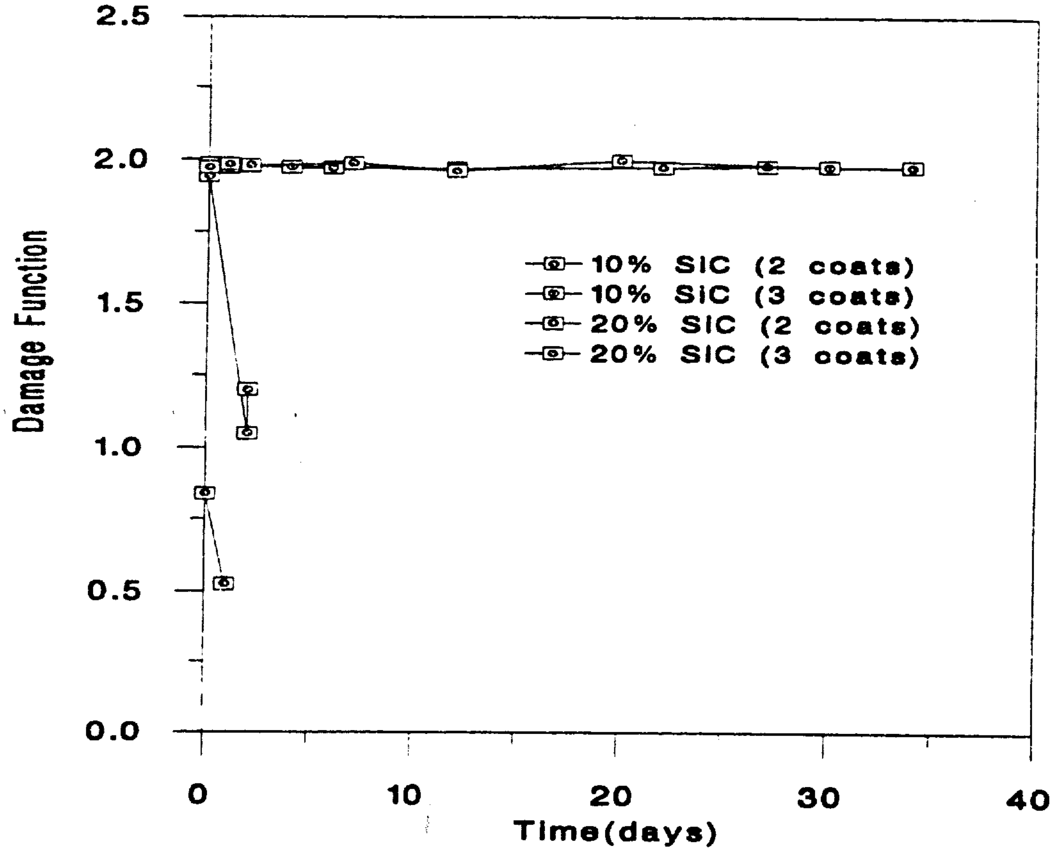

Figure 5.77 Damage function versus exposure time for A356/10% SiC and A356/20% SiC with two and three coats of Araldite 985.

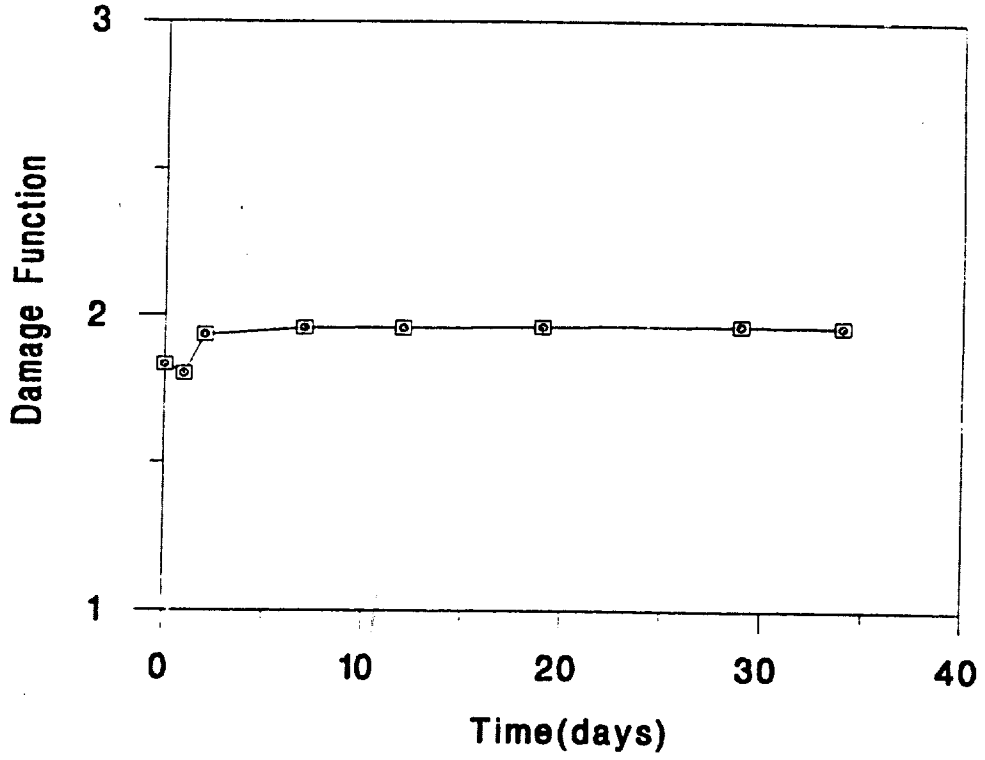

Figure 5.78 Damage function versus exposure time for 6061/10% Al_2O_3 with two coats of Araldite 985.

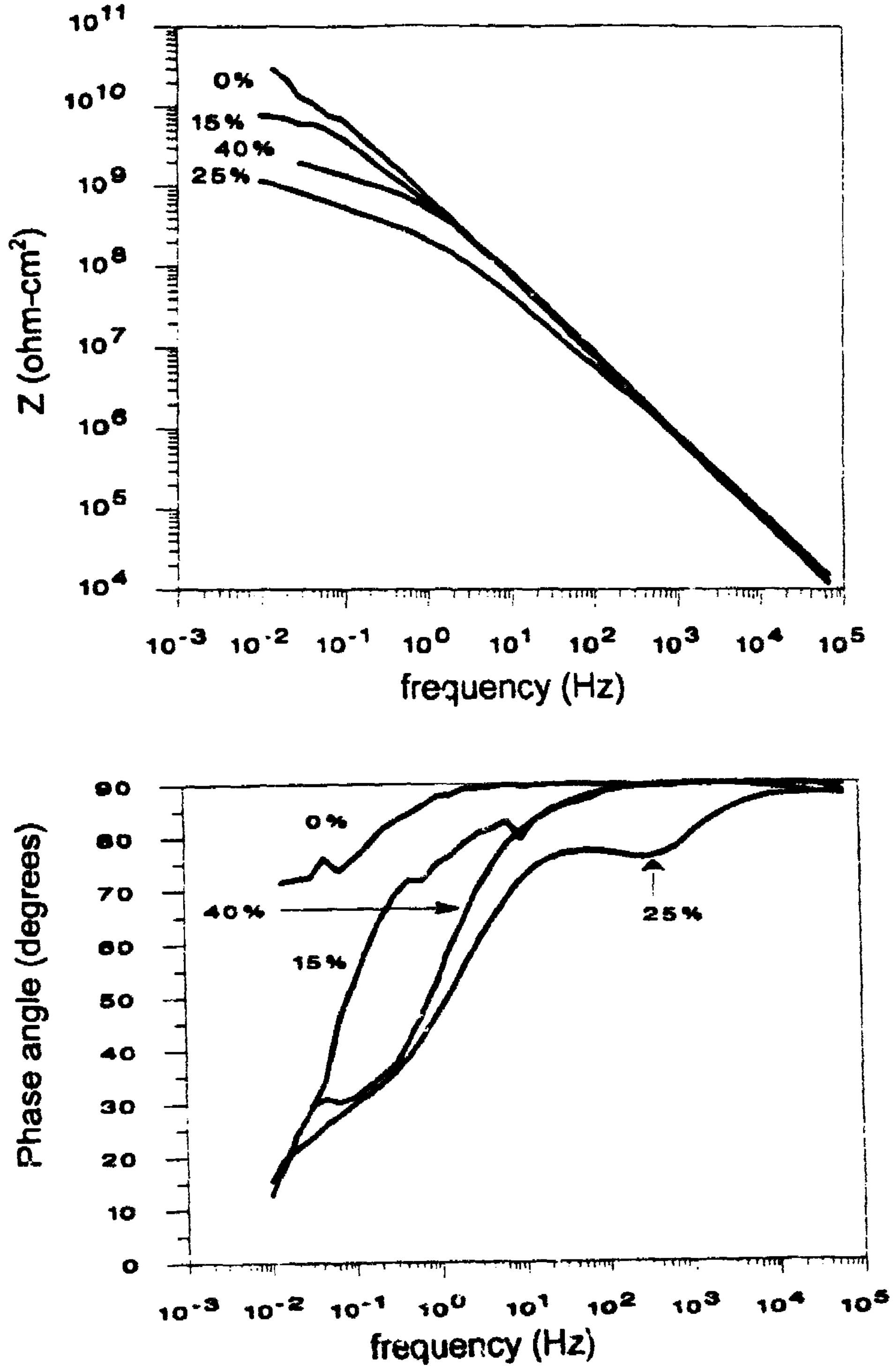

Figure 5.79 Bode plots for 6061/SiC MMCs with two coats of Araldite 985 after 34 days of exposure.

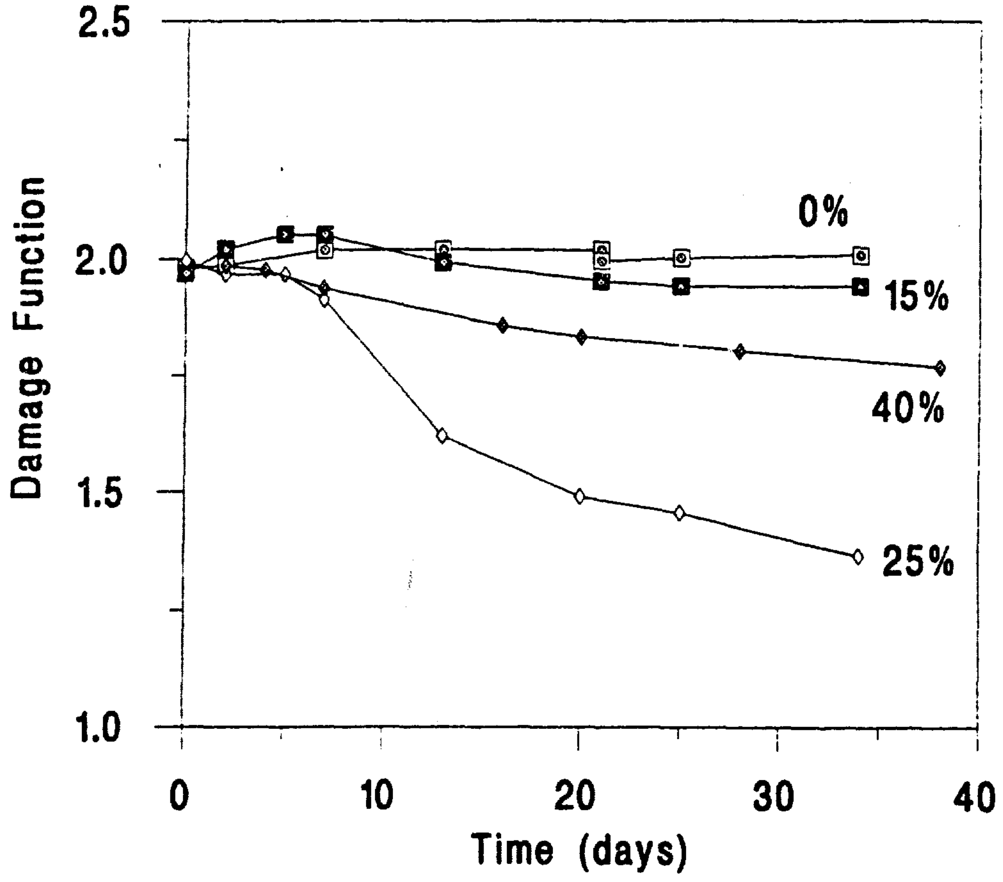

Figure 5.80 Damage function versus exposure time for 6061/SiC MMCs with two coats of Araldite 985.

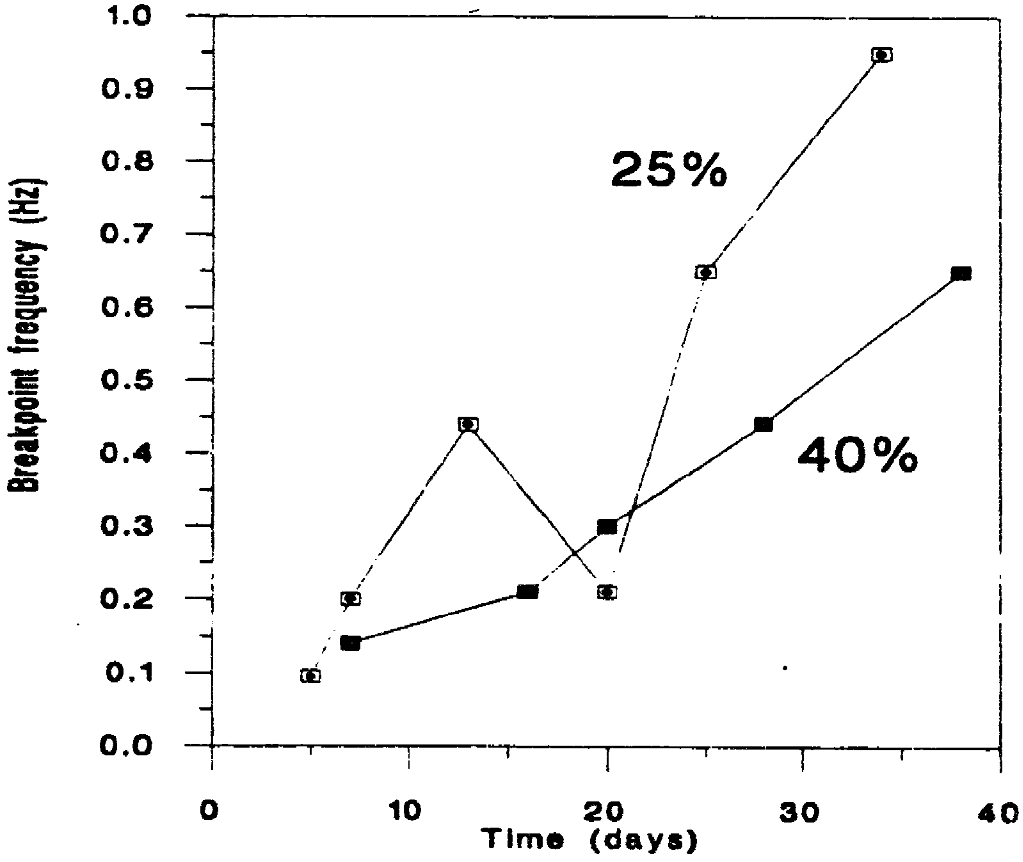

Figure 5.81 Lower breakpoint frequency versus exposure time for 6061/25% and 40% SiC MMCs.

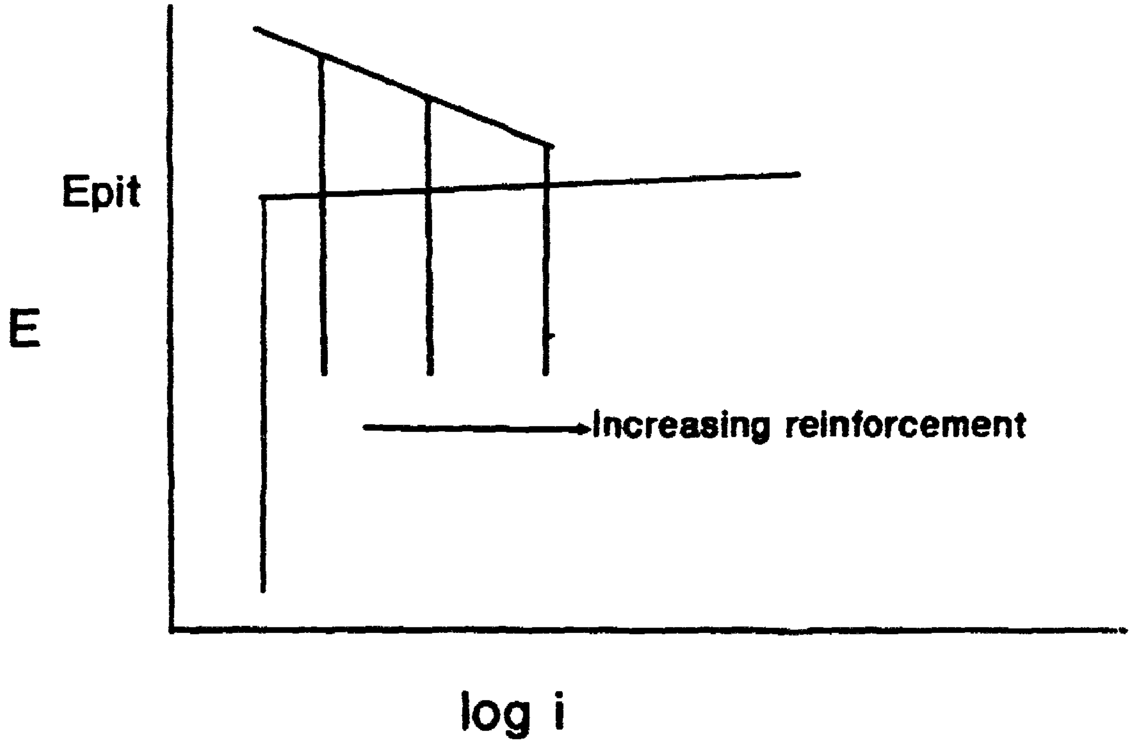

Figure 6.1 Schematic polarization curves for Al MMCs with increasing reinforcement concentration.

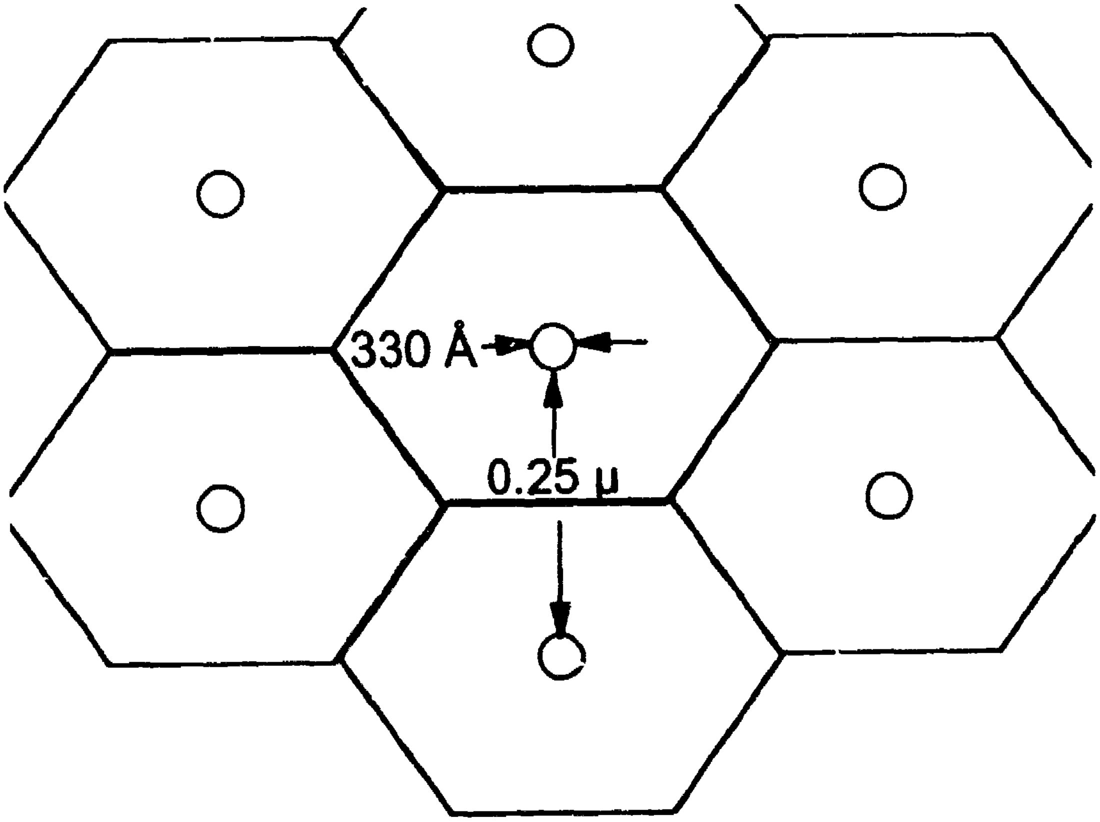

Figure 6.2 Schematic diagram of the top view of the porous layer for anodized Al. Approximate dimensions are from reference 107.

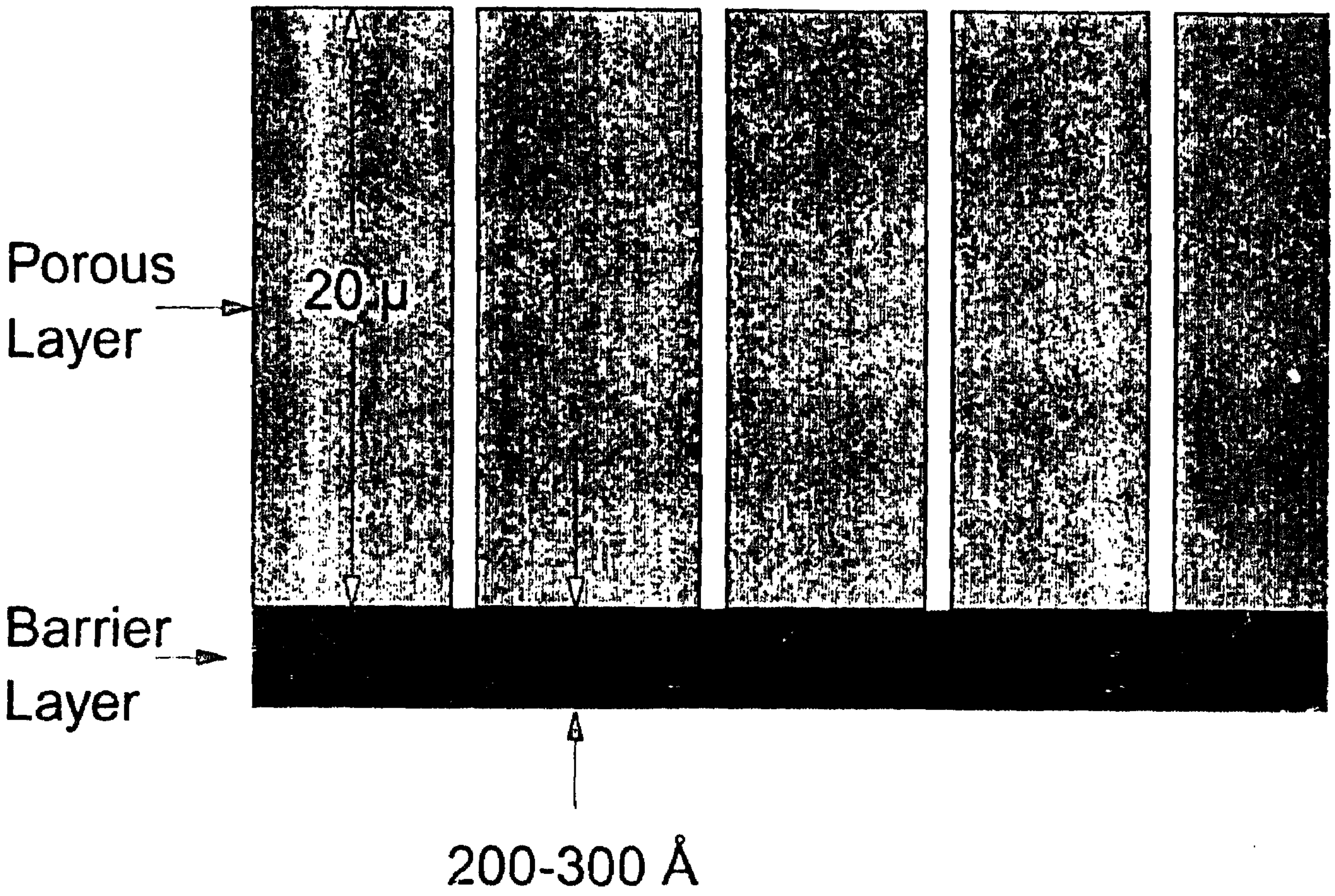

Figure 6.3 Schematic diagram of the cross-section of the porous and barrier layers of anodized Al. Approximate Dimensions are from references 6 and 107.

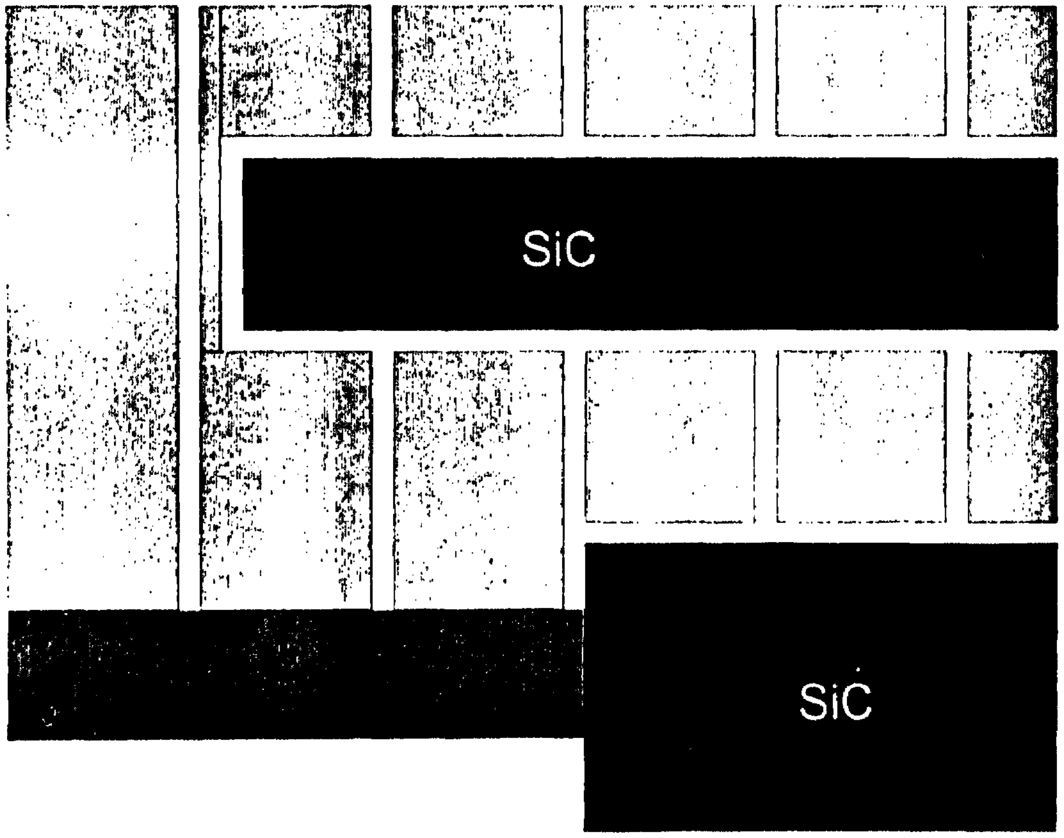

Figure 6.4 Schematic diagram of the cross-section of the porous and barrier layers of anodized Al MMCs.

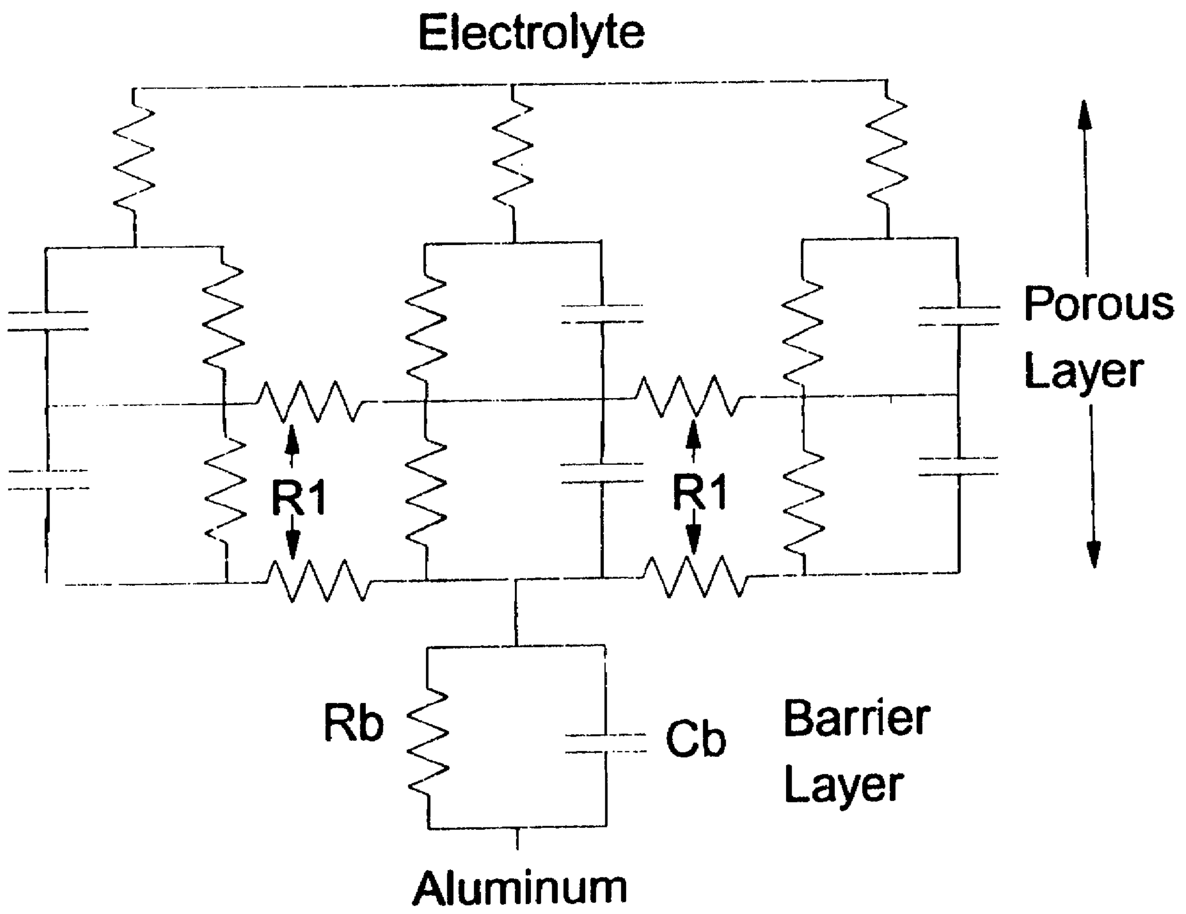

Figure 6.5 Branched network resulting from anodizing of Al MMCs.

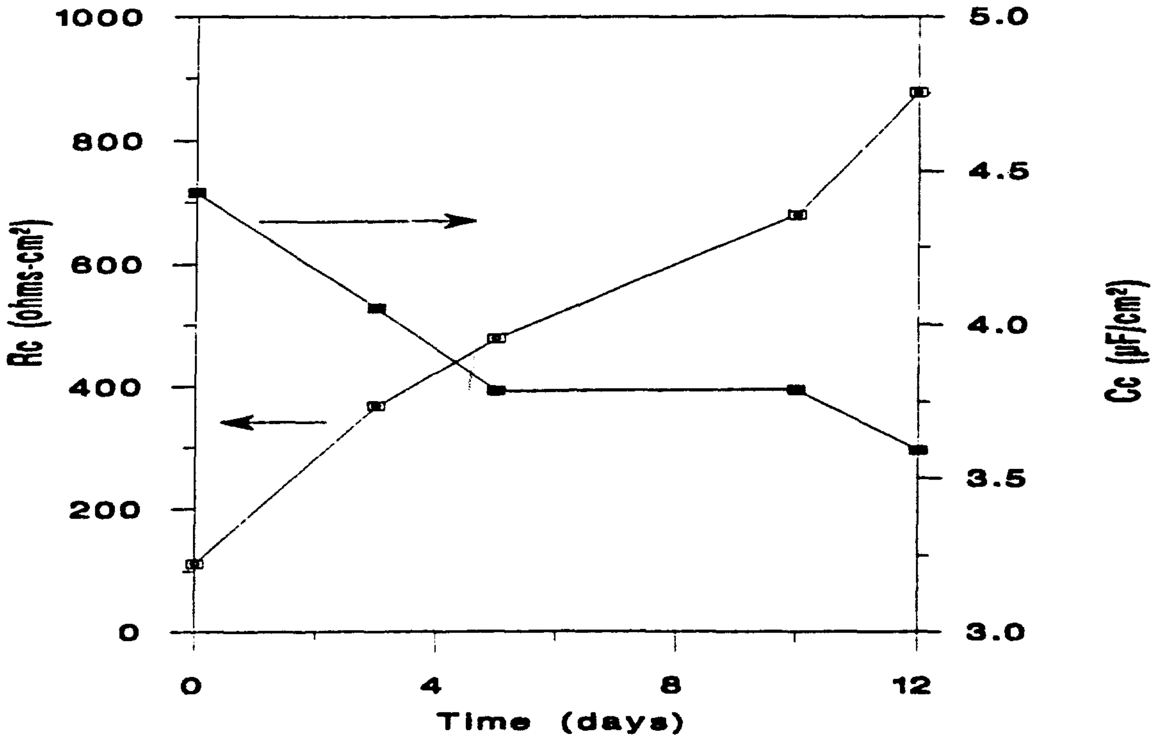

Figure 6.6 Coating resistance, R_c, and coating capacitance, C_c, versus exposure time for conversion coated AA6061.

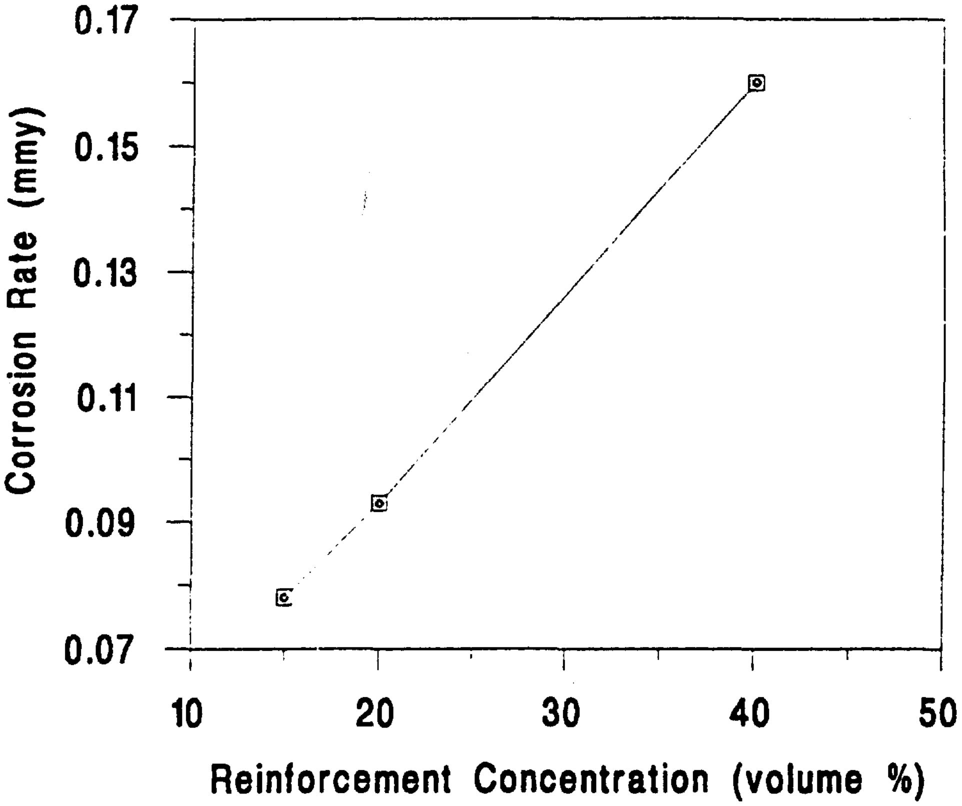

Figure 6.7 Calculated corrosion rate versus percent reinforcement for conversion coated 6061/SiC MMCs after 12 days of exposure to 0.5 N NaCl.